Bulletin 56
(Part 2 of 3 Parts)

THE SHOCK AND VIBRATION BULLETIN

Part 2

Modal Test and Analysis, Testing Techniques, Machinery Dynamics, Isolation and Damping, Structural Dynamics

AUGUST 1986

A Publication of
THE SHOCK AND VIBRATION
INFORMATION CENTER
Naval Research Laboratory, Washington, D.C.

Office of
The Under Secretary of Defense
for Research and Engineering

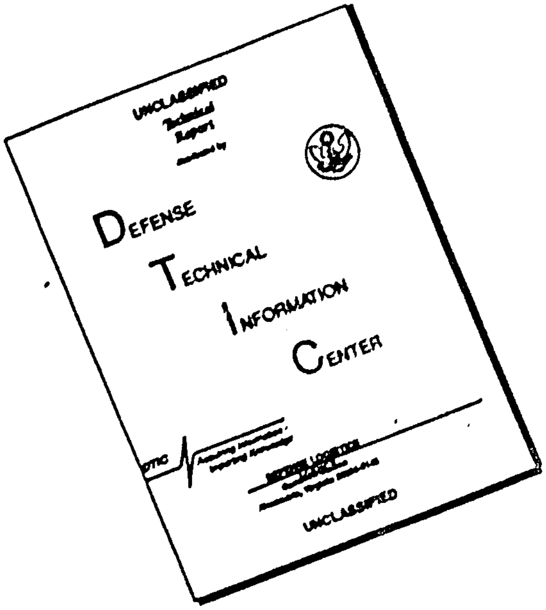

Bulletin 56
(Part 2 of 3 Parts)

THE
SHOCK AND VIBRATION
BULLETIN

AUGUST 1986

A Publication of
THE SHOCK AND VIBRATION
INFORMATION CENTER
Naval Research Laboratory, Washington, D.C.

The 56th Symposium on Shock and Vibration was held in Monterey, California, October 22-24 1985. The Naval Postgraduate School and the Defense Langauge Institute were the hosts.

Office of
The Under Secretary of Defense
for Research and Engineering

cont

Isolation and Damping

Structural Dynamics

Fatigue and Acoustics

CONTENTS

PAPERS APPEARING IN PART 2

Partial contents:

Modal Test and Analysis

Testing Techniques

Machinery Dynamics

PAPERS APPEARING IN PART I

Welcome

Invited Papers

Shipboard Shock

Blast and Ground Shock

Shock Testing and Analysis

PAPERS APPEARING IN PART 3

Invited Papers — Plenary A

Pyrotechnic Shock

Pyrotechnic Shock Workshop

SESSION CHAIRMEN AND COCHAIRMEN

56th Shock and Vibration Symposium
October 22-24, 1985, Monterey, CA

Date	Session Title	Chairmen	CoChairmen
Tuesday 22 October, A.M.	Opening Session	Dr. Young S. Shin, Naval Postgraduate School, Monterey, CA	Dr. J. Gordan Showalter Shock and Vibration Information Center, Naval Research Laboratory, Washington, DC
Tuesday 22 October, P.M.	Pyrotechnic Shock/ Shipboard Shock	Mr. Henry N. Luhrs, TRW Electronics Systems, Redondo Beach, CA	Dr. John DeRuntz, Lockheed Palo Alto Research Laboratory, Palo Alto, CA
Tuesday 22 October, P.M.	Blast and Ground Shock	Mr. James D. Cooper, Defense Nuclear Agency, Washington, DC	Dr. Anatole Longinow, Wiss, Janney, Elstner Associates, Inc. Northbrook, IL
Wednesday 23 October, A.M.	Plenary A	Dr. J. Gordan Showalter, Shock and Vibration Information Center, Naval Research Laboratory Washington, DC	
Wednesday 23 October, A.M.	Pyroshock Workshop, Session I, Data Interpretation, Design and Test Requirements	Mr. Daniel Van Ert, The Aerospace Corporation, El Segundo, CA	Mr. Henry N. Luhrs, TRW Electronics Systems, Redondo Beach, CA
Wednesday 23 October, A.M.	Modal Test and Analysis	Dr. Robert Coppolino, MacNeal Schwendler Corporation, Los Angeles, CA	Mr. Strether Smith, Lockheed Palo Alto Research Laboratory, Palo Alto, CA
Wednesday 23 October, A.M.	Testing Techniques	Mr. Steven Tanner, Naval Weapons Center, China Lake, CA	Mr. Peter Bouclin, Naval Weapons Center, China Lake, CA

Wednesday 23 October, P.M.	Pyroshock Workshop, Session II, Instrumentation, Data Acquisition, and Data Bank	Mr. Glen Wasz, TRW, San Bernardino, CA	Mr. Paul Strauss, Rocketdyne, Canoga Park, CA
Wednesday 23 October, P.M.	Pyroshock Workshop, Session III, Simulation and Testing	Mr. Dan Powers, McDonnell Douglas Astronautics, Huntington Beach, CA	Mr. Robert E. Morse, TRW, Redondo Beach, CA
Wednesday 23 October, P.M.	Machinery Dynamics	Mrs. Milda Z. Tamulionis, Vibration Institute, Clarendon Hills, IL	Mr. Robert L. Leon, Liberty Technology Center, Inc., Conshohocken, PA
Wednesday 23 October, P.M.	Isolation and Damping	Dr. Bhakta B. Rath, Naval Research Laboratory, Washington, DC	Mr. Ahid Nashif, Anatrol Corporation, Cincinnati, OH
Thursday 24 October, A.M.	Plenary B	Mr. Rudolph H. Volin, P.E., Shock and Vibration Information Center, Naval Research Laboratory, Washington, DC	
Thursday 24 October, A.M.	Structural Dynamics	Dr. John L. Gubser, McDonnell Douglas Astronautics Company, St. Louis, MO	Mr. David W. Gross, RCA Astroelectronics, Princeton, NJ
Thursday 24 October, A.M.	Fatigue, Acoustics and Fluid Flow	Mr. Leonard L. Shaw, Air Force Wright Aeronautical Laboratories, Wright-Patterson Air Force Base, OH	
Thursday 24 October, P.M.	Shock Testing and Analysis	Mr. John D. Favour, Boeing Aerospace Company, Seattle, WA	Mr. William J. Kacena, Martin Marietta Denver Aerospace, Denver, CO
Thursday 24 October, P.M.	Short Discussion Topics	Mr. Howard Camp, U.S. Army Electronics Research and Development Command, Ft. Monmouth, NJ	Mr. Tommy Dobson, 6585 Test Group, Holloman Air Force Base, NM

MODAL TEST AND ANALYSES

MULTIPLE TESTS CONCEPT FOR IMPROVED VALIDATION OF LARGE SPACE STRUCTURE MATHEMATICAL MODELS*

Wada, B. K.
Kuo, C-P
Glaser, R. J.

Jet Propulsion Laboratory
California Institute of Technology
Applied Technologies Section
Building 157, Room 507
4800 Oak Grove Drive
Pasadena, CA 91109

For the structural dynamic analysis of large space structures, the technology in structural synthesis and the development of structural analysis software have increased the capability to predict the dynamic characteristics of the structural system. The various subsystems which comprise the system are represented by various displacement functions; the displacement functions are then combined to represent the total structure. Experience has indicated that even when subsystem mathematical models are verified by test, the mathematical representations of the total system are often in error because the mathematical model of the structural elements which are significant when loads are applied at the interconnection points are not adequately verified by test. A multiple test concept, based upon the Multiple Boundary Condition Test (MBCT), is presented which will increase the accuracy of the system mathematical model by improving the subsystem test and test/analysis correlation procedure.

* The research described in this paper was carried out by the Jet Propulsion Laboratory, California Institute of Technology, under a contract with the National Aeronautics and Space Administration.

INTRODUCTION

Historically, most new designs of aircraft and space structures have been partially verified by full-scale dynamic ground tests prior to its initial flight. Even with the recent advances in computers and finite element codes, which allow solution of large complex structures, structures with dynamic characteristics which are significant to mission success have been tested at great expense. An example is the full-scale modal test of the Shuttle. Often, modal tests performed on large structures reveal errors or omissions in the system analytical model which had been verified by tests at the subsystem level. The major source of errors has been at the interconnection between the subsystems. This paper addresses an approach to obtain better test verified mathematical models at the subsystem level to obtain a better systems mathematical model using modal synthesis [1,2] methods. The work is of current and future interest because many large space structures currently (Space Station) under investigation must depend on validation of the models through subsystem testing. System testing of the Space Station is not feasible because of the large potential errors in ground testing, and the unavailability of the total system at one time and in one location.

The approach is based upon an extension of the Multiple Boundary Condition Tests (MBCT) [3,4] approach developed for obtaining good dynamics data on a large flexible antenna rib built by Lockheed Missiles and Space Company (LMSC) as a part of a wrapped rib antenna effort sponsored by NASA/JPL. Modal test approaches considered for the rib revealed the potential difficulty in obtaining valid results using the traditional state-of-the-art test approaches. The MBCT takes advantage of the flexibility of the large structures, which makes the existing standard modal test procedures very difficult, if not impossible, to implement on the ground. To demonstrate the feasibility of testing a flexible rib to obtain data required for the MBCT approach, a series of static and dynamic tests were successfully performed on a single rib.

Since the parameters of the mathematical model in the vicinity of the test supports may not be adequately tested in a single test configuration, the system should be analyzed and tested with a variety of constraint conditions and constraint locations. This will provide the data necessary to upgrade [5,6] all the mass and stiffness parameters of interest in the structural model. Additionally, the increased quantity of test data to estimate any given mass and stiffness parameter will improve the parameter estimates used for the mathematical model. This is the technical reasoning behind the MBCT approach.

In the MBCT approach, the increased number of test data improved the estimate of the mathematical parameters. The approach to be presented is to increase the number of the estimates of the significant structural parameters when the subsystem interfaces are loaded by performing a larger variety of tests at the interface. The standard approach is to statically load the subsystem interfaces at which the subsystems are interconnected to obtain the interface stiffness and to determine the internal load distribution. Additional estimates of the structural parameters that are significant to the interface stiffness and the internal load distribution can be obtained by performing a series of simple modal and/or static tests which loads the interfaces of the subsystem. The number and type of tests are determined by the number of estimations of the significant structural parameters necessary to obtain the required accuracy. The paper will include a computer simulation to illustrate and validate the approach.

MODAL SYNTHESIS

Development of a system structural dynamic model by combining various subsystems represented by an appropriate set of displacement functions has been an effective and reliable approach. Future space structures such as Space Station, will rely upon a mathematical model of the total system which is comprised of test verified subsystems. The size of the total structure and the evolution of the structure over many years will preclude the availability of the structure for dynamic ground testing. Even if the structure were available for test, the ability to reliably test the structure is questionable. Modal synthesis of subsystems has been used to accurately define the total system dynamic characteristics; however, special procedures must be used to test and update portions of the mathematical models which are affected by loads at the interconnection points of the subsystems. A brief review of modal synthesis is presented for clarity.

Figure 1 illustrates the subsystems 1,2... interconnected at the various attachment points. In most cases, the displacement functions used to represent each subsystem must include more than a set of rigid body and normal modes to properly represent the dynamics of the entire system. Various types of displacement functions which can be used are:

$$\{u\} = q_R^i[\phi]_R^i + q_C^i[\phi]_C^i + q_N^i \phi_N^i + q_A^i[\phi]_A^i + q_Q^i[\phi]_Q + q_I^i[\phi]_I^i + q_{RE}^i[\phi]_{RE}^i + \ldots + q_U^i[\phi]_u^i \quad (1)$$

where
$[\phi]$ R = rigid body modes
$[\phi]$ C = constraint modes
$[\phi]$ N = normal modes
$[\phi]$ A = attachment modes
$[\phi]$ Q = quasi-static modes, displacement functions corresponding to a combination of the six rigid body accelerations to a structure
$[\phi]$ I = imposed modes, displacement functions arbitrarily selected as important and significant to describe the system dynamics of the structure
$[\phi]$ RE = relative modes, subset of imposed modes where displacement functions representing relative motions on the subsystem are defined.
$[\phi]$ U = user defined modes, any other displacement function which the engineer may consider to be important.

Superscript i is used to represent subsystem i.

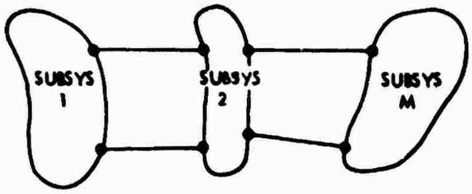

FIGURE 1

Effective test procedures have been developed to measure normal modes to verify the terms in the mathematical model which are significant to the normal modes. Many of the errors in development of the system modes are a result of inadequacies of the test program to verify the terms in the mathematical model represented by displacement functions which should be introduced to account for the influence by the various subsystem on the others through the interconnection points. Although most of the displacement functions shown in Eq. (1) are in this category, emphasis is usually placed in the validation of $[\phi]_N^i$ through modal testing of subsystem and very little emphasis is placed in test validation of the portions of the mathematical model associated with the other displacement functions.

A description of the substructure combination into a system dynamic equation is illustrated in References 1 and 2.

TEST VERIFICATION OF MATHEMATICAL MODEL

As mentioned previously, the use of modal test results to verify the mathematical model of the subsystem verifies only a subset of the significant terms of the mass and stiffness matrices. Modal test data can be used to verify the mass terms corresponding to joints with large relative deflection in the experimental modes and the stiffness terms corresponding to structural members which are loaded by the experimental modes. Often the structural members which are important for loads transmission through the subsystem interconnections are not experimentally verified. The objective of the paper is to present a technique to verify these structural members or the elements in the stiffness matrix which represent these members.

Several methods can be used to establish the elements of the stiffness matrix or structural members which have been verified by a modal test and the structural members which are significant in the dynamic characteristics of the total structural system. One obvious selection is to determine by analysis and/or test those members which transmit the largest forces during the modal test. However, the magnitude of force, as a measure of importance, can be misleading because a very flexible member may have a small force and yet contribute significantly to the final system dynamic modes. A parameter which has been valuable in the analysis/test correlation effort and promises to be valuable in the mathematical model updating process is strain energy. In fact, strain energy is directly related to the stiffness matrix and kinetic energy is directly related to the mass matrix. The other advantage of strain energy and kinetic energy is that they are algebraic terms which can be summed in any manner defined by the engineer. Thus the total number of quantities to be identified can be reduced to an arbitrarily small manageable quantity.

Although the following discussion will be based upon stiffness matrices, in practice the objective will be to identify errors in parameters which define the physical structural element from which [K] is derived.

The subsystem stiffness matrix can be subdivided into three submatrices:

$$[K]^i_T = [K]^i_N + [K]^i_I + [K]^i_u \qquad (2)$$

where

$[K]^i_T$ = total stiffness matrix of subsystem i

$[K]^i_N$ = subset of the total stiffness matrix of subsystem i which are verified by modal tests

$[K]^i_I$ = subset of the total stiffness matrix of subsystem i which are significant to the system modes but not verified by modal tests

$[K]^i_u$ = subset of the total stiffness matrix of subsystems i which are relatively unimportant to the system modes.

A similar set of equations can be written for the mass matrix. An outline of a procedure which can be used to establish the above submatrices is:

(1) The $[K]^i_T$ is the total mathematical model representation of subsystem i and it is assumed to be complete. Namely, the model is an adequate discretization of the structure.

(2) The $[K]^i_N$ is defined as the stiffness matrix of all structural members of subsystem i that contains 10% or more of the strain energy in any of the significant modes (the strain energy of the structural members are most likely evaluated by analysis and may be partially verified directly during the modal test). The stiffness elements of $[K]^i_N$ are assumed to be updated and verified by using the subsystem modal data and the analysis/test [5,6] correlation procedures.

(3) The $[K]^i_I$ is defined as a subset of the stiffness matrix from all structural members of the mathematical model representing subsystem i which contains 3% or more of the strain energy of any significant mode from the original system dynamic analytical model. The system dynamic model is created by combining the various subsystems using modal synthesis methods. The $[K]^i_I$ is determined from the members which meet the above criteria minus $[K]^i_N$. The matrix $[K]^i_I$ is mathematically determined. Mathematically, the characteristics of the subsystems should be varied within anticipated inaccuracies to determine if additional structural members should be included in the definition of $[K]^i_I$. Especially if small changes in the subsystem characteristics might introduce a new mode shape such as a non-symmetric mode which didn't previously exist.

(4) The $[K]^i_u$ is the stiffness matrix developed from structural members that are excluded from $[K]^i_N$ and $[K]^i_I$.

Similar procedures can be used for the mass matrix elements. In the establishment of a mathematical modal to correlate with the modal test data for the Galileo program, the criteria to retain all mass degrees-of-freedom which correspond to 10% or more of the kinetic energy in any of the modes selected for correlation gave very favorable results.

As stated before, the objective is to test verify and update the mathematical terms relevant to describing the overall dynamic characteristics of the total system. Current methods have been developed and the need has been established to verify and update $[K]^i_N$. Many of the problems have arisen because the need to validate and update $[K]^i_I$ have not been specifically identified. The primary objective of the paper is to identify and to define a test and test/analysis procedure to update $[K]^i_I$ to represent the structure.

TEST VERIFICATION $[K]^i_I$

The test verification of the structural members which contribute to $[K]^i_I$ is obtained by loading the subsystem i at the interconnection points. The approach used is an extension of the Multiple Boundary Condition Test (MBCT) [3,4] approach. The MBCT has been proposed to verify the mathematical models of structures by ground tests of structures which can't be ground tested because of its sizes and/or flexibility by conventional test methods. The MBCT approach obtains a number of test data from a number of various test conditions established by varying the boundary conditions. Any number of estimates for stiffness and/or mass terms of interest can be obtained at the discretion of the engineer. By this method a "good" estimate of the stiffness and mass terms can be obtained.

For the verification of $[K]^i_I$, the principal objective will be to apply a number of static and/or dynamic forces at the interconnection points to obtain a multiple estimate of the terms of $[K]^i_I$. In most cases the boundary conditions will not be changed. The multiple set of forces applied during the test should be designed to load each structural member comprising $[K]^i_I$ to a significant strain energy level by at least one set of forces. A pre-test analysis should be performed to establish the sets of forces which meets the above criteria and provides the required number of estimates.

Examples of the type of loads that can be applied at the interconnection point I as shown in Figure 2 are:

(1) Any number of static force and moment loads.

(2) Any number of modal tests using various combinations of test masses (M(test)) and test structure (l(test)).

For multiple interconnections, loads may be simultaneously applied to the various interconnection points.

The above procedure describes a method by which a test verified model of $[K]^i_I$ can be accurately obtained. Subsystem tests with validated $[K]^i_N$ and $[K]^i_I$ values can then be used with confidence as a building block for the total system.

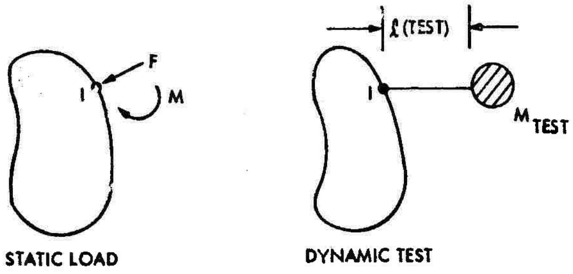

FIGURE 2

EXAMPLE

The sample problem selected to illustrate the approach proposed in this paper is shown in Figure 3. The two-dimensional truss structure is comprised of two subsystems, 1 and 2 which are interconnected at joints 15 and 16. Errors in the mathematical model are in members 25 and 27 (the area of member 25 is in error by 100% and the area of member 27 is in error by 100%) and the objective is to locate and correct the errors. The resonant frequencies of the structure, in Hz, with and without the errors are listed in Table 1.

Since the errors were defined in the example problem to be in subsystem 1, the mathematical updating procedure is limited to subsystem 1. Usually the tests and test/analysis updating are performed on all subsystems.

The results from a modal analysis of subsystem 1, shown in Figure 4, for the structure with and without errors in members 25 and 27 are listed in Table 2.

The members with 10% or more of the strain energy in any of the first three modes from the subsystem modal test are indicated by bold lines in Figure 4. Since errors in these members can be detected and updated using the standard modal test methods [7,8], those elements will be assumed to be correct at the subsystem level. Note that errors in members 25 and 27 cannot be detected and corrected from a subsystem modal test as evidenced by the small difference in the frequencies shown in Table 2. The stiffness matrix represented by the members shown in the bold lines in Figure 4 is $[K]^1_N$.

The members with 3% or more of the strain energy in the first three (3) modes of the total system of Figure 3 are indicated by the dashed lines. The accuracy of these members are significant to the final system modes. Thus the other members are relatively unimportant. These members are shown as unhighlighted lines in Figure 4. The stiffness

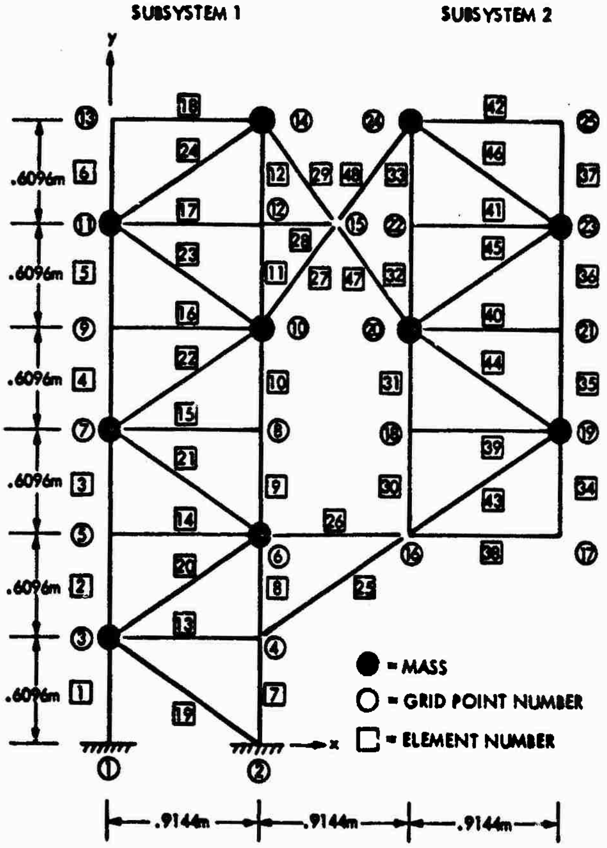

FIGURE 3. SAMPLE PROBLEM TOTAL SYSTEM

TABLE 1

System Frequencies, With and Without Errors

Mode No.	Correct Structure (Hz)	Structure with Errors (Hz)
1	4.044	4.030
2	15.209	14.748
3	27.054	26.133
4	30.077	29.701
5	35.832	35.809
	$A25 = .00645m^2$ $A27 = .00194m^2$	$A25 = .00323m^2$ $A27 = .00097m^2$

TABLE 2

Frequencies, Subsystem 1 With and Without Errors

Mode No.	Correct Subsystem 1 Structure (Hz)	Subsystem 1 Structure with Errors (Hz)
1	6.195	6.195
2	21.003	21.000
3	31.125	31.111
4	41.313	41.266
5	57.108	56.955
	A25 = .00645m^2 A27 = .00194m^2	A25 = .00323m^2 A27 = .00097m^2

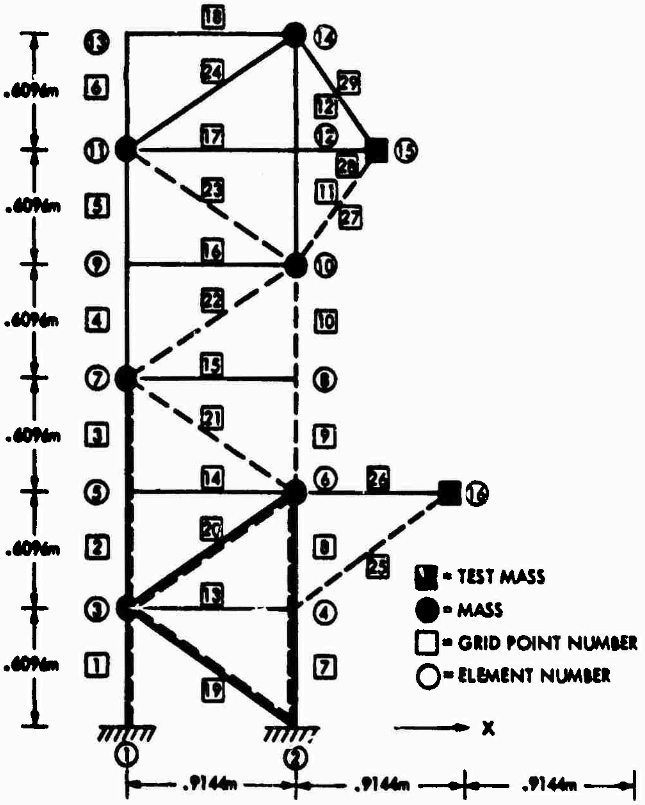

FIGURE 4. SUBSYSTEM 1

TABLE 3

Test Vs Members Which Are Significantly Loaded

Member Load/Test	1	2	3	4	5
21, 22, 23					X
9, 10	X		X		X
25		X		X	
27			X		

TABLE 4

Comparison of the Member Areas, Original vs Estimated vs Theoretically Correct

Member	Original Math Model With Error (m^2)	Estimates of Correct Value (m^2)	Theoretical Correct Values (m^2)	% Error
21,22,23	.00129	.00137	.00129	+ 6.45
9,10	.00258	.00202	.00258	-21.6
25	.00323	.00530	.00645	-17.89
27	.00097	.00195	.00194	+ 0.97

matrix associated with the members identified as significant in the system modes but not identified in the subsystem 1 modal test is $[K]_I^i$. (Members with only the dashed lines, namely 21,22,23,25,27,9, and 10). The objective is to apply various sets of loads at the interface joints, 15 and 16, in order to identify and correct the potential errors in $[K]_I^i$. Since the members which represent $[K]_I^i$ are four different types of members, (21,22, and 23 are identical; and 9 and 10 are identical) only four members parameters have to be updated to match with the test data.

The sets of loads applied to subsystem 1 at the interfaces are:

(1) Modal test with a "test" mass at joint 15

(2) Modal test with a "test" mass at joint 16

(3) Force at joint 15 in the x and y direction

(4) Force at joint 16 in the x and y direction

(5) Force at joint 10 in the x and y direction

The members with more than 10% strain energy in the above sets of loads are in Table 3.

Note that all of the loading conditions are relevant to the identification of the $[K]_I^i$ matrix, and at least one member type has significant strain energy from the set of five (5) loading conditions.

Using the system identification procedures which combine the static and dynamic test results, the re-estimates for the members, after only one iteration, are shown in Table 4.

Using the estimates of the correct values in the overall system analysis, the results are as shown in Table 5.

A comparison of the procedure proposed in this paper indicates that the model can be updated at the subsystem level with sufficient accuracy to give good system dynamic characteristics. The accuracy of the solution will improve as the number of iterations to update the subsystem model is increased.

CONCLUSION

The sample problem shows that the proposed procedure can be used to systematically test verify the subsystem models to the accuracy required to provide confidence in the final system model without a system test. At this time, the procedure doesn't appear to be limited in its application.

Additional work is in progress to establish the validity of the arbitrarily selected strain energy criteria for the identification of the significant elements and possible procedures to

TABLE 5

Comparison of Frequencies, Correct Structure vs Estimated Structure

Mode No.	Correct Structure (Hz)	Estimated Structure (Hz)
1	4.044	4.041
2	15.209	15.015
3	27.054	26.814
4	30.077	30.097
5	35.B32	36.222
	A21,22,23 = .00129m^2	A21,22,23 = .00137m^2
	A9, 10 = .00258m^2	A9, 10 = .00202m^2
	A25 = .00645m^2	A25 = .00530m^2
	A27 = .00194m^2	A27 = .00195m^2

minimize the change in the "accurately modeled members" as the errors in the other members are identified.

REFERENCES

1. Bamford, R., Wada, B., Garba, J., and Chisholm, J., "Dynamic Analyses of Large Structural Systems," Synthesis of Vibrating Systems, The American Society of Mechanical Engineers, New York, NY, November 1971.

2. Craig, Jr., R. R., "A Review of Time-Domain and Frequency-Domain Component Mode Synthesis Method," Combined Experimental/Analytical Modeling of Dynamic Structural Systems, AMD-Vol. 67, The American Society of Mechanical Engineers, New York, NY, June 24-26, 1985.

3. Wada, B. K., Kuo, C-P, and Glaser, R. J., "Extension of Ground-Based Testing for Large Space Structures," presented at the 26th AIAA SDM Meeting, Orlando, FL, April 1985, Paper No. AIAA-85-0757-CP.

4. Wada, B. K., Kuo, C-P, Glaser, R. J., "Multiple Boundary Condition Test (MBCT) Approach to Update Mathematical Models of Large Flexible Structures," was presented at the 1985 SAE Aerospace Technology Conference & Exposition, Long Beach, CA, October 14-17, 1985.

5. Chen, J. C., and Garba, J. A., "Structural Analysis Model Validation Using Modal Test Data," Combined Experimental/Analytical Modeling of Dynamic Structural Systems, AMD-Vol. 67, The American Society of Mechanical Engineers, New York, NY, June 24-26, 1985.

6. Wada, B. K., "Test and Analysis Correlation for Structural Dynamic Systems," Presented at the Second International Symposium on Aeroelasticity and Structural Dynamics, Aachen, Germany, April 1-3, 1985.

7. Chen, J. C., "Evaluation of Modal Testing Methods," AIAA Paper No. 84-1071 presented at the AIAA Dynamics Specialist Conference, May 17-18, 1984, Palm Springs, CA.

B. Wada, B. K., "Structural Qualification of Large Spacecraft," was presented at the AGARD-SMP Meeting on Mechanical Qualification of Large Flexible Spacecraft Structures, Oberammergau, Germany, September 9-10, 1985.

Discussion

Mr. Pinson (NASA Langley Research Center): I endorse what you are saying, Ben, because I think a systematic approach to multiple component testing is something that is badly needed. I think the question of directly addressing the interface problem is really at the heart of the matter. One of the things that is not addressed, and maybe it should not be addressed in this particular environment even though I think it is pertinent, is the question of when these tests are run. Typically, you don't get access to full scale hardware until way after CDR, and the spacecraft is about to fly. Unless you uncover a major "show-stopper" at that time, you will not really influence much other than to say, "Well, I have to go back and readjust my math model." I think you would like to establish that confidence early in the program. One way to do that is through the judicious use of models, which I noticed you didn't mention in your talk. I was wondering if you would comment on getting that confidence early in the program, and how you go about doing that.

Mr. Wada: I think there are certain pitfalls with the method that I used because you have to use the overall system dynamic models to determine which elements are important before anything is ever built. I think this is where perturbation methods, etc. really have to be incorporated - where you have to look at the overall system models and begin to perturb certain members. You have to say, "Look, this member may not be as stiff as it might finally be in the final situation," and run through fifty different conditions to really get an idea as to what the different possibilities are. So, you can't run just one system model, and say, "Yes, these are the important members," because the final design may not be the design due to changes during the program itself. However, I think if you run enough cases, you can begin to identify those members that might be important. That is the only way I know, Larry, of trying to handle some of the problems that you have.

Mr. Pinson: Whst about the dynamic characteristics of the joints, or the influence of joint slop on the dynamic characteristics of the joints or their adjacent members?

Mr. Wada: But the problem is you only know that after you have the model that you will fly, and if you can get at the model you will fly. I think some people feel you can predetermine the dynamic characteristics of joints or the influence of joint slop on the dynamic characteristics. Some people might feel, "Well, that will be very difficult to do," and the only way you will really know is once the entire structure has been built. However, I think this procedure requires getting at the flight structure. You might possibly attach another subsystem to the flight structure once it is flown; you may have to redesign the subsystem that you intend to attach to it to accommodate the differences in the final model versus what you thought the model would be. So, I think this approach will be very interactive.

THE ALGORITHM AND APPLICATION OF A NEW MULTI-INPUT-MULTI-OUTPUT MODAL PARAMETER IDENTIFICATION METHOD

Lingmi Zhang
Structural Vibration Research Lab.
Nanjing Aeronautical Institute
Nanjing, CHINA

and

Hiroshi Kanda
Yanmar Diesel Engine Co.
1-32 Chayamachi, Kita-ku
Osaka 530, JAPAN

This paper presents a new multi-input/multi-output modal parameter identification method that makes direct and simultaneous use of multiple frequency response function data with respect to multiple reference locations to estimate a global set of modal frequencies, damping ratios, mode shapes and modal participation factors. By employing the singular-value decomposition technique, the rank of the frequency response function matrix, i.e. the approximate number of effective modes in the frequency range of interests, is determined. A minimum-order system matrix is calculated by principal component decomposition and generalized inverse techniques. Modal parameters are then extracted by solving a standard eigenvalue problem.

INTRODUCTION

Experimental modal analysis has been widely involved in dynamic design engineering. The accuracy and consistency of modal data bases derived from parameter identification are becoming increasingly important for the purpose of finite element model validation, structural modification and experimental/analytical modeling.

With respect to modal testing, the trend in recent years is to apply multiple input excitation [1] and to measure multiple response functions. The frequency response functions estimated from the multi-input/multi-output technique are generally more accurate and consistent because of uniform distribution of the excitation energy and hence more uniform response level. Another attractive benefit of multiple input excitation is that the total test time can be reduced.

In the area of modal parameter identification, great progress has been achieved in the past few years. Multi-input/multi-output parameter estimation methods in the time domain have been developed to take full advantage of redundancy amd consistency with respect to multiple input or reference locations, such as the Polyreferense Complex Exponetial method [2], the Eigensystem Realization Algorithm [3] and the Direct Parameter Estimation technique [4]. The multi-input/multi-output methods not only improve the quality of the parameter estimation, but also have the ability to handle closely spaced modes, repeated roots and high damping cases. The user interaction and judgement is also reduced.

Several shortcomings, however, still exist in the time domain multi-input/multi-output modal parameter identification methods. One of the major problems is in the determination of the number of effective modes for a measured data set. The second problem is how to distinguish between computation modes and actual modes of the structure to be identified. Computation modes for the time domain estimation algorithms are necessary for unwanted effects, such as noise, leakage and nonlinearity. Most time domain methods employ impulse response function data calculated from measured frequency response function and hence introduce another source of error -- so-called "time domain leakage" [5].

This paper presents a new frequency domain multi-input/multi-output modal parameter identification method. The new method (called the Frequency Domain Poly-Reference method, FDPR) makes direct and simultaneous use of a measured frequency response data set relative to all reference locations to identify a global set of modal parameters. By employing the singular-value decomposition technique in the frequency domain, the rank of the frequency response function matrix, i.e. the number of effective modes in the frequency range of interest, can be determined easily. Therefore, the shortcomings of the time domain polyreference methods mentioned above can be avoided. As a result, user interaction and judgement will be further reduced. The principle component response analysis technique is then used to calculate a minimum order system matrix. Modal parameters -- modal frequencies, damping ratios and mode shapes -- can be determined by solving an eigenvalue problem. Modal participation factors is calculated by a least square approach. Analytical frequency response function can then be synthesized from the identified modal data base.

After discussion of the theory and algorithm of the frequency domain polyreference method, three application examples are given to demonstrate the features of the method, such as the ability of extracting accurate and consistent modal parameters with noise-contaminated measured frequency response data, and the capability to handle very closely spaced modes and repeated-root cases. The first example uses noise-contaminated simulated data from an assumed system. The second application example processes the data from impulse testing of a circular plate. Experimental results for a more complex structure -- an aircraft are shown as the third example.

THEORY AND ALGORITHM

Basic Equations

For a linear, viscously damped multi-input/multi-output mechanical structure, one can derive the relationship between inpulse response functions and modal parameters as follows [6],

$$H(t) = \Phi e^{\Lambda t}\Gamma \tag{1}$$

where

$H(t)$	$(m \times l)$ impulse response function matrix, m and l are the number of measurement coordinates and reference locations, respectively
Φ	$(m \times 2n)$ mode shape matrix, n is the number of modes,
Λ	$(2n \times 2n)$ diagonal eigenvalue matrix,
Γ	$(2n \times l)$ modal participation factor matrix.

In the Laplace domain, one obtains,

$$H(s) = \Phi[sI-\Lambda]^{-1}\Gamma \tag{2}$$

where

$H(s) = L[\,H(t)\,]$, transfer function matrix,

Eigenvalue problem

In the frequency domain, "displacement" and "velocity" frequency response function (FRF) matrices with dimension of $m \times l$ can be expressed, according to the above basic equations, as

$$H(j\omega) = \Phi[sI-\Lambda]^{-1}\Gamma + R_2 \tag{3}$$

$$\dot{H}(j\omega) = \Phi\Lambda[sI-\Lambda]^{-1}\Gamma + \dot{R}_2 \tag{4}$$

where Λ is $n \times n$ diagonal matrix, whose elements are the eigenvalues with positive imaginary part, Φ is corresponding $m \times n$ eigenvector matrix, and Γ is $n \times l$ modal participation factor matrix (for simplicity, the same notations are used). The influences of complex conjugate modes are expressed by residual terms R_2 and $\dot{R}_2$, respectively. The following matrix equation can be derived,

$$\begin{bmatrix} H(j\omega) \\ \dot{H}(j\omega) \end{bmatrix} = \begin{bmatrix} \Phi \\ \Phi\Lambda \end{bmatrix} Q(j\omega) \tag{5}$$

where, for the purpose of simplicity, residual terms are omitted and

$$Q(j\omega) = [sI-\Lambda]^{-1}\Gamma$$

For the most practical applications, the number of measurement coordinates is larger than the number of modes in the frequency range of interest, i.e.,

$$m > n$$

Therefore, the matrix $\begin{bmatrix}\Phi \\ \Phi\Lambda\end{bmatrix}$ has at least m more rows than columns. There must exist an m×m nontrivial matrix A such that

$$[A:1]\begin{bmatrix}\Phi \\ \Phi\Lambda\end{bmatrix} = 0 \qquad (6)$$

The Equation (6) can be placed in the form of a standard eigenvalue problem,

$$A\Phi = \Phi\Lambda \qquad (7)$$

The matrix A is referred to the system matrix (in physical coordinates) and contains information characterizing the complete set of modal parameters of the structural system. Due to the possibility of repeated roots, the eigensolvers from the EISPAC library [7] were chosen for this implementation. The desired modal frequencies(ω) and damping ratios(ζ) are determined from the eigenvalues(λ) of the system matrix A,

$$\omega_r = \sqrt{Re(\lambda_r)^2 + Im(\lambda_r)^2} \qquad (8)$$

$$(r=1,2,\ldots n)$$

$$\zeta_r = Re(\lambda_r)/\omega_r \qquad (9)$$

Calculation of System Matrix, Singular Value Decomposition

According to Equation (5), one can obtain another matrix equation as below,

$$A\ H(j\omega) = \mathring{H}(j\omega) \qquad (10)$$

For discrete frequencies ω_i, where $i=1,2,\ldots,p$, Equation (10) can be arranged as,

$$A\ H(j\omega_1):H(j\omega_2):\ldots:H(j\omega_p) = \mathring{H}(j\omega_1):\mathring{H}(j\omega_2):\ldots:\mathring{H}(j\omega_p) \qquad (11)$$

or simply,

$$A\ D = V \qquad (12)$$

where D and V are m×lp displacement and velocity frequency matrices, respectively. It is noticed that matrix D usually is singular, thus Equation (12) cannot be solved by the normal equation least square approach. A singular-value decomposition technique [8] is then employed,

$$D = P\ \Sigma\ Q^H \qquad (13)$$

where P, Q are m×m and lp×lp unitary matrices, Σ is an m×lp singular - value matrix.

$$\Sigma = \left[\begin{array}{c|c} \begin{matrix} d_1 & & 0 \\ & d_2 \ddots & \\ 0 & & d_n \end{matrix} & 0 \\ \hline 0 & 0 \end{array}\right] \qquad (14)$$

The system matrix A can then be calculated by the generalized inverse technique [8],

$$A = V\ D^+ \qquad (15)$$

where the superscript "H" stands for complex conjugate and transpose, and the superscript "+" for generalized inverse. Assume that the system has a rank of n,

$$D^+ = Q_1\, \Sigma_1^+\, P_1^H \qquad (16)$$

Matrix Σ_1^+ is an n×n diagonal matrix whose elements are equal to $1/d_r$ $(r=1,2\ldots n)$ and P_1, Q_1 are m×n and lp×n matrices, which are constructed from the first n columns of P and Q respectively.

In the FDPR algorithm, the only data needed is FRF matrix D (displacement, velocity or acceleration). There is a simple relation between "velocity" and "displacement" FRF's,

$$\mathring{H}(j\omega) = j\omega H(j\omega) - X \qquad (17)$$

where X is the initial condition. Therefore, one has the following equation,

$$V = D\Omega - XE \qquad (18)$$

where

$$\Omega = \begin{bmatrix} \ddots & & 0 \\ & j\omega_i & \\ 0 & & \ddots \end{bmatrix} \quad ; \quad E = [1:1:\ldots:1]$$

The system matrix A can then calculated by following augmentated matrix equation.

$$[A:X]\begin{bmatrix} D \\ E \end{bmatrix} = [D:\Omega] \qquad (19)$$

Principal Component Response Analysis

It can be observed that the system matrix has the dimension of m×m. One has to solve an m×m eigenvalue problem to obtain n eigenvalues and eigenvectors. In order to reduce the size of the eigenvalue problem, principal component response technique is used to derive a minimum-order realization system system.

Let D_p represent the frequencey response matrix at n response coordinate (principal coordinate) and related to matrix D by a linear transformation.

$$D_p = T\ D \tag{20}$$

It can be proved that

$$T = P_1^H \tag{21}$$

Matrix P_1, is the singular vector matrix, which minimizes simultaneously all singular value of ε, where

$$\varepsilon = D - \hat{D} = [I - P_1 P_1^H]\ D \tag{22}$$

where

$$\hat{D} = P_1 D_p = P_1 P_1^H\ D$$

If matrix D has rank n, the norm of the error

$$\| D\ D^H - \hat{D}\, \hat{D}^H \|^2 = \sum_{i=n+1}^{m} d_i \tag{23}$$

will be equal zero. When the measured frequency response function matrix D is contaminated with noise and/or there is some nonlinearity in system, the singular values might be trancated after n values, the remainding singular values being neglectiblely small. In many cases, n is equal to the number of effective modes in the frequency range of interest. But, in case that the effect of the residual modes (modes outside the frequency range of interest) is large, the rank of D can be greater than the number of effective modes. And in case that some modes are not independent from other modes, the rank of D can be less than the number of effective modes. In this case, higher order deviation must be considered to get good results.

Calculation of Modal Participation factors and Synthesis of Analytical FRF

After identifying eigenvalues (modal frequencies and damping) and eigenvectors (mode shapes), modal paticipation factors can be calculated from equation (3) by a least square solution. The analytical frequency response function can then be synthesized from the identified modal data base and compared with experimentally measured data sets.

ANALYTICAL EXAMPLE
(NUMERICAL SIMULATION)

In order to evaluate the accuracy and effectiveness of the frequency domain polyreference method, the capability of handling closely spaced modes or repeated roots and the sensitivity to random errors, a numerical simulation of a four degrees-freedom system with two reference locations was conducted.

Frequency response functions were synthesized. Random uncorrelated noise, with zero mean value and peak value equal to a specified fraction of the maximum peak value of the FRF was then added to these measurements.

Tables 1 and 2 show the identified modal frequencies and damping ratios with 1,2 and 5% noise-contaminated "measured" data. The results indicate that the algorithm is quite robust in the presence of random noise. The identified modal parameters, including modal frequencies, damping ratios, mode shapes and modal participation factors, can be utilized to synthesize analytical FRF's. Figure 1 shows the synthesized FRF compared to the "measured" one with 5% random noise.

Table 1. Identified modal frequency for various noise levels

Noise(%)	Modal frequencies (Hz) 1	2	3	4
0.0*	5.000	10.000	10.500	15.000
1.0	5.005	10.003	10.505	15.001
2.0	5.011	10.003	10.502	14.996
5.0	5.053	10.003	10.503	14.934

*Theoretical data.

Table 2. Identified modal damping (%) for various noise levels

Noise(%)	Modal damping (%) 1	2	3	4
0.0*	3.000	3.000	3.000	3.000
1.0	3.005	3.000	2.994	3.017
2.0	3.007	2.995	2.997	3.009
5.0	2.938	2.989	2.992	3.048

*Theoretical data.

As a check of the estimated modal vectors, Table 3 gives modal assurance criterion (MAC) values between the theoretical modal vectors and the estimated ones from the simulated FRF data with 5% random noise. The result is almost perfect.

Table 3. MAC values between theoretical and identified mode shapes (with 5% noise data)

	1	2	3	4
1	0.99989			
2	0.00001	0.99980		
3	0.00003	0.00002	0.99996	
4	0.00000	0.00000	0.00002	0.99997

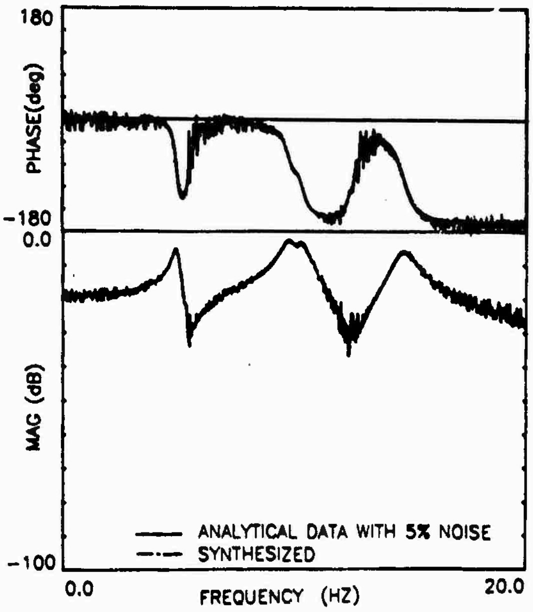

Fig.1 Frequency Response Function with 5% Noise and Synthesized Result

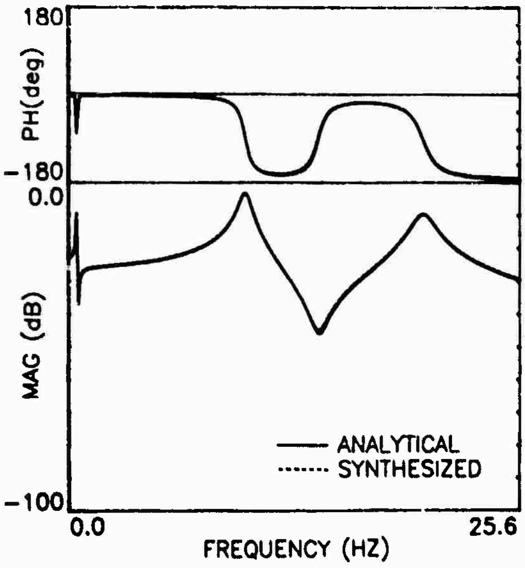

Fig.2 Synthesized Result for Broad Band Case

Table 4. Identified modal frequency and damping in the repeated roots case. (with 5% noise data)

	1	2	3	4
Freq. Damp.	5.080 2.968	10.002 2.913	10.005 2.996	14.976 2.973

To illustrate the capability of handling repeated roots, the third modal frequency is changed from 10.5 Hz to 10.0 Hz, equal to that of second one. Table 4 shows the results in the case of 5% noise added to the FRF data. In order to demonstrate the capability of processing broad-band FRF data, the third model with modal frequencies of 0.5, 10, 10 and 20, Hz was generated. Figure 2 shows the result of curve fitting.

CIRCULAR PLATE APPLICATION EXAMPLE

A circular plate structure was utilized as a test article to demonstrate the capabilities of the frequency domain polyreference modal identification method. Impact test was used to acquire FRF data. There are 36 measurement points and 6 reference locations. All of the 216 FRF's were employed simultaneously for modal identification.

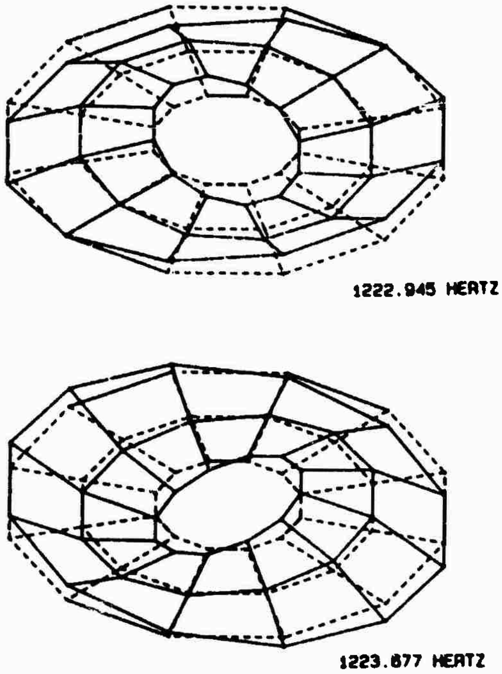

Fig.3 Typical Repeated Roots Mode Shape

Table 5. Identified modal frequencies and damping ratios, compared to FDPR method

Mode	FDPR method		PRCE method	
No.	Freq. (Hz)	Damp. (%)	Freq. (Hz)	Damp. (%)
1	362.6	0.884	362.4	0.880
2	363.9	0.921	363.7	0.960
3	557.1	0.535	557.0	0.512
4	761.1	0.707	761.2	0.664
5	764.2	0.338	764.2	0.345
6	1222.9	0.347	1223.1	0.336
7	1223.7	0.319	1224.0	0.320
8	1328.7	0.463	1328.0	0.491
9	1329.3	0.438	1328.8	0.420

Table 5 shows estimated modal frequencies and damping ratios, compared with the results obtained by the Poly-Reference Complex Exponential method. Nine modes, including four pairs of nearly repeated modes, were identified in the frequency range. Figure 3 shows a pair of mode shapes with nearly repeated modal frequencies.

The two methods give approximately the same results. But the frequency domain polyreference method has no computational mode while the time domain counterpart found 7 computational modes.

Synthesized FRF's were generated from the identified modal data base. Figures 4 and 5 show the two sets of synthesized FRF's compared with the experimentally measured ones.

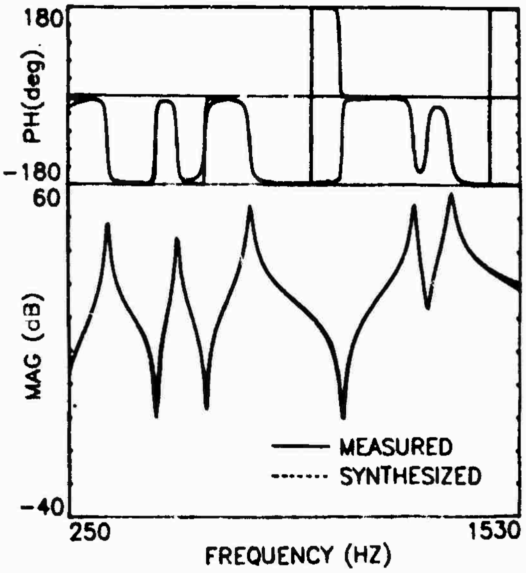

Fig.4 Comparison of Measured and Synthesized FRF (1Y-1Y)

AIRCRAFT APPLICATION

The third application example is a large complex structure -- an aircraft. Usually, an aircraft structure will have a number of very closely coupled symmetric and anti-symmetric modes, that may be difficult to detect with standard experimental modal analysis methods. The aircraft was tested using random uncorrelated dual inputs for various symmetric configuration of the two input locations and all response data were processed to FRF's. The data sets contain FRF's at 78 measurement coordinates for two random inputs, symmetrically located at the wingtips. The FRF's were processed for the zoom range from 4.25 Hz to 16.75 Hz with a frequency resolution of 0.0244 Hz. Table 6 shows the identified modal frequencies and damping ratios of 7 modes in the frequency range from 7.5 to 13.7 Hz. One can observe that the results compare very well with the results of the PRCE method, which are also given in Table 6. Again, the time domain method needed much more computational modes.

Figures 6 and 7 show a pair of mode shapes with closely spaced modal frequencies around 8,9 Hz. It is observed that the mode of 8.896 Hz and 9.039 Hz are very similar: the first one is an antisymmetric mode (the wings move out of phase) and the second one is a symmetric mode (the wings move in phase). Figure 8, 9 show the synthesized FRF's (driving point and cross point) in comparison with measured FRF data sets.

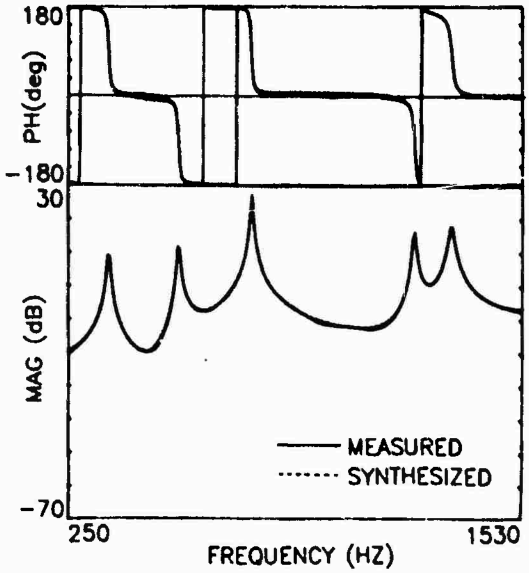

Fig.5 Comparison of Measured and Synthesized FRF (1Y-4Y)

Table 6. Identified modal parameters using FDPR, compared to PRCE

No. of Modes	Frequency(Hz)		Damp. Ratio(%)	
	FDPR	PRCE	FDPR	PRCE
1	8.896	8.883	0.606	0.631
2	9.046	9.039	0.671	0.669
3	10.069	10.065	0.967	1.069
4	10.115	10.078	1.169	1.167
5	12.782	12.785	0.814	0.820
6	13.204	13.228	0.825	0.740
7	13.245	13.254	0.808	0.711

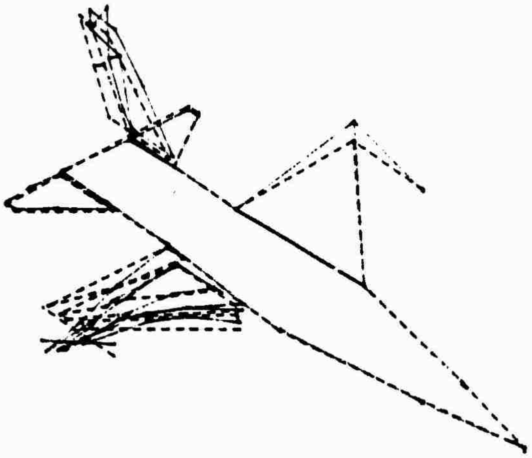

Fig.6 Mode Shape of Airplane at 8.896Hz

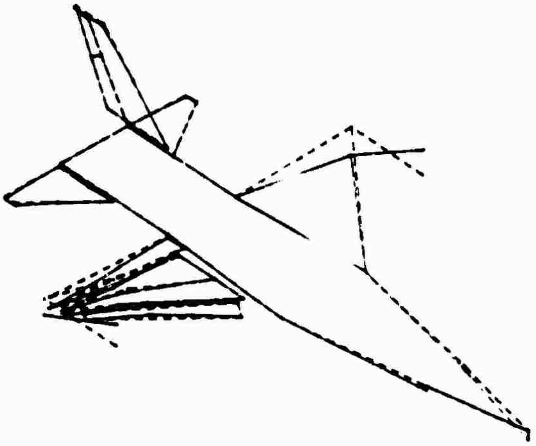

Fig.7 Mode Shape of Airplane at 9.046Hz

CONCLUDING REMARKS

A frequency domain polyreference modal parameter identification method has been developed and implemented in a mimi-computer environment. Based on the above discussion of the theoretical formulations, algorithm and application examples, this new method shows some

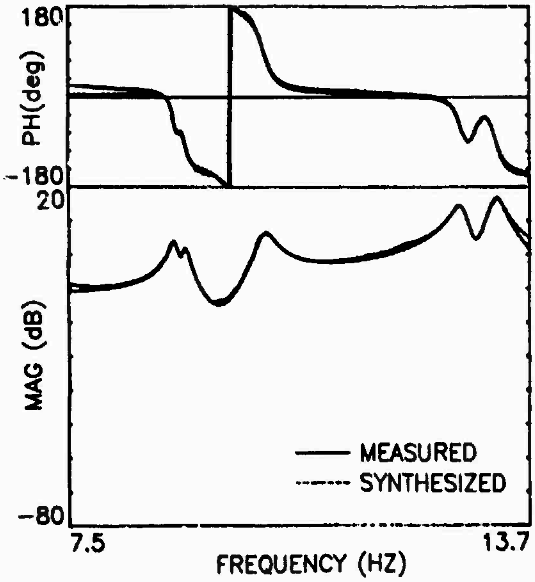

Fig.8 Comparison of Measured and Synthesized FRF (1Z-1Z)

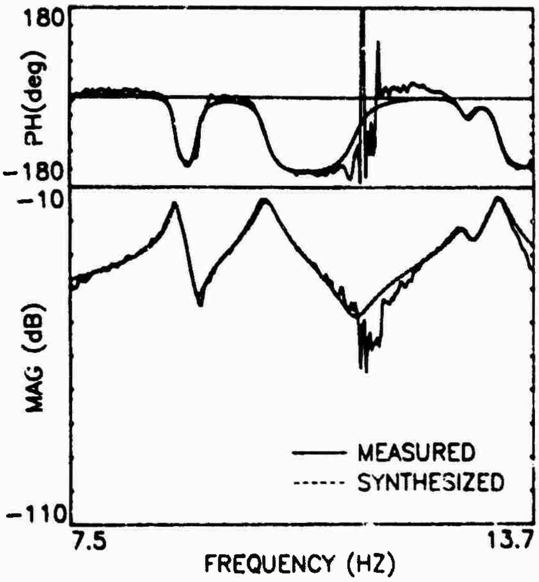

Fig.9 Comparison of Measured and Synthesized FRF (1Z-34Z)

inherent advantages. Common to other multi-input/multi-output methods, some of the advantages are:

(1) The ability to extract an accurate and consistent modal data base by simultaneouly processing multi-input/multi-output FRF data sets;

(2) The elimination of parameter combination schemes for building a composite modal model with respect to different reference locations;

(3) The ability to determine very closely spaced and repeated modes.

Compared to time domain methods, this frequency domain technique has some important features:

(1) Further reduce user interaction and judgement, because there is less need to distinguish between computational and actual modes;

(2) Further increase the accuracy of the estimation by direct using FRF data, eliminating the "time domain leakage" error source introduced by the inverse Fast Fourier Transform;

(3) Have the flexibility of choosing measured FRF data, such as band selection, frequency domain weighting function, and FRF data with unequal frequency steps. The frequency domain polyreference method shows promise for use with future multi-input digital swept sine excitation techniques, which may become attractive since all channels can be sampled simultaneously and processed in parallel, and the time required for FRF measurements can be reduced drastically [9].

ACKNOWLEDGEMENT

The research project of frequency domain polyreference modal parameter identification was accomplished in the Structural Dynamics Research Lab (SDRL) at University of Cincinnati. The authors wish to express their thanks to Dr. David Brown, Director, and Dr. Randy Allemang of UC-SDRL.

REFERENCES

[1] Allemang, R., Rost, R., Brown, D. "Multiple Input Estimation of Frequency Responce Functions : Excitation Considerations", ASME Paper No. 83-DET-73, 1983

[2] Vold, H., Rocklin, T. "The Numerical Implementation of a Multi-Input, Modal Estimation Method for Mini-Computers", Proc. of 1st International Modal Analysis Conference, pp.542-548, 1982

[3] Juang, J.-N., Pappa, R. "An Eigensystem Realization Algorithm for Modal Parameter Identification and Model Reduction", Journal of Guidance, Control, and Dynamics, Vol.8, NO.5, Sept.Oct. pp.620-627, 1985

[4] Leuridan, J. and Vold, H. "A Time Domain Linear Model Estimation Technique for Grobal Modal Parameter Identification", Proc. of 2nd International Modal Analysis Conference, pp.443-451, 1984

[5] Brown, D. et al. "Parameter Estimation Techniques for Modal Analysis", SAE Paper No. 790221, 1979

[6] Zhang, L.-M., Kanda, H., Brown, D., Allemang, R. "A Polyreference Frequency Domain Method for Modal Parameter Identification", ASME Paper 85-DET-106, 1985

[7] Smith, B.T., Boyle, J.M. et al., Matrix Eigensystem Routines - EISPACK Guide, SpringerVerlag, New York, 1976

[8] Garbow, B.S., Boyle, J.M. et al., Matrix Eigensystem Routines - EISPACK Guide Extension, pp.69-76 Springer Verlag, New York, 1977

[9] Hamma, G., Smith, Stroud, R. "An evaluation of Excitation and Analysis Methods for Modal Testing", SAE Paper No. 760872, 1976

Discussion

Mr. Ewins (Imperial College of Science and Technology): How many excitation points or how many columns of the response matrix were measured for the circular plate?

Mr. Kanda: Six reference points were tried, but the data were actually corrected using the hammering technique.

Mr. Ewins: So, you used six times 36 frequency responses?

Mr. Kanda: Yes.

MODAL PARAMETER IDENTIFICATION USING
ADAPTIVE DIGITAL FILTERS

B.H. Wendler
Engineering & Test Division
TRW Space & Technology Group
Redondo Beach, CA 90278

Recent advances in the use of adaptive digital filters has shown promise in their application as stochastic models of dynamic structures. Certain classes of digital filters allow modeling the structure as a set of Z-transform filters. The filter model can be analyzed using Z-transform methods for frequency, damping, and modal residues to define mode shapes. The Auto Regressive Moving Average (ARMA) filter formulation as selected for study. A closed solution for computing the ARMA residues is demonstrated.

INTRODUCTION

Many dynamic structures require some kind of experimental characterization to validate a dynamic model or design capability of the system. In general, normal modes of the system are desired where each mode is orthogonal to each other with respect to the inertia of the system. This implies that the modes form a linear independent set for describing the structure. Various techniques have been introduced over the years to accomplish this. Techniques have focused on using a Fast Fourier Transform (FFT) processor to describe transfer functions of the structure or sine dwell techniques which can adjust the force patterns on the structure to mechanically isolate a mode at resonance. Various papers in the literature discuss random normal mode testing [1-3] or sine dwell testing [4-5], each of which have merit and varying complexity in their application. Results from using various types of techniques have shown some nonduplication of results for the same structure [6].

The need for accurate estimates for modal parameters is also being driven by new processes being introduced to update analytical lumped parameter models by various techniques. The following equation demonstrates that if the residue (R) and the damped frequency W_d are known, then the stiffness for a one-degree-of-freedom system is simply:

$$k = -j\ (\omega_d/2R)$$

where

$$j = \sqrt{-1}$$

For accurate multi-degree-of-freedom estimates, accurate estimates of the structures residues are required [7]. Residues are usually normalized against some value and presented as modal coefficients in almost all the commercially available modal testing systems.

These issues keep advancing the modal parameter identification state of the art. Recent applications with digital adaptive filters for identifying structural characteristics have been successful in determining system stability and divergence properties [8-10]. The filters were considered adaptive in that as the poles of the system moved, the filter coefficients changed to reflect the current system. Figure 1 is an overlay of power spectral density plots using the FFT approach and a lattice filter adaptive model. The filter model was analyzed for its poles (frequency and damping) and accurately identified a high frequency aileron mode suspect of being a flutter mechanism. Actual test results have successfully shown that pole information can be determined from the time difference equation modeling approach. Complete characterization of a dynamic structure requires pole and residue information. An investigation was initiated to determine a scheme to solve residues using the difference equation modeling

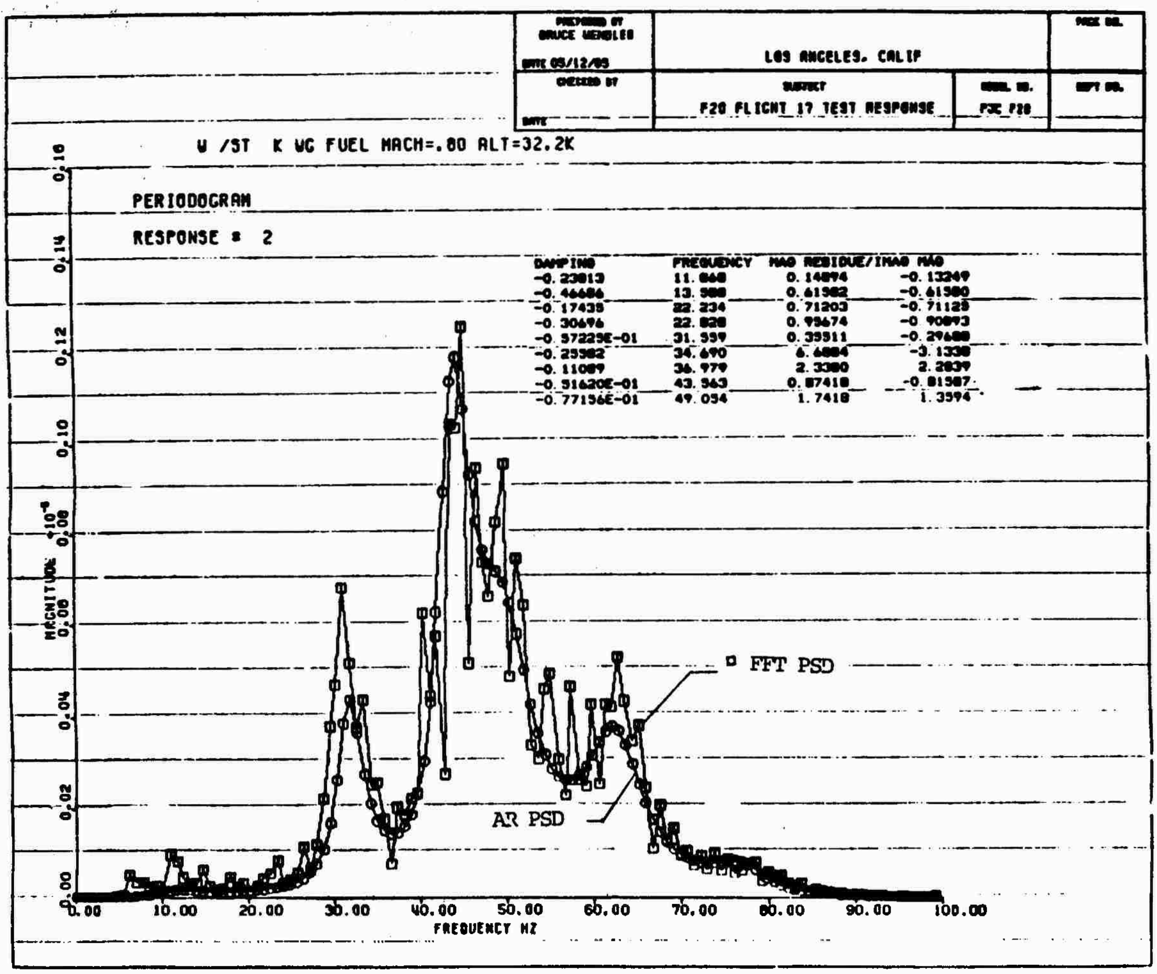

DAMPING	FREQUENCY	MAG RESIDUE/IMAG MAG	
-0.23813	11.868	0.14894	-0.13249
-0.46686	13.588	0.61382	-0.61380
-0.17438	22.234	0.71203	-0.71128
-0.30696	22.828	0.95674	-0.90893
-0.57225E-01	31.559	0.35511	-0.29688
-0.25382	34.690	6.6884	-3.1338
-0.11089	36.979	2.3380	2.2839
-0.51620E-01	43.563	0.87418	-0.81387
-0.77156E-01	49.094	1.7418	1.3594

Fig. 1 - Overlay of an FFT periodogram over a lattice forward/backward PSD estimate

approach. A closed form solution for residues was derived from this investigation.

This paper summarizes the theoretical approach and some preliminary results from the approach. Frequency, damping, and residue data then form a system characterization of a dynamic structure in a nomenclature familiar to a structural dynamicist.

ANALYTICAL APPROACH

The formulation for the direct computation of modal residues from rational function transfer functions follows. Many deterministic discrete time-processes in practice can be well approximated by a rational transfer function model [11]. One of the most general linear modals is the autoregressive moving average (ARMA) model. Here the driving input sequence $\{X_n\}$ and output sequence $\{Y_n\}$ can be modeled by the linear difference equation:

$$Y_n = \sum_{k=o}^{M} b_k x_{n-k} - \sum_{\ell=1}^{N} a_\ell Y_{n-\ell} \quad (1)$$

where

M = order of zeroes

N = order of poles

$b_k a_\ell$ = linear coefficients

The difference equation can be written as a system function via the Z-transform technique. The ARMA function is rational fraction series as:

$$H(z) = \frac{\sum_{k=o}^{M} b_k z^{-k}}{1+\sum_{\ell=1}^{N} a_\ell z^{-\ell}} \quad (2)$$

For lightly damped structures, the order of zeroes equals the pole order where M=N. Then the transfer function in the Laplace domain can be written as a summation.

$$H(S) = \sum_{k=1}^{M} \left(\frac{R_k}{s-s_k} + \frac{R_k^*}{s-s_k^*} \right) \qquad (3)$$

where

s_k = Laplace root = $-\iota\omega_n + j\omega_d$
R_k = residue
ω_n = natural frequency
ω_d = damped frequency
$*$ = indicate conjugate
ι = viscous damping

The denominator of Eq. (2) multiplied by z^M, can be written as a complex polynomial equal to the product sum of its roots:

$$z^M \cdot \left[1 + \sum_{k=1}^{M} a_k z^{-k} \right] = \prod_{k=1}^{M} (z-z_k) \qquad (4)$$

where

z_k = roots of the series

Also the Laplace descriptor in the Z-transform rational fraction expansion is:

$$s = T^{-1} \cdot \ln(z) \qquad (5)$$

where

T = sampling period

Therefore substituting Eq. (5) into (3) and setting the left hand (LH) resultant equal to Eq. (2) multiplied by z^M/z^M, then substituting the LH side denominator by Eq. (4), the resulting equation is:

$$\frac{\sum_{k=o}^{K} b_k z^{M-k}}{\prod_{k=1}^{M} (z-z_k)} = T \sum_{k=1}^{K} \left(\frac{R_k}{\ln z-\ln z_k} + \frac{R_k^*}{\ln z-\ln z_k^*} \right) \qquad (6)$$

or

$$\frac{1}{T} \sum_{k=o}^{M} b_k z^{M-k} =$$

$$\sum_{k=1}^{M} \left[\frac{R_k \ (z-z_1)\ldots.(z-z_k)\ldots.(z-z_M)}{\ln z-\ln z_k} \right] + (*)$$

Setting the variable z to zi to solve for a particular residue, it can be observed that all residues, other than R_k at k=i, drop out of the formulation (they are multiplied by (z_k-z_k) in the numerator). This leaves Eq. (7) with:

$$\frac{1}{T} \sum_{r=o}^{M} b_r z_k^{M-r} \qquad (7)$$

$$= R_k(z_k-z_1) \cdot \lim_{z \to z_k} \left(\frac{z-z_k}{\ln z-\ln z} \right) \ldots.(z_k-z_M)$$

To solve the fraction in Eq. (7) as z approaches z_k, note:

$$\lim_{z \to z_k} \frac{z-z_k}{\ln z-\ln z_k} = \lim_{z \to z_k} \frac{d(z-z_k)/dz}{d(\ln z-\ln z_k)/dz} \qquad (9)$$

$$= \frac{1}{\frac{1}{z_k}} = z_k$$

Therefore the residue R at i=k equals:

$$R_k = \frac{1}{T} \frac{\sum_{r=o}^{M} b_r \ z_k^{M-r}}{(z_k-z_1)\ldots.(z_k)\ldots.(z_k-z_M)} \qquad (10)$$

Eq. (10) shows how the residues can be solved directly by knowing the moving average filter weights and the pole roots. Further the residues do not have any influence from other residues giving theoretically an uncontaminated estimate.

The autoregressive formulation (AR) is similar where it can be shown that:

$$R_k = \frac{\sigma^2 \ z^M}{(z_k-z)\ldots.(z_k)\ldots.(z_k-z_M)} \qquad (11)$$

where

σ^2 = Mth order predictor error

A variety of numerical schemes exists for solving the model order and the linear coefficients [11]. A simple least squares approach was utilized for this paper. An adaptive formulation could have been used where nonstationary phenomina are expected.

EXPERIMENTAL INVESTIGATION

Use of a digital filter stochastic model has several advantages. Properly used, they are a noise separation process where harmonics are identified out of signal with random noise. Unlike FFT or other time averaging processes which try to minimize noise, the AR and ARMA processes can run the risk of not modeling certain weaker harmonics or introduce noise roots into the model. System order then can be important. A popular way to determine the system order is to observe the AR predictor error for convergence. Since the model does not improve after all the harmonics are identified, then the order can be observed.

For this paper, the number of roots were limited due to computer size, therefore, a simple visual check of the fit of the ARMA or AR PSD to an FFT PSD was utilized. It is important to note that the FFT process does not always produce a true PSD, thus its application was not for a standard, just a data point.

The experimental data base consisted of vibration response data from a FLTSATCOM spacecraft modal test. Figure 2 shows the spacecraft mounted to a large inertia mass. Modal testing called for both random and some dwell test using multiple shakers for input. Modes were checked for orthogonality with respect to the inertia matrix. Results of the test are documented in Ref. [3]. In general, all the modes below 40 Hz had excellent orthogonality (less than 10% off diagonal terms). The residue and pole data form a reliable data base.

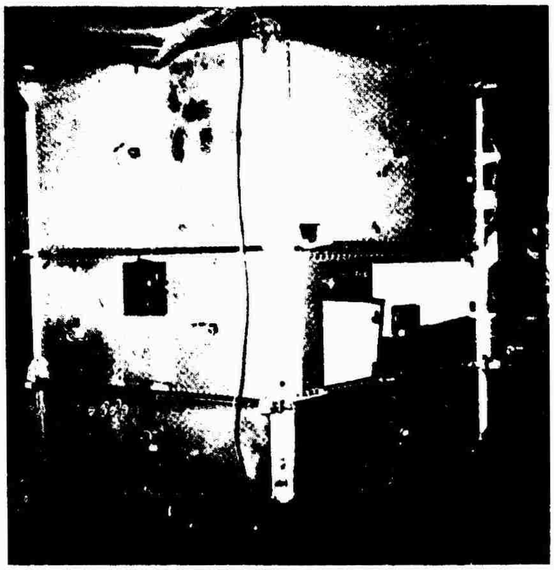

Fig. 2 - Spacecraft installation at the test site

A separate mini-run was made with an initial four shaker setup using one shaker for random excitation and measuring 8 key reference locations. Data were digitized at a 256 samples-per-second rate. Over 30,000 samples per channel were collected along with the force input.

Digitized data were reduced via an experimental program designed to solve for the rational function linear coefficients using least squares where:

$$[U] = \begin{bmatrix} X(o) \cdot & X(-1) \cdot & Y(-1) \cdot \\ X(1) & X(o) \cdot & Y(o) \cdot \\ \vdots & \vdots & \vdots \\ X(P-1) & \cdots & Y(P-2) \cdot \end{bmatrix}; \qquad (12)$$

$$; \{c\} = \begin{Bmatrix} b_o \\ \vdots \\ b_M \\ -a_1 \\ \vdots \\ -a_m \end{Bmatrix} \quad ; \{y\} = \begin{Bmatrix} yo \\ \vdots \\ yP-1 \end{Bmatrix}$$

P = number of data samples used

The least squares is any simulataneous solution for $\{c\}$:

$$[U]^T \, [U] \, \{c\} = [U]^T \, \{y\} \qquad (13)$$

The pole series was then investigated for its root by writing the coefficients into an M order upper Hessenberg matrix and using the QR algorithm [12]. Poles are solved in the Z plane and transformed into the Laplace domain with a direct solution. The closed formed solution for residues in Eq. (10) was used once the poles were known. A standard FFT butterfly algorithm was used to form frequency response functions.

Figure 3 is a magnitude plot of the transfer function for response 16 over the random source. Response 16 has some of the largest responses out of the eight accelerometers monitored. The figure overlays the FFT periodogram with the ARMA PSD estimate. Some peaks match well, other have discrepancies in describing the peaks. Eleven averages were used to form the periodogram. The same amount of data were utilized with the ARMA model. ARMA modeling focused on the 32 Hz and below area (1/2 f_{max} from the decimated sampling rate). The roots are listed in Table 1 showing the two closely spaced modes at 16.9 and 17.2 Hz.

TABLE 1
Residue Listings for 8 References Transducers

Mode No.	Frequency (Hz)	Damp %C/CR	Modal Residues #9	#10	#11	#12	#13	#14	#15	#16
1	16.91	0.75	-.025	.001	-.193	-.099	-.333	-.019	.048	1.000
2	17.26	1.38	.265	.001	.131	.365	-.001	.445	.031	1.00
3	21.18	0.53	.0	.0	.177	.073	.065	-.115	.305	1.000
4	24.18	0.28	-.262	.205	.308	.140	1.0	-.933	.270	.785
5	25.01	0.47	-.128	-.030	.242	-.099	.036	.355	.330	1.000
6	25.49	0.81	-.113	.078	-.147	.464	.023	.122	.132	1.000
7	26.24	0.68	-.145	.001	-.037	-.104	-.047	-.064	.078	1.000
8	27.21	0.81	-.451	-.726	.252	-.687	-1.0	-.565	.256	.200
9	28.24	0.87	.517	.039	.569	-.427	-.017	.118	1.000	.712
10	28.90	0.73	.158	.003	-.125	-.076	.040	.043	-.402	1.000
11	30.83	0.27	.064	.002	-.054	1.000	-.073	-.152	.001	-.004

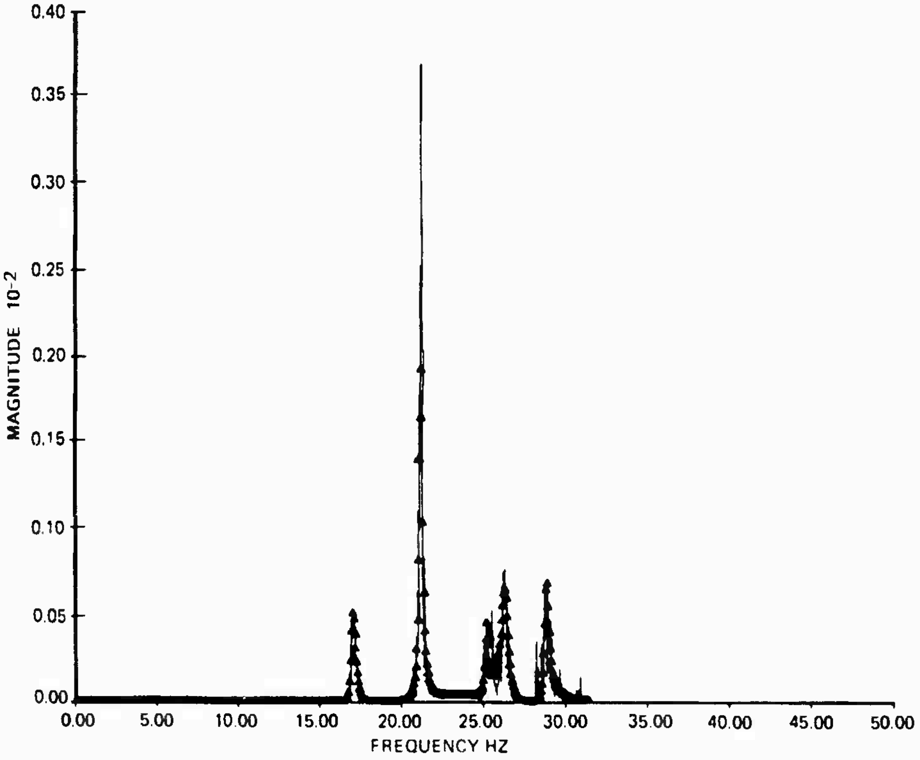

Fig. 3 - Magnitude transfer function plot for response 15

Also listed in Table 1 are the residue results for 11 modes identified by test between 15 and 31 Hz. Modal results are listed for the polyreference [13] approach using burst random. Polyreference results were spot checked by sinedwell test and found to be accurate. Table 2 lists the results using the QR algorithm to solve for the roots and Eq. (10) for the residues. Frequency and damping estimates compare favorably with those in Table 1. For weakly excited modes, a convergence on a root did not occur, thus no residues were solved for. Mode 3 was a relatively well excited isolated mode and the modal coefficients compare favorable for that condition.

Another run at calculating the residues was made by forcing the poles in Eq. (10) to equal those solved for in Table 2. The numerator weights in Eq. (10) were reestimated with the associated poles. Residues for each root were then tabulated for Table 3. Results again were inconclusive for the higher modes, however, the lower modes compare favorably. It was noted that the resulting autoregressive filter weights were all positive when the roots were set to the 11 values in Table 2, whereas the original coefficients for the responses include several negative weights.

CONCLUSION AND RECOMMENDATIONS

Modeling via a difference equation/adaptive digital filters is undergoing extensive research by linear systems researchers. Several algorithms exist even for the ARMA model used in this paper. The poor consistancy of residue estimates for the higher frequency modes shows the modeling order needs to be larger than 17 conjugate pairs for 11 actual mode pairs and that an algorithm with strong LH plane (poles with frequencies greater than f_{max} divided by 2) estimation capability would have been desirable in this case.

Results prove that a closed form solution for residues from a rational function exist. Transfer functions can be matched using a rational function, and accurate estimates of frequency and damping can be made even for closely spaced modes which require multishaker applications to currently identify.

The issues suggesting use of a digital filter stochastic model are vastly different than those using the complex exponential via an FFT process. Little in the use of a digital filter has been published by mechanical system users. This paper attempts to show the feasibility of the concept and although the concept was not validated, the

TABLE 2
ARMA Data with 34 DOF Model 64 Samples/Second

Mode No.	Frequency (Hz)	Damp %C/CR	Modal Residues #9	#10	#11	#12	#13	#14	#15	#16
1	16.96	.85	-	-	-.220	.309	-.242	-.010	.016	1.0
2	17.23	1.75	.246	.002	.050	.526	-	.379	-	1.0
3	21.20	0.56	.037	0.0	.182	.074	.065	-.109	.332	1.0
4	24.20	0.73	-.209	0.0	1.0	.105	-.136	.689	-	.142
5	25.06	0.76	-.504	-	1.0	-	-	.198	.394	-
6	25.55	0.97	-	.169	-	1.0	-	-	-	-
7	26.33	0.98	-.169	-	-	-	.004	-.113	-	1.0
8	27.16	4.26	-	-.033	-	-.695	-.167	-	1.0	-
9	28.05	1.42	-	-	1.0	-	-	-	-	-
10	28.83	0.53	-.558	-	-	.426	.075	.070	-.472	1.0
11	30.78	0.95	-	-	-.274	1.0	-.087	-.149	.102	-

TABLE 3
ARMA Model with Fixed 17 Conjugate Root Pairs

Mode No.	Frequency (Hz)	Damp %C/CR	Modeal Residues #9	#10	#11	#12	#13	#14	#15	#16
1	16.9	0.85	-.004	.001	-.162	-.070	-.305	-.010	.051	1.0
2	17.2	1.7	.226	-.002	.109	.296	-.033	.366	.027	1.0
3	21.2	.56	-.080	.008	.190	.038	.030	-.176	.484	1.0
4	24.2	.74	.118	-.043	.194	.125	.160	-.021	-.189	1.0
5	25.1	.73	.170	-.010	.158	.208	.190	.084	-.202	1.0
6	25.5	.98	.213	.032	.091	.278	.225	.185	-.184	1.0
7	26.4	1.0	.163	-.023	.191	.181	.174	.049	-.216	1.0
8	27.2	4.2	.215	-.014	.205	.239	.187	.112	-.286	1.0
9	28.1	1.4	.125	-.024	.168	.167	.181	.015	-.171	1.0
10	28.8	.56	.036	-.187	.446	.139	.155	-.243	-.480	1.0
11	30.8	.95	.173	-.053	.287	.174	.170	.018	-.298	1.0

feasibility was demonstrated. Further research into the modeling accuracies using a complete data base of a properly instrumented structure needs to be made. Then orthogonality can be estimated to check the linear independence of the modal estimates of each mode. Work is progressing on using other formulations of the rational function where the poles are initially estimated, then the moving average coefficients adjusted. This enables a residue to be estimated on every root and transfer function of the system.

REFERENCES

1. H. Vold, et al, "A Multi-Input Modal Estimation Algorithm for Mini-Computers," SAE 820194, Feb. 1982

2. R. Zimmerman and D. Hunt, "Multiple Input Excitation Using Burst Random," 55th Shock and Vibration Symposium, Oct. 1984

3. B.H. Wendler, D. Hunt, and S. Soule, "A Normal Mode Identification Test Using Multiple Inputs," SAE 851924, Oct. 1985

4. S.A. Anderson, "Another Look at Sine Dwell Mode Testing," AIAA Journal of Guidance, Control, and Dynamics, Vol. 5, pp. 358-365; Jul.-Aug. 1982

5. D.L. Hunt, J. Matthews, and R. Williams, "An Automated Tuning and Data Collection System for Sine Dwell Modal Testing," AIAA 25th Structures, Structural Dynamics, and Materials Conference, May 1984

6. J.C. Chen, "Evaluation of Modal Testing Methods," AIAA 84-107, 25th Structures, Structural Dynamics and Materials Conference, May 1984

7. A.M. Kabe, "Stiffness Matrix Adjustment Using Mode Data," accepted for the AIAA Journal, Fall, 1985

8. B.H. Wendler, "Near-Real-Time Flutter Boundary Prediction from Turbulence Excited Response," AIAA Paper 83-0814, May 1983

9. B.H. Wendler, "Predicting Dynamic Instability Boundaries Using Lattice Filters," SAE Paper 831432, Oct. 1983

10. Y. Matsuzaki, and Y. Ando, "Flutter and Divergence Boundary Prediction from Nonstationary Random Responses at Increasing Flow Speeds," AIAA Paper 85-0691, Apr. 1985

11. S.M. Kay and S.L. Marple, "Spectrum Analysis - A Modern Perspective," Proc. of the IEEE, Vol. 69, No. 11, Nov. 1981

12. Germund Dahlquist, Numerical Methods, trans. Ned Anderson, Englewood Cliffs, NJ, 1974

13. J.R. Crowley, et al, "The Practical Use of the Polyreference Method," International Modal Analysis Conference, Feb. 1984

SAFE/DAE: MODAL TEST IN SPACE

T. E. Nesman and D. K. Reed
Marshall Space Flight Center
Huntsville, Alabama

INTRODUCTION

In September of 1984, NASA performed a series of experiments on orbit with a large solar wing attached to the Space Shuttle orbiter. These experiments, the Solar Array Flight Experiment (SAFE), mark the first tests of a large space structure in space. Extension, retraction, and dynamic tests had to be performed in space due to the fragility of the solar array. Due to the extendable and retractable design of the solar array, accelerometers and associated wires could not be used; therefore, remote sensing, the Dynamics Augmentation Experiment (DAE), was added to the SAFE program. The DAE uses a remote sensor based on star tracker technology to measure the dynamic response of the solar array. The DAE sensor tracked 18 targets on the solar array during free-decay response to a transient excitation. This paper is an overview of the SAFE/DAE, highlighting analysis results from the remotely sensed data. Modal parameter estimates from the remotely sensed data were computed using the complex exponential and polyreference techniques.

TEST ARTICLE DESCRIPTION

The primary objectives of SAFE were to demonstrate extension/retraction of the solar array and to verify electrical, thermal, and dynamic characteristics. The solar array main components are a blanket and mast. The mast and blanket are joined together only at the top and bottom of the mast as shown in Figure 1. The mast is made of three fiberglass longerons which are held together with battens and crossing tension wires. The mast can be extended and retracted by coiling it into and out of a cylindrical canister, Figure 2. The blanket is constructed of thin plastic (Kapton) hinged panels. The solar array blanket can extend to 105 feet in length or can fold "accordion-like" into a box 7 inches high. For this mission, only a few top panels held active solar cells; the rest of the blanket held aluminum sheets designed to simulate the mass and thickness of solar cells. The array could be extended to 70 percent or 100 percent of its full length, i.e., 71 feet or 105 feet, respectively.

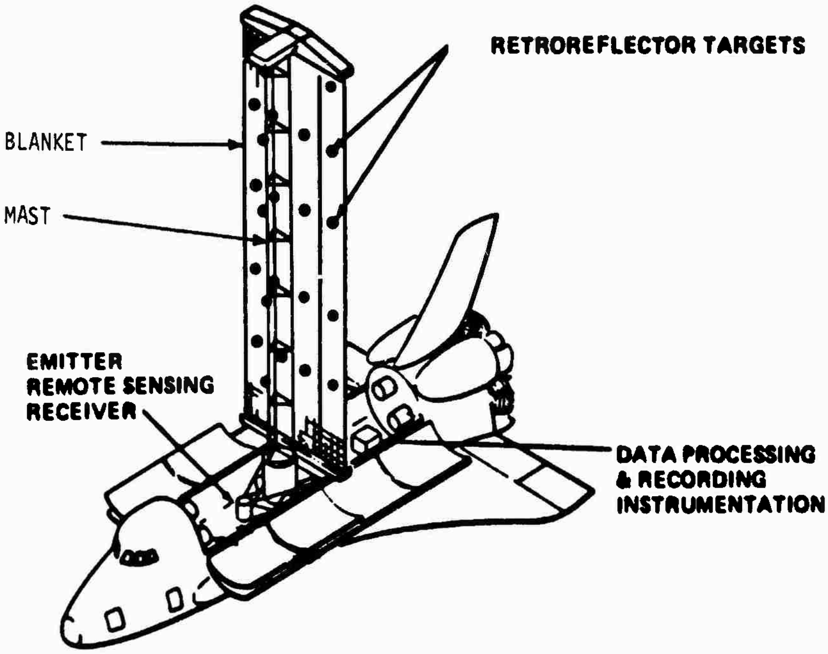

Figure 1. SAFE dynamics augmentation experiment.

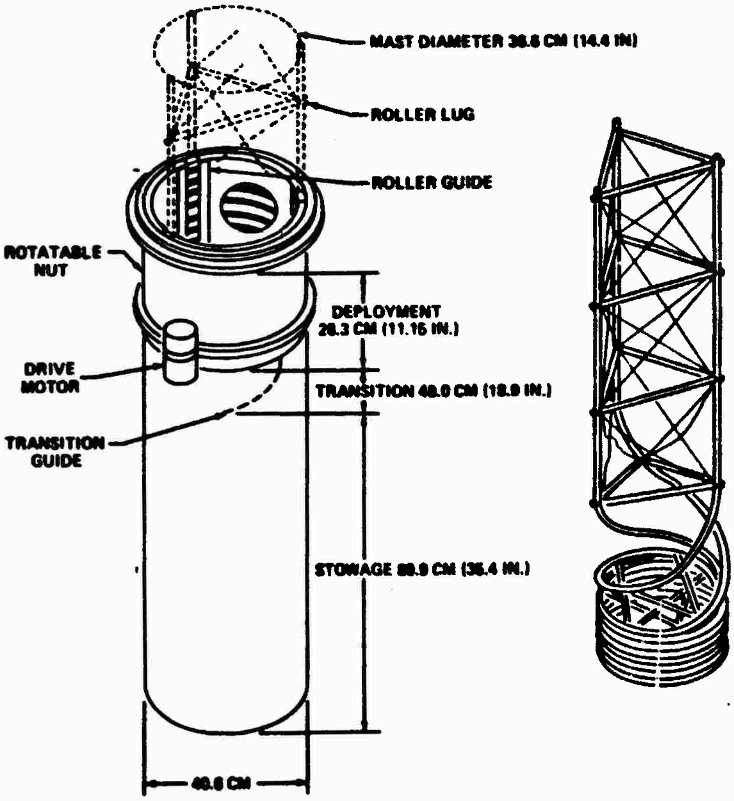

Figure 2. Solar array extension mast.

The DAE primary objectives were to determine the solar array's dynamic characteristics using remote sensing. A remote sensing system was developed by Ball Aerospace for NASA. The DAE consisted of 18 "pop-up" targets on the mast and blanket, infrared lasers to illuminate the targets, a sensor that "looked" at the targets, and the supporting electronics to track 18 targets and digitally record their displacements on magnetic tape, Figure 3. The target positions before the first dynamic experiment, DAE 1, are shown in Figure 4. Target motion was recorded in two directions parallel and laterally perpendicular to the longitudinal axis of the orbiter. Sensor operation was limited to the dark side of an orbit because of the sunlight, earthlight, and associated reflections.

PROCEDURES AND RESULTS

Testing

In January of 1984, performance tests of the sensor were run at Marshall Space Flight Center. These tests verified the target "zones of operation," target tracking accuracy, and the sensor's dynamic range. After these tests, the acquired data had to be converted into a format compatible with our software. The solar array was flown on STS-41D, which lifted off in the morning of August 30, 1984. The solar array went through a rigorous schedule during mission 41-D. The solar array extension and retraction history pertaining to the DAE is shown in Table 1. Six DAE tests were conducted over three days: one out-of-plane, two in-plane, and three multi-modal. These tests are named for the type of motion the excitation is to produce: out-of-plane, motion out of the plane of the blanket; in-plane, motion in the plane of the blanket and; multi-modal, this test was designed to excite as many modes as possible. All DAE tests were performed on the dark side of an orbit with the solar array at 70 percent deployment (orbiter safety required 70 percent deployment for dark side dynamic testing). Each test consisted of a quiescent period; then commands to start the sensor and recorder; next, excitation using the orbiter vernier reaction control system (VRCS); and last, the free-decay response of the array. The thrust time histories are superimposed on target responses for three of the six DAE's in Figure 5. Short duration pulses of the VRCS were intended to excite the array and to leave the orbiter in a favorable attitude and stable orbit. Overall operation of SAFE was very successful. The only structural variation noted was a slight twist of the array upon deployment, and the blanket curved slightly about the mast during the dark side of the orbit. After the flight, the tape recorders were returned to MSFC for data processing and format conversion. Post flight analysis revealed the sensor package worked better than expected. The twist in the array moved a few targets out of their zone of operation, but this deviation did not prevent

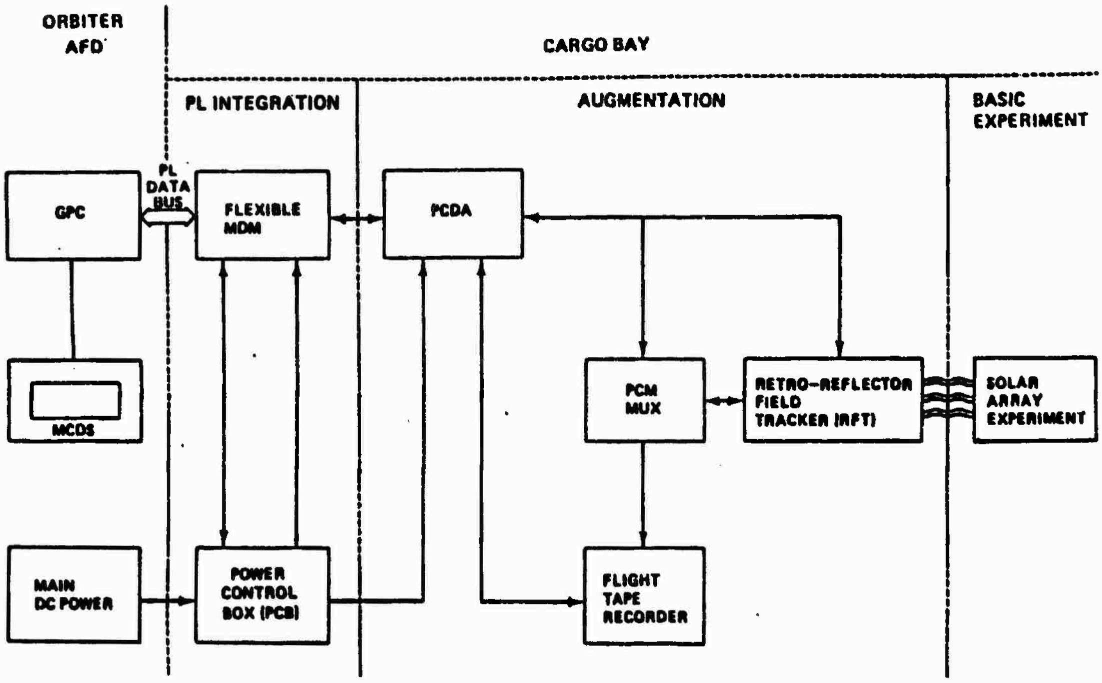

Figure 3. Dynamics augmentation experiment.

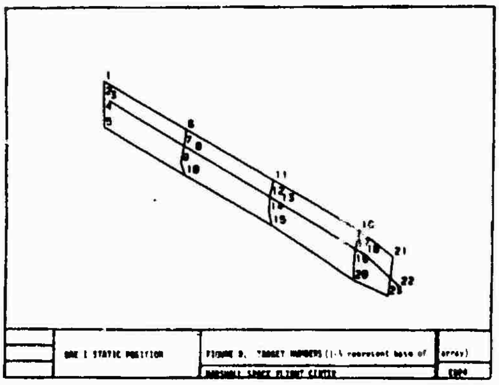

Figure 4. Target numbers (1-5 represent base of array).

TABLE 1
Solar Array Extension/Retraction History

Event	Date	Excitation
Extend		
DAE 1	Sept. 1, 1984	Out-of-Plane
Retract		
Extend		
DAE 2	Sept. 2, 1984	Multi-Modal
DAE 3	Sept. 2, 1984	In-Plane
DAE 4	Sept. 2, 1984	Multi-Modal
Retract		
Extend		
DAE 5	Sept. 3, 1984	Multi-Modal
DAE 6	Sept. 3, 1984	In-Plane
Retract		

the sensor from tracking all targets successfully. Modal parameters were estimated from the target displacement data.

Measurements

Modal analysis is typically performed using acceleration responses. This is particularly useful when modes encompassing a relatively wide frequency range are sought. The acceleration amplitude of higher order modes will be maintained while the displacement amplitude is severely attenuated. Because of the remote sensing requirement, displacements were measured for the DAE modal analysis. Three x and y displacements of target 19 are shown in Figure 5, where x is out-of-plane, y is in-plane, and the units are centimeters. The thrust time histories in Figure 5 are reconstructed from telemetry data, however, the pulse amplitudes are not shown to scale and the duration and occurrence of each pulse is approximate. These excitations were executed manually by the astronauts. Due to the manual excitations, pre-test underestimation of array damping, and thruster constraints to minimize orbiter rotation, the optimum levels were not obtained. This is particularly obvious from the in-plane or y-direction where the free-decay response levels are close to the quantization level of the DAE sensor.

The sensor was placed at the base of the array to minimize ranging errors, therefore, target displacements were obtained in only two directions. The modal analysis is therefore performed under the assumption of negligible longitudinal motion. An additional constraint was that the input force would not be measured. All measurements on the structure, therefore,

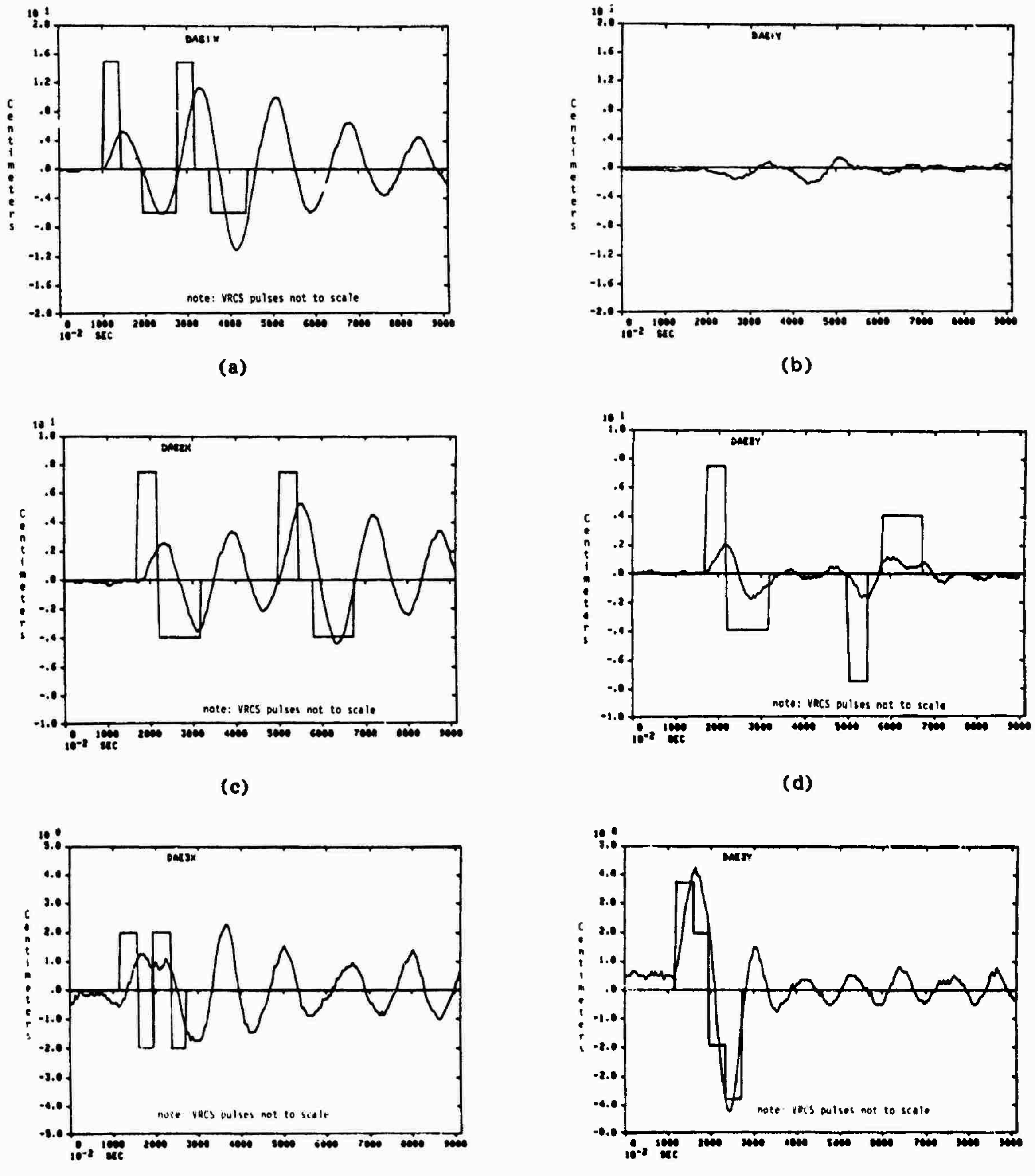

(a) (b)

(c) (d)

(e) (f)

Figure 5. VRCS pulses/target 19 response vs. time.

must be obtained simultaneously to preserve both the amplitude and phase with respect to each measurement.

Complex Exponential Technique

The complex exponential parameter estimation technique provides frequency and damping values for one excitation. This technique "fits" the complex exponential form of the impulse response function using the method of least squares.

The software used for the analysis of the solar array data was developed by University of Cincinnati [1] for use on the HP5451C Fourier Analyzer. The input typically requires a frequency response function (FRF) at each response point. The inverse Fourier transform of each FRF is curve fit using the complex exponential algorithm to provide estimates of frequency and damping. The residues are determined in a conventional manner, i.e., from the least squares curve fit of the FRF.

Since the excitation is not known, the solar array data was analyzed by substituting the Fourier transform of the free decay response of each measurement for the FRF. In this case, the impulse response function is replaced by the free decay response of the solar array. The residue estimates are obtained from the Fourier coefficients of each response.

Using the complex exponential technique, four out of the first five mode shapes were obtained. Figures 6 through 9 show the first out-of-plane bending, first torsion, second out-of-plane bending, and second torsion of the cantilevered solar array. The in-plane bending modes were not detected in the response data.

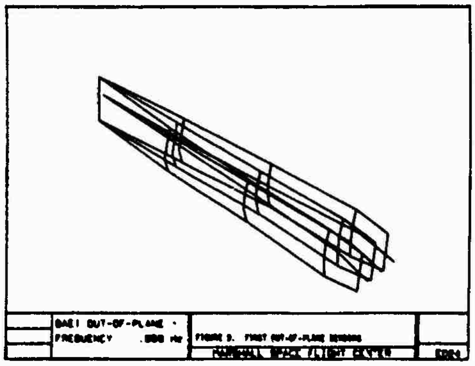

Figure 6. First out-of-plane bending.

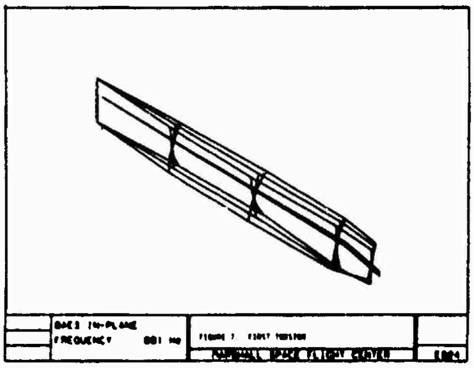

Figure 7. First torsion.

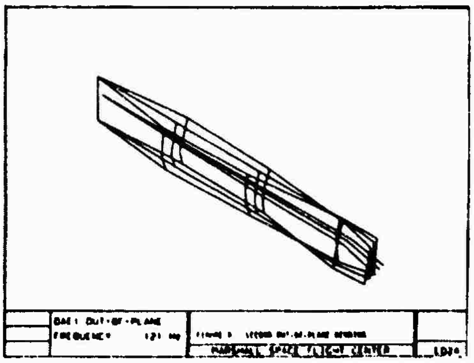

Figure 8. Second out-of-plane bending.

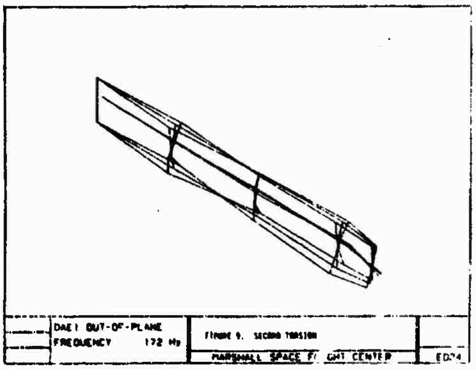

Figure 9. Second torsion.

Polyreference Technique

The polyreference technique is an advanced algorithm developed by Vold et al. [2] and is similar to one that is used by Ibrahim [3]. It has been shown [4] that both the complex exponential and the Ibrahim technique are special cases of the polyreference technique. The details of these algorithms are explained in the literature; however, some important points are included in the following.

Similar to the complex exponential technique, this algorithm makes use of the unit impulse response or free-decay response time history. In this case, however, responses from several locations on the structure and from multiple excitations are used simultaneously to extract modal parameters. For modal synthesis, modes relative to any exciter location are complete and equally accurate. Each mode is scaled to a unit impulse at the corresponding excitation point. In the case of the solar array on-orbit displacement data, the scaling is superfluous. Since the excitation for each DAE is not measured, the free-decay responses are combined to form modes whose amplitude depends on the response only.

The polyreference technique is useful when closely spaced modes or repeated roots are encountered. Also, when analyzing linear systems, this technique will help overcome noise when free-decay response data is used. The polyreference algorithm could not be applied to any combinatin of DAE's, because the frequencies and damping varied significantly from test to test.

Nonlinear Analysis

Detailed analysis was required to determine the nonlinear behavior of the solar array. The free-decay response time history of each measurement could not be analyzed as a complete record because variations in frequency and damping were noticed from beginning to end. Piece-wise linear analyses were performed by assuming frequency and damping do not change significantly over a short time. Several different analyses of this type were performed to describe the nonlinearity throughout the free-decay response time history.

One way to illustrate the nonlinearity is using frequency spectra. By weighting a portion of a time record and then Fourier transforming, the frequency variation is shown as the weighting window is moved across the response time record. Superimposing these spectra, we see the frequency shift increase as amplitude decreases (Figure 10).

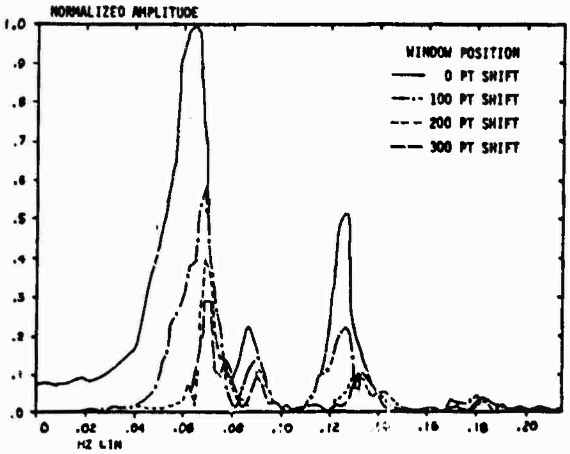

Figure 10. DAE 1 target 6X spectra.

Consider now curve fitting in the time domain. By taking a short portion of a time record, a least squares complex exponential curve fitting technique will provide estimates of frequency and damping, and by fitting all of the measurements together, a global estimate is obtained. This can be repeated across selected time periods of the records to map changes in frequency and damping. A modified version of the polyreference software was developed by the University of Cincinnati to restrict analysis to a selectable portion of the response time record. This technique was applied to portions of individual DAE response time records to obtain frequency and damping estimates. There is a trade-off between frequency bandwidth and time resolution for this type of analysis. A review of the mode shape variation with frequency variation shows only slight changes in shape that can most probably be attributed to noise. Two modes are illustrated in Figures 11 and 12 where the frequency has changed, but the shape is essentially the same. Modal analysis of the DAE data produced the parameter estimates in Table 2. The algorithms used in the analysis sometimes overestimate damping with noisy data, however, the values in Table 2 were consistent with "logarithmic decrement" and "half power point" damping estimates. Damping decreased and frequency increased as the response amplitude decreased. This is not unusual for structures of this type where the impact of joints cause increased damping and preload causes a frequency shift.

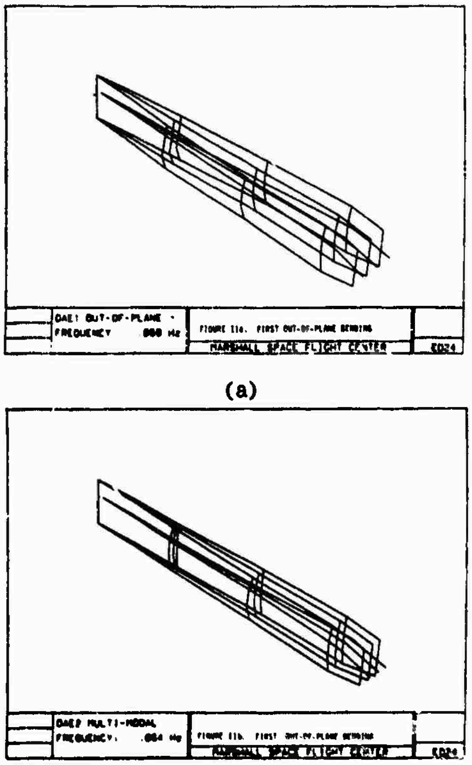

(a)

(b)

Figure 11. First out-of-plane bending.

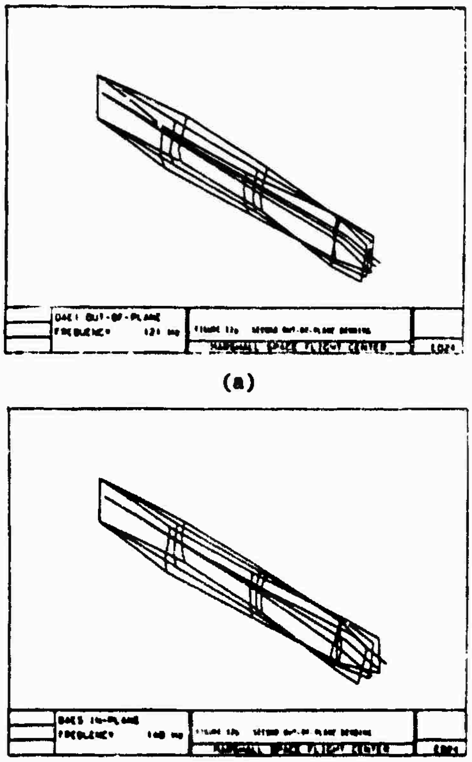

(a)

(b)

Figure 12. Second out-of-plane bending.

TABLE 2
DAE Parameter Estimates

Mode	Frequency Hz	Damping	Description
1	0.059 - 0.071	12 - 1.5%	Out-of-Plane First Bending
2	-	-	In-Plane First Bending
3	0.089 - 0.098	6 - 1%	First Torsion
4	0.120 - 0.140	4 - 1%	Out-of-Plane Second Bending
5	0.172 - 0.210	2.4 - 1%	Second Torsion

CONCLUSIONS

Remote Sensing

One of the objectives of the DAE is to determine if remote sensing can be adapted to on-orbit dynamic testing of large space structures (i.e., space station, space platforms, large antennae). Advantages of this type of measurement system are: (1) very little mass is added to the structure being tested (low frequency/small amplitude accelerometers generally have large mass; (2) no contact between structure and sensor (i.e., no accelerometer wires) - this was a key issue for the SAFE; (3) the sensor was quite accurate (1 mm resolution). Limitations of the DAE sensor are: (1) sunlight, earthlight, moonlight and associated reflections would confuse the sensor; (2) only measures deflection in two directions; (3) this particular remote sensor required preflight target locations with respect to the sensor, whereas these target locations were stored in firmware, not easily changed. Considering the limitations of the DAE remote sensor and the relatively small deflections of the solar array, the data are quite good. The data have very few dropouts and no known nontarget reflections.

Solar Array

The SAFE solar array is an interesting structure for modal analysis. Four modes were successfully extracted from the remotely sensed data. Distinctive features of the solar array are:

1. Large and flexible.
2. Very low natural frequencies.
3. Nonlinear dynamic characteristics.
4. Thermal sensitivity.
5. Retractable and deployable.

This structure is typical of future large space structures in some ways. Remote sensing and modal analysis in space may be required to verify analysis for many of these structures.

The nonlinear behavior of the solar array is probably typical of future large space structures. Thermal sensitivity of the array serves as a reminder of the harsh environment in space that can significantly affect structural dynamics.

REFERENCES

1. Model Analysis Software, RTE Modal Program, University of Cincinnati, January 1985.
2. Vold, H., Kundrat, J., Rocklin, T., and Russell, R., "A Multi-Input Modal Estimation Algorithm for Mini-Computers," SAE Paper No. 820194, 1982.
3. Ibrahim, S., Goglia, G., "Identification of Structures from Responses and Random Decrement Signatures," NASA-CR-155321, 1977.
4. Polyreference Software, Department of Mechanical and Industrial Engineering, University of Cincinnati, Interim Report - NAS8-34503, September 1984.
5. Brown, D. L., Allemang, R. J., Zimmerman, R., Mergeay, M., Parameter Estimation Techniques for Modal Analysis, Society of Automative Engineers, Inc., SAE Technical Paper No. 790221, 1979.
6. Ibrahim, S. R., "Modal Identification Techniques Assessment and Comparison," Sound and Vibration, August 1985.
7. Jones, J. H., "Modal Analysis for the Solar Array Flight Experiment," NASA, ED24, Unpublished notes, May 1983.
8. Nesman, T. E.: "SAFE/DAE Data Evaluation Simulation," NASA, MSFC, ED-24-67-83, September 1983.
9. Schock, R. W., "SAFE Dynamic Augmentation Experiment Review," Large Space Antenna Systems Technology 1984 Conference NASA, Langley Research Center, December 1984.

Discussion

Voice: Did both the frequency and the damping shift with time?

Mr. Nesman: Yes.

Voice: How do you explain the changes in damping?

Mr. Nesman: The damping was related to the amplitude of the excitation. Each test did not excite the same amount of response. However, if you line up the amplitude and the damping from test to test, there is a correlation. For example, on the first test the amplitude was almost 20 centimeters peak-to-peak, initially. On the third test it was only about five centimeters peak-to-peak. Well, if you went on the first test to where the amplitude was about five centimeters peak-to-peak, and computed the damping around there, you would get the same answer as you did on the third test, or close to it.

Voice: Could you tell us a little more about the wobbling of the array?

Mr. Nesman: All of these tests were on the dark side of an orbit. Photographs of the light side, when it was in the sun, showed the array was flat. When it was on the dark side, it curved.

Voice: No one knows why?

Mr. Nesman: I don't know why. Nobody has satisfactorily explained it yet.

Voice: Was it thermal curvature?

Mr. Nesman: It is thermal. However, that should have been anticipated, in my mind, but it wasn't. It still hasn't been explained adequately.

TESTING TECHNIQUES

RANDOM VARIATION OF MODAL FREQUENCIES - EXPERIMENTS AND ANALYSIS

Thomas L. Paez
Linda J. Branstetter
Danny L. Gregory

Sandia National Laboratories
Albuquerque, NM

When a mechanical system is subjected to a dynamic environment it executes dynamic response, and the character of the response depends on the features of the excitation and the structural system parameters. In order to predict the structural system response, it is necessary to know both the excitation and structural system characters. The modal frequencies are among the most basic system properties and are often used in dynamic analysis. Frequently, one or more structural parameters is random, and this causes the modal frequencies to vary randomly. This investigation shows how random variation in modal frequencies can be estimated using a combination of experiments and analysis. One experimental and three numerical examples are presented.

Introduction

The purpose of dynamic structural analysis is the prediction of system response. Before a structural analysis can be performed the parameters describing the characteristics of a system and the loading on the system must be known. In many situations, the analytically or experimentally determined modal characteristics of a structure are used to perform a dynamic analysis. Regardless of the type of analysis performed, correct prediction of response depends on accurate determination of the system parameters. In the case of modal analysis the parameters of interest are the modal frequencies. Response is particularly sensitive to these frequencies when the excitation signal content varies rapidly with frequency. In other applications, frequency shifts are often used as a diagnostic tool in evaluating structural damage. In these cases measured change in modal frequencies must be attributed to either inherent structural randomness or actual damage. In view of this, it is important to understand and accurately account for factors that affect variation in modal parameters.

Experiments have shown that the modal frequencies of structures vary randomly. Specifically, experiments with nominally identical structures and experiments with a single structure tested at different times show random variation in modal frequencies. Some sources that cause this random variation are variation in material properties, variation in the character of internal joints, randomness in structural dimensions, and variation in boundary conditions. These random variations may be incorporated in a dynamic analysis as randomly varying structural parameters. It is desirable to statistically characterize these parameters.

The purpose of this investigation is to establish an analytic technique for the estimation of the second order statistical moments (mean, variance, covariance) of modal frequencies when one or more underlying structural parameters are random variables. (The moments of the underlying random variables are assumed to be known from experiments.) The results of a simple laboratory experiment are summarized to show that the analytic technique yields accurate results in a particular case. The analytical investigation summarized here shows that the moments of modal frequencies can be defined in terms of some simpler measure of structural characteristics. For example, in the experiment, the mean and variance of the fundamental frequency are defined in terms of the mean and variance of a structural stiffness parameter. The advantage in having this capability is that in many situations, it is relatively easy to find the moments of a simple structural parameter experimentally (possibly through static experiments). These moments can be used analytically to establish the moments of the modal frequencies. In many situations it is difficult to establish the mean and variance of modal frequencies without using such an analytic technique, and it is always more difficult and time consuming to find modal frequency moments from experiments alone.

Other investigators have studied parts of this same general problem. In particular, several applied mathematics studies have considered the random eigenvalue problem. These studies have sought to establish the probability distribution and/or moments of linear systems. Reference 1 pursues the type of investigation in a general mathematical framework; references 2 and 3 pursue the problem in a structural engineering framework. It appears that no experimental investigations have considered the random variation of modal frequencies.

The following section shows how the second order moments of a structural system can be evaluated approximately. Then some examples are presented. The first example shows the results of a sequence of experiments in which the fundamental frequency of a cantilever beam is evaluated repeatedly. The fundamental frequency varies randomly, and its mean and variance are estimated from measured data. In the same example, the mean and variance of an underlying random variable (base stiffness of the cantilever beam) are estimated from data, and it is shown that these moments can be used in the analytic framework developed here to estimate the mean and variance of the fundamental frequency. Good agreement exists between the experimental and analytical results. Two other numerical examples are presented to show how random variation occurs in higher modal frequencies and how random variation occurs when more than one underlying variable is random. Finally, a discussion and conclusions are presented.

Analysis of Random Variation in Modal Frequencies

A complete characterization of the potential for random variation in modal frequencies is important because it establishes a description of possible levels of structural response. For example, consider the case where one mode of a structure is excited, and assume that the excitation is a stationary random process. If the structural modal frequency has an average value of ω_0 and a range of likely values spanning the frequency interval from $\omega_0 - \Delta\omega$ to $\omega_0 + \Delta\omega$, then the mean square response of the structure can vary greatly from one trial (in which a structure is excited and its response is measured) to another. The situation becomes more complicated when more modes of response are excited, but an understanding of the random variation in modal frequencies is still important.

A method for estimating the statistics of the modal frequencies of a structure is developed in the following. First, consider the deterministic modal analysis problem. Every structural system is an assembly of continuous structural elements. The motion of each structural system is governed by a set of coupled, partial differential equations involving the mass and stiffness characteristics of the structure. The unforced form of these equations can be solved to establish a sequence of frequencies where the system will execute harmonic response. These frequencies are the system modal frequencies, and the configurations that the structure assumes while executing motion at the modal frequencies are the mode shapes. Alternately, the structure can be spatially discretized, or the partial differential equations governing motion can be discretized to obtain a sequence of ordinary differential equations governing structural motion. The unforced form of these equations can be solved to establish the modal frequencies and mode shapes of the structure. Whichever approach is chosen, the modal frequencies are established (in most cases) by numerical solution of a transcendental equation or a polynomial. The modal frequencies can be denoted

$$f_i = g_i(a_1, a_2, \ldots), \quad i=1,2,3,\ldots \qquad (1)$$

where g_i is a function that cannot usually be written explicity, even for simple structures, and the a_j, $j = 1, 2, \ldots$, are the structural mass and stiffness parameters upon which the modal frequencies depend. Because the functions g_i in Equation 1 cannot be written explicitly, the equation must simply be interpreted as an expression of the fact that the modal frequencies can be computed when the structure parameters are given.

When the mass and stiffness characteristics of a structure are random, then the parameters a_j, used in Equation 1, are random variables. Consider this case and denote the mass and stiffness random variables A_j, $j = 1, 2, \ldots, N$. The modal frequencies can be expressed

$$F_i = g_i(A_1, A_2, \ldots), \quad i=1,2,3,\ldots \quad (2)$$

where the frequency variable has been capitalized to indicate that it is random. The F_i, $i = 1, 2, \ldots$, are random variables because of their functional dependence on random variables A_j, $j = 1, 2, \ldots, N$. The objective of this analysis is to find the second order statistics of the F_i. This can be done, approximately, by writing the g_i using Taylor series expansions about the means of the random variables A_j. Then F_i can be expressed

$$\begin{aligned} F_i &= g_i(\mu_1, \mu_2, \ldots, \mu_N) \\ &+ \sum_{j=1}^{N} \left.\frac{\partial g_i}{\partial a_j}\right|_{a_j=\mu_j} (A_j - \mu_j) \\ &+ \sum_{j=1}^{N}\sum_{k=1}^{N} \left.\frac{\partial^2 g_i}{\partial a_j \partial a_k}\right|_{\substack{a_j=\mu_j \\ a_k=\mu_k}} (A_j-\mu_j)(A_k-\mu_k) \\ &+ \ldots, \qquad i=1,2,3,\ldots \quad (3) \end{aligned}$$

where μ_i is the mean value of the random variable A_i. When the series in Equation 3 is truncated following a finite number of terms, the resulting expressions can be used to approximate the moments of the modal frequencies. For example, when the series are truncated following the quadratic terms, and the random variables A_j, $j = 1, \ldots, N$ are assumed to be normally distributed, the mean of F_i is

$$\begin{aligned} E(F_i) &= g_i(\mu_1, \mu_2, \ldots, \mu_N) \\ &+ \sum_{j=1}^{N}\sum_{k=1}^{N} \left.\frac{\partial^2 g_i}{\partial a_j \partial a_k}\right|_{\substack{a_j=\mu_j \\ a_k=\mu_k}} \rho_{jk}\, \sigma_j\, \sigma_k \\ &\qquad i=1,2,3,\ldots \quad (4) \end{aligned}$$

where σ_j^2, $j = 1, \ldots, N$, is the variance of the random variable A_j, and ρ_{jk} is the correlation coefficient between the random variables A_j and A_k. (Note that $\rho_{jj} = 1$.)

The variance of F_i can be obtained by subtracting the mean from Equation 3, squaring the result, and taking the expected value. When Equation 3 is truncated following the quadratic terms, the result is

$$\begin{aligned} V(F_i) &= \sum_{j=1}^{N}\sum_{k=1}^{N} \left(\left.\frac{\partial g_i}{\partial a_j}\right|_{a_j=\mu_j} \right) \left(\left.\frac{\partial g_i}{\partial a_k}\right|_{a_k=\mu_k} \right) \\ &\qquad \rho_{jk}\, \sigma_j\, \sigma_k \\ &+ \sum_{j=1}^{N}\sum_{k=1}^{N}\sum_{\ell=1}^{N}\sum_{m=1}^{N} \left(\left.\frac{\partial^2 g_i}{\partial a_j \partial a_k}\right|_{\substack{a_j=\mu_j \\ a_k=\mu_k}} \right) \\ &\quad \left(\left.\frac{\partial^2 g_i}{\partial a_\ell \partial a_m}\right|_{\substack{a_\ell=\mu_\ell \\ a_m=\mu_m}} \right) \sigma_j \sigma_k \sigma_\ell \sigma_m (\rho_{jk}\rho_{\ell m} \\ &\quad + \rho_{j\ell}\rho_{km} + \rho_{jm}\rho_{k\ell}), \quad i=1,2,3,\ldots \\ &\qquad (5) \end{aligned}$$

where it has again been assumed that the random variables A_j, $j = 1, \ldots, N$, are normally distributed, for ease in computation of the fourth order moments. The technique developed here does not depend on the normal distribution assumption; any joint distribution of the A_j can be incorporated in the moment equations for the F_i. Finally, the covariances between pairs of modal frequencies can be obtained by subtracting the mean values from Equation 3 and taking the expected values of products like

$$(F_{i_1} - E[F_{i_1}])\,(F_{i_2} - E[F_{i_2}]).$$

The covariance between the modal frequencies F_{i_1} and F_{i_2} is

$$\mathrm{Cov}(F_{i_1},F_{i_2}) = \sum_{j=1}^{N}\sum_{k=1}^{N}\left(\left.\frac{\partial g_{i_1}}{\partial a_j}\right|_{a_j=\mu_j}\right)\left(\left.\frac{\partial g_{i_2}}{\partial a_k}\right|_{a_k=\mu_k}\right)\rho_{jk}\,\sigma_j\,\sigma_k$$
$$+\sum_{j=1}^{N}\sum_{k=1}^{N}\sum_{\ell=1}^{N}\sum_{m=1}^{N}\left(\left.\frac{\partial^2 g_{i_1}}{\partial a_j\partial a_k}\right|_{\substack{a_j=\mu_j\\ a_k=\mu_k}}\right)\left(\left.\frac{\partial^2 g_{i_2}}{\partial a_\ell\partial a_m}\right|_{\substack{a_\ell=\mu_\ell\\ a_m=\mu_m}}\right)\sigma_j\sigma_k\sigma_\ell\sigma_m(\rho_{jk}\rho_{\ell m}$$
$$+\rho_{j\ell}\rho_{km}+\rho_{jm}\rho_{k\ell}),\quad i=1,2,3,\ldots \tag{6}$$

Some numerical examples presented later in this paper show how moments like the mean, variance and covariance of modal frequencies given in Equation 4, 5 and 6 can be computed in specific cases.

The moments of the modal frequencies based on Equation 3 can be evaluated when two types of information are available. First, it is required that a method for evaluating the functions g_i and their derivatives be available. Second, it is required that the moments of the underlying random variables, A_j, be available. Consider first the functions g_i and their partial derivatives. It is generally true that the g_i functions cannot be written explicitly. However, when parameter values, a_j, $j = 1,\ldots,N$ are specified, Equation 1 can be solved numerically to obtain a modal frequency. Because of this, it is possible to numerically approximate the derivatives of the g_i using, for example, finite difference formulas. The central difference formulas for the first and second derivatives of g_i with respect to a_j and the second partial derivative of g_i with respect to a_j and a_k are,

$$\left.\frac{\partial g_i}{\partial a_j}\right|_\mu = \frac{1}{2\varepsilon_j}\{g_i(a_1,\ldots,a_j+\varepsilon_j,\ldots) - g_i(a_1,\ldots,a_j-\varepsilon_j,\ldots)\} \tag{7a}$$

$$\left.\frac{\partial^2 g_i}{\partial a_j^2}\right|_\mu = \frac{1}{\varepsilon_j^2}\{g_i(a_1,\ldots,a_j+\varepsilon_j,\ldots) - 2g_i(a_1,\ldots,a_j,\ldots) + g_i(a_1,\ldots,a_j-\varepsilon_j,\ldots)\} \tag{7b}$$

$$\left.\frac{\partial^2 g_i}{\partial a_j\partial a_k}\right|_\mu = \frac{1}{4\varepsilon_j\varepsilon_k}\{g_i(a_1,\ldots,a_j+\varepsilon_j,\ldots,a_k+\varepsilon_k,\ldots) - g_i(a_1,\ldots,a_j-\varepsilon_j,\ldots,a_k+\varepsilon_k,\ldots) - g_i(a_1,\ldots,a_j+\varepsilon_j,\ldots,a_k-\varepsilon_k,\ldots) + g_i(a_1,\ldots,a_j-\varepsilon_j,\ldots,a_k-\varepsilon_k,\ldots)\} \tag{7c}$$

where ε_j and ε_k are small, positive increments in the values of A_j and A_k, respectively. Evaluation of the derivatives in Equations 7a, 7b and 7c, requires, respectively, two, three and four evaluations of g_i. The derivatives can be approximated because, as mentioned above, g_i can be numerically evaluated. Recall that it is necessary to obtain the derivatives through a differencing procedure because the functions g_i are not known in closed form.

The moments of the random variables, A_j, are also required as input to the calculation of the moments of the F_i. It is assumed that at least the first and second order moments of the A_j are available, and usually, these would be obtained through experiment. However, higher order moments are required when terms beyond the linear ones in Equation 3 are retained. For example, Equations 4, 5 and 6 were developed by including quadratic terms in the expression for F_i, and the fourth order moments of the A_j were required in obtaining the results in Equations 4, 5 and 6. In general, when terms up to degree n are retained in Equation 3, the moments of the A_j up to order 2n are required in the analysis. Higher order moments of A_j can be obtained in one of two ways. First, they can be obtained directly from the data; however, higher order moment estimates tend to have limited confidence when they are based on limited data. Second, when the probability distribution of the data is available, the higher moments can be obtained from the definition and the statistical parameters of the distribution. (The parameters can be obtained from the first and second order moments.) A typical approach would be to assume that the data come from a normally distributed source. This was the assumption used in obtaining Equations 4, 5 and 6, and it is an approach that usually yields reasonable results.

One matter not yet considered is the number of terms retained in the series for F_i, Equation 3. Several factors affect the number of terms retained, but most important, enough terms must be retained to render the series, Equation 3, an accurate approximation of g_i. The accuracy of the approximation is especially important over the range of the most probable values of the random variables A_j. Further, the number of terms retained determines the order of partial derivatives of the function g_i that must be approximated and the order of the moments of the A_j that must be estimated. Estimating higher order moments of the A_j may not be a problem, but approximating high order derivatives of the g_i may be a problem especially if the numerical evaluation of g_i is a time-consuming process. For this reason, the series of Equation 3 will usually be truncated following the linear or, at most, the quadratic terms. The examples presented later in this paper show that this yields good accuracy.

Examples

The examples described in this section summarize two types of results: experimental and analytical. The experimental results first demonstrate that randomness occurs in relationships between quantities that measure structural parameters, structural loads and structural responses. Second, the experimental results provide a standard to which the results of an analysis can be compared. The results of the numerical analyses demonstrate the applicability (in a specific case) of the analytical technique developed in this study, when compared to the experimental results. The numerical studies also show some applications of the analytical technique.

Example One - Experiment

The physical system studied in the experimental investigation is a simple, base-supported, cantilever beam, shown in Figure 1. An aluminum mass is attached near the free end of the beam; the mass is a pair of aluminum bars. The beam is attached to a fixture by placing one washer above and one below the base of the beam, passing an $0.794\text{x}10^{-2}$ m (5/16 in) screw through the washers and beam and into the fixture, and then applying a torque to the screw. The torque in the screw establishes a preload, and this causes the base of the beam to be connected to the fixture with varying stiffness. The fixture is attached to a Ling 330 vibration exciter through which the input is applied. The beam and washers are made from 6061-T6 aluminum, and the screw is steel.

The characteristics of the beam, its end mass and the washers at its base are given in Figure 1.

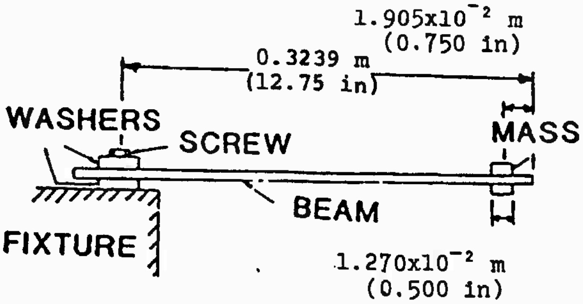

Beam

thickness = $0.635\text{x}10^{-2}$ m (0.250 in)

width = $5.062\text{x}10^{-2}$ m (1.993 in)

material density = $0.2674\text{x}10^{-8}$ kg/m^3 (0.09662 lb/in^3)

End mass = 0.0892 kg (0.1967 lb)

Washers at support

thickness = $0.635\text{x}10^{-2}$ m (0.250 in)

outside diameter = $2.540\text{x}10^{-2}$ m (1.000 in)

inside diameter = $0.864\text{x}10^{-2}$ m (0.340 in)

Figure 1. Cantilever beam of Example One.

The random excitation is controlled on the fixture, near the base of the beam, using a closed loop control procedure, and using an Endevco 2222B accelerometer to measure the environment. The response is measured near the end of the beam using an Endevco 2222B accelerometer attached to the mass. The accelerometer mass is small compared to the mass attached to the beam. The response is continuously monitored while the input is applied.

A general experimental procedure was established and repeated several times to generate the data for this study. The procedure includes the following steps. (1) Sandwich the base of the beam between washers, and pass the screw through the washers and beam into the fixture. Apply a torque to the screw using a calibrated torque wrench, and increase the torque until a pre-established level is reached. (2) Attach a Kaman KD-2300-6C non-contacting, eddy current displacement transducer to the vibration fixture as shown in Figure 2. Apply an 0.2522 kg weight near the end of the beam, as shown in Figure 2. Note and record the voltage change (related to displacement) that occurs during application of the load. Remove the 0.2522 kg weight and the displacement transducer. (3) Apply a band-limited white noise excitation to the system. Define the excitation so that it has lower and upper cutoff frequencies of 10 Hz and 120 Hz, respectively, and a one-sided spectral density of 0.0091 g^2/Hz. During the excitation continuously monitor both the input and response. Use these to estimate the input spectral density and the input/response cross spectral density; then use the spectral densities to estimate the frequency response function of the structure. Use the computer program SMS MODAL4 (Reference 4) to estimate the first modal frequency, f_1, of the structure. This completes the experiment.

Following the experiment, another structural parameter is estimated. This is the base stiffness of the beam structure. Figure 3 shows a schematic model of the beam tested. It is assumed that the stiffness of the beam (excluding the base spring) is known, and that the base spring stiffness, s, is unknown. The value of s is important to the overall stiffness of the structure, and the presence of the spring at the base of the beam arises from the fact that the preload in the screw retaining the base of the beam is finite. The value of s can be inferred from static analysis and the overall stiffness of the structure. The overall stiffness can be obtained from the information gathered in step (2), above, simply by computing the ratio of the applied static load to the displacement. Denote the load of step (2) as P and the displacement as D; then s can be computed using the formula

$$s = \frac{Pzx}{Px^2(x-3z)/6EI - D} \qquad (8)$$

Figure 2 defines x and z as load application and measurement points. EI is the beam stiffness.

Nineteen experiments were run following the procedure described above. Torque was controlled, and the information leading to preload and static displacement under static load were measured. Then the parameters s and f were estimated. The results are listed in Table 1.

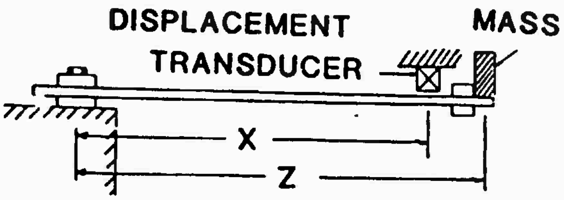

Figure 2. System used to measure base stiffness

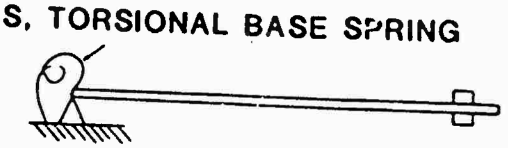

Figure 3. Simplified beam model.

The ultimate objective of this example is to show that some simple experimental results can be used along with analytical procedures to predict random variation in the fundamental frequency. Several statistical analyses are possible using the data generated in the experiments described above, but only one analysis, useful in the following investigation, is pursued. Specifically, the mean and variance of the base stiffness corresponding to one torque value (1.808 N-m or 16 in-lb) and the natural frequency corresponding to the same torque value are estimated. The other data generated in the experiments are used later.

Standard formulas can be used to estimate the mean and variance of a random variable, given that measured realizations of the random variable are available. In the present application, the mean and variance of the base stiffness random variable, S, and the fundamental frequency random variable, F, corresponding to the 1.808 N-m (16 in-lb) torque are sought. These are estimated using the data in Table 1; the results are

$$\bar{S} = 4755 \text{ N-m/rad } (42088 \text{ in-lb/rad}) \qquad (9a)$$

$$\sigma_S^2 = 1.970\times10^5 \ (\text{N-m/rad})^2 \quad (1.543\times10^7 \ (\text{in-lb/rad})^2) \qquad (9b)$$

$$\bar{F} = 32.02 \text{ Hz} \qquad (9c)$$

$$\sigma_F^2 = 0.0642 \text{ Hz}^2 \qquad (9d)$$

where a bar over the variable refers to a mean estimate, and the square of $\hat{\sigma}$ is a variance estimate. The corresponding standard deviations are

$$\sigma_S = 444 \text{ N-m/rad } (3929 \text{ in-lb/rad}) \tag{9e}$$

$$\sigma_F = 0.2535 \text{ Hz} \tag{9f}$$

The mean and variance of the base stiffness random variable, S, estimated here correspond to the moments of the random variable A, in Equation 3. These are used as input to the analysis of this experiment presented in the next section. The mean and variance of the fundamental frequency random variable, F, are the moments that can be estimated using the analysis method developed here. The analytical estimates are obtained in the following paragraphs.

Table 1. Experimental Results

Test No.	Torque N-m (in-lb)	Base Rotat. Stiffness N-m/rad (in-lb/r)	Fundam. Frequency Hertz
1	1.13 (10)	2928 (25918)	30.57
2	1.36 (12)	3250 (28767)	30.92
3	1.58 (14)	4033 (35699)	31.78
4	1.81 (16)	4304 (38095)	31.65
5	2.03 (18)	5544 (49073)	32.66
6	2.26 (20)	6370 (56386)	32.79
7	2.49 (22)	7635 (67575)	33.09
8	2.71 (24)	6267 (55468)	32.77
9	2.94 (26)	13089 (115849)	33.51
10	3.16 (28)	7950 (70367)	33.01
11	1.81 (16)	5036 (44577)	32.19
12	1.81 (16)	4304 (38095)	31.87
13	1.81 (16)	4908 (43440)	32.19
14	1.81 (16)	4614 (40835)	31.73
15	1.81 (16)	5795 (51291)	32.53
16	1.81 (16)	4785 (42359)	32.00
17	1.81 (16)	4846 (42893)	32.09
18	1.81 (16)	4506 (39879)	31.92
19	1.81 (16)	4453 (39417)	32.00

Example One - Analysis

In this analysis the formulas of Equations 4 and 5 are used to estimate the mean and variance of the fundamental frequency of the beam used in the experiments described above. This implies an assumption that the variation of modal frequency can be accurately approximated by including three terms in the series expansion, Equation 3. The torsional stiffness, S, is taken to be the underlying random variable, A. (In the present application there is only one underlying random variable, A_j, and this is denoted A.) The moments of torsional stiffness are given in Equations 9a, 9b and 9e.

The fundamental frequency of the beam is evaluated using a simple finite element program. The beam parameters and a spacial discretization are first specified, and the program is then run to obtain the fundamental frequency. In this application the 32.39 cm beam was divided into 192 elements with two degrees of freedom (translation and rotation) at each node. Figure 4 shows a curve of fundamental frequency versus base stiffness for the results obtained experimentally and using the finite element program. The curve defines the function $g_1(A)$. Good agreement is evident, and this is required in order for the analysis to yield statistical results comparable to the experiment.

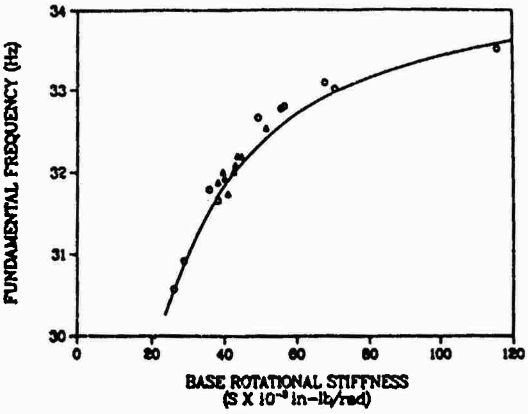

Figure 4. Frequency versus stiffness. Data and analysis (solid line).
Δ 16 in-lb torque
o other torque values

In this example the mean and variance of the fundamental frequency are estimated when the torque value on the base support bolt is 1.808 N-m (16 in-lb). In that case the mean and variance of the random variable A are 4755 N-m/rad and 1.970×10^5 $(\text{N-m/rad})^2$. The function $g_1(A)$ and its approximate derivatives are obtained using the finite element program. They are

$$g(\mu) = 31.92 \text{ Hz} \qquad (10a)$$

$$\left.\frac{\partial g(a)}{\partial a}\right|_{a=\mu} = 5.047 \times 10^{-4} \text{ Hz/N-m/rad} \qquad (10b)$$

$$(5.703 \times 10^{-5} \text{ Hz/in-lb/rad})$$

$$\left.\frac{\partial^2 g(a)}{\partial a^2}\right|_{a=\mu} =$$

$$-1.892 \times 10^{-7} \text{ Hz/(N-m/rad)}^2 \qquad (10c)$$

$$(-2.415 \times 10^{-9} \text{ Hz/(in-lb/rad)}^2)$$

where $\varepsilon = \sigma_g$. These results are used in Equations 4 and 5 to show that the mean and variance of the fundamental frequency are

$$E[F] = 31.90 \text{ Hz} \qquad (11a)$$

$$V[F] = 0.0512 \text{ Hz}^2 \qquad (11b)$$

The standard deviation of the fundamental frequency is

$$\sigma_F = 0.2264 \text{ Hz} \qquad (11c)$$

These results are the analytical analog of the experimental results given in Equations 9c, 9d and 9f.

The results of this example show that although it is possible to evaluate the mean and variance of a modal frequency random variable experimentally, an easier method is available. This easier method combines the use of experimental results with analysis. Some simple, static experiments are used to characterize random variation in an underlying variable, base stiffness. Then that information is used with analysis to characterize random variation in a modal frequency. The results of the analysis compare well with the experimental results.

Example Two

The numerical analysis summarized in this section considers a structure similar to the one in Example One. It is a uniform cantilever beam whose rotation is finitely constrained at the base. Figure 5 shows a schematic of the beam. The beam length is taken to be 0.305 m(12 in), its area is 3.226×10^{-4} m^2 (0.50 in^2) and its EI constant is 68.88 N-m^2 (24000 lb-in^2.). The beam material density is 0.2768×10^4 kg/m^3 (0.10 lb/in^3). The stiffness of the base spring is taken to be a normally distributed random variable with mean value 4519 N-m/rad (40000 in-lb/rad) and variance, 2.042×10^5 $(\text{N-m/rad})^2$ (1.6×10^7 $(\text{in-lb/rad})^2$).

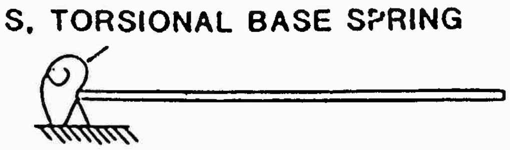

Figure 5. Cantilever beam of Example Two.

The characteristics of the first five beam modal frequencies are considered in this example. They are deterministically evaluated through an analysis of the partial differential equation of the continuous beam. The values of the first five modal frequencies and the first and second derivatives of these modal frequencies with respect to base stiffness are listed in Table 2. The values and partial derivatives are all taken at the mean value of base spring stiffness.

The quantities given in Table 2 and the structural parameters specified above can be used to approximately evaluate the means, variances and covariances of the modal frequencies through application of Equations 4, 5 and 6. The means and variances of the modal frequencies are listed in Table 3. The covariances between modal frequencies are not listed because the mode frequencies are nearly perfectly correlated with one another. That is

$$\text{Cov}(F_i,F_j) = (V(F_i)V(F_j))^{1/2} \qquad (12)$$

Table 2

Modal frequencies and their approximate partial derivatives for the beam of Example Two.

Mode No.	Modal Frequency hz	First Partial Derivative hz/N-m/rad (hz/in-lb/rad)	Second Partial Derivative hz/(N-m/rad)^2 (hz/(in-lb/rad)^2)
1	48.27	8.982×10^{-4} (1.015×10^{-4})	2.873×10^{-8} (3.667×10^{-10})
2	306.41	4.205×10^{-3} (4.751×10^{-4})	3.680×10^{-7} (4.697×10^{-9})
3	865.93	9.186×10^{-3} (1.038×10^{-3})	1.203×10^{-6} (1.536×10^{-8})
4	1710.1	1.419×10^{-2} (1.603×10^{-3})	2.388×10^{-6} (3.048×10^{-8})
5	2844.8	1.885×10^{-2} (2.130×10^{-3})	3.748×10^{-6} (4.784×10^{-8})

Table 3

Means and variances of modal frequencies for cantilever beam of Example Two

Mode No.	Mean of Frequency hz	Variance of Frequency hz^2
1	48.28	0.17
2	306.45	3.62
3	866.05	1727
4	1710.3	41.3
5	2845.2	73.0

The reason is that the high order terms in the representation of f_i are small; therefore the modal frequencies are linear functions of one random variable, and this makes their covariance high.

Figure 6 shows a plot (on a log-log scale) of modal frequency standard deviation versus mean modal frequency. The points shown here nearly fall along a straight line; this implies a power law relation between modal frequency standard deviation and mean modal frequency. The standard deviation of modal frequency clearly increases with mean modal frequency implying an increase in absolute random variation of higher frequency modes. However, the coefficients of variation of the modal frequencies can be computed, and these decrease from nearly one percent to about three-tenths of one percent. This shows a decreasing tendency in normalized random variation with increasing frequency. The coefficient of variation for modal frequencies is shown in Figure 6.

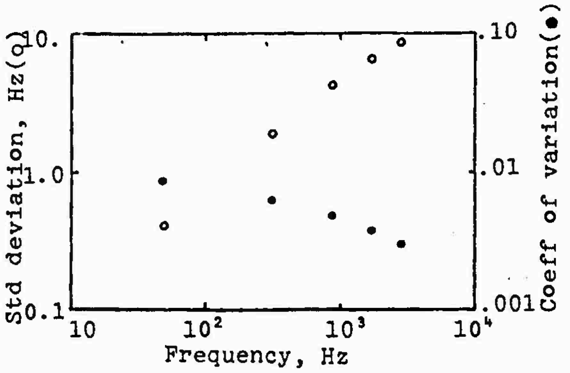

Figure 6. Standard deviation and coefficient of variation of modal frequency versus mean modal frequency.

Another scale by which modal frequency variation must be measured considers the differences between modal frequencies. When the standard deviation of modal frequencies becomes large compared to the difference between modal frequencies, then it may become difficult to distinguish modal frequencies. A measure of the magnitude of modal frequency variation relative to modal frequency spacing may be defined as

$$r_i = \frac{\sqrt{V(F_i)}}{\frac{1}{2}(E(F_{i+1})+E(F_{i-1}))}, \quad i=1,2,\ldots \qquad (13)$$

This quantity is plotted in Figure 7 for the data in Table 3. Note that $E[F_0] = 0$ is the zeroth, or rigid body, frequency. In this example r_i, the ratio of the magnitude of modal frequency standard deviation to mean modal frequency spacing, tends to increase with frequency, but it is much lower than one at the first four modal frequencies. Therefore, there is no problem with confusing modes here. The circumstances under which r_i will tend to increase with frequency and under which r_i will tend to be large can be determined as follows.

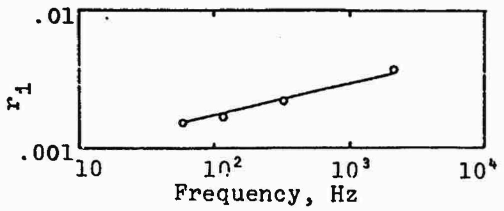

Figure 7. Modal frequency standard deviation - modal frequency spacing ratio, r_1, versus frequency.
Data (open circles)
Equation 17 (line)

Note that the modal frequencies of a beam increase as a quadratic function of the mode number. (See Reference 5, for example.) In the case of a cantilever beam, for example, the modal frequencies are, approximately,

$$f_i = q\,(2i-1)^2, \quad i=1,2,\ldots \tag{14}$$

where q is a constant that depends on E, I, m and l. Note also that the standard deviation of modal frequency is approximately a power law function of frequency, therefore,

$$\sqrt{V(F_i)} = C_1 f^{C_2}, \quad i=1,2,\ldots \tag{15}$$

Using Equations 14 and 15 in Equation 13 yields the result

$$r_i = \frac{C_1}{8}\, q^{C_2-1}\, \frac{(2i-1)^{2C_2}}{(i-\frac{1}{2})}, \quad i=1,2,\ldots \tag{16}$$

For higher modes this can be accurately approximated as

$$r_i = Q\, i^{2C_2-1}, \quad i=1,2,\ldots \tag{17}$$

This expression establishes the relation between the modal standard deviation - modal spacing ratio r_i, and the mode number, i. It is correct, in general, for beams because the beam modal frequency is always a quadratic in mode number. The quantity tends to increase with mode number (and frequency) when $2C_2-1$ is positive, and this occurs when the slope of the standard deviation of modal frequency versus frequency curve has a value greater than 0.5 (on a log-log graph). The r_i tends to be large when Q is large, and when this occurs depends on the values of C_1, C_2 and q (Equation 16).

Equation 17 was fit to the data in Figure 7 by (1) noting that $C_2 = 0.73$, from Figure 6, (2) noting that the mode number is approximately proportional to the square root of f, and (3) solving for Q at the fourth mode. The entire curve is plotted in Figure 7, and it accurately represents the observed variation past the first mode.

Example Three

This example considers a system identical, in every respect but two, to the structure used in the previous example. In the present example, in addition to admitting randomness in the support spring, randomness is also admitted in the area moment of inertia, I, and the area, A. The area moment of inertia is taken to be a normally distributed random variable with mean 9.990×10^{-10} m^4 (0.0024 in^4) and variance of 6.387×10^{-21} m^8 (3.686×10^{-8} in^8). The area is taken to be a normally distributed random variable with mean value 3.226×10^{-4} m^2 (0.50 in^2) and variance 1.665×10^{-10} m^4 (0.0004 in^4). The modulus of elasticity of the beam material is taken as 6.895×10^{10} Pa (10^7 psi). This yields a mean EI constant identical to the one used in the previous example. Five levels of correlation between the area moment of inertia and beam area are considered in the example. These are correlation coefficients of 0.0, 0.25, 0.50, 0.75 and 1.00. The analysis used in this example includes only terms up to the first derivative in Equation 3; therefore, Equations 4, 5 and 6 are modified by elimination of their final term. This means that variation of the modal frequencies is modeled as a linear function of base support stiffness, area moment of inertia and cross sectional area, in the vicinity of the mean values of these variables. The analysis is executed for the first two modes of the beam.

Table 4 lists the modal frequencies, first partial derivatives of modal frequencies with respect to base stiffness, first partial derivatives of modal frequencies with respect to area moment of inertia, and first partial derivatives of modal frequencies

Table 4

Modal frequencies and their approximate first partial derivatives with respect to base stiffness, s, area moment of inertia, I, and cross sectional area, A, for the beam of Example Three.

Mode No.	f_i hz	$\partial f_i/\partial s$ hz/N-m/rad (hz/in-lb/rad)	$\partial f_i/\partial I$ hz/m^4 (hz/in^4)	$\partial f_i/\partial A$ hz/m^2 (hz/in^2)
1	48.27	8.892×10^{-4} (1.015×10^{-4})	2.416×10^{10} (1.006×10^{4})	-7.481×10^{4} (-4.827×10^{1})
2	306.41	4.205×10^{-3} (4.751×10^{-4})	1.534×10^{11} (6.384×10^{4})	-4.749×10^{5} (-3.064×10^{2})

Table 5

Means, variances and covariances for modal frequencies of the beam of Example Three. (ρ_{IA} is the correlation coefficient between the area moment of inertia, I, and cross sectional area, A.)

Mode No.	Mean Frequency hz	Variance of Frequency hz^2 for $\rho_{IA}=0$	$\rho_{IA}=0.5$	$\rho_{IA}=1.0$
1	48.27	4.83	2.96	1.10
2	306.41	191.40	116.29	41.18

Covariance between f_1 and f_2 hz^2 for $\rho_{IA}=0$	$\rho_{IA}=0.5$	$\rho_{IA}=1.0$
30.36	18.53	6.69

with respect to cross sectional area. All these are evaluated at the mean of base stiffness, area moment of inertia and cross sectional area. The quantities in Table 4 can be used in the abbreviated forms of Equations 4, 5 and 6 to obtain the means, variances and covariances of the modal frequencies. This was done and the results are given in Table 5.

The random variation that occurs here is substantially greater than what occurs in the previous example. This indicates that randomness in area moment of inertia and cross sectional area can influence overall randomness to a greater degree than base stiffness when the moments of these random variables are those given above. In fact, the area moment of inertia has the greater influence of the two because its variance is the greater in value. When beam dimensions vary randomly, the area moment of inertia will normally display greater random variation than cross sectional area because moment of inertia is a function of dimension to the fourth power, whereas area is a function of dimension squared. Because the randomness in area moment of inertia dominates the result, the coefficient of correlation between beam modal frequencies is near one. This result occurs because all modal frequencies are approximately linear functions of one random variable.

Discussion, Conclusions and Recommendations

This investigation shows through simple experiment and analysis that random variation occurs in the modal frequencies of a structure, and that this randomness can be accurately described using a combination of experimental information and numerical analysis. Clearly, practical physical systems are more complicated than the system tested in this investigation. However, the fact that randomness occurs in this system shows that randomness can occur in other, more complicated systems, and how it can occur. Most important, this investigation shows that the degree of randomness in modal frequencies can be quantified, and this study demonstrates a technique that can be used to quantify random variation in modal frequencies.

The numerical examples presented in this paper show what may be trends in the random behavior of simple structures. First, while the absolute random variation in modal frequencies increases with the mean modal frequency, the coefficient of variation decreases slowly as frequency increases. Second, the magnitude of random variation in modal frequency can become greater than the spacing between modal frequencies as frequency increases. Third, the random variation in modal frequencies is very sensitive to random variation in dimensions, especially as they relate to area moment of inertia in a beam. Third, when one source of random variation dominates the others, the modal frequencies are strongly correlated to one another.

Further investigation into random variation in modal characteristics should be pursued. Specifically, variation arising from randomness in material properties, and the character of internal joints, from nonlinear structural response behavior, and in more complicated structures must be studied.

References

1. W. E. Boyce, Random Eigenvalue Problems. In Probabilistic Methods in Applied Mathematics. (A. T. Barucha-Reid, Ed.) Vol. 1, pp 1-73, Academic Press, New York, 1968.
2. J. D. Collins, W. T. Thomson, "The Eigenvalue Problem for Structural Systems with Statistical Properties," AIAA Journal, Vol. 7, No. 4, April, 1969.
3. T. K. Hasselman, G. C. Hart, "Modal Analysis of Random Structural Systems," Journal of the Engineering Mechanics Division, ASCE, June, 1972.
4. SMS 500A, MODAL 4.0 Operating Manual. Structural Measurement Systems, Inc., San Jose, California, 95134, December, 1982.
5. Hurty, W. C., Rubinstein, M.F., Dynamics of Structure, Prentice Hall, Englewood Cliffs, New Jersey, 1964.

Discussion

Mr. Tustin (Tustin Institute of Technology): I am not surprised at your results. Many years ago when people were starting to do random vibration testing with peak-notch networks, they found this all the time. They could not take the item off the shaker, put it back, and get the same equalization that they had done before. We have forgotten about this though with our automatic equalizers; that has covered up these changes.

Mr. Paez: That is one of the reasons we are starting to pursue this investigation; (there are a lot of other reasons, too) because it is important in analysis and understanding how this variation can occur. We have seen it many times, too, because we do a lot of testing. In the past we have not paid much attention to it because we thought it would be very difficult to analyze. So, we thought we would try to pursue an analysis and see if we can understand the sources of this variation.

Mr. Shin (Naval Postgraduate School): As you did a very, very good study for the random variation of the frequencies, as a by-product, you can also get damping. I think with damping the randomness concerned is more severe than anything else. Did you study that?

Mr. Paez: We pursued some preliminary studies on that, and they are not included in the paper. As a matter of fact, we also looked at random variation in mode shapes because that is another thing that is important to us. One of the underlying motivations for doing this was under certain circumstances we might have trouble testing with single point control because it may be difficult to control a system at a single point. We thought this might provide a motivation for using average control on structural testing. If there is random variation in mode shapes - certainly that might be one reason why it is difficult to control a system at one point. That might give us a motivation for doing average control on structural testing. However, there certainly is a random variation in the modes. In my opinion, that is probably more difficult to tie down analytically than the random variation in modal frequencies. There is also random variation in mode shapes, and that is something that needs to be pursued later.

STRUCTURAL DEGRADATION OF IMPACTED GRAPHITE/EPOXY LAMINATES

Dahsin Liu
Metallurgy, Mechanics, and Materials Science Department
Michigan State University
East Lansing, MI 48824-1226

and

C. T. Sun and L. E. Malvern
Engineering Sciences Department
University of Florida
Gainesville, FL 32611

Graphite/epoxy laminates fabricated from Hercules' AS4/3501-6 prepreg tapa were studied. The investigations included three different symmetric laminations of cross-ply plates: 3-layer, 5-layer, and 15-layer. Each square specimen was clamped around four edges and impacted at the center by a blunted steel impactor, 9.5 mm in diameter and 25.4 mm in length. The delamination areas caused by impact were measured by ultrasonic C-scan and x-ray radiography. The fundamental vibration frequency and damping coefficient of each cantilever plata before and after impact were measured by an FFT analyzer. After these nondestructive tests, every impacted specimen was subjected to a three-point bend test for the measurements of residual stiffness and residual strength. Results show the possibility of using the changes in damping coefficiant and vibration frequency as nondestructive evaluations for damaged composite plates.

INTRODUCTION

Because of their high stiffness and high strength to weight ratios, fiber reinforced composite materials have been used in structures where weight reductions are highly desired. However, the stiffness and strength of a fiber-reinforced composite material is dependent on the fiber orientation. If two adjacent layers in a composite plate have different fiber orientations, the material properties will be mismatched in the in-plane direction as well as in the through-the-thickness direction. These material property mismatches and the low strength of the matrix will increase composite materials sensitivity to delamination. In addition to the material property mismatch, some types of loading such as nonuniform banding and impact which generate high interlaminar shear stresses will accelarate the formation of delamination.

Most composite materials are very sensitive to impact loads. The failure modes of impacted composite platas can be classifiad into fiber breakage, matrix cracking, and delamination. In high-velocity impact, the penatration-induced fibar breakage is one of the major damage modes. However, delamination has been found to be the major failura mode in a composite plate subjected to subperforation impact [1]. For some other research on low-velocity impact, sea [2-7]. It is baliaved that in low-velocity impact most of the impacting energy added to a composite plata transforms into fractura surface anergy and damage in the material adjacent to tha delamination. Although the degree of the material property mismatch between two adjacent layers is constant in a laminate, the interlaminar stresses decrease as the impacting energy propagates from the impacting zone to the edge of the laminate. Therefore, tha area of the dalamination is determined by the loading condition, as well as by the degree of the material proparty mismatch.

Since delamination is the major failure mode in this study, it is useful to develop a relationship between the dalamination area and tha impacting energy [8]. However, the accuracy in measuring the delsmination area by nondestructive tests such as ultrasonic C-scan and x-ray radiography is dependent upon the sensitivity of each method. In addition, the effects of fiber breakage and matrix cracking are not considered in the relationship between the delamination area and the impacting energy. Therefore, a method which can measure the total damage will be very useful for the evaluation of an impacted composite plate. The changes in stiffness [9], vibration frequency [10], and damping coefficient [11] have been used as nondestructive evaluations for damaged composite materials. These measurements were extended to the investigations for damaged composite plates in this study.

EXPERIMENTAL TECHNIQUES

1. Impacting Test

In this study, three kinds of symmetric cross-ply plates were fabricated from graphite/epoxy prepreg tape AS4/3501-6 manufactured by Hercules [12]. They were: $[0_{10}/90_{10}/0_{10}]$, $[0_6/90_6/0_6/90_6/0_6]$, and $[0_2/90_2/0_2/90_2\ldots]_{30}$. These will be called 3-layer, 5-layer, and 15-layer respectively. Each specimen dimension was 152 mm by 152 mm and thickness of 3.8 mm. The specimen was clamped around four edges by two aluminum holders. The specimen-holder was then fixed on a steel frame in front of an air gun and was subjected to an impacting load. The impactor was a circular steel cylinder which was 9.5 mm in diameter and 25.4 mm in length. The impactor mass was 14 gm, and it had a blunt end. Depending upon the air pressure used in the test, the impacting velocity ranged from 20 m/s to 100 m/s. This range of impacting velocity did not cause any perforation of the specimen. Also, the delamination caused by this kind of impact did not propagate to the specimen's boundary and interact with the specimen holder. Both the impacting velocity and the velocity of the impactor rebound from the specimen were measured by two photocells mounted on a frame close to the specimen. The kinetic energy applied to a specimen was defined to be the difference of the kinetic energy of the impactor before and after impact and was used as a measure of the impact. The experimental set-up for the impacting test is shown in Figure 1.

2. Vibration and Damping Measurements

In measuring the vibration frequency and damping coefficient, each specimen was clamped along one edge by a steel holder having seven bolts on it. A torque wrench was used to apply 27.1 N-m (20 lb-ft) torque to every bolt in order to keep each specimen similarly clamped before and after impact. A small impulsive load was then introduced on the centerline perpendicular to the clamped edge with an instrumented hammer. For a better measurement, this load should be applied to the specimen as close to the clamped edge as possible. The hammer had a force transducer on it for recording the load, and the displacement history of the free edge opposite to the clamped side was measured by a second transducer. This non-contacting eddy-current displacement transducer was mounted on an independent support and was about 2 mm from the specimen surface on which an aluminum foil was attached for a better signal recording. Figure 2 shows the overall arrangement of the vibration and damping measurement. The histories of the applied force and the displacement of the plate were recorded and processed by a Fast Fourier Transform analyzer and thus different modes of vibration frequencies and damping coefficients could be obtained.

3. Delamination Measurements

Both ultrasonic C-scan and x-ray radiography were used in the measurement of the delamination area. A small hole with diameter of 1.4 mm was drilled at the center of the impact area. As a penetrant iothalamate sodium was applied to the delamination area through this small hole by a syringe. For better penetration several shots of penetrant were required while one side of the hole was blocked by a piece of tape. A long period of time was necessary for the penetrant to dry before the specimen was photographed by x-ray. In addition to x-ray radiography, ultrasonic C-scan was also used for the delamination detection. Because of good resolution, x-ray was able to show the delamination area on every single interface for 3-layer and 5-layer specimens. However, the ultrasonic C-scan only gave information of projected delamination area, and did not resolve overlapping delaminations.

4. Stiffness and Strength Determinations

After an impacted specimen had been investigated by the FFT analyzer for vibration frequency and damping coefficient and by ultrasonic C-scan and x-ray radiography for delamination area, the specimen was tested for residual stiffness and residual strength. A three-point bend test was conducted. Since the residual strength in compression is more sensitive to delamination than when in tension, the bend tests were arranged so that the front half, which includes the impacted surface, was in tension while the bottom half, which has relatively larger delamination area than the front half, was in compression. Residual stiffness and residual strength were determined from the load-displacement curve.

EXPERIMENTAL RESULTS

1. Vibration Frequency and Damping Coefficient

Before each specimen was impacted, the fudamental vibration frequency and the corresponding damping coefficient were measured. Since the specimens used in this study were rectangular cross-ply plates, the material properties were symmetric with respect to the centerlines of the specimens. The specimens were stiffer in the direction parallel to the surface fiber direction, 0-degree direction, than perpendicular to the surface fiber direction, 90-degree direction. The vibration frequency and damping coefficient were measured for both 0-degree and 90-degree directions. Results shown in Figure 3 are plots of vibration frequency and damping coefficient versus the flexural stiffness D_{11} in the 0-degree direction, where the higher the flexural stiffness, the higher is the vibration frequency. However, the damping coefficient does not have a monotonic relation with the flexural stiffness.

It is also interesting to investigate the relationship between the vibration frequency and the damping coefficient. Both measurements before and after impact are shown in Figure 4. The open symbols represent the information before impact while the solid symbols represent the measurements after impact. The data points in the upper part of the figure are more scattered than those in the lower part. It is believed that the measurements for the higher vibration frequencies are more sensitive to the condition of the clamp than those of the lower vibration frequency. However, it is not clear why the data points in the lower part of Figure 4 are grouped into three curved bands.

2. Projected Delamination Area and Total Delamination Area

Figure 5 shows the projected delamination area versus impacting kinetic energy. Raw data obtained from C-scan is presented with the least-squares from both C-scan and x-ray. Linear relationships have been found between the kinetic energy and the delamination areas obtained from both C-scan and x-ray. The result from C-scan show a higher sensitivity in detecting the delamination area than that from x-ray. Under the same kinetic energy, a 3-layer specimen suffers a larger delamination area than a 5-layer specimen, and the 5-layer a larger area than a 15-layer. The kinetic energies which are required to initiate delaminations in all three kinds of cross-ply plates are less than 3 joules. This shows that the graphite/epoxy used in this study is very sensitive to impact.

The total delamination areas, which are defined to be the summations of the delamination area at every interface in a laminate, obtained from x-ray radiography for both 3-layer and 5-layer specimens are shown in Figure 6. In order to keep the delamination from reaching the boundary of the specimen holder, lower impacting velocity was used for 3-layer plates than for 5-layer plates. Thus the plot extends to much smaller total delamination areas for the 3-layer plates than for 5-layer plates. There is no sufficient data for the 3-layer plates to determine if a single curve can represent the relation between the total delamination area and the kinetic energy. Larger size specimens would be necessary for the determination of such a relation.

3. Relations between Kinetic Energy and Vibration Frequency and Damping

The vibration frequencies measured before and after impact on a specimen are not the same. The relationship between the percentage of change in vibration frequency and the kinetic energy applied to a specimen is shown in Figure 7. All three kinds of plates (3-layer, 5-layer, and 15-layer) are shown in the same figure. The open symbols are for 0-degree measurements while the solid symbols are for 90-degree measurements. The data points obtained from 3-layer specimens are concentrated on the left hand side of Figure 7 and form a very steep band. For a 3-layer specimen, a small increment in kinetic energy will result in a very high percentage change in the vibration frequency. The data points of the 15-layer ones are located in the lower part of the figure and form a horizontal band. The vibration frequency does not change significantly in a 15-layer specimen even though the kinetic energy is increased remarkably. Generally speaking, the data points of 5-layer specimens are located between the 3-layer and 15-layer ones.

The change in damping coefficient before and after impact is shown in Figure 8. In many cases, the damping coefficients increase after impact, however, in some other cases it decreases. We believe that the increase in damping coefficient after impact is caused by the energy loss due to the friction between the newly generated surfaces in a delaminated specimen. However, it is not clear why in some cases of low kinetic energy the damping coefficients decrease after impact. Despite the changes in sign, Figures 7 and 8 have a similar trend. Compared with the measurement of vibration frequency, the measurements of damping coefficient are very scattered. This may result from the difficulty in measuring the damping coefficient which is very sensitive to the boundary condition and the contact time of the applied load.

4. Relations between Delamination Area and Vibration Frequency and Damping

The change in vibration frequency is also plotted versus projected delamination area evaluated by ultrasonic C-scan. The least-squares fits for all three laminations are shown in Figure 9. However, raw data is presented only for the 15-layer specimens. The 3-layer one hss a steeper slope than the other two laminations. This indicates that the sensitivity of the vibration frequency, as a nondestructive evaluation for delamination, is dependent on the lamination of a specimen. For plates with a constant thickness, the fewer the layers, the bigger the change is in vibration frequency. In addition, for all three cases the vibration frequencies change about 1% or 2% even when there is no delamination. This decrease in vibration frequency is believed to be caused by the matrix cracks resulting from impact.

In Figure 10, good correlations are found between the change in damping coefficient and total delamination area for both 3-layer and 5-layer specimens. The change in the damping coefficient of a 3-layer specimen is more sensitive to delamination than that of a 5-layer specimen. The results point out the possibility of evaluating the damage by measuring the change in damping coefficient in an impacted composite plate, even though the decrease is not completely understood.

5. Residual Stiffness and Residual Strength

After having been investigated by the nondestructive tests such as the measurements of the vibration frequency and damping coefficient and the measurements of the delamination areas by ultrasonic C-scan and x-ray radiography, each specimen was destructively tested for the evaluations of residual stiffness and residual strength. Every specimen was loaded to failure by a three-point bend test. A non-impacted specimen of each lamination group was used as a control specimen. The ratios of the residual stiffness and residual strength of impacted specimens and the control specimens are plotted versus the applied kinetic energy and results are shown in Fig. 11 and Fig. 12. In both figures, the 3-layer one has the highest reduction rate while the 15-layer one has the lowest. Compared with the reduction in strength, the reduction in stiffness has a lower rate in all three kinds of laminations.

CONCLUSIONS AND DISCUSSIONS

1. In a composite laminate subjected to subperforation impact, the thicker the adjacent layers, the larger is the projected delamination area on the interfaces. This is believed to be caused by the fact that the material property mismatch between two adjacent layers is much higher in thick-layer plates than in thin-layer plates. Thus, the increase of the thickness in each layer will result in the increase of delamination area and the decrease of strength. Accordingly, for specimens with a constant thickness, the higher the number of the layers, the smaller is the delamination area. However, the thicker the specimen, the larger is the projected delamination area.

2. In a subperforation impact, the projected delamination area has an approximately linear relation with the kinetic energy. Since delamination is the major failure in this study, the projected delamination can be used as an indicator of the impact damage. However, the relationship between the projected delamination area and the kinetic energy is dependent on the stacking sequence of the specimen. It would be useful to find a parameter which is independent of the stacking sequence of the specimen. The total delamination area may be a potential one.

3. The vibration frequency always decreases after impact. Such decrease is approximately linear with the kinetic energy added to a specimen and to the delamination area caused by this kinetic energy. The relationship between the change in vibration frequency and the kinetic energy and delamination area indicate the feasibility of using the change in vibration frequency as a nondestructive evaluation for damaged composite plates. However, the change in damping coefficient may either increase or decrease after impact. The damping coefficient increases when the total delamination area is large enough, while it decreases when the total area is small. The scattered results are caused by the difficulty in the measurement of the damping coefficients. As mentioned previously, damping coefficient is very sensitive to the boundary condition. For the larger total delamination areas, the change in damping coefficient has similar trends with the kinetic energy and delamination area as those shown in the study of vibration frequency. Because the percentage change in damping is larger, the relationship between the change in damping coefficient and total delamination area could be used as a nondestructive evaluation for the damage of a composite plate.

4. Compared with the plots of delamination area versus kinetic energy, (see Figs. 5 and 6) the data points in the figures of the vibration frequency and damping coefficient versus kinetic energy (Figs. 7 and 8) are very scattered. The changes of vibration frequency and damping coefficient are affected by all kinds of failure modes such as delamination, matrix cracking, and fiber breakage in a laminate. Each kind of failure mode makes a contribution to the structural degradation. The interaction among these three failure modes also affects the measurements of vibration frequency and damping coefficient of a damaged composite plate. In this study, only the linear relationship between the projected delamination area and the kinetic energy has been obtained. The effects of matrix cracking, fiber breakage, and the interactions among the three failure modes on the damping coefficient may be responsible for the decrease in the damping coefficient after impact.

ACKNOWLEDGMENT

Most of the investigations reported here were supported by the U.S. Army Research Office, Research Triangle Park , N.C. under Contract No. DAAG 29-83-K-0107.

REFERENCES

1. Sierakowski, R. L., Ross, C. A., Malvern, L. E., and Doddington, H. W., "Studies on the Fracture Mechanisms in Partially Penetrated

Filament Reinforced Laminated Plates," U.S. Army Research Office DAAG 29-79-G-0007, 1982

2. Foreign Object Impact Damage to Composites, American Society of Testings and Materials, STP 568, 1973

3. Guynn, E. G. and O'Brien, T. K., "The Influence of Lay-Up and Thickness on Composite Impact Damage and Compression Strength," AIAA/ASME/SAE 26th Structures, Structural Dynamics, and Materials Conference, Orlando, FL, 1985

4. Sharma, A. V., "Low-Velocity Impact Tests on Fibrous Composite Sandwich Structures," American Society of Testings and Materials, STP 734, 1981

5. Elber, W., "Failure Mechanics in Low-Velocity Impacts on Thin Composites Plates," NASA TP-2152, 1983

6. Sankar, B. V. and Sun, C. T., "Low-Velocity Impact Response of Laminated Beams Subjected to Initial Stresses," to be published, Journal of Composite Materials

7. Takeda, N., "Experimental Studies of the Delamination Mechanism in Impacted Fiber-Reinforced Composite Plates," Ph.D. Dissertation, University of Florida, 1980

8. Sierakowski, R. L., Malvern, L. E., and Ross, C. A., "Dynamic Failure Modes in Impacted Composite Plates," Failure Modes in Composite III, American Institute of Mining, Metallurgical, and Petroleum Engineers, Inc., N. Y., N. Y., 1976

9. Adams, R. D., Cawley, P., Pye, C. j., and Stone, R. J., "A Vibration Technique for Non-Destructive Evaluation by Assessing the Integrity of Structures," J. Mechanical Engineering Science, Vol. 20, No. 2, 1978

10. O'Brien, T. K., "Stiffness Change as a Nondestructive Damage Measurement," Mechanics of Nondestructive Testing, edited by W. W. Stinchcomb, Plenum Press, N.Y., 1980

11. Lee, B. T., Sun C. T., and Liu, D., "Evaluation of Damage Composite Beams by Damping Measurements," submitted to Composites

12. Hercules Incorporated, Aerospace Division, Bacchus Works, Magna, UT 84044

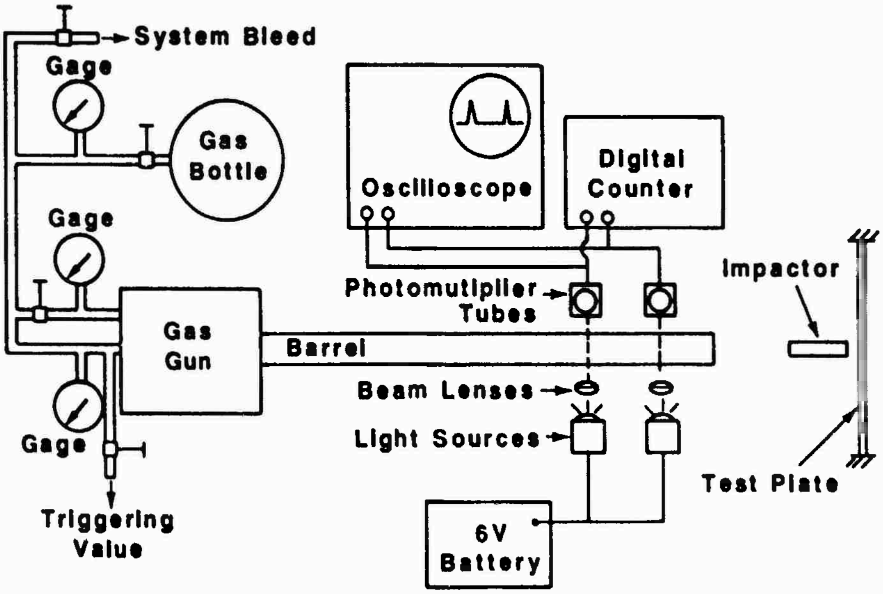

Fig. 1 Schematic drawing of gas gun assembly and related equipments

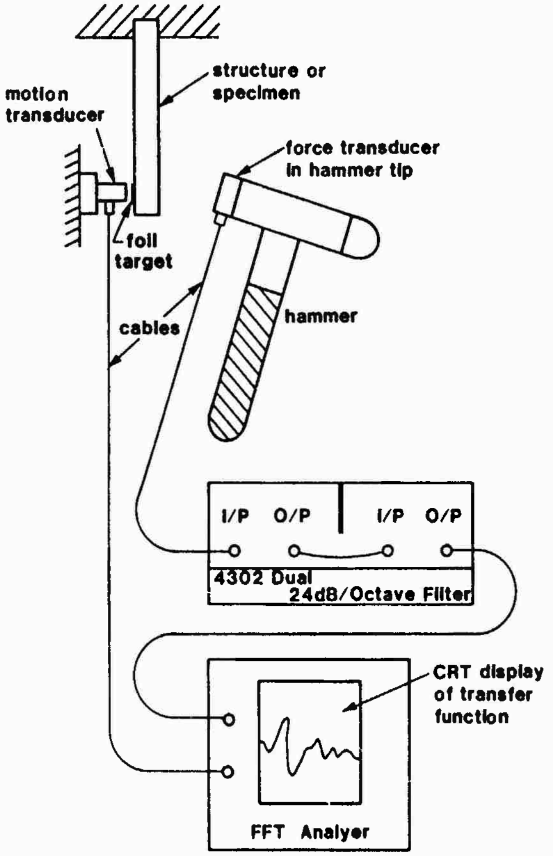

Fig. 2 Schematic drawing of the impulse hammer experimental set-up

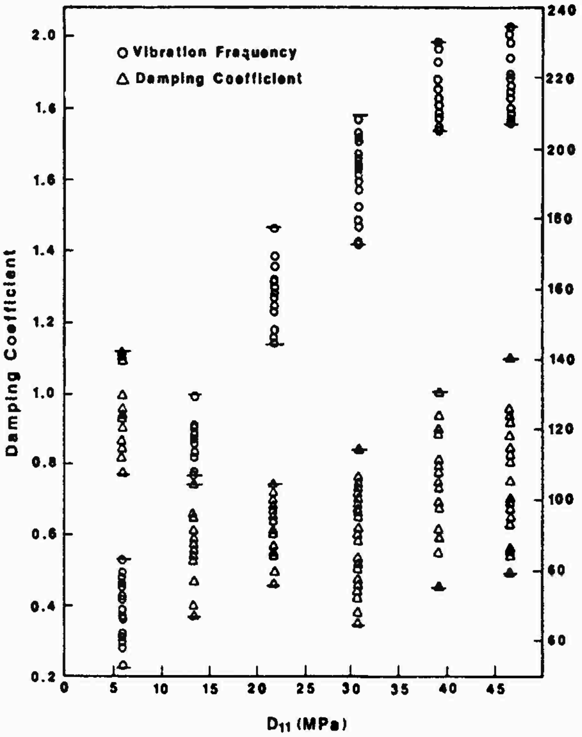

Fig. 3 Relation between vibration frequency and damping coefficient and D_{11}

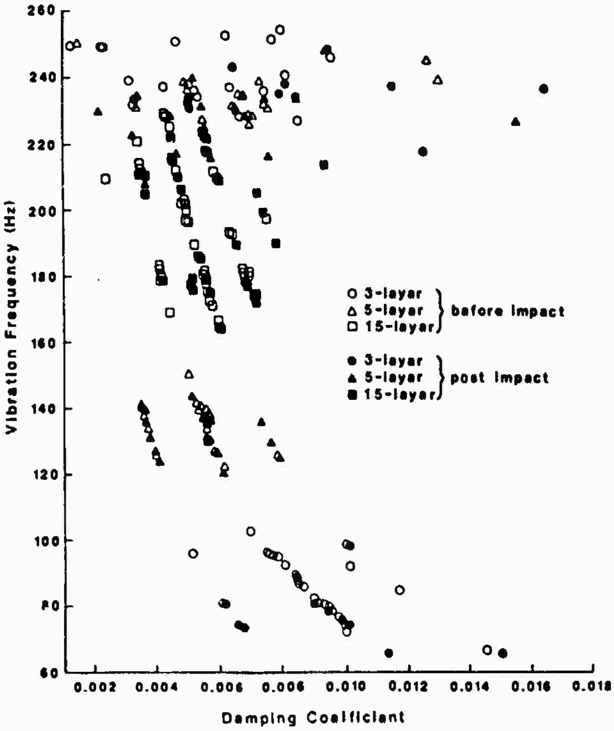

Fig. 4 Relation between vibration frequency and damping coefficient

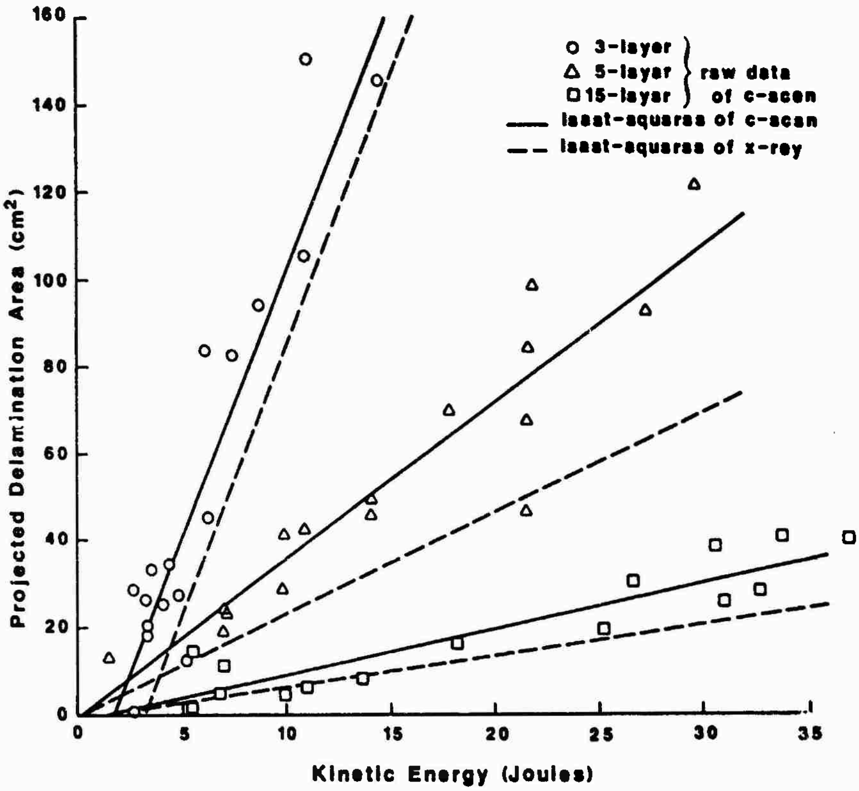

Fig. 5 Relation between projected delamination area and kinetic energy

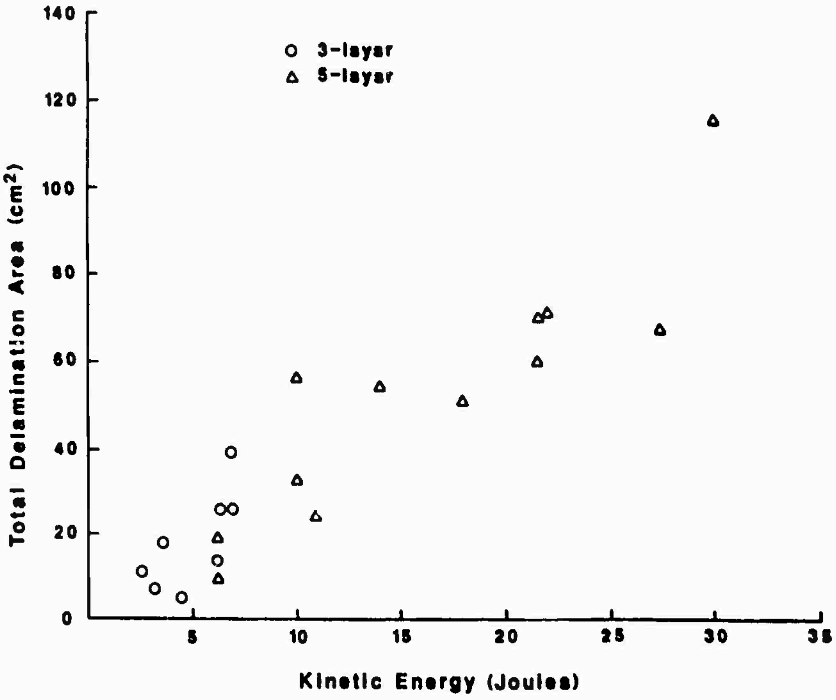

Fig. 6 Relation between total delamination area and kinetic energy

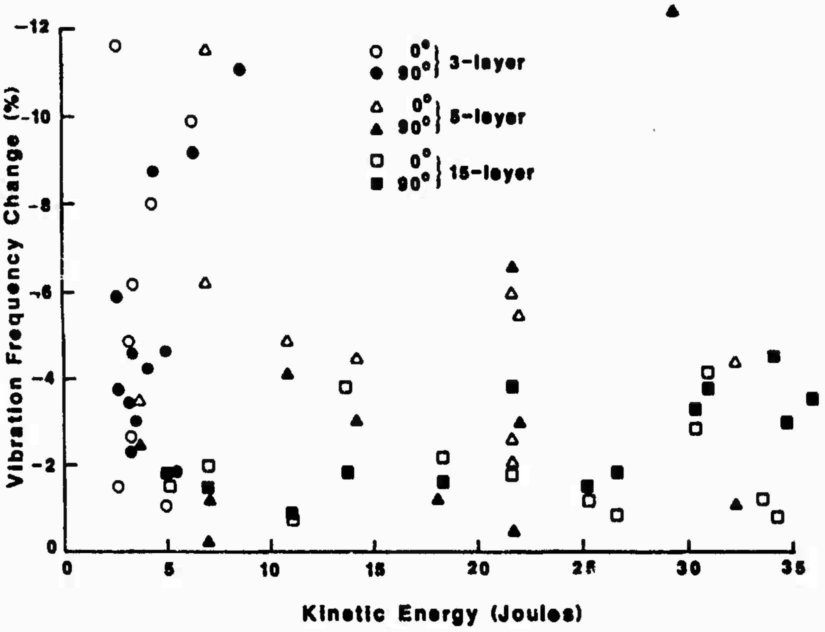

Fig. 7 Relation between vibration frequency change and kinetic energy

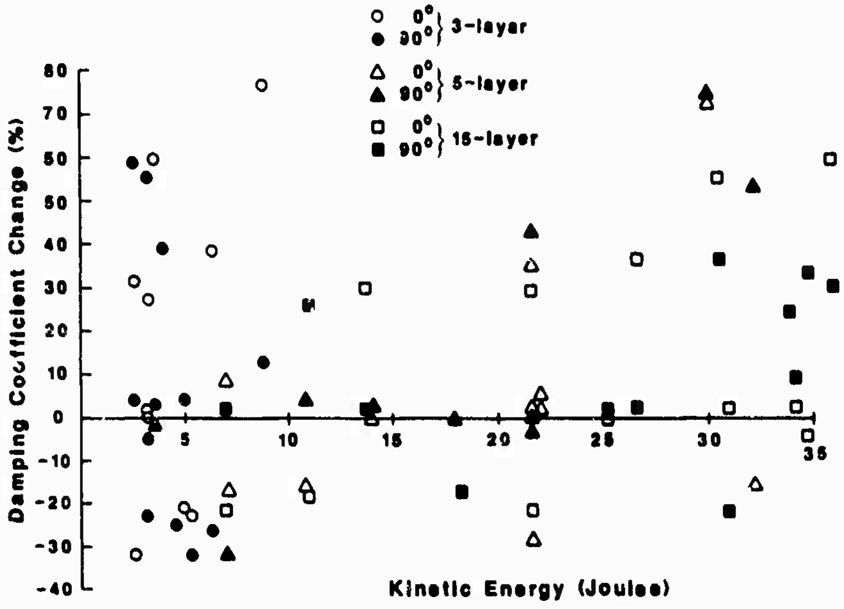

Fig. 8 Relation between damping coefficient change and kinetic energy

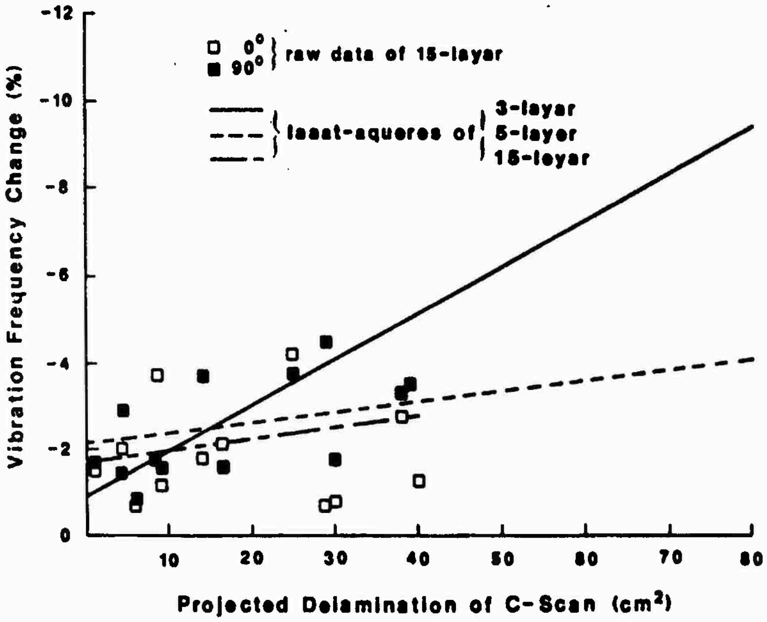

Fig. 9 Relation between vibration frequency and projected delamination area

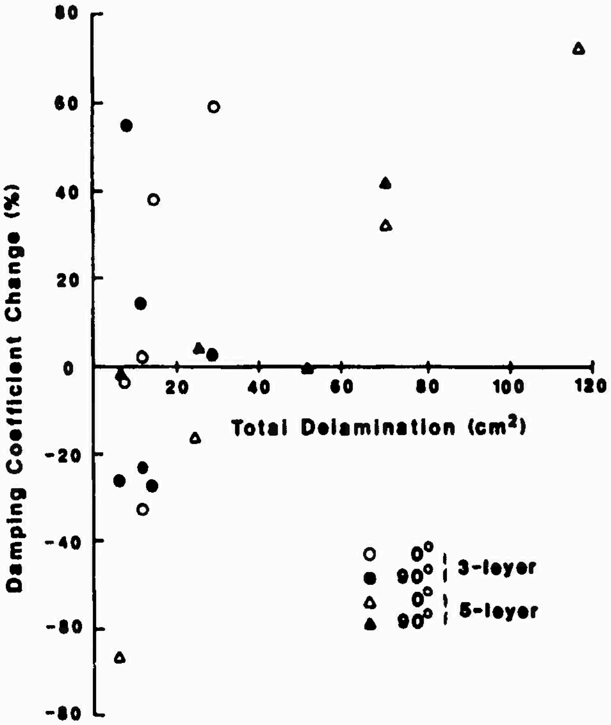

Fig. 10 Relation between damping coefficient change and total delamination area

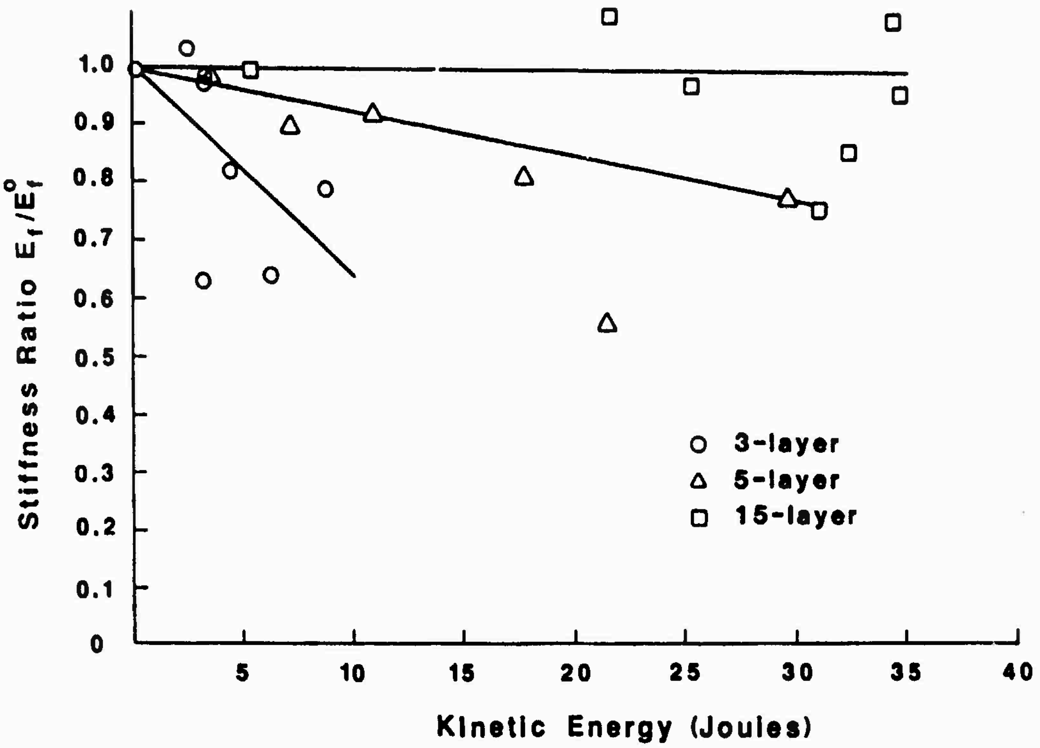

Fig. 11 Relation between stiffness ratio and kinetic energy

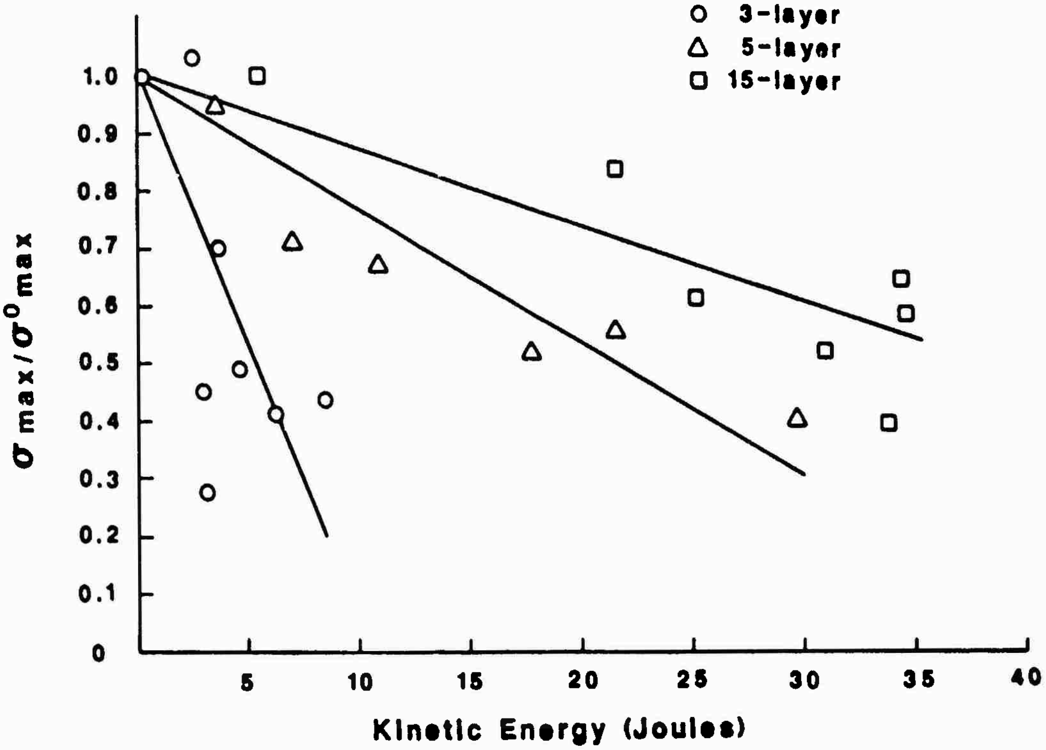

Fig. 12 Relation between strength ratio and kinetic energy

UPDATING RAIL IMPACT TEST METHODS

Robert A. McKinnon
U.S. Army Combat Systems Test Activity
Aberdeen Proving Ground, Maryland

Rail impact tests are conducted to verify that materiel will not be degraded by the shock and vibration environment associated with rail transport. Presently, there are several rail impact test procedures and each produces different test results. The objective of this study was to determine the most appropriate test method, instrumentation and data analysis techniques to be used for rail impact tests.

DEVELOPMENT OF A METHOD FOR CONDUCTING RAIL IMPACT TESTS

The primary objective of this study was to develop a realistic and repeatable method for conducting rail impact tests. This was due to the existence of several different methods plus the need for repeatable results.

Existing Rail Impact Testing Procedures

The existing rail impact test procedures were found to have been developed to test for three distinct objectives. These objectives are:

a. To be reasonably sure the test item will be operable after rail shipment.

b. To test the tiedown (restraint) system.

c. To insure the test item will remain on the railcar during rail shipment.

Table 1 gives a brief summary of the nine rail impact test procedures researched during this investigation. There is no way to be certain that these are the only existing procedures; however, any procedures not included in this table probably would only be slight variations of the procedures listed. Each of the test procedures listed have their own objectives. Some of the procedures were developed for certain items, while others are more general in nature. The number of impacts required varies from four to twelve. The largest variable is the number and weight of the buffer cars or hammer cars. None of the test procedures listed requires both a hammer car and buffer car, as does the procedure developed in this report.

Development of a New Rail Impact Test Procedure

This new procedure was developed by examining existing rail impact test procedures, analyzing their purposes, and reviewing actual railroad procedures. All of the variables were taken into account individually and collectively and were examined as follows:

a. Buffer car or hammer car.

The decision to use buffer cars and a hammer car is based on the real world rail impact environment. Actual rail impacting occurs during the process of making up trains. This process takes place in either a flat yard or a hump yard. A flat yard is one in which car movements are accomplished by a locomotive without material aid from gravity. A hump yard utilizes gravity to expedite switching of cars. The train of cars is pushed up an incline to a hump, at which point one or more cars are successively uncoupled while moving and allowed to roll down the incline from the hump into the classification yard. The hump must be of sufficient height to impart enough velocity to overcome the rolling resistance of each car and permit it to reach the farthest point in the yard. Thus, if the distance from the hump to the farthest point is 1000 m (3280 ft) and the rolling resistance of the slowest-rolling car under adverse weather conditions is 5 gm per kg (10 lb per ton), which equates to a 0.5% slope as shown in Figure 1, then a minimum hump height of 5 meters (16.4 ft) would be required. Another requirement is that the decline from the hump must be steep enough and long enough to separate the cars a sufficient distance to permit operation of switches and to clear the switches ahead of the following car.

Usually the hump height is from 5 to 6 meters (16 to 20 ft). Two or three sets of car retarders are provided for controlling the speeds of the cars onto the classification tracks. The retarders are set so that each car will roll the desired distance and couple to a standing car without what the railroads consider to be an overspeed impact, which is any speed greater than 6.4 km/hr (4 mph).

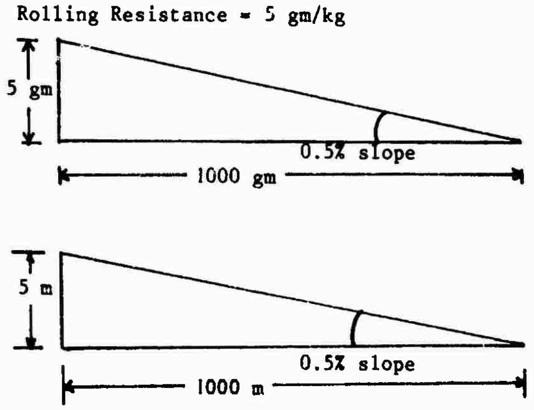

Figure 1. Hump yard diagram.

The use of a two-car buffer string is based on experimental evidence that, according to Appendix B, Reference 1, for all arrangements tested, any additional cars would have negligible effect on the forces transmitted to the test item. This was determined through studying the force-versus-time records (from the instrumented coupler and tiedowns) made during impact and reported in the reference.

The total weight of the two buffer cars was selected to be 1,112,000 N (250,000 lb). This weight is the load specified by the Association of American Railroads (AAR) and must be used in tests witnessed by the AAR to approve a tiedown procedure for a particular item before active rail shipment can occur. The weight on the buffer cars should be equally distributed between the two cars even though having the railcar weights differ should not affect the test results, providing each car and its load is configured as a single mass. However, since the question of equal-weight cars is often raised, equal distribution of the weight would avoid any concerns.

As mentioned above, the weights added to the buffer cars should be rigidly secured to each railcar. A factor that affects the repeatability of rail impact testing is an unsecured buffer car load. Under actual testing, an unsecured buffer load of several steel plates has been observed to slide on the railcar almost 1 meter, accompanied by a trail of smoke resulting from the heat of friction between the plates and wooden floor. This sliding was observed on high-speed films of rail impact tests. In analyzing this undesired test configuration, shown in Figure 2, these sliding plates are found to have a pronounced effect on the test results.

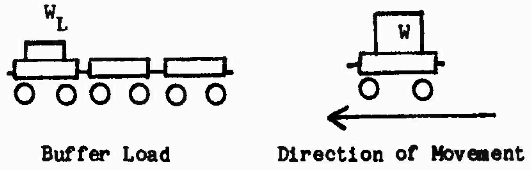

Figure 2. Test conditions.

Addressing the moving car first, the following parameters are assigned:

W_c = weight of car = 222,410 N (50,000 lb)

W_L = weight of load = 142,342 N (32,000 lb)

Speed at the instant of impact = 12.87 km/hr (8 mph) or 3.57 m/sec (12 ft/sec).

First, assuming there is no relative motion between the load and the car before, during, or after impact, the kinetic energy (KE) at the instant of impact is given as:

$$KE_o = 1/2 \times M_o V^2 = \frac{1/2 \times (W_c + W_L)}{g} \times V^2$$

$$= 1/2 \times \frac{(222{,}410\ N + 142{,}343\ N)}{9.81\ m/sec^2} \times (3.57\ m/sec)^2$$

$$= 2.370 \times 10^5 J\ (1.75 \times 10^5\ ft\text{-}lb)$$

If, however, at impact the load slides relative to the car, this results in a frictional force developing between the load and car (Figure 3).

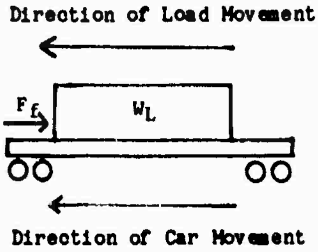

Figure 3. Frictional force.

The friction is calculated from the free body diagram of Figure 4 for the load.

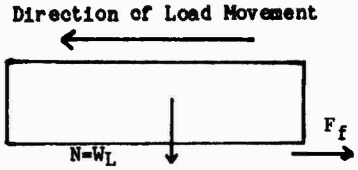

Figure 4. Free body diagram.

F_f = uN where u is the coefficient of sliding friction, which in this case is assumed to be 0.5 (cast iron on oak)

$F_f = 0.5\ W_L = 0.5 \times 142{,}342$ N

$F_f = 7.11 \times 10^4$ N (16,000 lb).

The work of friction of this plate sliding is equal to

$W_f = F_f \times$ distance traveled.

Assume the plate slides 0.6096 meters (2 ft) (which has been observed in actual impact tests):

$$W_f = 7.11 \times 10^4 \text{ N} \times 0.6096 \text{ m} = 4.33 \times 10^4 \text{ J (32,000 ft-lb)}$$

According to the conservation-of-energy theorem, the total energy present if the load slides has to equal the total energy present if it did not slide, or:

$$KE_0 = KE + W_f$$

where

KE_0 = actual kinetic energy of the system

KE = actual kinetic energy of the car

W_f = work (kinetic energy) of friction

$$KE = KE_0 - W_f$$
$$= 2.370 \times 10^5 \text{ J} - 4.33 \times 10^4 \text{ J}$$
$$= 1.94 \times 10^5 \text{ J } (1.43 \times 10^5 \text{ ft-lb})$$

This value of KE represents only 82% of KE_0; thus, at impact, the energy of the system under the sliding load condition is 18% less than if the load did not slide. This is an appreciable difference which will certainly cause disparity in data from similar tests.

This analysis can be extended to the buffer cars of Figure 2. With a total buffer weight of 118,843 kg (262,000 lb), the weight of the load on the third car shown is:

$$\begin{array}{l} 1{,}165{,}000 \text{ N} \\ \underline{-\ 667{,}000 \text{ N}} \text{ (3 cars at 222,400 N each)} \\ 498{,}000 \text{ N (112,000 lb)} \end{array}$$

Calculating the frictional force during sliding:

$$F_f = uN = 0.5 \text{ (498,000 N)} = 249{,}000 \text{ N (56,000 lb)}.$$

The corresponding work, based on this plate moving 76 mm (3 in.) at impact, is:

$$W_f = F_f \times d = 249{,}000 \text{ N} \times 0.076 \text{ m} = 18{,}920 \text{ J (14,000 ft-lb)}.$$

For convenience, it is assumed the compressed couplers do not absorb any of the energy of the impact. This certainly is not true, but the amount they do absorb should be close to being constant; thus, for this illustration, this will be assumed to be zero.

With no sliding of the load, $KE_0 = 2.37 \times 10^5$J (151,354 ft-lb) as calculated above.

With a sliding load:

$$KE = KE_0 - W_f = 1.94 \times 10^5 \text{ J} - 18{,}920 \text{ J}$$

$$KE = 1.75 \times 10^5 \text{ J } (1.29 \times 10^5 \text{ ft-lb})$$

This figure represents a 10% loss in the energy content of the impact due to friction. Combining these two numbers, a total of 28% of the total energy is expended in friction.

The above-described conditions therefore become a contributing factor in the large spread of data taken from rail hump tests conducted under the same conditions of impact speed and buffer load configuration. This condition of plate sliding will certainly not be the same each time. The plate can be restrained by a high board on the floor, or some other type of restriction, so that it will not slide on impact and not cause any difference in the energy of impact between tests.

The coupler shanks between the two buffer cars should be completely compressed. This will eliminate another friction-related problem (similar to the one discussed above) which will cause results to become nonrepeatable. The coupler shanks shall not be held in the compressed state by the railcars brakes.

The hammer car weight should be 734,000 N (165,000 lb), which is based on the requirements of MIL-S-55286 and MIL-S-52059B. The weight should be rigidly mounted on the car for the same reason discussed for the buffer cars. The hammer car, like the buffer cars, should be equipped with standard draft gear, which will provide the worst case environment. The hammer and buffer cars should be reinforced, especially in highly stressed areas, to insure that damage does not occur to these cars during testing, since damage to these cars will affect test repeatability.

b. Test speeds and number of impacts.

The rail impact test speeds selected were 9.6, 11.3 and 12.9 km/hr (6, 7, and 8 mph). These speeds are based on actual rail impact speeds measured in three independent studies. The studies cover a total of 16,216 impacts and are summarized in Table 2. The data for this table were found in Reference 1 of Appendix B.

TABLE 2. RAIL IMPACT SPEEDS

Speed Range km/hr	(mph)	Percent of Impacts
Below 9.7	(6)	65.9
9.7 to 11.3	(6 to 7)	18.1
11.3 to 12.9	(7 to 8)	8.1
12.9 to 14.5	(8 to 9)	4.2
14.5 to 16.1	(9 to 10)	2.4
>16.1	(>10)	1.3

This indicates that 92.1% of the rail impacts were below 12.9 km/hr (8 mph). For this reason (and others contained in the following discussion), the maximum speed of 12.9 km/hr was selected. Rail impact speeds greater than 12.9 km/hr may be used to evaluate the safety factor in either the tiedown design or the design of the test item.

As more rail hump yards are modernized and computerized, the rail impact speeds will probably decline. In a fully automated or so-called pushbutton hump yard, the operator pushes a button corresponding to the track onto which a car is to go. When the car is uncoupled, it rolls down the hump and is weighed, if desired, on an electronic, uncoupled-in-motion, track scale. Also, the car's rolling resistance is determined from the change in speed over a given length of track. This information is entered into the control computer.

The approximate wheel load is measured by a track device. This reading is also entered into the computer in order to limit the amount of retardation so that the wheels will not be forced out of the car retarder during the retardation process. The car speed is measured as it approaches each retarder, and this information also goes into the computer. When the operator initially pushes the button for the desired track, the computer is given the total rolling resistance to the farthest point on that track. The rolling resistance is based on the slope of the downgrade. A wheel trip on each track corrects this value for the distance taken up by the number of cars that have already been placed on that track. From all these data, the control computer determines the speed the car should have as it leaves the last retarder in order to roll to the desired point; and it then controls the retarder to slow the car to that speed.

Another reason for the 12.9-km/hr (8-mph) maximum speed is that the AAR-approved tiedowns are only designed for 12.9 km/hr. Therefore, at speeds greater than 12.9 km/hr there is a greater chance of a tiedown failure.

A comparison of the energy of the system was made with the two types of impacts: (1) test item into buffer cars; and (2) hammer car into test item and buffer cars. The amount of energy input to the system with a 734,000 N (165,000-lb) hammer car at a speed of 12.9 km/hr (8 mph) was calculated from:

$$KE = 1/2\ mv^2.$$

Since 12.9 km/hr = 3.57 m/sec, the resulting KE is:

$$KE = 1/2\ \frac{(734{,}000\ N)}{9.81\ m/sec^2} X\ (3.57\ m/sec)^2$$

$$KE = 477{,}000\ J\ (352{,}000\ ft\text{-}lb).$$

Using the same formula, the amount of energy input to the system with a 133,400 N (30,000-lb) test item secured to a 222,400 N (50,000-lb) railcar and impacting into two buffer cars at a speed of 12.9-km/hr is 230,500 J (170,050 ft-lb).

This shows that unless the mass of the test item plus the mass of the test railcar is greater than the total mass of the hammer car, the hammer car impact will be more severe. Therefore, in most cases the two impacts will be conducted in order of increasing severity; yet the primary reason for the 2-impact sequence is that it best simulates actual rail impacting.

The rail impact test should be conducted in both directions in order to eliminate the possibility that if the test item is more fragile in one direction than the other, this fragility will not go unnoticed. An example of this would be equipment mounted to a surface of (such as a shelter wall) facing one end of the railcar. During impacts in one direction, bolts and similar components will be in tension. These same components will be in compression in the opposite direction. By testing in both directions, deficiencies due to both tension and compression will be discovered.

The rail impact test speeds should be within ±5% of the nominal speed as compared to some procedures where either a minimum speed must be obtained or the impact must be repeated. The ±5% tolerance should reduce overspeed impacts and the total number of impacts performed: nominal speeds are specified so that the railroad crew can either exceed or fall short of the desired speeds by the allowable 5%; otherwise, by specifying only a minimum speed, only exact and overspeed impacts would be allowed. Any underspeed impacts would have to be repeated.

It is the author's experience that an experienced railroad crew can accomplish speeds within ±3%. An inexperienced railroad crew or ramp operator should practice attaining the correct impact speed on a different section of track without impacting any railcars.

The three sets of impacts in each direction will give the tester/ evaluator an adequate sample of data. The rail impact test procedure simulates the events in a total of six rail hump yards. Trains pass through rail switching yards each time the railcar is switched from one railroad to another, and six impacts are not considered unrealistic for a cross-country trip. (An exact number of impacts occurring in a cross-country trip cannot be stated since it is dependent on the routing of the shipment.)

The new procedure specifies that all buffer car air and handbrakes be set. Figure 5 shows the effect of the brakes set and not set on the impact coupler force. The slope of the curve with the brakes set is steeper than the curve with the brakes released, indicating that the coupler force increased faster as the speed increased with the brakes set. The brakes being set represents or approximates the worst real-world case in which the brakes are set on railcars and/or the railcars are up against a stop.

Variations in rail impact data can also be caused by different degrees of brake wear on the railcars. Variations in the brake wear on different cars will have an effect on the friction forces which restrain the buffer cars. In order to control the repeatability of the tests, periodic checks should be made of both brake systems (air and hand) for deterioration. If any deterioration is found, corrections should be made prior to further testing.

Data Required from Rail Impact Tests

Impact speed.

The rail impact speed should be recorded for each impact. The speed can be measured by any one of several techniques, such as electronic timers or radar. It is the author's experience that, of those two methods, the electronic timers are more accurate. The speed should be measured accurately to 0.15 km/hr (0.1 mph), as close to the point of impact as possible. An accurate speed measurement is required so that data from different impacts can yield valid comparisons.

Coupler force.

The coupler force should also be recorded for each impact. This gives the tester/evaluator a known input to the test railcar. With this value, along with information about the railcar (including its transfer function), the tester/evaluator can calculate the forces in the tiedowns which restrain the test item. From these forces, other information, such as stress on the test item, can be calculated.

The railcar loaded with the test item should be equipped at both ends with instrumented couplers capable of measuring coupler force. With impacts occurring successively at alternate ends of the railcar, having two instrumented couplers will greatly decrease total test time. The instrumented couplers are commercially available and consist of strain gages installed on the shank. A calibration is performed to develop a force-versus-strain curve. From this curve, coupler force can be obtained from strain data.

Initial tiedown loadings.

The amount of tension in the tiedowns should be specified in the tiedown design. Prior to rail impact testing, each tiedown should be tightened to that specified tension. The tiedown configuration used should be the AAR-approved procedure, if it exists, since this is the only configuration in which the item can be shipped.

In the event that the cable tension is not specified, the tension should be measured and recorded following tiedown so that the same conditions can be repeated in any additional rail impact tests which the item may encounter. In addition to cable tensions, the entire blocking and bracing design/configuration and procedure should be documented.

The AAR tiedowns are designed to restrain the test item at impact speeds up to and including 12.9 km/hr. In the event of a tiedown failure, a decision must be made as to whether the test should be continued without repairing the failure or repairing the failure and restarting the test.

Additional data.

In addition to the above-mentioned data, additional data such as acceleration may be recorded if more information about the test item is needed. The locations for these measurements should be selected after carefully considering why the data are needed and how the data will be used. In order to get a better description of what happens when the test item is rail impacted, shock-response spectrum analysis can be used. Shock-response spectrum analysis is defined as a plot of the peak responses of an infinite number of single-degree-of-freedom systems to an input transient. In the classical definition, the systems are undamped. Sometimes the systems are also termed "massless" to indicate that they do not load the input. In assuming no damping, the intent is to obtain a conservative estimate of the damage potential of the transient; it is, in fact, on the high side of reality because all systems have some degree of damping.

It is general practice when designing equipment to withstand a shock environment to assume that failure will occur in a particular component because the maximum allowable stress level is exceeded in that component. The shock-response spectrum provides the designer with some readily usable information about the input transient. It describes the effect of the transient rather than the transient itself. Some individuals feel this is wrong from the standpoint that several different configurations of transients can produce the same shock-response spectrum. While this is true, the designer needs to know the effect regardless of the input configuration. If the effect is known, it can be related directly to the system to determine if it will pass or fail.

The forces in the test item tiedowns can be measured by installing a load cell in each tiedown. These load cells are commercially available and can easily be installed in the tiedown system. During past rail impact tests, the author has used eyebolts with strain gages internally installed. Similar to the calibration technique used for the instrumented couplers, a strain-versus-load curve was developed. From this curve, the load can be extracted from the strain readings.

DISCUSSION OF DATA COLLECTION TECHNIQUES

Collection of Impact Speed Data

The rail impact speed can be measured by several methods. These methods include electronic timers or radar. Whichever method is used, the speed should be accurately measured to 0.15 km/hr.

Collection of Coupler Force Data

The coupler force can be measured by strain gaging a coupler shank and calibrating the coupler by developing a strain-versus-force curve. In order to expedite testing, the test item car should be equipped with an instrumented coupler at both ends. A 1-channel on-site recorder should be acquired or developed to record this coupler force data.

Collection of Additional Data

Accelerometer data should be recorded on magnetic tape so that a permanent record can be maintained. The data can be transferred from the railcar to its permanent storage medium using any of a variety of techniques. These techniques include a direct cable link, FM-FM Telemetry or pulse code modulation (PCM) telemetry. When using these techniques, the data should be low-pass filtered above the highest frequency of interest. Rail impact testing generally excites frequencies in the 0 to 100 Hz range. If test item components are sensitive to higher frequencies, the filtering levels should be increased to include these frequencies.

Additionally, if a digital data acquisition system is used the data should be sampled at a rate of at least four times the filtered frequency to eliminate aliasing of the data.

Generally, aliasing occurs from the presence of signals which are only slightly above the Nyquist frequency (1/2 the sampling frequency).

If the data are to be used in Fourier transform applications (power spectral density (PSD) analysis; shock-response spectrum analysis), the resolution characteristics of the Fast Fourier transform (FFT) must be considered. The frequency resolution of the FFT is:

$$F = fs/2N$$

where

fs = sampling rate is samples/sec
N = FFT size.

This relationship indicates that the resolution degrades with increasing sampling rate. For these types of applications, a sampling rate on the order of 3.5 to 4 is appropriate. Larger transform sizes on the other hand, will enhance resolution.

SUMMARY

The resulting rail impact test procedure, while not exactly like any of the researched test procedures, is essentially a compromise between all of the different techniques. The reason for this approach is that the proposed procedure tries to duplicate actual railyard impacting. The facilities and equipment necessary for conducting the test includes:

a. A straight level section of track (minimum of 60 meters).

b. A device for setting the railcars in motion: either an inclined ramp or a locomotive.

c. Two 56,700-kg (125,000-lb) rigidly loaded, standard draft gear buffer cars.

d. One 74,800-kg (165,000-lb) rigidly loaded, standard draft gear hammer car.

e. One standard draft gear railcar on which the test item is securely fastened.

f. A speed measuring device.

g. Two railcar couplers instrumented to measure coupler force.

The rail impact test procedure is as follows. The first impact consists of impacting the railcar on which the test item is securely loaded into the two stationary buffer cars (with the air and handbrakes set and the coupler shanks compressed) at a speed of 9.6 km/hr (6 mph) ±5%. At the conclusion of this first impact, the three cars are repositioned; the coupler shanks connecting all three cars are compressed; and the air and handbrakes on all three cars are set. The second impact consists of the hammer car impacting the test item car (which is coupled to the two buffer cars) at a speed of 9.6 km/hr (6 mph) ±5%. This two-impact procedure is then repeated at 11.3 km/hr (7 mph) ±5% and at 12.9 km/hr (8 mph) ±5%. At the conclusion of the sixth impact the test car is turned around and the six-impact sequence is repeated. Rail impact test speeds greater than 12.9 km/hr may be used to evaluate the safety factor in either the tiedown design or the design of the test item.

During each of the impacts, the impact speed and coupler force should be recorded. To reduce test time, each end of the test item car should be equipped with an instrumented coupler designed to measure the coupler force. The tiedown system should not be adjusted (cables tightened or loosened) once the test begins. In the event of a tiedown failure, a decision should be made by the project director as to whether the test should be continued without repairing the failure, or repairing the failure and restarting the test. Prior to testing, the tension in the tiedown system should be measured and set to the tension specified in the tiedown procedure.

Speed and coupler force data are required on all tests as previously discussed. Any additional data requirements should be carefully thought-out ahead of time, and only the necessary data should be collected. This will reduce the test setup, data analysis and report time frames.

TABLE 1. EXISTING RAIL IMPACT TEST METHODS

TEST METHODS	SPEEDS*(mph)	BRAKES	BUFFER OF HAMMER CARS	DIRECTION OF IMPACTS
MIL-STD-705B	8, 8, 9, 9, 10, 10	Set	Gondola & Boxcar w/lading 2 to 3 times wt of item and railcar. (Buffer car)	Test item into two Buffer cars.
MIL-S-55286(EL)	9, 9, 9R*, 9r	Off	One 165,000 lb Hammer Car	Hammer car into test item car and two empty cars.
MIL-G-52282(MO)	10, 10, 10R, 10R, 10(1/4)*, 10(1/4), 10(3/4)*, 10(3/4)	Set	Gondola & Boxcar w/lading 2 to 3 times wt of item and railcar. (Buffer cars)	Test item into two Buffer cars.
MIL-S-52059(EL)	9, 9, 9, 9, (Direction determined by Govt)	Off	One 165,000 lb Hammer car.	Hammer car into test item car and two empty cars.
MIL-STD-810C	8, 8, 9, 9, 10, 10, 8R, 8R, 9R, 9R, 10R, 10R or 8, 9, 10, 8R, 9R, 10R, 8(1/4), 9(1/4), 10(1/4), 8(3/4), 9(3/4), 10(3/4)	Set	Two Buffer cars with a minimum additional weight of 140,000 lbs.	Test item into two Buffer cars.
MIL-STD-810D	8, 8, 9, 9, 10, 10, 8R, 8R, 9R 9R, 10R, 10R or 8, 9, 10, 8R, 9R, 10R, 8(1/4), 9(1/4), 10(1/4), 8(3/4), 9(3/4), 10(3/4)	Set	One Buffer car, minimum total weight of 220,000 lb.	Test item into one Buffer car.
AR 55-355	4, 6, 8, 8R	Set	Two to five Buffer cars, total weight of 169,000 lb.	Test items into two to five Buffer cars.
TR 55-100	8, 8, 8, 8R, 8R, 8R or 10, 10, 10, 10R, 10R, 10R (speed depends on priority, value and item sensitivity)	Off	Buffer car is test item car or other car with a minimum weight of 169,000 lb., whichever is lighter.	Depends on weight of test item car.
TM 55-2200-001-12 AAR	4, 6, 8, 8R	Set	Five Buffer cars, total weight of 250,000 lb.	Test item into five Buffer cars.

* R - Indicates an impact in the Reverse Direction
1/4 - Indicates remounting the test item on the railcar and impacting at 90° from its original position.
3/4 - Indicates remounting the test item on the railcar and impacting at 270° from its original position.

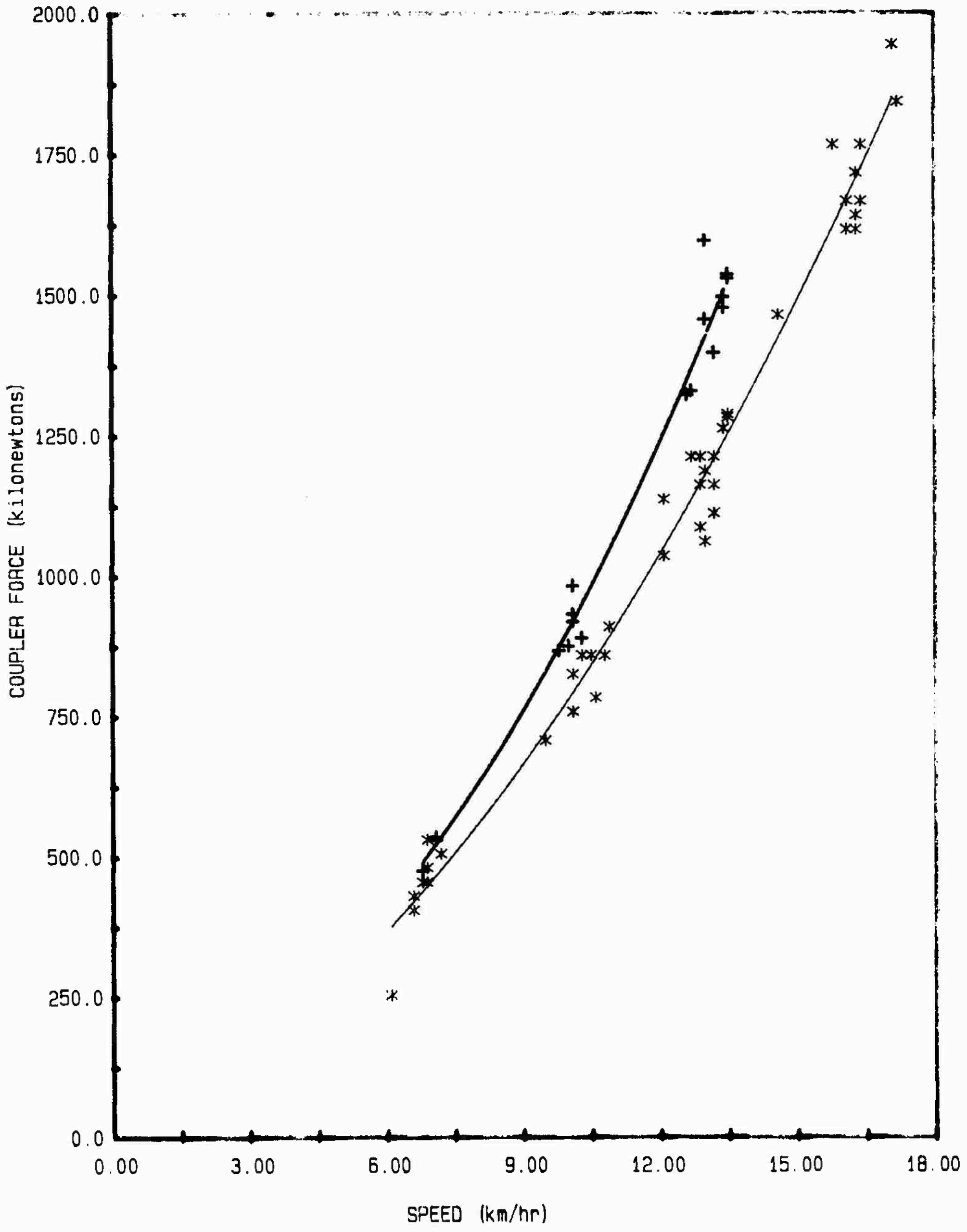

FIGURE 5. COUPLER FORCE vs. IMPACT SPEED
* BRAKES RELEASED
+ BRAKES APPLIED

APPENDIX A - ABBREVIATIONS

AAR = Association of American Railroads
FFT = Fast Fourier Transform
ft-lb = foot-pounds
F_f = friction force
g = acceleration due to gravity (9.8 m/sec^2)
gm = grams
J = joules
KE = kinetic energy
N = Newton
lb_m = pounds-mass
PSD = power spectral density
PCM = pulse code modulation

APPENDIX B - REFERENCES

1. Guins, S.G. and Tack, C.E., Anthology of Rail Vehicle Dynamics, Freight Car Impact, Volume I, New York, The American Society of Mechanical Engineers, 1971.

2. Merritt, Frederick S., Standard Handbook for Civil Engineers, New York, McGraw-Hill, 1976.

3. Military Standard 810C, Environmental Test Methods, 10 March 1975.

4. Military Standard 705A, Generator Sets, Engine Driven, Methods of Tests and Instruction, 5 March 1963.

5. Military Standard 705B, Generator Sets, Engine Driven, Methods of Tests and Instructions, 26 June 1972.

6. Military Specification MIL-S-55286 (EL), Shelter, Electrical Equipment S-280 ( )/G, 10 September 1964.

7. Military Specification MIL-G-52282 (MO), Generator.

8. Military Specification MIL-S-52059 B (EL), Shelter, Electrical Equipment S-250 ( )/G.

9. Department of the Army Technical Bulletin, TB 55-100, Transportability Criteria Shock and Vibration, Washington, DC, 17 April 1964.

10. Military Standard 810D, Environmental Test Methods, 19 July 1983.

MACHINERY DYNAMICS

PREDICTION OF NATURAL FREQUENCIES OF FLEXIBLE SHAFT-DISC SYSTEM

P. Brémand, G. Ferraris, M. Lalanne
I.N.S.A.
Laboratoire de Mécanique des Structures
U.A. C.N.R.S. 862
20, avenue Albert Einstein
69621 Villeurbanne - France

Today the dynamic behavior of rotors must be predicted with the greatest care. This work deals with the influence of disc flexibility on the natural frequencies of rotors.
The rotors considered here are made of a shaft, symmetric bearings and flexible disc. The kinetic and strain energies of the element are calculated, the finite element method is used and the Lagrange's equations applied.
The solution of the equations is performed through a modal method. The application is an industrial gas turbine. Its natural frequencies as a function of the speed of rotation are obtained, which gives critical speeds.

INTRODUCTION

In industrial applications related to rotordynamics discs are taken as rigid. When they are thin this hypothesis can introduce an error as the interaction disc-shaft can then be misrepresented.

It is thus interresting when calculating the behavior of rotors to be able to consider the disc as flexible or at least to have an idea of the influence of its flexibility.

Dopkin and Shoup |1| have presented results on a symmetric rotor in steady state motion using transfer matrices. Hagiwara et al |2| have also used the transfer matrix method and have dealt with the unbalance response of an impeller-shaft system. In those two papers the effect due to the initial stresses has not been introduced.

Chivens and Nelson |3| have performed a parametric study of the dynamic behavior of a simply supported rotor. Their equations include the centrifugal effect and are solved by the Laplace method. They have shown that the influence of the flexibility is more significant on the backward whirl than on the forward whirl.

Wilgen and Schalck |4|, using a Rayleigh-Ritz technique have also made a parametric study of the critical speeds and instabilities.

Klompas |5| has calculated the behavior of a rotor on disymmetric bearings. He has shown that excitation forces created in the disc give new critical speeds and instabilities. He has extended his work to multirotors with linear |6| or nonlinear |7| hydrodynamic bearings.

Sakata et al |8| have calculated, using a Runge - Kutta - Gill method, the transient vibrations of a rotor subjected to a sudden unbalance.

Palladino and Rossetos |9| have used the finite element method, built a specific beam element taking into account analytical solutions of the disc and studied several examples.

Loewy and Khader |10| used also finite elements for the rotor containing disc-blades assemblies which are modelled through a substructuring method. The displacements of the shaft and the lowest modes are the generalized coordinates used for Lagrange's equations. The application to an industrial example shows the influence of the gyroscopic (Coriolis) and flexibility effects of the disc.

In what follows a method of analysis of rotors having a flexible disc is presented. The shaft is modelled as a beam including, torsional and longitudinal motions. The disc is an axisymmetric thin plane structure having rigid body and axisymmetric motions. Strains include second order terms to take into account the stiffening due to the initial stresses. The finite element method is used for obtaining the expression of the strain and kinetic energies of the element, the Lagrange's equation (appendix 1), are then applied. The bearings are symmetric and have stiffness and viscous damping characteristics. The order of the systems to be solved is greatly reduced through a modal method. The results show the coupling between the bending of the shaft and the axisymmetric motion with one nodal diameter (n = 1) of the disc. They show also two couplings, which to our knowledge have not yet been shown, one between the longitudinal motion of the shaft and the bending of the disc (n = 0) and another one between the torsional motions of the shaft and of the disc (n = 0). The industrial gas turbine presented has already been studied with the disc considered rigid |11|.

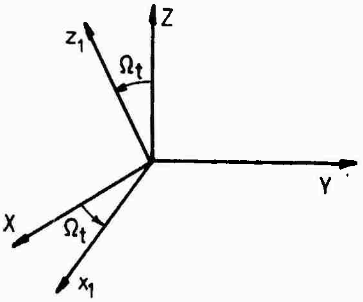

Fig.1 : Reference frames

Kinetic energy

The expression for shaft elements of length L is given by the addition of three terms :

$$2T_{S1} = \int_0^L \rho(S(u^{\circ 2} + v^{\circ 2} + w^{\circ 2}) + I_x\,\theta^{\circ 2} + I_z\,\psi^{\circ 2} + I_y\,\beta^{\circ 2})dy, \qquad (1)$$

mass kinetic energy.

$$T_{S2} = \Omega \int_0^L \rho S(u^\circ w - w^\circ u)dy \quad , \qquad (2)$$

gyroscopic (Coriolis) kinetic energy.

$$2T_{S2} = \Omega^2 \int_0^L \rho(S(u^2 + w^2) - I_x\,\theta^2 - I_z\,\psi^2)dy \quad , \qquad (3)$$

supplementary kinetic energy.
With u, v, w components in R1 of the neutral axis displacements.
ρ, mass per unit volume.
S, cross-sectional area.
I_x,I_z, diametral area moments of inertia of the shaft cross section.
I_y, polar moment of inertia of the shaft cross section.

The kinetic energy of the disc (fig.3) is given by the addition of three groups of terms. The first group corresponds to the rigid body motion.

EQUATIONS OF THE SYSTEM

The development of the equations is detailed in |12|.

The axes X Y Z (Ro) are an inertial frame while the axes x_1 Y z_1 are fixed to the rotor in undeformed position and rotate at constant angular velocity (Ω). The axes x y z (R2) are fixed to the cross section of the deformed rotor (fig.1). The R2 system is related to the R1 system through a set of three angles β, ψ, θ (fig.2). All the equations are written in R1.

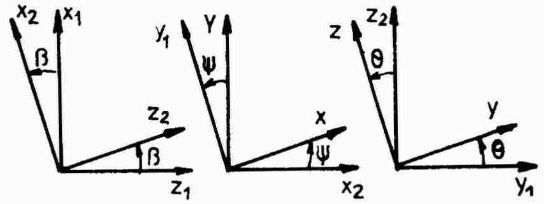

Fig.2 : Angles of rotation

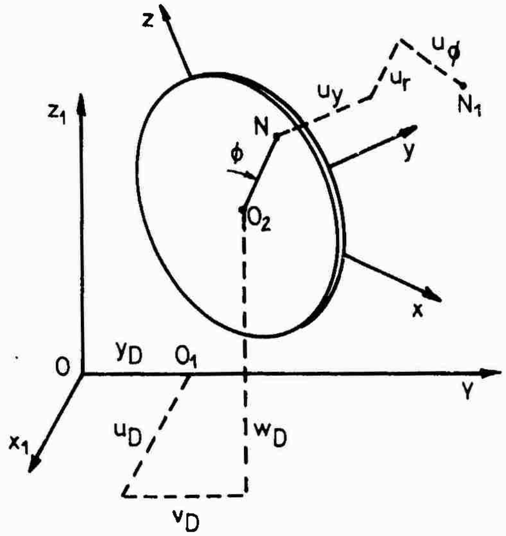

Fig.3 : Disc coordinates

$$2T_{DR1} = m_D({u^\circ_D}^2 + {v^\circ_D}^2 + {w^\circ_D}^2) + I_{DX}\,{\theta^\circ_D}^2 + I_{DZ}\,{\psi^\circ_D}^2 + I_{DY}\,{\beta^\circ_D}^2 \quad , \qquad (4)$$

mass kinetic energy.

$$T_{DR2} = \Omega(m_D(u^\circ_D w_D - w^\circ_D u_D) + I_{DX}\,\theta^\circ_D\,\psi_D + (I_{DY} - I_{DZ})\,\psi^\circ_D\,\theta_D) \quad , \qquad (5)$$

Coriolis kinetic energy.

$$2T_{DR3} = \Omega^2(m_D(u_D^2 + w_D^2) + I_{DX}\,\psi_D^2 + I_{DZ}\,\theta_D^2 - I_{DY}\,(\psi_D^2 + \theta_D^2)) \quad , \qquad (6)$$

supplementary kinetic energy.

with :

m_D, mass of the disc
I_{DX}, I_{DY}, I_{DZ}, mass moment of inertia of the disc with respect to X Y Z.

The second group of terms corresponds to the axisymmetric motion :

$$2T_{DA1} = \int_{(V)} \rho({u^{\circ}_r}^2 + {u^{\circ}_\phi}^2 + {u^{\circ}_y}^2)\, dV \quad , \qquad (7)$$

mass kinetic energy.

$$T_{DA2} = \Omega \int_{(V)} \rho(u^{\circ}_\phi u_r - u^{\circ}_r u_\phi)\, dV \quad , \qquad (8)$$

Coriolis kinetic energy.

$$2T_{DA3} = \Omega^2 \int_{(V)} \rho({u_r}^2 + {u_\phi}^2)\, dV \quad , \qquad (9)$$

supplementary kinetic energy.

$$T_{DA4} = \Omega^2 \int_{(V)} \rho\, r\, u_r\, dV \quad , \qquad (10)$$

centrifugal forces kinetic energy.

The third group comes from the coupling between rigid body and axisymmetric motions.

$$\begin{aligned} T_{DC1} = \int_{(V)} & \rho(u^{\circ}_D(u^{\circ}_r \sin\phi + u^{\circ}_\phi \cos\phi) \\ & + w^{\circ}_D(u^{\circ}_r \cos\phi - u^{\circ}_\phi \sin\phi) + v^{\circ}_D u^{\circ}_y \\ & + r\, u^{\circ}_y(\psi^{\circ}_D \sin\phi - \theta^{\circ}_D \cos\phi) \\ & + r\, \beta^{\circ}_D u^{\circ}_\phi)\, dV \quad , \end{aligned} \qquad (11)$$

mass kinetic energy.

$$\begin{aligned} T_{DC2} = \Omega \int_{(V)} & \rho(u^{\circ}_D(u_r \cos\phi - u_\phi \sin\phi) \\ & - w^{\circ}_D(u_r \sin\phi + u_\phi \cos\phi) \\ & - u_D(u^{\circ}_r \cos\phi - u^{\circ}_\phi \sin\phi) \\ & + w_D(u^{\circ}_r \sin\phi + u^{\circ}_\phi \cos\phi) + 2r\, \beta^{\circ}_D u_r)dV \quad , \end{aligned} \qquad (12)$$

Coriolis kinetic energy.

$$\begin{aligned} T_{DC3} = \Omega^2 \int_{(V)} & \rho(u_D(u_r \sin\phi + u_\phi \cos\phi) \\ & + w_D(u_r \cos\phi - u_\phi \sin\phi) \\ & + r\, u_y(\theta_D \cos\phi - \psi_D \sin\phi))\, dV \quad , \end{aligned} \qquad (13)$$

supplementary kinetic energy.

The axisymmetric displacements are then expressed by developments in Fourier's series and written as :

$$\begin{aligned} u_r &= u_{ro} + \sum_{n=1}^{\infty} (u_{rn} \cos n\phi + \overline{u_{rn}} \sin n\phi) \\ u_\phi &= u_{\phi o} + \sum_{n=1}^{\infty} (u_{\phi n} \cos n\phi + \overline{u_{\phi n}} \sin n\phi) \\ u_y &= u_{yo} + \sum_{n=1}^{\infty} (u_{yn} \cos n\phi + \overline{u_{yn}} \sin n\phi) \end{aligned} \qquad (14)$$

It is also convenient to define :

$$|\delta_D|^t = |{q_s}^t\ {q_o}^t\ {q_1}^t\ {\overline{q}_1}^t \ldots {q_n}^t\ {\overline{q}_n}^t|$$

where

$$|q_s|^t = |u_D\ v_D\ w_D\ \theta_D\ \psi_D\ \beta_D| \qquad (15)$$

$$|q_n|^t = |u_{rn}\ u_{\phi n}\ u_{yn}| \quad \text{if} \quad n \geqslant 0$$

$$|\overline{q}_n|^t = |\overline{u_{rn}}\ \overline{u_{\phi n}}\ \overline{u_{yn}}| \quad \text{if} \quad n > 1$$

The expressions (14), (15) can be used in the several terms of the disc kinetic energy (4), (13). An integration for the polar coordinate ϕ in the interval $0, 2\pi$ give, when Lagrange's equations are applied, the mass, Coriolis, supplementary stiffness matrices and the vector of centrifugal forces. In appendix 2 the mass matrix M_D of the disc is presented. The Coriolis and supplementary stiffness matrices, not presented here, lead to important conclusions, which are the same as those shown by the M_D matrix. A coupling appears between the rigid body motion degrees of freedom and the Fourier coefficient terms when n = 0. This shows a coupling between the longitudinal motion of the shaft v_D and the bending u_{yo} of the disc and another coupling between the torsion of the shaft β_D and the disc $u_{\phi o}$.

A coupling appears between the rigid body motion degrees of freedom and the Fourier coefficient terms when n = 1. This shows a coupling between the shaft bending u_D, w_D, θ_D, ψ_D and the disc displacement u_{r1}, $\overline{u_{r1}}$, $u_{\phi 1}$, $\overline{u_{\phi 1}}$, u_{y1}, $\overline{u_{y1}}$.

There is no coupling between the shaft and the disc for n > 1.

The centrifugal force vector only has components for n = 0.

Strain energy

The strain energy of the shaft includes two terms. The first one is the classical strain energy, the second one is the strain energy due to a constant axial force F.

Their expressions are :

$$\begin{aligned} 2U_{S1} = \int_0^L ES \left(\frac{\partial v}{\partial y}\right)^2 dy &+ \int_0^L E\left(I_z \left(\frac{\partial^2 u}{\partial y^2}\right)^2\right. \\ &\left. + I_x \left(\frac{\partial^2 w}{\partial y^2}\right)^2\right) dy + \int_0^L GJ \left(\frac{\partial \beta}{\partial y}\right)^2 dy \end{aligned} \qquad (16)$$

with :

G, shear modulus

E, Young's modulus

J, area moment of inertia about the longitudinal axis.

$$2U_{S2} = \int_0^L F\left(\left(\frac{\partial w}{\partial y}\right)^2 + \left(\frac{\partial u}{\partial y}\right)^2\right) dy \qquad (17)$$

The strain energy of the disc is caused by the axisymmetric motion and includes two terms. The first one is the classical strain energy, the second one is the strain energy due to the initial stresses σ_{orr}, $\sigma_{o\phi\phi}$, $\sigma_{or\phi}$. Their expressions are |13| :

$$\begin{aligned}
2U_{D1} = \int_{(V)} \frac{E}{1-\nu^2} \{ & \left(\frac{\partial u_r}{\partial r}\right)^2 + \frac{1}{r^2} u_r^2 + \frac{1}{r^2}\left(\frac{\partial u_\phi}{\partial \phi}\right)^2 \\
& + \frac{2}{r^2} u_r \frac{\partial u_\phi}{\partial \phi} + 2\frac{\nu}{r}\frac{\partial u_r}{\partial r}\frac{\partial u_\phi}{\partial \phi} + 2\frac{\nu}{r} u_r \frac{\partial u_r}{\partial r} \\
& + \frac{1-\nu}{2}\left(\frac{\partial u_\phi}{\partial r}\right)^2 + \frac{1-\nu}{2r^2} u_\phi^2 + \frac{1-\nu}{2r^2}\left(\frac{\partial u_r}{\partial \phi}\right)^2 \\
& - \frac{1-\nu}{r} u_\phi \frac{\partial u_\phi}{\partial r} + \frac{1-\nu}{r}\frac{\partial u_\phi}{\partial r}\frac{\partial u_r}{\partial \phi} - \frac{1-\nu}{r^2} u_\phi \frac{\partial u_r}{\partial \phi} \\
& + y^2\left(\left(\frac{\partial^2 u_y}{\partial r^2}\right)^2 + \frac{1}{r^4}\left(\frac{\partial^2 u_y}{\partial \phi 2}\right)^2 + \frac{1}{r^2}\left(\frac{\partial u_y}{\partial r}\right)^2\right. \qquad (18) \\
& + \frac{2}{r^3}\frac{\partial u_y}{\partial r}\frac{\partial^2 u_y}{\partial \phi 2} + 2\nu \frac{\partial^2 u_y}{\partial r^2}\left(\frac{1}{r^2}\frac{\partial^2 u_y}{\partial \phi^2} + \frac{1}{r}\frac{\partial u_y}{\partial r}\right) \\
& + 2\frac{1-\nu}{r^2}\left(\frac{\partial^2 u_y}{\partial r \partial \phi}\right)^2 + 2\frac{1-\nu}{r^4}\left(\frac{\partial u_y}{\partial \phi}\right)^2 \\
& \left. - 4\frac{1-\nu}{r^3}\frac{\partial u_y}{\partial \phi}\frac{\partial^2 u_y}{\partial r \partial \phi}\right)\} \; dV \quad ,
\end{aligned}$$

with ν, Poisson's ratio.

$$\begin{aligned}
2U_{D2} = \int_{(V)} & \left(\frac{1}{4}(\sigma_{orr} + \sigma_{o\phi\phi})\left(\frac{1}{r}\frac{\partial u_r}{\partial \phi} - \frac{\partial u_\phi}{\partial r} - \frac{u_\phi}{r}\right)^2\right. \\
& + \sigma_{orr}\left(\frac{\partial u_y}{\partial r}\right)^2 + \frac{1}{r^2}\sigma_{o\phi\phi}\left(\frac{\partial u_y}{\partial \phi}\right)^2 \qquad (19) \\
& \left. + \frac{2}{r}\sigma_{or\phi}\frac{\partial u_y}{\partial \phi}\frac{\partial u_y}{\partial r}\right) dV \quad ,
\end{aligned}$$

The relationship between initial stresses (σ_{orr}, $\sigma_{o\phi\phi}$, $\sigma_{or\phi}$) and displacement is :

$$\begin{vmatrix} \sigma_{orr} \\ \sigma_{o\phi\phi} \\ \sigma_{or\phi} \end{vmatrix} = \frac{E}{1-\nu^2} \begin{vmatrix} \partial u_r/\partial r + \nu(\partial u_\phi/\partial \phi + u_r)/r \\ (\partial u_\phi/\partial \phi + u_r)/r + \nu \partial u_r/\partial r \\ (1-\nu)(r\partial u_\phi/\partial r - u_\phi + \partial u_r/\partial \phi)/2/r \end{vmatrix} \qquad (20)$$

It is convenient to define :

$$\begin{aligned}
|\delta_D^*|^t = |& u_{ro}\; u_{\phi o}\; u_{yo}\; \frac{\partial u_{ro}}{\partial r}\; \frac{\partial u_{\phi o}}{\partial r}\; \frac{\partial u_{yo}}{\partial r}\; \frac{\partial^2 u_{yo}}{\partial r^2} \;\vdots \\
& u_{r1}\; u_{\phi 1}\; u_{y1}\; \frac{\partial u_{r1}}{\partial r}\; \frac{\partial u_{\phi 1}}{\partial r}\; \frac{\partial u_{y1}}{\partial r}\; \frac{\partial^2 u_{y1}}{\partial r^2}\; \overline{u}_{r1}\; \overline{u}_{\phi 1}\; \overline{u}_{y1}\; \overline{\frac{\partial u_{r1}}{\partial r}}\; \overline{\frac{\partial u_{\phi 1}}{\partial r}}\; \overline{\frac{\partial u_{y1}}{\partial r}} \\
& \overline{\frac{\partial^2 u_{y1}}{\partial r^2}} \;\vdots \cdots \vdots\; u_{rn}\; u_{\phi n}\; u_{yn}\; \frac{\partial u_{rn}}{\partial r}\; \frac{\partial u_{\phi n}}{\partial r}\; \frac{\partial u_{yn}}{\partial r}\; \frac{\partial^2 u_{yn}}{\partial r^2} \\
& \overline{u}_{rn}\; \overline{u}_{\phi n}\; \overline{u}_{yn}\; \frac{\partial u_{rn}}{\partial r}\; \frac{\partial u_{\phi n}}{\partial r}\; \frac{\partial u_{yn}}{\partial r}\; \frac{\partial^2 u_{yn}}{\partial r^2} \;\vdots \cdots | \qquad (21)
\end{aligned}$$

and using (14), (15) with equations (18), (19), (20) the new expressions of strain energies are obtained and show no coupling between Fourier's series 0, 1, 2, ...

Finite element

The shaft element is a beam element with two nodes, with six degrees of freedom by node. Classical shape function have been used, cubic in y for bendings linear in y for both longitudinal and torsional motions, (fig.4). In addition :

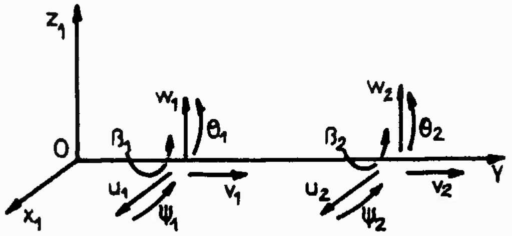

Fig.4 : Beam finite element

$$\theta = \frac{\partial w}{\partial y} \qquad \psi = -\frac{\partial u}{\partial y} \qquad (22)$$

The thin disc element has two nodes with also six degrees of freedom by node. Classical shape functions are used, cubic in r for u_{yn}, $\overline{u}_{yn}$ linear in r for u_{rn}, $\overline{u}_{rn}$, $u_{\phi n}$, $\overline{u}_{\phi n}$.

In a compact form the degrees of freedom are :

$$|\delta_e|^t = |q_s{}^t\; d_o{}^t\; d_1{}^t\; \overline{d_1}{}^t \cdots d_n{}^t\; \overline{d_n}{}^t \cdots|$$

with :

$$|q_s|^t = |u_D\; v_D\; w_D\; \theta_D\; \psi_D\; \beta_D| \qquad (23)$$

$$|d_n|^t = |u^n_{r1}\; u^n_{\phi 1}\; u^n_{y1}\; -\frac{\partial u^n_{y1}}{\partial r}\; u^n_{r2}\; u^n_{\phi 2}\; u^n_{y2}\; -\frac{\partial u^n_{y2}}{\partial r}| \qquad (n \geqslant 0)$$

$$|\overline{d_n}|^t = |\overline{u}^n_{r1}\; \overline{u}^n_{\phi 1}\; \overline{u}^n_{y1}\; -\frac{\overline{\partial u}^n_{y1}}{\partial r}\; \overline{u}^n_{r2}\; \overline{u}^n_{\phi 2}\; \overline{u}^n_{y2}\; -\frac{\overline{\partial u}^n_{y2}}{\partial r}| \qquad (n \geqslant 1)$$

It has been shown, appendix 2, that the couplings exist for n = 0 and n = 1. The application of Lagrange's equations is much easier if the use of multipliers can be avoided, therefore the axisymmetric degrees of freedom are written in R1.

For n = 0, the axisymmetric degrees of freedom u°_r, u°_ϕ, u°_y, $-\partial u^\circ_y/\partial r$ are expressed (fig.5) as a function of the following degrees of freedom.

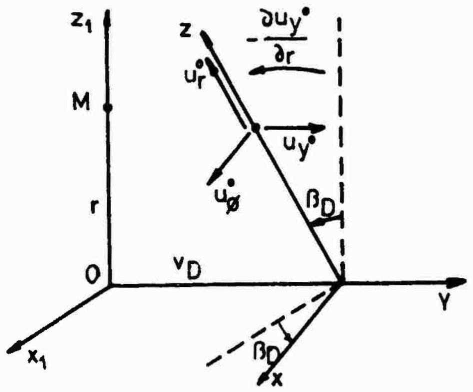

Fig.5 : n = 0, shaft disc connection

$$u^\circ = u^\circ_\phi + r.\beta_D \qquad v^\circ = u^\circ_y + v_D$$
$$w^\circ = u^\circ_r \qquad \alpha^\circ = -\frac{\partial u^\circ_y}{\partial r} \tag{24}$$

For n = 1, the axisymmetric degrees of freedom u_r^1, ..., $\partial u_y^1/\partial r$ are expressed (fig.6) as a function of the following degrees of freedom :

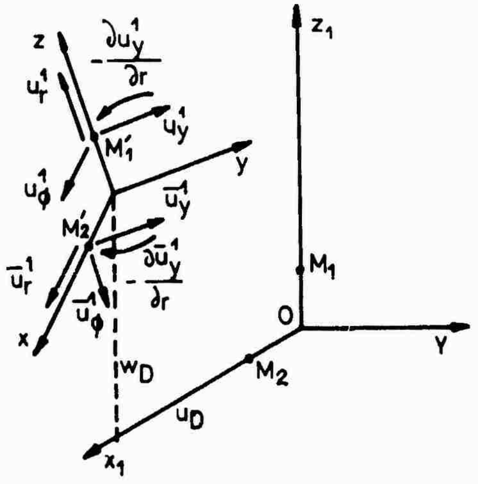

Fig.6 : n = 1, shaft disc connection

$$u^1 = u_D + u_\phi^1 \qquad v^1 = u_y^1 - r\theta_D$$
$$w^1 = w_D + u_r^1 \qquad \alpha^1 = \theta_D - \frac{\partial u_y^1}{\partial r}$$
$$\bar{u}^1 = u_D + \bar{u}_r^1 \qquad \bar{v}^1 = \bar{u}_y^1 + r\psi_D$$
$$\bar{w}^1 = w_D - \bar{u}_\phi^1 \qquad \bar{\alpha}^1 = \psi_D + \frac{\partial \bar{u}_y^1}{\partial r} \tag{25}$$

Equations

The expression of the kinetic and strain energies of the shaft and disc elements are, using (24), (25), a function of generalized independent coordinates. Through the Lagrange's equations one gets the general equations for the system :

$$M_n\delta^{\circ\circ}_n + C_n\delta^\circ_n + (K_{en} + K_{gn} - M_{sn})\delta_n = F_{cn} \tag{26}$$

where matrices are functions of n.

For n = 0, (26) gives the coupling between longitudinal or torsional motion of the shaft and the symmetric motions of the disc with no nodal diameter.

For n = 1, (26) gives the coupling between the bending of the shaft and the axisymmetric motion of the disc with one modal diameter.

For n ⩾ 2, (26) gives the axisymmetric motion of the disc with n nodal diameters and no coupling with the shaft.

The solution of (26) requires two steps. First of all for n = 0, it is necessary to solve

$$(K_{eo} + K_{go} - M_{so})\,\delta_{os} = F_{co} \tag{27}$$

This solution gives the initial displacements δ_{os} and stresses. Then, it is possible to solve the eigenvalue-eigenvector problem :

$$M_n\delta^{\circ\circ}_n + C_n\delta^\circ_n + (K_{en} + K_{gn} + M_{sn})\delta_n = 0 \tag{28}$$

The number of the degrees of freedom is highly reduced through a modal method based on the behavior of the rotor at rest. Then, the QR algorithm is used. It is thus possible to have the evolution of the natural frequencies, then the critical speeds, as a function of the speed of rotation Ω.

APPLICATION |12|

The equation and the corresponding computer program have been at first tested with simple applications and examples from (1), (3), the results obtained were satisfactory.

The rotor of an industrial gas turbine, in the case of symmetric undamped bearings, has been calculated. In figure 7 the shaft finite element modelisation is shown, four finite elements are used for the disc considered as flexible. The results shown in what follows are compared with results already obtained for this rotor, the disc being supposed rigid, (11).

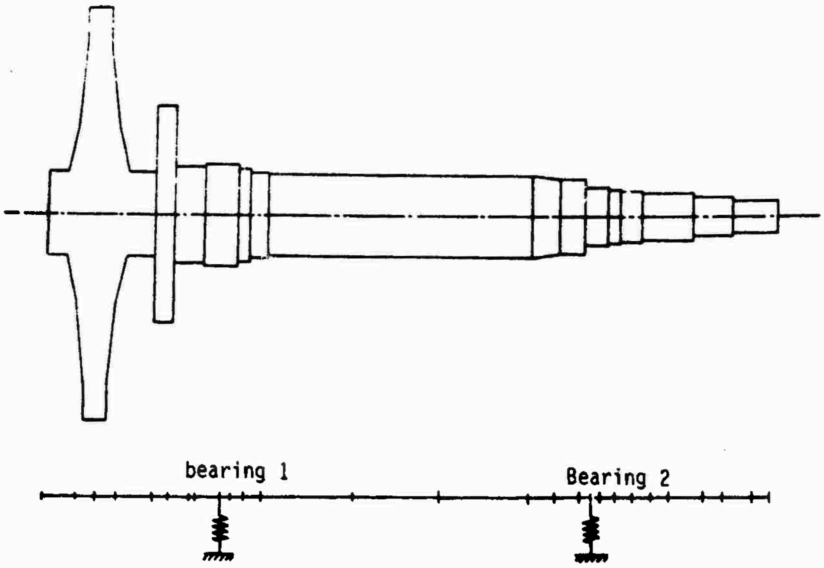

Fig.7 : Rotor of the gas turbine

Cas n = 0 (figure 8)

The natural frequencies with the rigid disc are independent of the speed of rotation and are represented by 1, 3, 5. The natural frequencies with flexible disc are represented by 1, 2, 4. The type of motion observed is in table 1.

Frequency	1	2	3	4	5
Shaft	T	L	L	T	T
Disc	R-F	F	R	F	R

Table 1

with T,L, respectively torsional or longitudinal motion

R,F, respectively rigid or flexible disc.

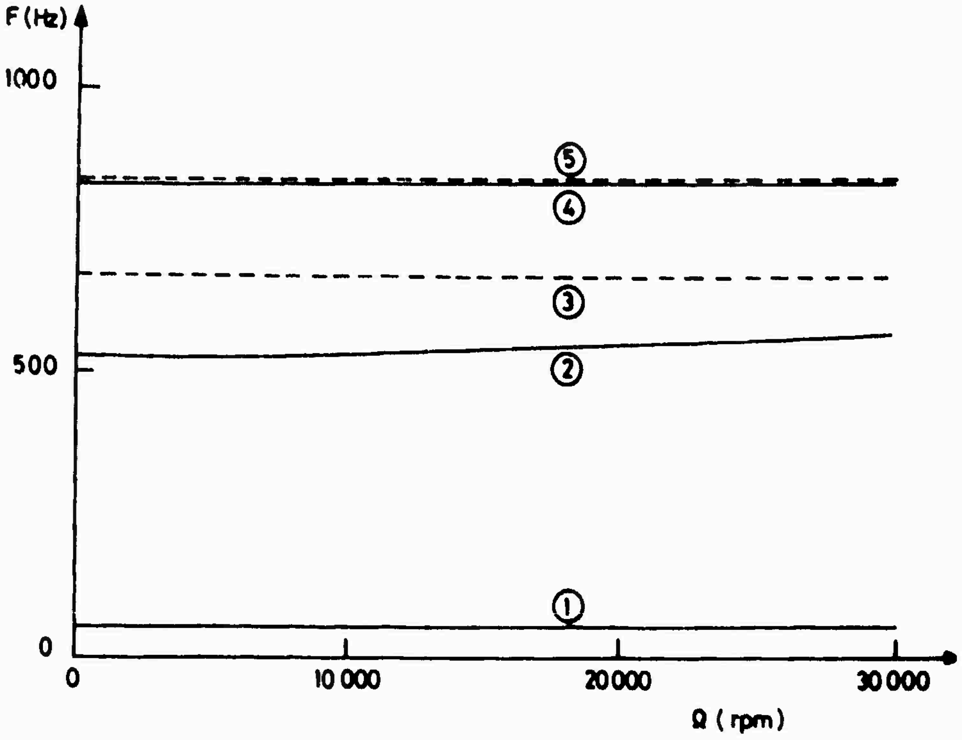

Fig.8 : Case n = 0, natural frequencies versus speed of rotation

It can be observed that the lowest torsional frequency is not influenced by the flexibility of the disc and that the conclusion is nearly the same for the second torsional frequency 4, 5. The first frequency corresponding to the longitudinal motion is reasonably affected by the disc flexibility.

Case n = 1 (figure 9)

This is the most practical because of excitations and particularly the unbalance exitation give a force component in bending. The frequencies corresponding to the rigid disc are presented in 2, 4, 6, 8, those corresponding to the flexible disc are presented in 1, 3, 5, 7.

Due to the operating speed the practical interest is in the evolution of the lowest frequency 1, 2. The flexibility of the disc decreases the corresponding critical speed of 3,5 %.

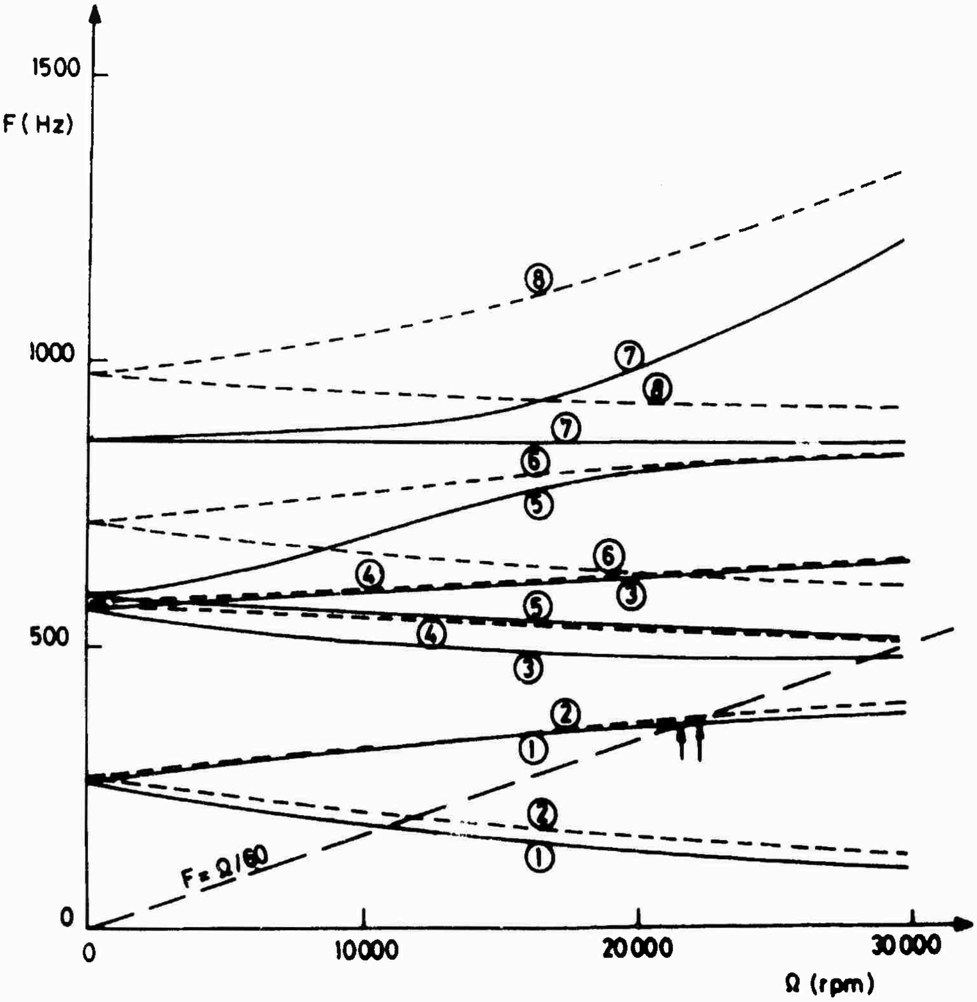

Fig.9 : Case n = 1, natural frequencies versus speed of rotation

CONCLUSION

The equations of rotors composed of a shaft and a flexible disc have been presented through kinetic and strain energies expressions and use of Lagrange's equations and have been solved using a modal method. The shaft and disc coupling, which exists only for n = 0 and n = 1, have been studied.

An industrial gas turbine has been presented and the evolution of the natural frequencies calculated. It has been shown that in the case considered, the critical speed due to unbalance is slightly decreased.

In the future, it will be probably necessary to consider the discs as flexible. Unfortunately, it is difficult to include flexibility influence in a computer program dealing with rotordynamics.

At this time, it is suggested to perform the calculations at rest with a classical finite element computer program. The disc is supposed to be rigid or flexible and then the flexibility influence, if it exists, can be roughly estimated.

ACKNOWLEDGEMENTS

Part of the computation cost was financed by "le Conseil Scientifique du Centre de Calcul Vectoriel pour la Recherche".

APPENDIX 1

The Lagrange's equations may be written as

$$\frac{d}{dt}\left(\frac{\partial T}{\partial q^{\circ}_i}\right) - \frac{\partial T}{\partial q_i} + \frac{\partial U}{\partial q_i} - Q_i = 0 \qquad (29)$$

with :

T, kinetic energy

U, strain energy

q_i, i^{th} generalized independent coordinate

Q_i, i^{th} generalized force, such as this due to the bearings.

APPENDIX 2

$$M_D = \pi\rho r \quad \begin{array}{cccccc|ccc|cccccccccccccc|c}
u^\circ_D & v^\circ_D & w^\circ_D & \theta^\circ_D & \psi^\circ_D & \beta^\circ_D & u^\circ_{ro} & u^\circ_{\phi o} & u^\circ_{yo} & u^\circ_{r1} & u^\circ_{\phi 1} & u^\circ_{y1} & \overline{u}^\circ_{r1} & \overline{u}^\circ_{\phi 1} & \overline{u}^\circ_{y1} & \cdots & u^\circ_{rn} & u^\circ_{\phi n} & u^\circ_{yn} & \overline{u}^\circ_{rn} & \overline{u}^\circ_{\phi n} & \overline{u}^\circ_{yn} & \cdots & \\
\hline
2 & 0 & 0 & 0 & 0 & 0 & 0 & 0 & 0 & 0 & 1 & 0 & 1 & 0 & 0 & & & & & & & & & u^\circ_D \\
 & 2 & 0 & 0 & 0 & 0 & 0 & 0 & 2 & 0 & 0 & 0 & 0 & 0 & 0 & & & & & & & & & v^\circ_D \\
 & & 2 & 0 & 0 & 0 & 0 & 0 & 0 & 1 & 0 & 0 & 0 & -1 & 0 & & & & & & & & & w^\circ_D \\
 & & & r^2+2y^2 & 0 & 0 & 0 & 0 & 0 & 0 & 0 & -r & 0 & 0 & 0 & & & & & & & & & \theta^\circ_D \\
 & & & & r^2+2y^2 & 0 & 0 & 0 & 0 & 0 & 0 & 0 & 0 & 0 & r & & & & & & & & & \psi^\circ_D \\
 & & & & & 2r^2 & 0 & 2r & 0 & 0 & 0 & 0 & 0 & 0 & 0 & & & & & & & & & \beta^\circ_D \\
\hline
 & & & & & & 2 & 0 & 0 & & & & & & & & & & & & & & & u^\circ_{ro} \\
 & & & & & & & 2 & 0 & & & & & & & & & & & & & & & u^\circ_{\phi o} \\
 & & & & & & & & 2 & & & & & & & & & & & & & & & u^\circ_{yo} \\
\hline
 & & & & & & & & & 1 & 0 & 0 & 0 & 0 & 0 & & & & & & & & & u^\circ_{r1} \\
 & & & & & & & & & & 1 & 0 & 0 & 0 & 0 & & & & & & & & & u^\circ_{\phi 1} \\
 & & & & & & & & & & & 1 & 0 & 0 & 0 & & & & & & & & & u^\circ_{y1} \\
 & & & & & & & & & & & & 1 & 0 & 0 & & & & & & & & & \overline{u}^\circ_{r1} \\
 & & & & & & & & & & & & & 1 & 0 & & & & & & & & & \overline{u}^\circ_{\phi 1} \\
 & & & & & & & & & & & & & & 1 & & & & & & & & & \overline{u}^\circ_{y1} \\
\hline
 & & & & & & & & & & & & & & & \ddots & & & & & & & & \vdots \\
 & & & & & & & & & & & & & & & & 1 & 0 & 0 & 0 & 0 & 0 & & u^\circ_{rn} \\
 & & & \text{SYM.} & & & & & & & & & & & & & & 1 & 0 & 0 & 0 & 0 & & u^\circ_{\phi n} \\
 & & & & & & & & & & & & & & & & & & 1 & 0 & 0 & 0 & & u^\circ_{yn} \\
 & & & & & & & & & & & & & & & & & & & 1 & 0 & 0 & & \overline{u}^\circ_{rn} \\
 & & & & & & & & & & & & & & & & & & & & 1 & 0 & & \overline{u}^\circ_{\phi n} \\
 & & & & & & & & & & & & & & & & & & & & & 1 & & \overline{u}^\circ_{yn} \\
 & & & & & & & & & & & & & & & & & & & & & & \ddots & \vdots \\
\hline
\end{array}$$

BIBLIOGRAPHY

|1| - J.A. Dopkin, T.A. Shoup, "Rotor resonant speed reduction caused by flexibility of disks", A.S.M.E., J. Eng. Pow., pp.1328-1333, (1974).

|2| - N. Hagiwara, S. Sakata, M. Takayanagi, K. Kikuchi, I. Gyobu, "Analysis of coupled vibration response in a rotating flexible shaft-impeller system", A.S.M.E. paper n°79-DET-69.

|3| - D.R. Chivens, H.D. Nelson, "The natural frequencies and critical speeds of a rotating flexible shaft-disk system", A.S.M.E. J. Eng. Ind., pp.881-886, (1975).

|4| - F.J. Wilgen, A.L. Schlack, "Effects of disk flexibility on shaft whirl stability", A.S.M.E. paper n°78-WA/DE-4.

|5| - N. Klompas, "Theory of rotor dynamics with coupling of disk and blade flexibilities and support structure asymmetry", A.S.M.E. paper n°74-GT-15.

|6| - N. Klompas, "Significance of disk flexing in viscous-damped jet engine dynamics", A.S.M.E., J. Eng. Pow., pp.647-654, (1978).

|7| - N. Klompas, "Blade exitation by elliptical whirling in viscous-damped jet engine", A.S.M.E. paper n°80-FT-168.

|8| - M. Sakata, T. Aiba, H. Onabe, "Transient vibrations of high-speed lightweight rotors due to sudden unbalance", A.S.M.E. J. Eng. Pow., pp.480-486, (1983).

|9| - J.A. Palladino, J.N. Rossetos, "Finite element analysis of the dynamic of flexible disc-rotor system", A.S.M.E. paper n°82-GT-240.

|10| - R.G. Loewy, N. Khader, "Structural dynamics of rotating bladed disk assemblies coupled with flexible shaft motions", A.I.A.A. J., pp.1319-1327, (1984).

|11| - P. Berthier, G. Ferraris, M. Lalanne, "Prediction of critical speeds, unbalance and non synchronous forced response of rotors", 53th Shock Vib. Bull.

|12| - P. Brémand, "Influence de la flexibilité d'un disque sur le comportement dynamique des rotors", Thèse D.I., I.N.S.A. de Lyon, (1985).

|13| - V.V. Novozhilov, "Thin shell theory", Walter Noordhoff, (1970).

Discussion

Mr. Eshleman (Vibration Institute): It looked like the flexibility effect was small compared to the gyroscopic effect in that case. Did you try it with a smaller diameter disc that did not have a gyroscopic effect?

Mr. LaLanne: No.

Mr. Eshleman: Do you think the rotor you analyzed is a typical industrial rotor? If it is, it seems there is probably no reason to worry about its flexibility. However, I have heard of other people worrying about the flexibility of the disc.

IMPLEMENTATION OF ACTIVE FORCE CONTROL FOR ROBOTS SUBJECT TO DYNAMIC LOADING

R. Hollowell, R. Guile, P. FitzPatrick, S. Foley
United Technologies Research Center
East Hartford, CT 06108

A force control servo for robotic machining was designed and studied based on structural and servo dynamic tests. Results of the studies indicate the feasibility of robotic chamfering using force control and the need for considering robot structural modes in stable force control design. An autoregressive moving average identification technique was used to develop a procedure for model parameter identification from digital sampled impulse response data. A gain scheduling technique is described for achieving stable force control during light metal cutting, while compensating for varying robot structural modes.

INTRODUCTION

Automation of light machining processes such as chamfering and deburring is desirable because these processes are repetitive, error prone, and in some cases hazardous. Anthropomorphic robots are attractive candidates for achieving this automation because their dexterity and large work volume make them especially versatile machine tools. However, an articulated structure results in a robot having high structural compliance and poor positioning accuracy relative to traditional machine tools, characteristics that complicate the problem of programming a robot to perform light machining tasks. In particular, part misorientation relative to a taught robot path will result in either too little material removal or excessive interference between the tool and the part, possibly resulting in part damage. A number of researchers have described approaches to using compliantly mounted tools to accommodate part misorientation (Ref. 1,2,3,4). Experience has shown that with light cutting forces, the tool compliance can couple with robot compliance resulting in tool chatter and unsatisfactory metal removal.

Development of active tool force control is expected to overcome some of the problems of passive compliant mounts. Previous work on active force control is summarized by Whitney in Ref 5. For active control, instrumentation measures the force between the tool and part, providing feedback to a controller that regulates the cutting force at a desired level. To implement such a strategy for precision chamfering, an articulated machine tool was developed which provides an additional degree of freedom (DOF) that can be controlled to regulate force. The requirement imposed on the robot controller is that the robot degrees of freedom be controlled to maintain proper alignment of this force control motion normal with the local part surface. Important features of such a tool include the ability to compensate for:

1. Inaccuracies of the robot and workpiece positioning,
2. Configuration dependent dynamic characteristics of the robot arm.

The tool and control algorithm must maintain material removal rate tolerances and control stability sufficient for the manufacture of precision aerospace parts.

This paper discusses the role of dynamic analysis in the design and implementation of an electro-mechanical feedback control system for robotic machining. First, servo system and arm structural models are described, and the dynamic testing and analysis used to validate and identify those models is reported. Then the implementation of active force control using the modelled tooling is discussed, closed loop cutting performance is assessed, and requirements for a second generation tool are identified. Finally, a strategy for designing and implementing a stable force controller that compensates for changing robot dynamics is discussed.

DYNAMIC SYSTEM MODELLING

The research was conducted using an ASEA IRb-6 five axis articulated robot with an S1 controller as shown in Figure 1. The tooling consists of a six axis force and torque sensor, a dc servo mechanism, a 30,000 rpm, 3mm collet pneumatic deburring spindle, and associated support structure. The spindle has a single degree of rotation relative to the support structure, and is driven by the servo motor through an elastic belt and a high ratio worm gearset. A resolver and tachometer attached to the motor shaft provide feedback to ASEA joint axis electronics, making the servo mechanism essentially a sixth robot axis. The support tooling assembly is attached to the force sensor which is attached to the robot tool mounting flange.

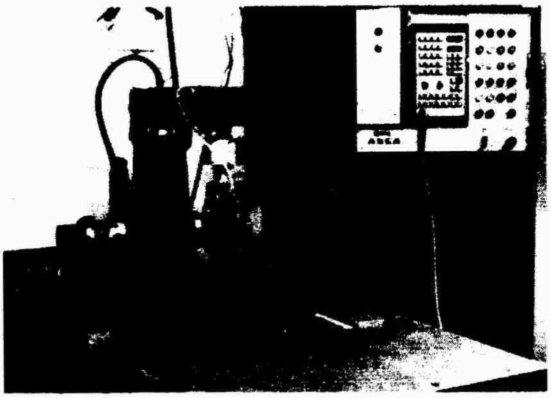

Figure 1. ASEA IRb-6 Robot, Six Axis Force Sensor and Sixth Axis Spindle Drive System

A linearized model of the sixth axis servo, given in Figure 2, was developed to understand the transfer function based force feedback control strategy implemented in the machining studies. The joint position commanded by the robot computer is compared to the resolver feedback, and the difference is converted to an analog velocity reference. This reference is input to a conventional velocity servo to produce motor velocity, while the motor position is geared to produce tool position. The loaded servo mechanism is not adequately modelled with linear elements because of the non-linear friction, backlash, and lack of back-driveability in the worm gearset. Figure 3 is a block diagram of the loaded mechanism showing the implemented force control algorithm, with the worm gear represented as a single block. The tool position is referenced with respect to the position of the workpiece surface, and the resulting workpiece-tool interference acts through the effective spring rate of the tool support and robot arm to yield the normal force acting between the workpiece and the cutter. This normal cutting force is calculated from the force sensor measurements and a known kinematic relationship, although the measurements are bandwidth limited due to the compliant structure separating the force sensor and the cutting forces.

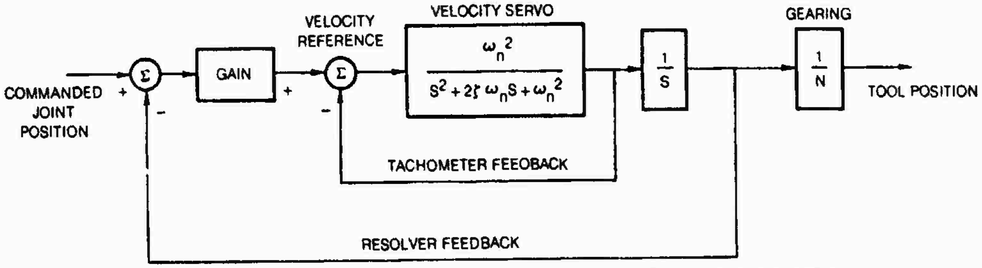

Figure 2. Linearized Block Diagram of Sixth Axis Servomechanism

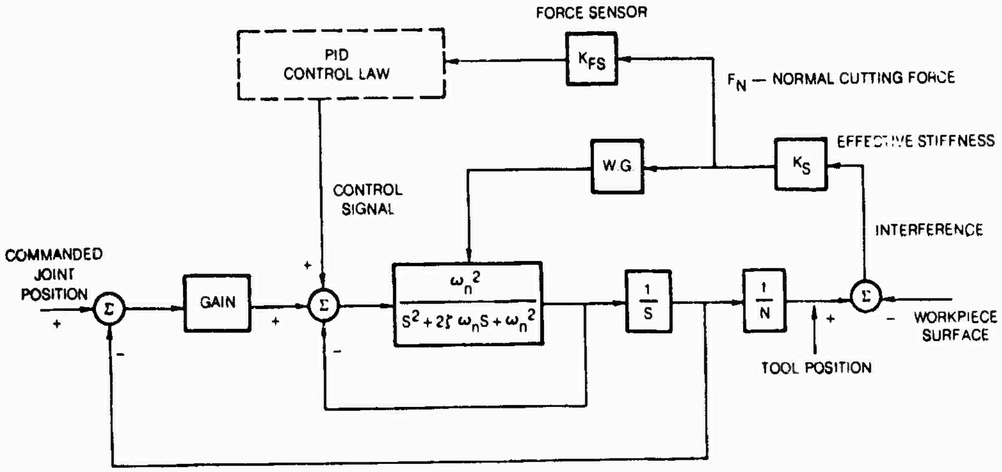

Figure 3. Block Diagram of 6th Axis Servomechanism Showing Cutting Force Control Algorithm

A lumped mass model containing identifiable physical parameters was developed to aid in the assessment of closed loop cutting performance and to serve as a basis for a complete model of the second generation tool, that will be designed to achieve control stability. Figure 4 shows a single axis two DOF lumped mass model and corresponding bond graph representation characterizing the dominant dynamic response of the robot arm (M1,K1,C1) and tool (M2,K2,C2), subject to a force input. The bond graph (see [6]) method of modelling and analysis lends itself to building state variable models of systems incorporating electrical, mechanical and hydraulic components. In a mechanical system bond graph model, energy is stored as kinetic energy in the masses (across element) and potential energy in the springs (through element). The model state variables are the velocities (potential) of the masses and the forces (flow) in the springs, and are selected based on system causality constraints. In this model, energy enters the system in the form of tool cutting forces Fs, is dissipated by system damping and exits the system to ground. The first order matrix differential equation resulting from a systematic analysis of the bond graph is:

$$\frac{d}{dt}\begin{bmatrix} V_2 \\ F_{K_2} \\ V_1 \\ F_{K_1} \end{bmatrix} = \begin{bmatrix} -c_2/M_2 & -1/M_2 & c_2/M_2 & 0 \\ K_2 & 0 & -K_2 & 0 \\ c_2/M_1 & 1/M_1 & \dfrac{-(c_1+c_2)}{M_1} & -1/M_1 \\ 0 & 0 & K_1 & 0 \end{bmatrix}\begin{bmatrix} V_2 \\ F_{K_2} \\ V_1 \\ F_{K_1} \end{bmatrix} + \begin{bmatrix} 1/M_2 \\ 0 \\ 0 \\ 0 \end{bmatrix} F_s \quad (1)$$

This matrix equation is reduced to yield a transfer function relating the acceleration A2 of mass M2, to the force input Fs.

$$\frac{A_2}{F_s} = \frac{\dfrac{1}{M_2}s^2\left[s^2 + \left(\dfrac{c_1+c_2}{M_1}\right)s + \dfrac{K_1+K_2}{M_1}\right]}{\left[s^4 + \left(\dfrac{c_2}{M_2} + \dfrac{c_1+c_2}{M_1}\right)s^3 + \left(\dfrac{K_1+K_2}{M_1} + \dfrac{K_2}{M_2} + \dfrac{c_1c_2}{M_1M_2}\right)s^2 + \left(\dfrac{c_1K_2+c_2K_1}{M_1M_2}\right)s + \dfrac{K_1K_2}{M_1M_2}\right]} \quad (2)$$

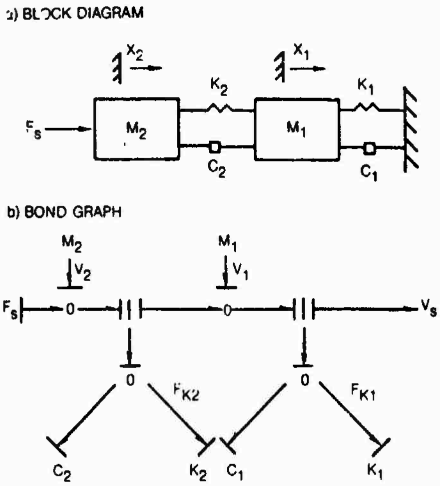

Figure 4. Block Diagram and Bond Graph of Two Mass Dynamic System

DYNAMIC SYSTEM ANALYSIS

This program of dynamic analysis was conducted to assess the phenomena observed during preliminary closed loop machining studies, so to develop mechanical and control design specifications for the second generation tool. Analog frequency response testing supported open loop transfer function analysis of the joint servo model. Computer based impulse response testing and data analysis was used for assessing cutting performance during active force control deburring tests. The computer based data acquisition and analysis tools that have been developed will be used for bond graph parameter identification, and implementation of a microprocessor based adaptive state controller for the second generation tool.

The open loop frequency response of the motor velocity servo was measured using a wave generator to excite the servo and a phase gain meter to compare the input signal to the responses from the tachometer and resolver. The Bode plots in Figure 5 and 6 compare the experimental data to the frequency response predicted by the block diagram model in Figure 2. The Bode plot of the tachometer response shows poorly damped poles at 8 Hz, and a lack of phase and gain correlation below 5 Hz. This low frequency deviation is attributed to nonlinear hysterisis in the worm gearset, which was not included in the analytic model. The resolver response also reveals the 8 Hz poles, and the high frequency attenuation is attributed to the lowpass filter in the resolver electronics.

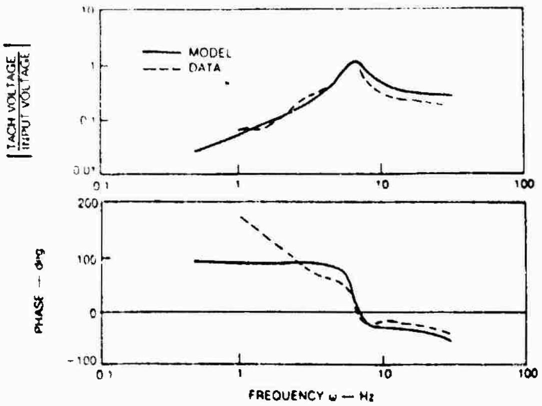

Figure 5. Bode Plot of Tachometer Response Referenced to Input

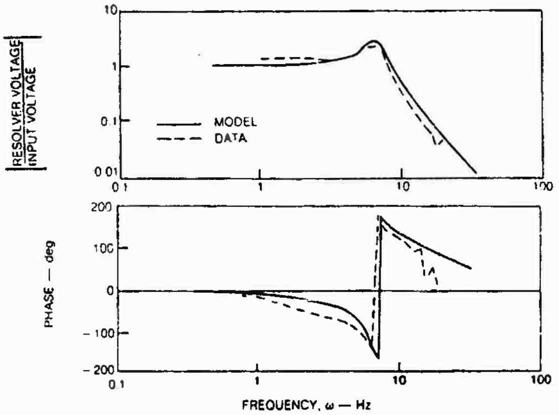

Figure 6. Bode Plot of Resolver Response Referenced to Input

The acceleration response of the spindle housing subject to impulse loading was measured using a strain gage accelerometer and a piezoelectric impulse hammer. Impulse response tests were performed with the robot and tool in the configuration shown in Figure 7, which was the configuration nominally assumed in the closed loop cutting experiments, to characterize the structural model in directions normal and tangent to the surface being cut. The analog data was conditioned with a 50 Hz fourth order low-pass filter, and was sampled and stored at 200 Hz using a Digital Equipment PDP 11/73 minicomputer. The digital data was transferred to a Vax 11/780 computer and analysed using the CTRL-C [7] signal processing and control system design software. A high order discrete transfer function autoregressive moving average (ARMA) model [8] was identified from the input force data, the output acceleration data, and the time history. The discrete model was converted to a continuous transfer function model, which was reduced to the form of Equation 2 by selectively removing poles and zeros. The bond graph parameters (M1,K1,C1,M2,K2,C2) were explicitly determined by equating the coefficients in Equation 2 to the coefficients of the reduced transfer function. The identified parameters were substituted into matrix Equation 1, and the output predicted by the state model was compared to the experimental data.

Figures 8 and 9 show good correlation between the experimental and simulated response for the tangential and normal cutting directions. The tangential axis response is clearly dominated by an 8 Hz mode, and a second order model adequately describes the system. This mode represents the lumped response of the tool structure and the robot fourth joint servo. The normal axis response shows coupling between an 8 Hz mode and an 18 Hz mode, and a fourth order model is required to adequately predict system behavior. The higher order effects seen in the data are attributed to the bandwidth characteristics of the accelerometer. The estimated bond graph parameters for the second and fourth order models agree with engineering estimates, and are liated in Table 1. Figures 10 and 11 compare data from a single impulse test to the response simulated using the previously developed model. The close correlation is additional proof that the bond graph model is a good representation of the dynamic system.

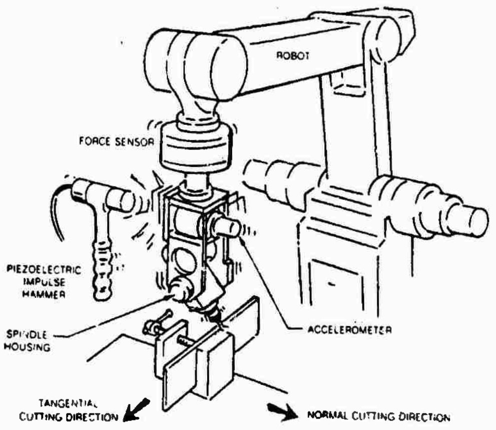

Figure 7. Robot Arm and Tool System Being Characterized thru Forced Response Testing

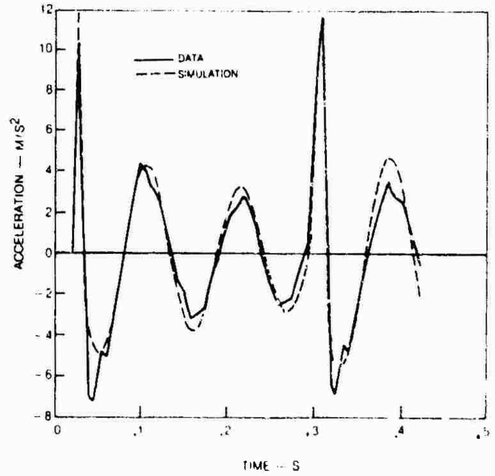

Figure 8. Tangential Axis Multiple Impulse Response

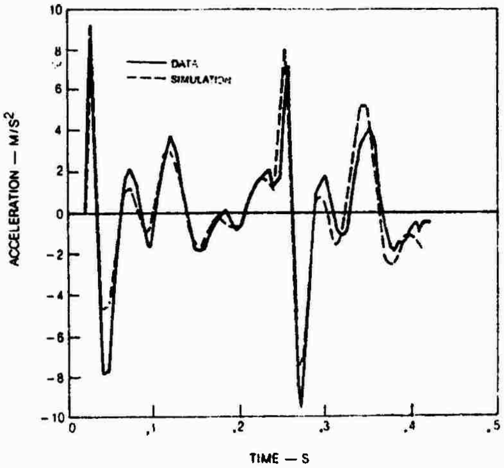

Figure 9. Normal Axis Multiple Impulse Response

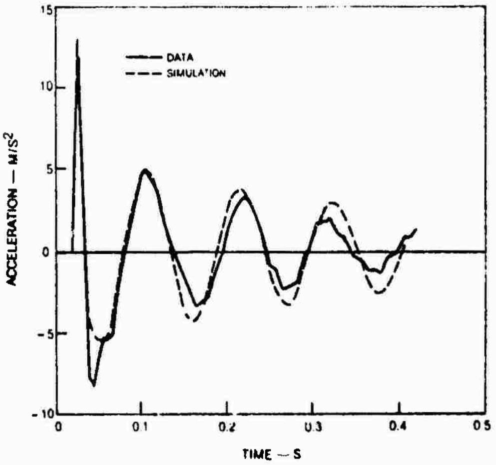

Figure 10. Tangential Axis Single Impulse Response

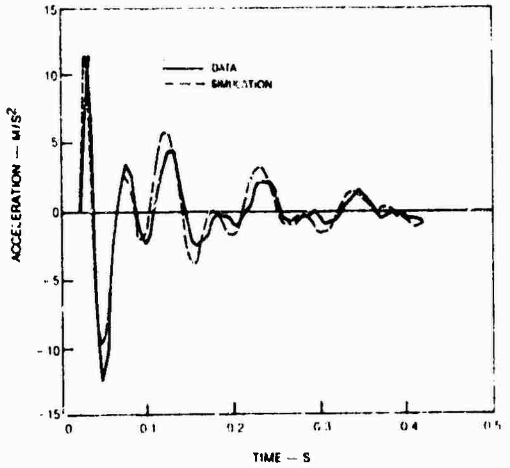

Figure 11. Normal Axis Single Impulse Response

Table 1. Bond Graph Parameters

CUTTING DIRECTION	MASS Kg		SPRING RATE N/mm		DAMPING N•S/m	
	M_2	M_1	K_2	K_1	C_2	C_1
TANGENTIAL	1.20	—	4.0	—	20	—
NORMAL	1.21	2.25	9.3	12	51	3

IMPLEMENTATION OF ACTIVE FORCE CONTROL

A physical prototype system for actively controlling the cutting force normal to the edge being machined was implemented using the tooling previously modelled and analyzed. The objective of these preliminary closed loop tests was to show the feasibility of maintaining a consistent chamfer when the workpiece is displaced and misaligned relative to the programmed path of the robot. The control strategy, represented by the block diagram in Figure 4, uses the position of the cutting surface as input, and the normal cutting force as output and the controlled variable. The force sensor output is sampled every 6 ms by the PDP 11/73 minicomputer and compared to the desired normal force to generate a discrete force error. This force error is processed by a discrete PID controller whose output is transmitted via a digital to analog converter to the sixth axis velocity servo.

The discrete PID controller is part of a versatile, user-oriented computer program that samples the force sensor, calculates the servo control signal, and communicates with the robot computer. The menu driven program first prompts the user to select the controller gains and saturation limits desired for the deburring test run. The software then initiates the pre-programmed robot deburring sequence, which begins with the pneumatic spindle being activated and the robot moving the spindle slowly toward the workpiece. Contact with the workpiece is detected by sensing when the force signal exceedes a preset force level. At this point, an adaptive feature of the robot is caused to be executed, transforming the programmed cutting path of the robot to reflect the shifted contact point. This adaptive path transformation feature compensates for gross displacement of the workpiece relative to the programmed path of the robot. After contact, the software controller continuously generates servo control signals while the robot executes the spindle motion, adjusting the spindle position to correct for misalignment of the workpiece relative to the transformed cutting path. If the normal cutting force exceeds a preset maximum force level, the controller commands the robot to stop its program execution and move away from the workpiece, thereby preventing permanent damage.

Active deburring simulations were conducted to select PID controller gains and to assess the capabilities and limitations of the existing tooling. The test plate was carefully aligned relative to the straight robot path, and the derivative and integral gains were set to zero. The proportional gain was increased until cutting performance, as indicated by the normal force history, began to degenerate. The derivative gain was then increased to achieve the best damping, again determined by visual inspection of the normal force history. Finally the workpiece was misaligned relative to the robot path, and the integral gain and saturation limit were increased until the desired normal force was maintained over the entire programmed path, with a minimum of force fluctuations.

The normal force error from controlled and uncontrolled cutting tests are shown in Figure 12. The dc trend of the uncontrolled force history is evidence of misalignment of the workpiece from the path of the robot. The controlled force history exhibits damped force fluctuations relative to those present in the uncontrolled force history, and the dc trend has been successfully removed. Visual inspection of the tool while cutting, revealed that structural tool vibration in the direction of travel (tangential cutting direction) is excited when a burr is encountered, and is coupled with structural vibration in the normal direction. The observation that coupling between tool structural characteristics in the normal and tangential directions is detrimental to cutting performance is supported by testing and analysis reported by Asada [9]. The observed motion of the servo actuator to control inputs was characterised by rapid oscillatory response followed by periods of no motion, indicating that non-linear friction (stick-slip) was a major source of the fluctuations seen in the closed loop tests. Some closed loop tests resulted in unstable 8 Hz force oscillations, indicating that the poorly damped servo mode was exciting the tool structural modes.

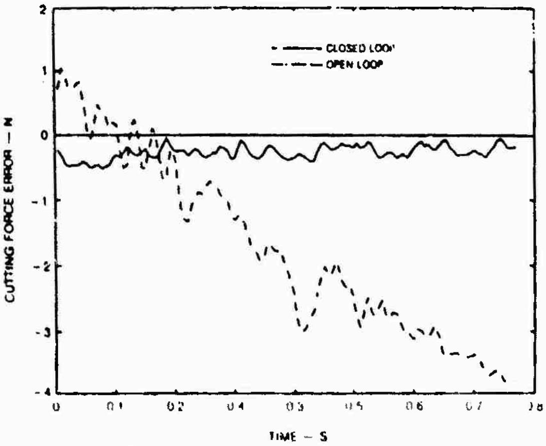

Figure 12. Normal Force Error Comparison for Uncontrolled and Controlled Cutting Tests

Preliminary specifications for the design of the second generation tool were developed based on the servo and structural model analysis, and the assessment of closed loop cutting performance. The first design requirement is that the structural stiffness of the spindle support in the normal cutting direction should be an order of magnitude less than in the tangential cutting direction, as suggested by Asada. This would prevent the dynamic coupling exhibited by the present tooling. The second desired feature of the tool is that the servo mechanism should be simple and capable of being modelled with linear elements, so that a bond graph of the entire system may be developed. This design characteristic would eliminate the stability problems caused by the nonlinear elements in the existing servo mechanism. The third and most important requirement of the second generation tool is that the controller be designed to avoid exciting the robot arm or tool dynamic modes. The controller must satisfy this specification to gaurantee stability, which is required for the machining of aerospace parts.

FORCE CONTROL STRATEGY WITH COMPENSATION FOR CHANGING ROBOT DYNAMICS

The results of the preliminary closed loop deburring studies suggest an alternative controller implementation to achieve reliable and stable force control using a closed loop spindle manipulator mechanism. The observation was made that interactions between robot arm dynamics and tool dynamics yields unsatisfactory performance. Moreover, the dynamic response of the tool mounting plate to force inputs varies with changing arm configuration, wrist orientation, and the direction of the applied forces. A strategy for designing a stable controller that compensates for changing robot arm dynamics in real time is described. The strategy is based on bond graph modelling of the manipulator mechanism and arm dynamics, experimental identification of arm model parameters for several discrete regions of operation, and state variable control theory.

A complete state variable model of the spindle manipulator mechanism should include the dynamics of the support (robot arm), actuator and associated electronics, spindle, and the process. Ideally, the state control law is based on knowledge of enough states to insure controllability, hence stable force control. Since it is impractical to measure all of the states that would be required for controllability, a state model observer will be constructed so that the unmeasured states are estimated from knowledge of the actuator position and the cutting forces. This state estimator and controller will be implemented with a microprocessor to achieve stable force control for a specific arm configuration and cutting force direction. The adaptive strategy is to experimentally identify, using the impulse response analysis previously described, the robot arm dynamic parameters for several discrete regions of input force direction and arm configuration. The observer and controller values will be updated as the process changes from one region to the next. This gain scheduler will be implemented with a second processor that retrieves the experimentally determined parameters from memory and communicates with the robot computer, the off-line program, and the microprocessor acting as the observer and controller. This strategy for stable force control will be implemented with a second generation machining tool currently under development.

CONCLUSIONS

A robot mounted one degree of freedom spindle manipulator was used in machining studies to demonstrate the feasibility of closed loop control of the normal cutting force. A model of the manipulator servo was developed and experimentally verified as an aid for designing the closed loop force feedback control algorithm, and for assessing closed loop cutting performance. A two degree of freedom lumped mass model of the manipulator support structure and robot arm was developed to serve as a basis for the design of a stable force controller. The supporting analysis showed that the model parameters are explicitly determined using an autoregressive moving average model estimation technique. The analysis characterized the dynamic tool and robot modes in directions normal and tangent to the cutting surface, information used in the assessment of tool behavior during closed loop tests.

Machining tests conducted using the spindle manipulator showed that closed loop force control substantially improves cutting performance relative to passive compliance, when the workpiece is misaligned relative to the programmed cutting path. Analysis of closed loop test results led to the development of several preliminary specifications for the design of the second generation machining tool. A force control strategy that compensates for changing robot arm dynamics is described, and will be implemented in the next tool to achieve control stability.

REFERENCES

1. Drake, S. K. and S. N. Simunovic, "The Use of Compliance in a Robot Assembly System," Reprints, IFAC Symp. on Info. and Control Problems in Manuf. Techn., Tokyo, 1977.

2. Watson, P. C., "A Multidimensional System Analysis of the Assembly Process as Performed by a Manipulator," 1st N. Am. Robot Conf., Chicago, 1976.

3. L. K. Gillespie, Precision Deburring Using NC and Robot Equipment (Final Report). Bendix Kansas City: BDX-613-2431, June 1980, (Available from NTIS).

4. "Industrial Robot System for Deburring", ASEA Pamphlet 09-6052E, 1983, ASEA, Incorporated, Troy, MI.

5. Whitney, D. E., "Historical Perspective and State of the Art in robot Force Control", IEEE Robotics and Automation Conference, St. Louis, March, 1985.

6. Karnopp, D., Rosenberg, R. C., Analysis and Simulation of Multiport Systems, 1968, MIT Press.

7. "CTRL-C Programming Manual," Systems Control Technology, Palo Alto, CA, March 1984.

8. Franklin, G. F., Powell, J. D., Digital Control of Dynamic Systems, Addison-Wesley, 1981.

9. Asada, H., Goldfine, N., "Optimal Compliance Design for Grinding Robot Tool Holders", IEEE International Conference on Robotics and Automation. 1985.

Discussion

Mr. Hanagud (Georgia Institute of Technology): Whenever you have a feedback system for vibration control, depending on the type of feedback, there may be instabilities associated with that. Did you filter or selectively filter the signal before you fed it back?

Mr. Hollowell: We had a PID control law; the way we designed it, because we did not have a complete model, and the PID control had several limits, was to begin by setting all of the gains to zero and increasing the proportional gain until the system began to go unstable. Then, we put in the derivative term to damp it.

FORCE MAGNITUDE AND ANGULAR VELOCITY FLUCTUATION REDUCTION IN A SPRING-RESTRAINED, FLEXIBLY-SUPPORTED FOUR-BAR MECHANICAL LINKAGE

by

ROBERT A. McLAUCHLAN, Ph.D., P.E.
Associate Professor, Mechanical Engineering
Texas A&I University
Kingsville, Texas 78363

and

SEUNG HO HONG, M.S. in M.E.
Masters in Mechanical Engineering, May 1985
Texas Tech University
Lubbock, Texas 79409

SUMMARY

Linear restraining spring potential energy storage elements and flexible vibration isolator support systems have been investigated as passive devices to control the highly-nonlinear motion of a planar four-bar mechanical linkage. Specific design/performance indices considered for the spring-restrained, flexibly-supported linkage were:

(1) Shaft angular speed variation over time
(2) Internal reaction force magnitudes
(3) Forces transmitted to the base of the linkage mechanism.

The design study was based upon the numerical solution in the time domain of the state vector equation for the four-bar mechanical linkage system. The state-vector equation was developed using Lagrange's form of D'Alembert's principle. Three different linkage systems were considered as follows:

(1) Four-bar linkage, rigidly mounted without restraining spring (Model 1)
(2) Four-bar linkage, rigidly supported with restraining spring (and damper) (Model 2)
(3) Four-bar linkage, flexibly-supported with restraining spring (and damper) (Model 3)

Frequency responses of the shaft angular velocities, etc. were also obtained using the Fast Fourier Transform of the time domain results. All computer program simulations were written in FORTRAN 77 and performed on an IBM 3033. They were also checked out against one another (Model versus Model) and against previously published experimental results.

For the four-bar linkage systems considered, the results indicate the following:

(1) Tension restraining spring elements produce angular speed fluctuation results (with a well defined minimum) which are superior to those for compression and tension-compression springs.
(2) Adding a damper in parallel with a restraining spring element:
    (a) Degrades tension spring element, angular speed fluctuation performance.
    (b) Can improve compression spring element, angular speed fluctuation performance, which at best is, for realizable damper values, less than that with the tension spring.
    (c) Has little effect on tension-compression spring element, angular speed fluctuation performance behavior.

(3) The use of flexible vibration isolator support systems along with restraining spring elements can considerably reduce the internal reaction forces on the pin connection bearings and the forces transmitted to the base of the mechanism. As for example, the peak forces transmitted to the base of the mechanism can be reduced by factors of 12.4 and 64.0 respectively (Model 3 versus Model 2 - 12.4, and Model 3 versus Model 1 - 64.0)

(4) The force magnitude reductions in (3) can be obtained with little increase in the minimal fluctuation of input crank shaft speed, which is obtained for the restraining-spring, rigidly-supported four-bar linkage system.

INTRODUCTION

Reduction of the variation in input shaft speed and in bearing and foundation interaction force magnitudes are important goals in the design of advanced mechanical linkages. Such reductions can lead to longer useful bearing and linkage member lifetimes, reduced machinery noise levels, as well as to high speed/high precision advanced manufacturing applications.

Past methods of balancing high-speed cyclic (four-bar, etc.) linkage systems have dealt with either balancing the shaking force and the shaking moment, or minimizing the input torque fluctuation. The work relevant these cyclic linkage balancing methods can be summarized as follows:

* Balancing of the shaking force and the shaking moment: This method employs redistribution of the masses of the moving links or counterweighting the linkage so that the centroid of the system remains stationary (Berkof 1-3, Lower and Tepper 2-3). This technique is limited by the fact that perfect balancing of the shaking moment obtains only when the shaking force is completely balanced. Furthermore, techniques which completely force and moment-balance linkages do not eliminate variations in the input torque. These input torque variations can result in (a) the cost of a larger motor to supply the increased peak input torque required, and (b) shorter system life due to greater bearing force.

* Minimization of the input torque variation: This torque minimization is obtained by the internal redistribution of the masses in the mechanism. Here after assuming constant speed of the driving link, the designer synthesizes (i.e., finds) the mass, mass moment of inertia, and the locations of the center of mass of the links to reduce the peak input torque. See Ogawa and Funabashi (4), Hocky (5), and Berkof (6) for the development and initial investigations of this method. Elliot and Tesar (7) and Lee and Chang (8) have considered the trade-off among the shaking force, shaking moment, and the input torque to obtain the optimum dynamic linkage response.

* Reduction of the driving shaft speed fluctuation about the steady-state rotation speed: The attainment of this reduction in driving shaft speed fluctuation has been considered in several different ways as, e.g., (a) Tuning the flywheel as per the optimum choice of flywheel inertia and connecting shaft stiffness (Mahig 9). Costs associated with this method are a larger (more massive, stiffer) linkage and the extra masses for the counterweight or flywheel. (b) Using an optimally chosen spring mechanism instead of the flywheel mass in (a). The spring mechanism is attached to a moving link and the mechanism frame. See the initial work done Genova (10) regarding this concept. Benedict and Tesar (11) employed this technique to optimize a soap stamp and indexing machine using the concept of influence coefficients. (c) Using more general force device systems (such as defined by-spring constants, damping coefficients and force device attachment points) to drive a mechanism to have a desired motion-time response. Halter (12,13) and Carson (13,14) designed such force device systems using a nonlinear programming technique to minimize an objective function consisting of the least-square error of the generalized force plus penalty functions to constrain the range of the force device design parameter

values. Carson (15) found that springs attached between non-adjacent links produced superior results as compared to those between adjacent links. He also pointed out that absorbers (spring plus damper force device systems) always dissipate or waste energy and other alternatives should be considered. It should be noted that considerable reduction in weight and more practical sizing of the complete linkage as well as a more nearly constant drive shaft speed can be obtained by applying synthesized (i.e., optimally chosen) force elements. The minimization of the fluctuation in input shaft speed is important to the proper design of any high-speed mechanism. This is because the balancing procedures are based upon the assumption of constant input shaft rotational speed.

* Flexible support of mechanical linkage: Allen (17) has applied the bond graph approach to a four-bar linkage with a flywheel and elastic drive shaft with a simple spring-damper/vertical vibration isolation system. He assumed a constant angular velocity of the drive shaft relative to the frame link and demonstrated that the input torque variation for the mechanical linkage can be reduced with respect to observations made in an accelerating reference frame.

Related experimental work has been done by Tacheny, Hagen, and Erdman (16). Here they presented an experimental technique relevant how to gather the time response data for the position, velocity, and torque of a four-bar linkage in detail. They also experimentally showed the effect of adding a spring to a coupler link on a four-bar mechanism.

Other references in the literature have shown that force devices can be employed in improving the function of specific mechanisms. Van Sickle and Goodman (18) used a compression spring force to increase the speed of the mechanical linkage in a circuit breaker. Bishop and Wilson (19) presented a method to control the velocity and acceleration of a spring-driven rotary paper-cutting mechanism by the use of a pneumatic cylinder to obtain an acceptable paper-cut quality as well as a reduction in the impact force, noise, and vibration.

Most design synthesis techniques for linkage mechanisms are based upon the usual assumption that the members of the linkage are mounted on a rigid frame. This rigid frame mounting can become a troublesome problem when inertial-shaking forces and moments transmitted to the base of a mechanism cause unnecessary vibration. Such vibration may result in motion innacuracy over time, shorter life of the linkage members and revolute-pair bearings, as well as the generation of excessive noise levels. The most effective method to eliminate such machine-produced vibration is to mount the machine-mechanical linkage system in this case, on a flexible support or vibration isolation system. A flexibly supported mechanical linkage or machine system is also useful when the machine is mounted on vibrating foundations and must be isolated from external disturbances.

A current design trend is to construct a machine or mechanical linkage system with minimal weight to satisfy requirements for high speed operation and/or to minimize input power consumption. Using extra balancing masses or more massive linkage members can result in larger machine size, increased material costs, and greater bearing forces. These considerations motivate the design synthesis or selection of force devices such as spring and/or damper systems. Their use can be much more desirable in mechanism design than adding a massive counterweight or flywheel.

This paper reports an investigation of (1) linear restraining spring potential energy storage elements and (2) flexible vibration isolator support systems--as passive devices to control the highly-nonlinear motion of a planar four-bar linkage. The remainder of the report is organized as follows. First, a brief discussion is given of the development and solution of the state vector equation for the four-bar mechanical linkage system. Next, numerical solution results are presented and discussed for a design study of three different linkage systems. These simulation study results compare the design performance for the spring-restrained, flexibly-supported four-bar linkage with those for the rigidly-supported linkage with and without spring-restraint elements. A conclusions section summarizes the force magnitude and velocity fluctuation reductions possible in a spring-restrained, four-bar linkage. The paper ends with recommendations for future work.

DEFINING THE MECHANICAL LINKAGE SYSTEM

Figure 1 depicts the flexibly-supported, spring-restrained four-bar mechanical linkage mechanism which is considered in this paper. Here the links

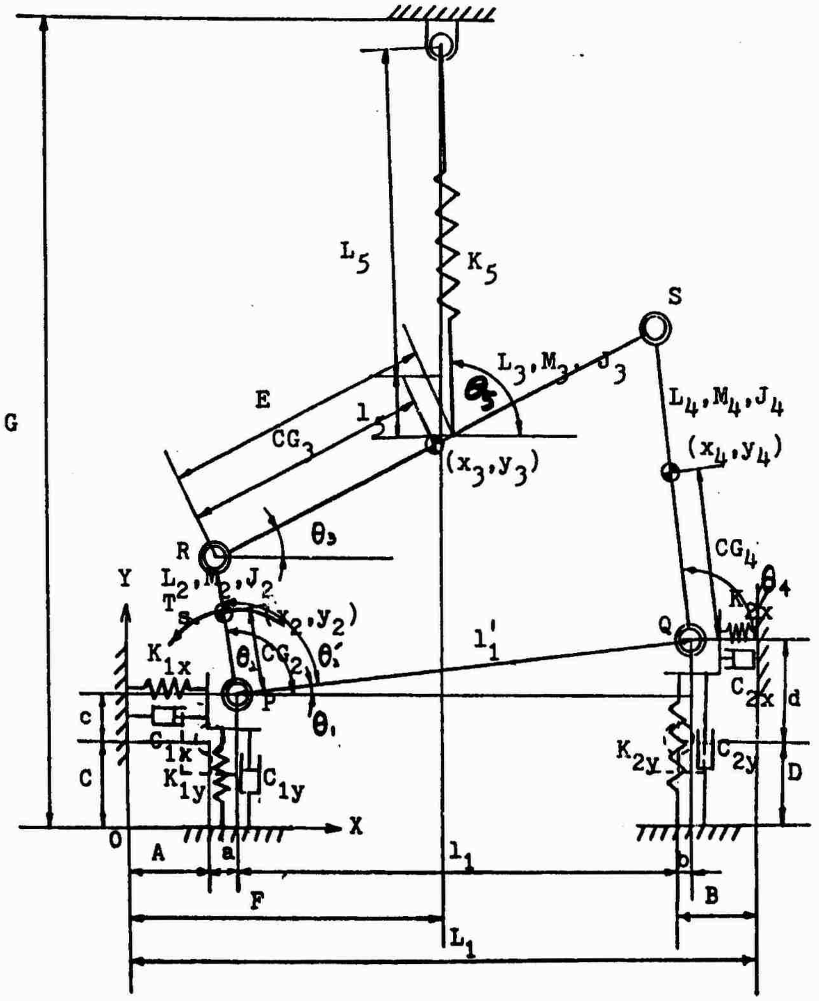

FIGURE 1 - A flexibly supported and synthesized-spring-restrained four-bar mechanical linkage(Model 3)

of the mechanism are rigid with in-line distributed mass. The crank is assumed to be driven by the constant input torque T_s. Gravity loading acts downward on the mechanism and damping is always present during its motion. In this study, the damping torques of the revolute pair bearings (P,Q,R, and S) and the damping forces of the support system (C_{1x}, C_{1y}, C_{2x}, C_{2y},) are assumed to be linearly proportional to their appropriate relative-angular and translational velocities. The forces in the support system springs (K_{1x}, K_{1y}, K_{2x}, K_{2y}) and the restraining-spring (K_5) are also considered to be linearly proportional to the appropriate relative displacements across each spring. A, B, C, and D in Fig. 1 represent the horizontal and vertical clearance distances between the base and the bearings P and Q at their initial static equilibrium state. L_5 is the free length of the restraining spring of stiffness K_5.

FORMULATING THE EQUATIONS OF MOTION

Unlike rotating machinery, machines with floating links are characterized by generalized inertia coefficients which vary continually as the system undergoes changes of configuration. This results in a high-nonlinearity of the governing differential equations of motion for such inertia-variant machines. There are a number of ways to formulate equations of motion for the dynamics of mechanisms, namely:

1. vector methods (Newton's Law)
2. D'Alembert's principle
3. Lagrange's equations with and without multipliers

4. Hamilton's equations
5. virtual work
6. energy methods.

Paul (20) summarized the numerous methods and approaches to solve the general dynamics of mechanisms problem in an excellent review. In this study, the method of Lagrange's form of D'Alembert's principle (20, 21, 22) is used to set up the equations of motion.

KINEMATIC CONSIDERATIONS

Thirteen Lagrangian coordinates ψ_i (variable lengths, variable angles in Fig. 1) can be used to define the configuration of the spring-restrained, flexibly-supported four-bar mechanical linkage. These are:

$$(\psi_1, \psi_2, \psi_3, \psi_4, \psi_5, \psi_6, \psi_7, \psi_8, \psi_9, \psi_{10}, \psi_{11}, \psi_{12}, \psi_{13}) = (l_1, l_1', l_5, a, b, c, \theta_1, \theta_2, \theta_2', \theta_3, \theta_4, \theta_5) \qquad (1)$$

Eight explicit sceleronomic constraint equations can be expressed in terms of the Lagrangian coordinates ψ_i. These length and angle geometry constraints follow from the configuration depicted in Fig. 1. A detailed summary of these constraints can be found in Hong (26).

Since the flexibly supported mechanism is a five degree of freedom system, five of the Lagrangian variables can be selected as primary variable (or generalized coordinates) q_i as per:

$$(q_1, q_2, q_3, q_4, q_5) = (\psi_4, \psi_5, \psi_6, \psi_7, \psi_9) = (a, b, c, d, \theta_2) \qquad (2)$$

The remaining Lagrangian coordinates are considered as the secondary variables ϕ_i. That is,

$$(\phi_1, \phi_2, \phi_3, \phi_4, \phi_5, \phi_6, \phi_7, \phi_8,) = (\psi_1, \psi_2, \psi_3, \psi_8, \psi_{10}, \psi_{11}, \psi_{12}, \psi_{13}) = (l_1, l_1', l_5, \theta_1, \theta_2, \theta_3, \theta_4, \theta_5) \qquad (3)$$

Successive differentiation of the eight constraint equations allows the first and second derivatives of the ϕ_i secondary variables to be expressed in terms of the appropriate first and second derivatives of the primary variables q_j. Similarly, the translational velocities and accelerations of the center of mass of each link as well as the link angular velocities and accelerations can also be defined in terms of the appropriate first and second derivatives of the primary variables. Hong (26) gives detailed derivations of these equations.

DIFFERENTIAL EQUATIONS OF MOTION

The principle of virtual work states that the net work of the active forces and the inertia forces must vanish during any small incremental admissible motion of the system defined by virtual displacements which are consistent with the constraints on the system. Applying this principle to a link i which is acted upon by:

- inertia forces, $-M_i\ddot{x}_i$, and $M_i\ddot{y}_i$, and an inertia torque, $-J\ddot{\theta}_i$.
- active forces X_i, Y_i, and an active torque T_i

and which undergoes virtual displacements $(\delta x_i, \delta y_i, \delta\theta_i)$, yields the Lagrange form of D'Alembert's Principle:

$$\sum_{i=2}^{4} (X_i - M_i\ddot{x}_i)\,\delta x_i + (Y_i - M_i\ddot{y}_i)\,\delta y_i + (T_i - J_i\ddot{\theta}_i)\,\delta\theta_i = 0 \qquad (4)$$

Substituting

$$\delta x_i = \dot{x}_i \delta t, \quad \delta y_i = \dot{y}_i \delta t, \quad \delta\theta_i = \dot{\theta}\delta t \qquad (5)$$

and using the relations between the first and second derivatives of x_i, y_i, θ_i and q_s, $1 \leq s \leq 5$ into equation 4 gives for arbitrary virtual displacements of the variables, $\delta q_s = q_s \delta t$, a set of 5 second order differential equations of motion of the form:

$$\sum_{i=1}^{5} I_{jr}\,\ddot{q}_j = Q_r - \sum_{j=1}^{5} \sum_{k=1}^{5} C_r^{jk}\,\dot{q}_j\,\dot{q}_k$$

in which

$$I_{jr} = \sum_{i=2}^{4} \left[M_i (u_{ij} u_{ir} + v_{ij}\, v_{ir}) + J_i\, \omega_{ij}\, \omega_{ir} \right]$$

$$C_r^{ij} = \sum_{i=2}^{4} \left[M_i (u_k^{ij} u_{ir} + v_k^{ij}\, v_{ir}) + J_i \omega_k^{ij} \omega_{ir} \right]$$

$$Q_r = \sum_{i=2}^{4} \left[X_i u_{ir} + Y_i v_{ir} + T_i \omega_{ir} \right] \qquad (6)$$

Detailed derivations of the terms in Eq (6) can be found in Hong (26).

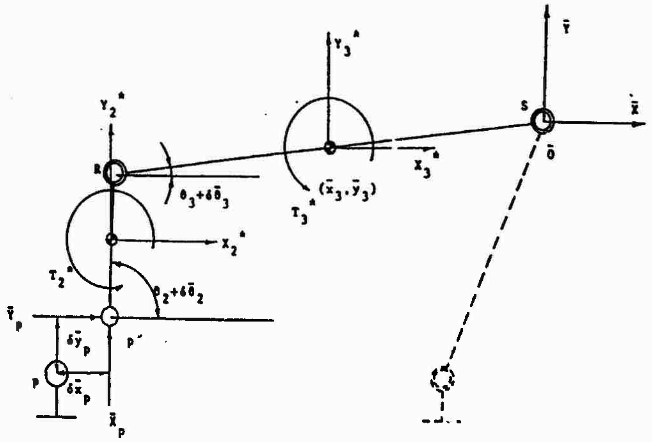

Figure 2 - Internal Reaction Forces at Bearing P

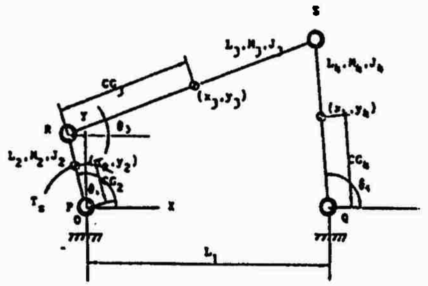

Four-bar mechanical linkage mounted on a rigid body without having any synthesized force device (Model 1)

Fig. 3(a)

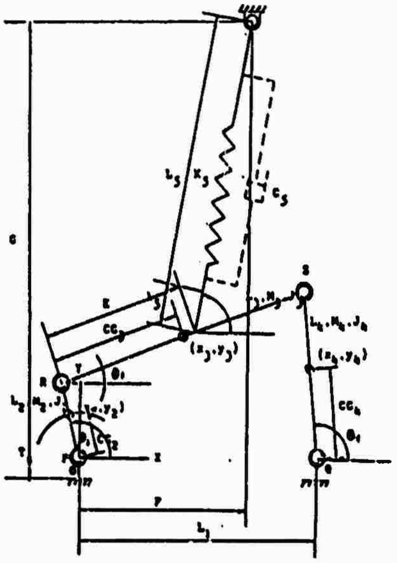

Synthesized-spring-restrained four-bar mechanical linkage mounted on a rigid body (Model 2)

Fig. 3 (b)

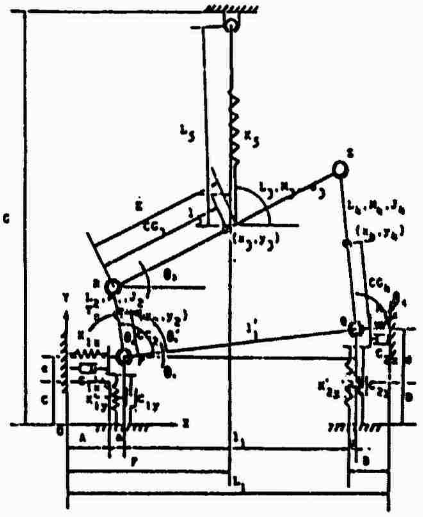

A flexibly supported and synthesized-spring-restrained four-bar mechanical linkage (Model 3)

Fig. 3 (c)

Figure 3 - Three Four-Bar Linkage Models With, Without-Restraining Element And Flexible Support System

Introducing the state vector $(\bar{w}_j)$, $1 \leq j \leq 18$ in accordance with the definition:

$$(q_1, q_2, q_3, q_4, q_5)=(w_1, w_2, w_4, w_5)$$

$$(\dot{q}_1, \dot{q}_2, \dot{q}_3, \dot{q}_4, \dot{q}_5)=(w_6, w_7, w_8, w_9, w_{10})$$

$$(\phi_1, \phi_2, \phi_3, \phi_4, \phi_5, \phi_6, \phi_7, \phi_8) =$$

$$(w_{11}, w_{12}, w_{13}, w_{14}, w_{15}, w_{16}, w_{17}, w_{18}) \tag{7}$$

allows the state vector system of differential equations to be written in explicit form as:

$$\dot{w}_j = w_{5+j} \qquad (j=1,\cdots,5)$$

$$\dot{w}_{5+j} = G_p(w,\ldots\ldots,w_{10}) =$$

$$\left[I_{rj}\right]^{-1}\left[Q_r - \sum_{j=1}^{5} \sum_{k=1}^{5} C_r^{jk} w_{5+j} w_{5+k}\right]$$

$$(j=1,\cdots\cdots,5)$$

$$\dot{w}_{10+1} = \sum_{j=1}^{5} k_{ij} w_{5+j} \qquad (i=1,\cdots\cdots,8) \tag{8}$$

Equations (8) constitute a standard form of a state variable system of differential equations of order 18 as per:

$$\frac{dw_i}{dt} = f_i(w_1, w_2, \ldots, w_{18}, t)$$

$$(i=1, \ldots, 18) \tag{9}$$

Given the initial values

$$w_i(0) = w_{io} \tag{10}$$

then the initial value problem defined by Eqs (9, 10) can be solved numerically using the digital computer.

EVALUATION OF INTERNAL REACTION FORCES AT BEARINGS

The method of virtual work can be applied to find the internal reaction force at each bearing. Here the linkage system in Fig. 1 can be considered as an assemblage of members in "static equilibrium" under the influence of the known effective forces:

$$X_i^* = X_i - m_i\ddot{x}_i$$

$$Y_i^* = Y_i - m_i\ddot{y}_i \qquad (i = 2, 3, 4)$$

$$T_i^* = T_i - J_i\ddot{\theta}_i \tag{11}$$

which are applied at the center of mass of each linkage member. Figure 2 shows these forces (Eq. 11), the two rectangular components $\bar{X}_p$, $\bar{Y}_p$ of the internal force acting at the revolute bearing P and the consistent, necessary virtual displacements x_p, y_p, θ_2, θ_3.

Applying the principle of virtual work to this - hinge pin P', bearing P, and two degree of freedom (θ_2,θ_3) with respect to ($\bar{X}\bar{O}\bar{Y}$) system gives:

$$W = (\bar{X}_p\delta\bar{x}_p+\bar{Y}_p\delta\bar{y}_p)+ X_2^*\delta\bar{x}_2+Y_2^*\delta\bar{y}_2 +$$

$$T_2^*\delta\bar{\theta}_2+X_3^*\delta\bar{x}_3+Y_3^*\delta\bar{y}_3+T_3^*\delta\theta_3 = 0 \tag{12}$$

Substituting the virtual displacement relations

$$\delta x_t = a_{t2}\,\delta\theta_2 + a_{t3}\,\delta\theta_3$$

$$\delta y_t = b_{t2}\,\delta\theta + b_{t3}\,\delta\theta_3 \tag{13}$$

in which,

$$t = p, 2, 3$$

into Eq. (12) yields for arbitrary (θ_2, θ_3), equations of the form

$$\bar{a}_{p2}\bar{X}_p+\bar{b}_{p2}\bar{Y}_p= -T_2^*-X_2^*\bar{a}_{22}-Y_2^*b_{22}-X_3^*\bar{a}_{32}-Y_3^*\bar{b}_{32}$$

$$\bar{a}_{p3}\bar{X}_p+\bar{b}_{p3}\bar{Y}_p= -T_3^*-X_2^*\bar{a}_{23}-Y_2^*\bar{b}_{23}-X_3^*\bar{a}_{33}-Y_3^*\bar{b}_{33} \tag{14}$$

which can be easily solved for the internal reaction $\bar{X}_p$, $\bar{Y}_p$.

This procedure can be repeated to find the rectangular force components $\bar{X}_t$, $\bar{Y}_t$ at bearings t=Q,R,S. Detailed derivations and computer implementations of these results are given in Refs (26,27), respectively.

MODEL VALIDATION WORK

Figures 3 a-c depict the three different mechanical linkage systems considered in conjunction with the flexibly-supported, spring-restrained four-bar linkage design studies reported herein. These three linkage systems can be described as follows

(1) Four-bar linkage, rigidly mounted without restraining spring (Model 1)
(2) Four-bar linkage, rigidly supported with restraining spring (and damper) (Model 2)
(3) Four-bar linkage, flexibly supported with restraining spring (and damper) (Model 3).

TABLE I. THE KINEMATIC AND DYNAMIC PARAMETERS OF MODELS 1, 2, AND 3

		Model 1	Model 2	Model 3
Length (m)	L_1	0.280	0.280	0.300
	L_2	0.087	0.087	0.087
	L_3	0.308	0.308	0.308
	L_4	0.183	0.183	0.183
	$L_5(T)^*$		0.300	0.300
	$L_5(T\text{-}C)$		0.400	0.400
	$L_5(C)$		0.500	0.500
Mass (Kg)	M_2	0.680	0.680	0.680
	M_3	1.150	1.150	1.150
	M_4	1.040	1.040	1.040
Mass moment of inertia** (Kgm^2)	J_2	0.0027	0.0027	0.0027
	J_3	0.017	0.017	0.017
	J_4	0.015	0.015	0.015
Center of gravity (m)	CO_2	0.049	0.049	0.049
	CO_3	0.154	0.154	0.154
	CO_4	0.099	0.099	0.099
Viscous damping coefficient of revolute bearings (Nsec/m)	C_p	0.100	0.100	0.100
	C_q	0.100	0.100	0.100
	C_r	0.100	0.100	0.100
	C_s	0.100	0.100	0.100
Design parameters (m)≠, #	A			0.010
	B			0.010
	C			0.010
	D			0.010
	E		0.165	0.165
	F		0.200	0.200
	G		0.483	0.483

*T: tension T-C: tension-compression C: compression

**with respect to the center of mass of each link

Desired motion : constant shaft angular speed of 11 rad/sec

Input torque ; 2.64 Nm

Initial conditions

a,b,c,d = 0 m ; $\dot{a},\dot{b},\dot{c},\dot{d}$ = 0 m/sec

θ_2 = 90 degree ; $\dot{\theta}_2$ = 0 rad/sec

≠A,B,C,D = x,y direction support clearances

#E = Restraining spring attachment point distance along connecting link from point R (input crank, connecting link).

F,G = x,y location of restraining spring fixed point P (support, input crank).

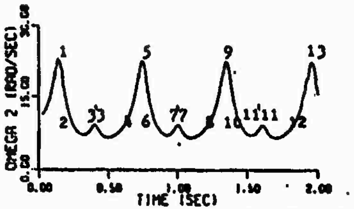

Model 1 (No synthesized spring, rigid support)

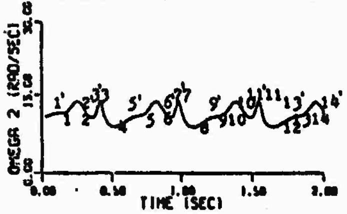

Model 2 (Synthesized spring, rigid support)

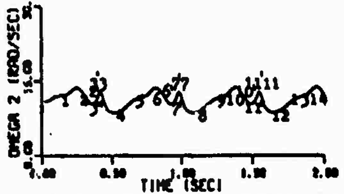

Model 3 (Synthesized spring, flexible support)

Figure 4 - Comparison of angular velocities of input crank shaft of Model 1,2 and 3

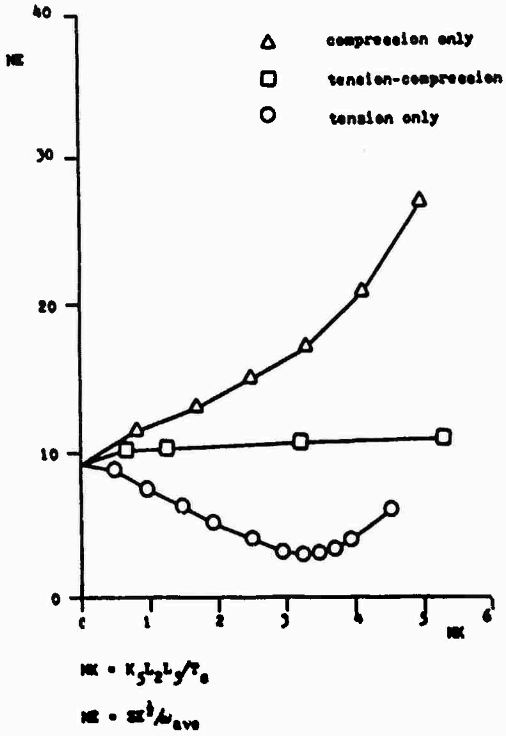

Figure 5 - Comparson of the performance of three types of synthesized springs

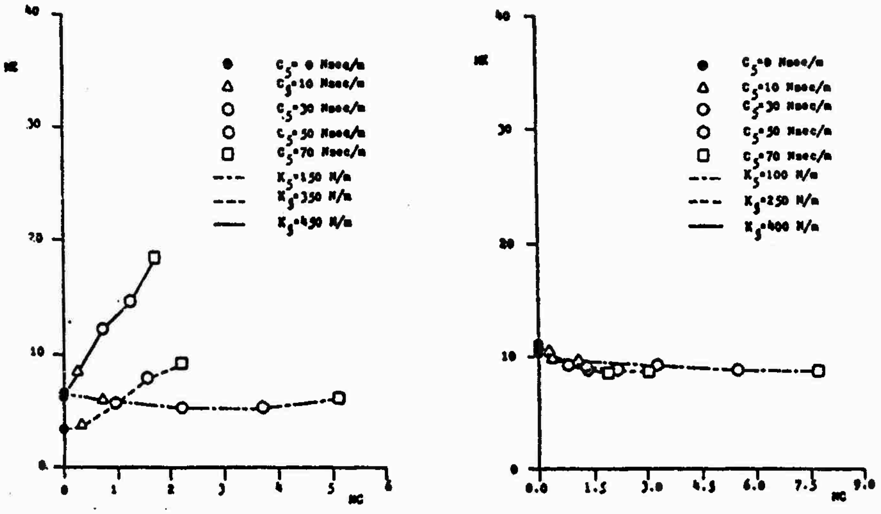

(a) Performance characteristic of damper synthesis with tension spring

(b) Performance characteristic of damper synthesis with compression-tension spring

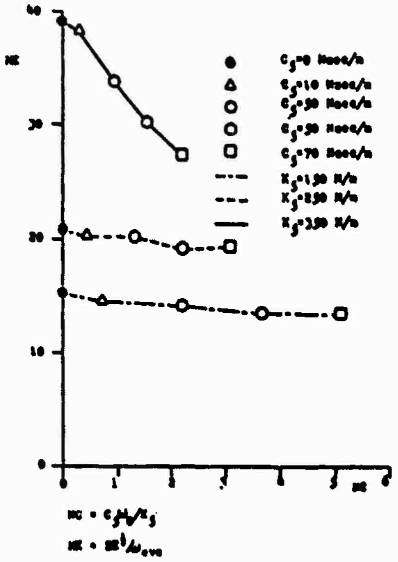

(c) Performance characteristic of damper synthesis with compression spring

FIGURE 6 IMPACT OF LINEAR DAMPING IN PARALLEL WITH RESTRAINING SPRING FORCE ELEMENT ON ANGULAR SPEED FLUCTUATION PERFORMANCE INDICE NE

The measured data results from the experimental work of Tacheny, Erdman, and Hagen (16) were used to validate the spring-restrained four-bar linkage models (a) With rigid support (Model 2 above) and (b) With flexible support (Model 3 above). Here the initial conditions for the four-bar linkage systems were "identified or backed-out" from the experimental conditions described in this reference (16). Then the state vector system of equations was solved in the time domain using single and double precision software implementations (IMSL and the authors' Runge-Kutta-Fehlberg 4-5th order (TRKF45)) of numerical integration prcedures. The authors' TRKF45 numerical integration software gave superior results and because of the greater flexibility it afforded was used for the design studies work. Frequency responses of the shaft angular velocities, etc. were also obtained using the Fast Fourier Transform (authors' FFT32 software package) of the time domain results. All computer program simulations (Models 1-3, etc.) were written in FORTRAN 77 and performed on an IBM 3033. Hong and McLauchlan (27) give complete listings and documentation for these software packages.

The solution results for MODEL 2 were found to be in excellent agreement with the dynamics response results given in Tacheny et al (16) and also in references (13,23). The spring-restrained, flexibly-supported four-bar mechanical linkage (Model 3) results were also compared with the results of the other two. Indeed, a consistency check was run using restraining spring of stiffness approaching zero and flexible support stiffness approaching infinity. Here the shaft speed and internal reaction force, etc. results were found to approach the corresponding results for the rigidly-supported, four-bar linkage with-and without- the restraining spring element.

RESTRAINING-ELEMENT, SUPPORT-SYSTEM DESIGN STUDIES

Table I summarizes the kinematic and dynamic parameters used for Models 1,2 and 3 of Figure 3. These parameters define the four-bar linkage plus the restraining force element and flexible support system-cases considered in the design study work discussed in this section of the paper. These cases examine the impact of the

(a) Restraining force-passive element spring (with, without damper) attached to the connecting link
(b) Flexible support, vibration isolation system upon the
(1) Shaft angular speed variation over time
(2) Internal pin-connection reaction force magnitudes
(3) Forces transmitted to the base of the linkage mechanism.

Figure 4 shows typical input shaft, angular speed results for Models 1,2, and 3. Here a maintenance torque of 2.64 Nm (see Table I) was found which is sufficient to overcome the linear viscous damping torques at bearings P,Q,R,S and drive the input crank at a nominal angular speed $\dot{\theta}=11$ Rad/sec. These results show the significant improvement in reducing the input shaft angular speed over time, which is possible with the synthesized, i.e., optimally-selected, restraining spring element. Detailed comparison of the angular speed results for Models 2 and 3 indicate that the behavior over time may be altered only slightly. The peak-to-valley fluctuations also show minimal if any increase with the change from rigid support (Model 2) to the flexible support system (Model 3).

Figure 5 presents results for the input shaft, angular speed fluctuation performance indice number (NE=($SE^{1/2}$/[illegible]AVE) as a function the restraining-spring stiffness number (NK=$K_5L_2L_5/T_5$). Here the type or regime of spring force behavior (a) tension only, (b) tension-compression, or (c) compression only is parameter. These results indicate that the tension restraining spring elements produce angular speed fluctuation results which

- Have a well defined minimum
- Are clearly superior to those for compression only and tension-compression springs.

The impact of passive linear damping in parallel with the linear restraining spring force element (see Figure 1) is shown in Figures 6 a-c. Here the normalized angular speed fluctuation performance indice NE is plotted as a function of the damping number (NC= C_5[illegible]AVE/K_5 for a range of (a) tension only, (b) tension-compression, or (c) compression only restraining spring stiffness values. The results plotted in Figures 6 a-c indicate that adding a damper in parallel with a restraining spring:

(a) Degrades tension spring element, angular speed fluctuation performance. That is, the performance indice number NE can be greatly increased with increasing damping at equal to or greater than the optimum stiffness number values (Fig. 6a). Very little improvement obtains with increasing damping at somewhat less than the optimum tension-only

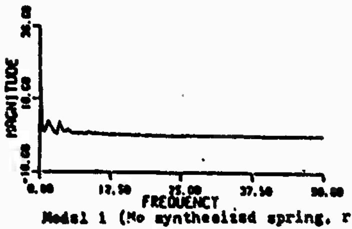

Model 1 (No synthesized spring, rigid supports)

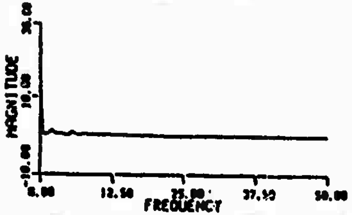

Model 2 (Synthesized spring, rigid supports)

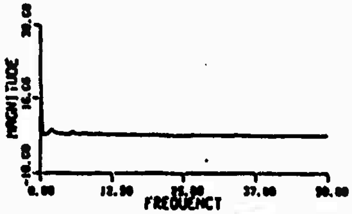

Model 3 (Synthesized spring, flexible supports)

Figure 7 - Comparison of the frequency responses of input shaft angular velocity of Models 1,2 and 3

TABLE 2 SUMMARY OF MAXIMUM FORCE MAGNITUDE (N) AT EACH PIN CONNECTION BEARING AS WELL AS THE FORCE TRANSMITTED TO THE BASE OF THE MECHANISM

	MODEL 1 RIGID SUPPORT NO RESTRAINING SPRING	MODEL 2 RIGID SUPPORT WITH OPTIMAL RESTRAINING SPRING	MODEL 3 FLEXIBLE SUPPORT WITH OPTIMAL RESTRAINING SPRING
BEARING P (SUPPORT, INPUT CRANK)	11192.3	2139.4	144.1
BEARING Q (SUPPORT, OUTPUT CRANK)	38.2	49.8	39.1
BEARING R (INPUT CRANK, CONNECTING LINK)	83.1	82.5	67.2
BEARING S (OUTPUT CRANK, CONNECTING LINK)	11120.7	2112.9	148.2
TRANSMITTED FORCE MEASURE	11202.8	2173.5	175.1

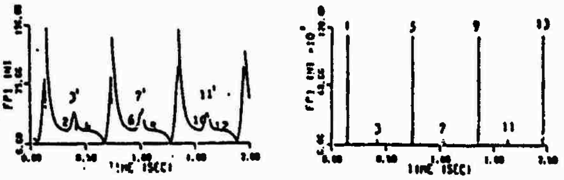

Model 1 (No synthesized spring, rigid supports)

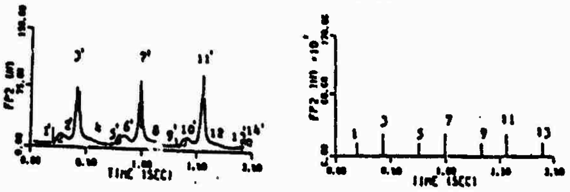

Model 2 (Synthesized spring, rigid supports)

Model 3 (Synthesized spring, flexible supports)

Figure 8 - Comparison of internal reaction forces at bearing P

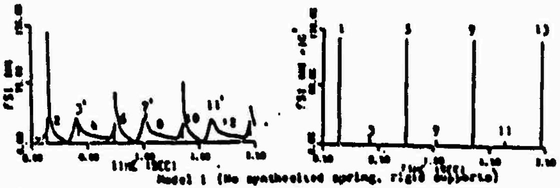

Model 1 (No synthesized spring, rigid supports)

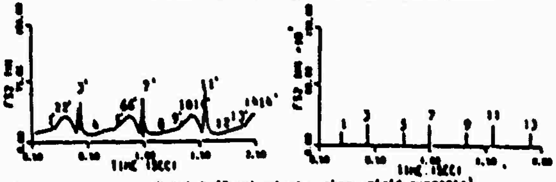

Model 2 (Synthesized spring, rigid supports)

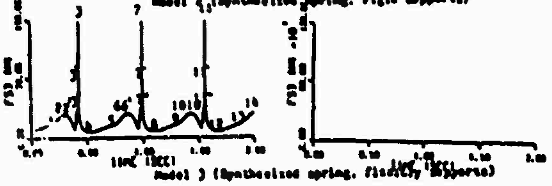

Model 3 (Synthesized spring, flexible supports)

Figure 9 - Comparison of internal reaction forces at bearing S

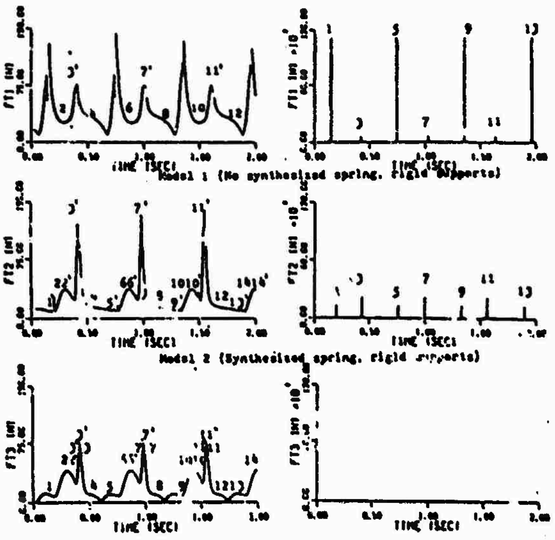

Figure 10 - Model 3 (Synthesized spring, flexible supports)

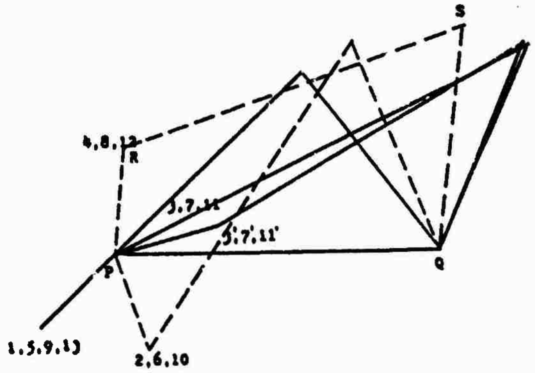

Figure 11(a) - Linkage configuration of Model 1 at each of the corresponding numbers

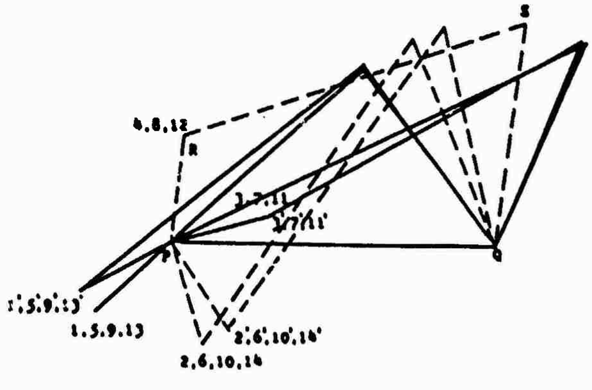

Figure 11(b) - Linkage configuration of Model 2 at each of the corresponding numbers

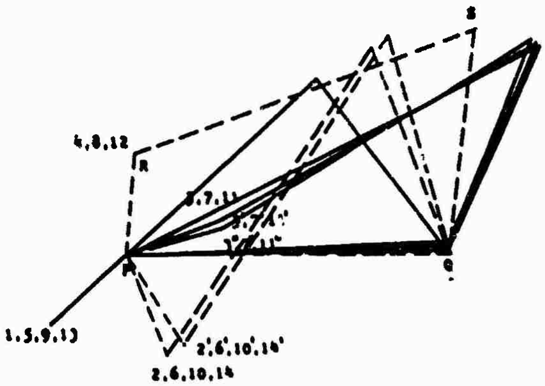

Figure 11(c) - Linkage configuration of Model 3 at each of the corresponding numbers stiffness number values.

(b) Can improve compression spring element, angular speed fluctuation performance. Examination of Figures 5, 6c indicates however, that the values of NE are, at best, for realizable damper values, somewhat greter than the best obtainable with the tension-only spring.

(c) Has little effect on tension-compression spring element, angular speed fluctuation behavior. Figure 6b shows that the performance indice NE is reduced only slightly with increasing damping.

Figure 7 shows the Fast Fourier Transforms (FFT's) of the angular speed fluctuation results shown in Figure 4 for Models 1,2,3. These results show that the nominal angular speed value (11 Rad/sec) is the peak "bias" or fundamental value as a function of frequency. The time-domain fluctuations shown in Figure 4 are the higher frequency amplitude components in Figure 7. These higher frequency components define the magnitude of the angular speed fluctuation $(SE)^{\frac{1}{2}}$ considered in the definition of the dimensionless performance indice number NE. Comparing Figure 7a with Figures 7b,7c shows the reductions possible in the higher frequency - angular speed fluctuation components possible with the optimal tension-only restraining spring system.

Typical pin connection reaction (i.e., bearing force magnitudes are shown in Figures 8,9 for three systems (Models 1-3) depicted in Figure 3. These time domain results are for bearings P,S at which the maximum peak reaction forces occur. Figure 10 gives a corresponding set of results comparing the forces transmitted to the base of the mechanism with Models 1-3 as functions of time.

The time points labelled (1,5,9,13) in these figures at which the largest or primary peak magnitudes occur for Model 1 (rigid support with no restraining spring) correspond to the linkage positions (1,5,9,13) depicted in Figure 11. The secondary or lesser maximum time points (3,7,11) for Model 1 are also indicated in Figure 11. Similarly the relative minima over time points (2,6,10) and (4,8,12) in Figures (8-10) are shown in Figure 11.

Examination of the force magnitude plots in Figures 8-10 in conjunction with the linkage configurations depicted in Figure 11 indicates that

(1) Primary maximum force magnitude values occur when the input crank and connecting link are in-line and their angular velocities have the same sign (CCW). Here the output crank position is at its maximum CCW or positive value.

(2) Secondary maximum force magnitude values occur when the input crank and connecting link are in-line (or nearly so) but their angular velocities have differing signs (input crank CCW, connecting link CW). Here the output crank position is at its minimum CW or negative value.

(3) Significant reductions are possible in the internal reaction forces on the pin connection bearings and the forces transmitted to the base of the mechanism-with the use of flexible vibration isolation support systems along with restraining spring elements.

Table 2 summarizes the maximum force magnitude at each pin bearing as well as the force transmitted to the base of the mechanism. Examination of Table 2 indicates that

(a) Peak bearing forces at worst-case bearings P,S can be reduced by nominal factors of 14.3 and 75.0, respectively (Model 3 versus Model 2 - 14.3 and Model 3 versus Model 1 - 75.0).

(b) Peak forces transmitted to the base of the mechanism can be reduced by factors of 12.4 and 64.0, respectively (Model 3 versus Model 2 - 12.4, and Model 3 versus Model 1 - 64.0).

Overall consideration of the angular velocity fluctuation results (Figure 4) with the force magnitude results (Figures 8-10 and Table 2) indicates that the force magnitude reduction discussed above can be obtained with little increase in the minimal fluctuation of input crank shaft speed. This minimal input crank shaft speed fluctuation is that obtained with the restraining-spring, rigidly-supported four-bar linkage system.

CONCLUSIONS

Linear restraining spring potential energy storage elements and flexible vibration isolator support systems have been investigated as passive devices to control the highly-nonlinear motion of a planar four-bar mechanical linkage. This investigation was based upon the numerical solution in the time domain of the state vector equation for the four-bar mechanical linkage system. The state-vector equation was developed using Lagrange's form of D'Alembert's principle.

Three different linkage systems were considered as follows

(1) Four-bar linkage, rigidly mounted without restraining spring (Model 1)
(2) Four-bar linkage, rigidly supported with restraining spring (and damper) (Model 2)
(3) Four-bar linkage, flexibly-supported with restraining spring (and damper) (Model 3).

Frequency responses of the shaft angular velocities, etc. were also obtained using the Fast Fourier Transform of the time domain results. All computer program simulations were written in FORTRAN 77 and performed on an IBM 3033. They were also checked out against previously published experimental results.

Specific design/performance indices considered for the spring-restrained, flexibly-supported linkage were

(1) Shaft angular speed variation over time
(2) Internal reaction force magnitudes
(3) Forces transmitted to the base of the linkage mechanism.

For the three four-bar linkage systems considered, the design study results indicate the following:

(1) Tension restraining spring elements produce angular speed fluctuation results (with a well defined minimum) which are superior to those for compression springs.
(2) Adding a damper in parallel with a restraining spring element:
    (a) Degrades tension spring element, angular speed fluctuation performance.
    (b) Can improve compression spring element, angular speed fluctuation performance, which at best is, for realizable damper values, less than that with the tension spring.
    (c) Has little effect on tension-compression spring element, angular speed fluctuation performance behavior.
(3) The use of flexible vibration isolator support systems <u>along with</u> restraining spring elements can considerably reduce the internal reaction forces on the pin connection bearings and the forces transmitted to the base of the mechanism. As for example, the peak forces transmitted to the base of the mechanism can be reduced by factors of 12.4 and 64.0, respectively (Model 3 versus Model 2-12.4, and Model 3 vesus Model 1 64.0).
(4) The force magnitude reductions in (3) can be obtained with little increase in the minimal fluctuation of input crank shaft speed, which is obtained for the restraining-spring, rigidly-supported four-bar linkage system.

RECOMMENDATIONS

Recommendations for further work based upon the results reported in this paper are as follows:

(1) Force magnitude and angular speed fluctuation behavior for more diverse linkage congurations should be investigated by altering the link lengths, masses, mass moments of inertia, etc. Here the application to an overall mechanical linkage as, e.g., slider crank mechanism or six-bar mechanical linkage aspects for cutting, shearing or punching operations, can be investigated. This work can include the effect of system excitation via the support frame.
(2) Optimization techniques, such as the steepest descent or the Box-Jenkins random search methods, should be applied to search the design space for the optimal robust design parameters, i.e., the best spring constants and/or damper coefficients as well as their best placements. Such optimal design work should also concentrate on different design or performance indices and constraint-problem structures. Examples here could be minimum speed fluctuation subject to constraints on pin and foundation interaction force magnitudes.
(3) Flexible link member characteristics should be included for high speed and low mass/volume mechanical linkages. This is because mechanisms designed using the assumption of rigid link members may not operate properly at higher speeds because of elastic deformations of the links, resonances in the linkage, etc. The problem of elastic effects on the dynamic response behavior of link members may be solved by utilizing extended finite-element or finite-difference techniques.
(4) Active force control should be considered to define optimal time domain, etc. shock reduction and vibration performance for the mechanical linkage

systems. Best realizations of the optimal control in terms of actual passive or perhaps semi-active elements can then be obtained.

(5) The feedback control of input shaft torque, etc. should be investigated to track the desired motion of output shaft angular velocity, etc. That is, to see if this can be done while minimizing or constraining peak input shaft torque.

REFERENCES

(1) Berkof, R.S., "Complete Force and Moment Balancing of In-Line Four-Bar Linkage," Mechanism and Machine Theory, 1973, Vol. 8, pp. 397-410.

(2) Berkof, R.S., Lowen, G.G., and Tepper, F.R., "Balancing of Linkages," The Shock and Vibration Digest, Vol. 9, No. 6, 1977, pp. 3-10.

(3) Lowen, G.G., Tepper, F.R., and Berkof, R.S., "The Quantitative Influence of Complete Force Balancing on the Forces and Moments of Certain Families of Four-Bar Linkage," Mechanism and Machine Theory, Vol. 9, 1974, pp. 299-323.

(4) Ogawa, K., and Funabashi, H., "On the Balancing of the Fluctuating Input Torques Caused by Inertia Force in the Crank-Rocker Mechanisms," ASME Journal of Engineering for Industry, Vol. 91, No. 1. Feb. 1969, pp. 97-102.

(5) Hockey, B.A., "The Minimization of the Fluctuation of Input-Shaft Torque in Plane Mechanism," Mechanism and Machine Theory, Vol. 7, 1972, pp. 335-346.

(6) Berkof, R.S., "The Input Torque in Linkages," Mechanism and Machine Theory, Vol. 14, 1979, pp. 61-73.

(7) Elliot, J.L., and Tesar, D., "The Theory of Torque, Shaking Force and Shaking Moment Balancing of Four Link Mechanisms," ASME Journal of Engineering for Industry, Vol. 99, No. 3, Aug. 1977, pp. 715-722.

(8) Lee, T.W., and Cheng, C., "Optimum Balancing of Combined Shaking Force, Shaking Moment, and Torque Fluctuation in High-Speed Linkages," ASME Journal of Mechanisms, Transmissions, and Automation in Design, Vol. 106, June, 1984, pp. 242-250.

(9) Mahig, J., "Minimization of Mechanism Oscillations Through Flywheel Tuning," ASME Journal of Engineering for Industry, Vol. 93, No. 1, Feb. 1971, pp. 120-124.

(10) Genova, P.I., "Synthesis of Spring Equivalent to Flywheel for Minimal Coefficient of Fluctuation," ASME paper 68-MECH-65.

(11) Benedict, C.E., and Tesar, D., "Optimal Torque Balance for Complex Stamping and Indexing Machine, ASME paper 70-MECH-82.

(12) Halter, J.M., "Force Synthesis to Produce a Desired Time Response of Mechanisms," Ph.D. Dissertation, University of Missouri-Columbia, May 1975.

(13) Halter, J.M., and Carson, W.L., "Mechanism-Force System Synthesis to Obtain a desired Motion-Time Response," Proceedings of the Fourth World Congress on the Theory of Machines and Mechanisms, Newcastle Upon Tyne, England, Sept. 1975.

(14) Carson, W.L., "How To Do It Computer Programs for Force System Synthesis," Linkage Design Monographs, 1975, pp. 73.1-73.6.

(15) Carson, W.L., "Example Applications Illustrating the Depth of Mechanism-Force System Synthesis for a Desired Motion-Time Response and/or Input-Output Forces, and Survey of Design Technique," Linkage Design Monographs, 1975, pp. 71.1-71.7.

(16) Tacheny, J.C., Erdman, A.G., and Hagen, D.L., "Experimental Determination of Mechanism Time Response," Proceedings of the Fifth World Congress on Theory of Machines and Mechanisms, 1979, pp. 130-133.

(17) Allen, R.P., "Dynamics of Mechanisms, and Machine Systems in Accelerating Reference Frames," ASME Journal of Dynamic Systems, Measurements, and Control, Vol. 103, December, 1981, pp. 395-403.

(18) Van Sickle, R.C., and Goodman, T.P., "Spring Actuated Linkage Analysis to Increase Speed," Product Engineering, July, 1953, pp. 152-157.

(19) Bishop, R.E., and Wilson, C.C., "Dynamic Control of Spring-Driven Mechanisms," IBM Journal of Research and Development, Vol. 16, No. 3, May, 1972, pp. 222-230.

(20) Paul, B., "Analytical Dynamics of Mechanisms - A Computer Oriented Overview," Mechanisms and Machine Theory, 1975, Vol. 10, pp. 481-507.

(21) Paul, B., and Krajcinovic, D., "Computer Analysis of Machines With Planar Motion, Part 1 - Kinematics," ASME Journal of Applied Mechanics, September, 1970, pp. 697-702.

(22) Paul, B., and Krajcinovic, D., Computer Analysis of Machines With Planar Motion, Part 2 - Dynamics," ASME Journal of Applied Mechanics, September, 1970, pp. 703-712.

(23) Erdman, A.G., and Sandor, G.N.,

Mechanism Design: Analysis and Synthesis, Vol. 1, Prentice-Hall, Inc., 1984, pp. 75-82.

(24) Bagci, C., "Dynamic Motion Analysis of Plane Mechanisms With Coulmb and Viscous Damping via the Joint Force Analysis," ASME Journal of Engineering for Industry, May 1975, pp. 551-560.

(25) Meirovitch, Leonard, Methods of Analytical Dynamics, McGraw-Hill, Inc., 1970, pp. 59-64.

(26) Hong, Seung Ho, "Dynamic Analysis of Flexibly-Supported, Four-Bar Mechanical Linkage, "M.S. Thesis, Department of Mechanical Engineering, Texas Tech University, Lubbock, Texas, May 1985.

(27) Hong, Seung Ho and McLauchlan, R.A., "Users' Manual for MLNSRS (Rigidly-Supported, Four-Bar Mechanical Linkage), MLSSRS (Spring-Restrained, Rigidly-Supported, Four-Bar Mechanical Linkage) and MLSSFS (Spring-Restrained, Flexibly-Supported, Four-Bar Mechanical Linkage," Department of Mechanical Engineering, Texas Tech University.

APPENDIX

Comment regarding Eq.(1) in the text: Note that although θ_2' is included in the Lagrange variables($\phi i, 1 \le i \le 13$) given in Eq.(1), it is redundant since $\theta_2' = \theta_2 - \theta_1$ (see Figure 1). θ_2' was, however, taken as a primary variable (or generalized coordinate)($q_i, 1 \le i \le 5$) for convenience. θ, θ_2- also in the set of Lagrange variables- were both taken as secondary variables ($\phi i, 1 \le i \le 8$) and carried through in the analysis. This was done both for design usage convenience and insight, as well as for a consistency check on the analytical/computer model results.

Discussion

Mr. Eshleman (Vibration Institute): Is the software available, or is it in the thesis?

Mr. McLauchlan: It is in the thesis, but it is stored on tape. There is a user's manual that goes with it. Right now, the tapes are on Wilbur-formatted tape, an IBM computer arrangement, so I need to translate them to the ASCII format. But once that is done, the software will be available. Incomplete listings of the program are also available.

Mr. Eshleman: It seems it would have many applications. Did you rule out zones of instability? If you lined the springs up right, could you get an instability?

Mr. McLauchlan: That has to do with the stiffness and with the A, B, C, D, X, and Y clearance parameters. Yes, that has to be done. So, that is also an important design aspect. That is something the dynamic portion and the initial condition portion, which I did not really talk about, can do for you in terms of actual design. That is an important aspect.

Mr. Eshleman: I could see where you would want to have an inertia and maybe an elastic connection on your driving torque. Have you thought about including that in the future?

Mr. McLauchlan: Yes.

BLADE DAMPING MEASUREMENTS IN A SPIN RIG WITH NOZZLE PASSING EXCITATION SIMULATED BY ELECTROMAGNETS

J.S. Rao
Science Counsellor
Embassy of India
Washington, D.C.

K. Gupta
Assistant Professor

and

N. Vyas

Research Scholar
Department of Mechanical Engineering
Indian Institute of Technology
New Delhi-110016, INDIA

This paper is concerned with experimental determination of overall damping in a rotating turbine disc-blade system. A test spin rig has been designed and fabricated. Nozzle Passing Excitation is simulated by electromagnets. Transient excitation of rotating blades is caused by suddenly shutting off the excitation to the rotating blades. Frequency analysis of the transient blade response gives the necesary information about the modal damping in several modes. The variation of modal damping with the speed of rotation and strain amplitude is obtained.

INTRODUCTION

Blade damping is an important parameter in the fatigue design of blades. The main damping mechanisms are the interfacial damping at the root, material damping and the gas dynamic damping. The possible contributions from these mechanisms are infinitely variable and therefore difficult to predict and test. Some of the early investigations in the estimation of blade damping are by Shannon [1]. Hansen et al. [2] described a rotating test rig for estimating turbine and compressor blade damping properties. They used half power method for determining the overall damping. Material and aerodynamic damping were determined both by theoretical and experimental means. Root damping was obtained both by theoretical and experimental means. Root damping was obtained by subtracting the aerodynamic and material damping effects from the overall damping. Goodman and Klumpp [3] investigated certain slip damping properties of rivetted sandwich beams. Grady [4,5] tested several dummy IP blades in disc attachments using a pull-test machine and used a dynamic shaker to excite the blades to specific force levels. Wagner [6] conducted a program of damping tests on rotating steam turbine blade groups in a test-turbine using axially directed water jets for impulse excitation.Jones and Muszynska [7-10] made a series of theoretical and experimental investigations on damping. They developed a simple two mass analytical model to represent the vibrational behaviour of a jet-engine compressor blade in its fundamental mode allowing for slip at the blade attachment interface. Some more recent investigations are given in references (11-13). State-of-art papers by Rao [14], Rieger [15] and Srinivasan [16] can be referred for a detailed review.

The investigations [3-13] have broadly shown that the blade damping coefficient decreases with increase in centrifugal load and increases almost linearly with the blade tip displacement.

In the present work the modal damping values in first four modes of a rotating turbine blade with a T root are determined experimentally and their variation with speed of rotation and strain amplitude is established.

THE TEST RIG

The rig shown in Fig.1 and P.1 essentially consists of a disc with two blades, mounted on an overhung rotor supported on two journal bearings and run by a 30 KW thyristor controlled motor. The disc is run in vacuum to reduce the motor torque and remove the effects of air resistance and thus the aerodynamic damping. The disc material is 28CrMoNi V49V steel. The rotorshaft made out of AISI 4340 steel (40NiCrMoI) carries a shrunk weight to balance the overhung disc. Multi-surface, non-circular journal bearings (Sartorious, Germany) are used. Oil is supplied to the bearings by a 0.5 HP pump through paper filters.

The blades made of 40Ni3 steel are tapered, twisted, having an asymmetric aerofoil cross-section, with a T-root. The disc carries corresponding slots in which the blades are assembled with two spacers on each side and two segments. Figs. 2 to 4 and P2 show the relevant features of the blade assembly on the disc. The two blades are fixed diagonally opposite to each other for reasons of balancing. Fig. 5 depicts the blade cross-sections at different points along the blade length.

Nozzle passing excitation of the blade is simulated by providing electromagnets around the periphery of the outer plate of the vacuum chamber.Twelve electromagnets oriented and placed at equiangular locations,(See P.2 and P.3) are connected in parallel and energised by a 12 V D.C. source, the overall current being monitored through a rheostat and an ammeter. During the rotation of the disc, the electromagnets cause excitation forces on the blade periodic with nozzle passing frequency, which in this case is equal to number of magnets times the angular frequency of the rotating disc. The electromagnets give a distributed excitation along the length of the blade.

INSTRUMENTATION

The instrumentation, see Fig. 6 and P.4 , employed for the measurement of damping values, includes a tri-axial set of semi-conductor strain gauges (at 120° angles) fixed at a point on the blade near its root. The lead wires from the strain gauges are taken to the slip-ring through a hollow shaft which holds the disc on one end and supports the slip ring on the other. The slip-ring unit (from IDM, England),with twelve channels has electrodeposited silver rings and two brushes per ring made of silver graphite and is designed to pass small signals with minimum noise and error. Using dummy strain gauges, half-bridges are formed with each of the gauges in the tri-axial set. The signals are taken through a four channel amplifying bridge (Vishay Model 2300) and recorded on a tape recorder (Racal-7). The rotational speed was measured by a photosensitive pick-up.

DAMPING MEASUREMENT

For the measurement of modal damping, the rotor is run at a constant speed with the electromagnetic excitation on. At an instant of time, the electromagnetic excitation is suddenly switched off, so that the transients are set up in the blade. The entire process of the initiation and decay of transient response of the blade caused due to shutting-off the magnetic excitation, is recorded through one of the strain gauges (G1) of the tri-axial set. The recording is repeated for several rotor speeds. From the decaying part of the recorded overall signal (P.5), the response for a particular blade natural mode is filtered through a tunable filter (with minimum available band width of 6.5%) and played on a dual trace oscilloscope, Fig. 7. The instant of the initiation and decay of the transient is caught and frozen on the screen. P.5 shows a typical overall signal on a highly compressed time-base. P.6 to P.9 show the filtered signals obtained for the first four blade natural modes. P.10 shows a typical decaying signal on an enalrged time base.

The transient vibratory response signals were obtained for the first four blade natural modes for rotor speeds upto 1000 rpm. The equivalent viscous damping values are determined for different amplitude values, cycle by cycle, for decaying part of each signal, using the formula

$$\delta = \frac{2\pi\zeta}{\sqrt{1-\zeta^2}} = \ln \frac{x_1}{x_2}$$

where x_1 and x_2 are successive strain amplitudes on a decaying signal (see P.6 to P.10). Modal damping ratios ζ thus obtained as functions of strain amplitude (x_1) at different rotor speeds are plotted for the first four modes in Figs. 8 to 11. Fig. 12 shows the

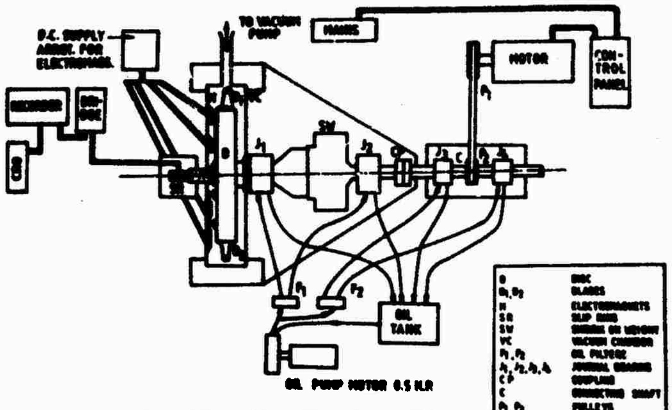

Fig 1 SCHEMATIC LAYOUT OF THE SYSTEM

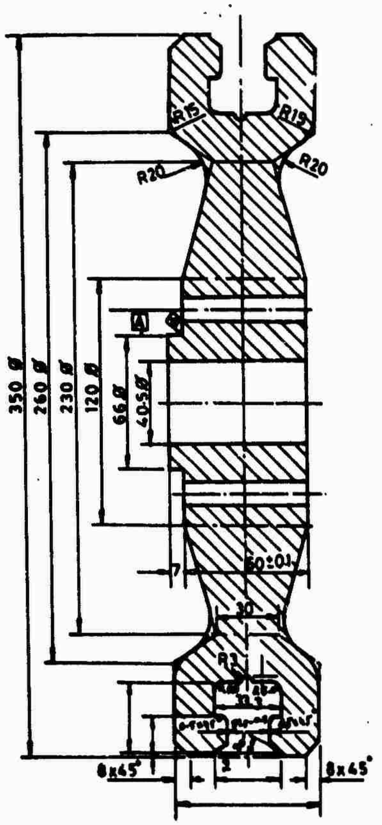

Fig. 2 THE DISC

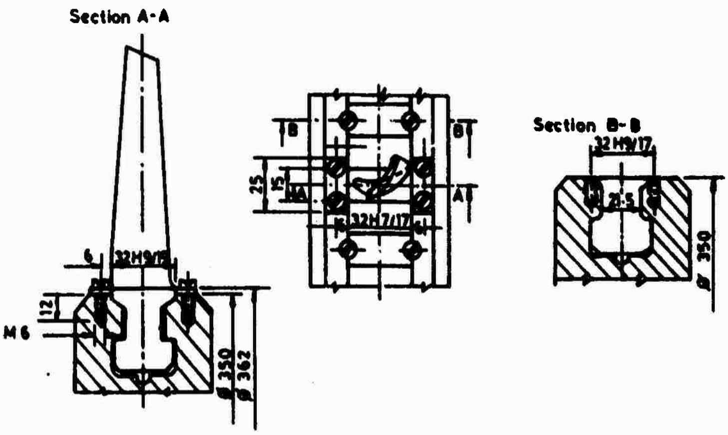

Fig. 4 THE BLADE ASSEMBLY

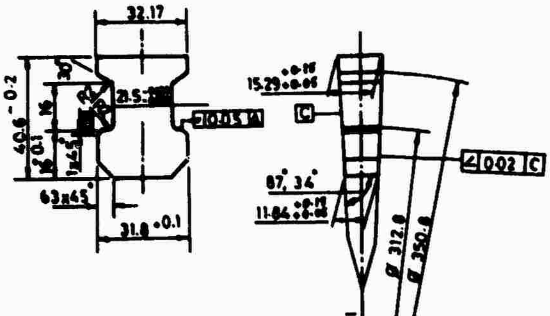

Fig. 3 THE SPACER

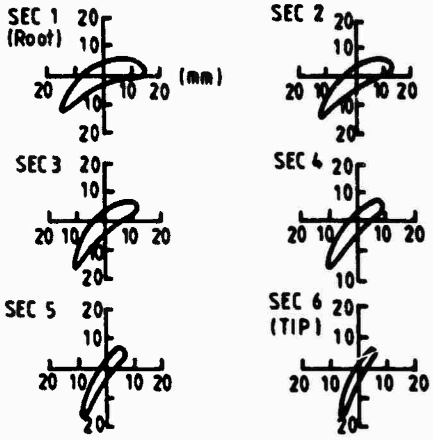

Fig. 5 BLADE SECTIONS AT VARIOUS LOCATIONS ALONG ITS LENGTH

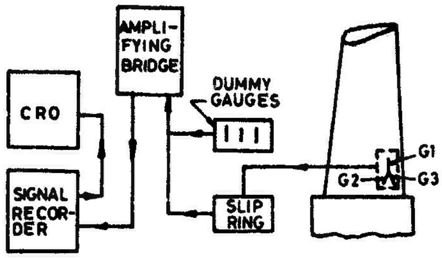

Fig. 6 INSTRUMENTATION

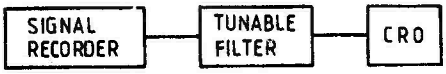

Fig.7 FREQUENCY ANALYSIS OF STRAIN SIGNAL FOR MODAL DAMPING

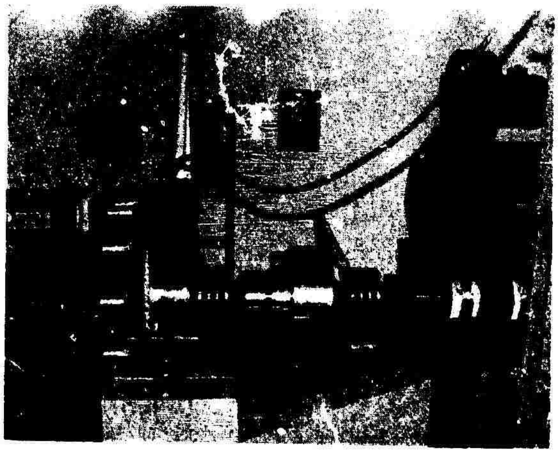

P.1 THE RIG

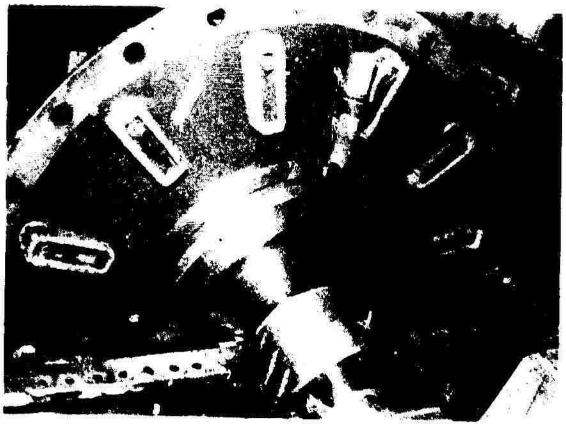

P.2 EXPOSED VIEW OF THE ELECTRO - MAGNETS AND THE INSTRUMENTED BLADE

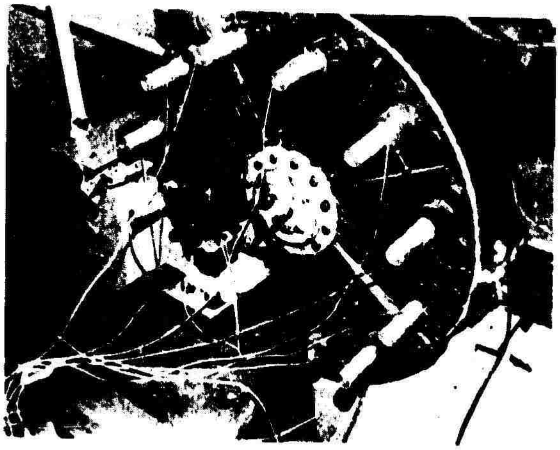

P.3 SIDE VIEW OF THE RIG: ELECTRO-MAGNET HOLDERS MOUNTED ON THE CASING, SLIP-RING

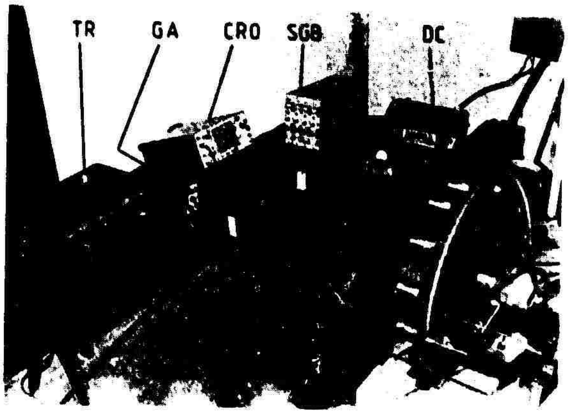

P.4 INSTRUMENTATION
DC - DC Battery; CRO-Dual Trace oscilloscope; TR-Tape Recorder; SGB-Strain Gauge Bridge Amplifier 4-channel Vishay Model 2300; PH-Photosensitive pick-up for speed measurement; GA-General purpose amplifier; EH-Electromagnet holders ; CS-Casing which encloses disc and blades

P.5 TYPICAL OVERALL SIGNAL ON A HIGHLY COMPRESSED TIME BASE

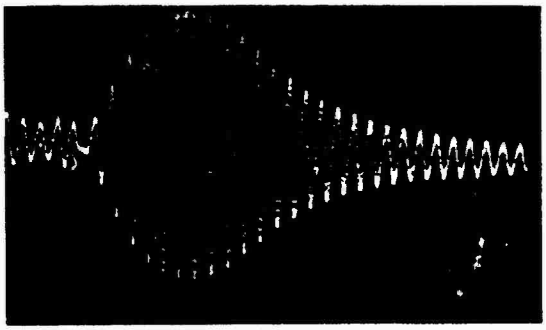

P.6 DECAYING TRANSIENT SIGNAL, I MODE, 700 RPM, 20 mv/cm

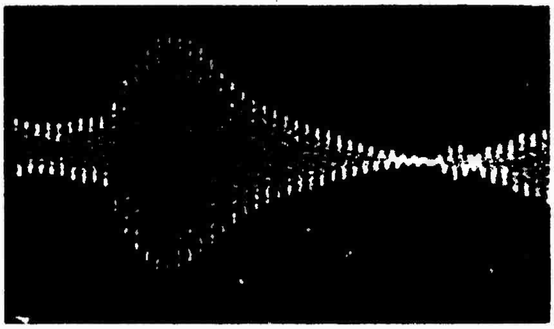

P.7 II MODE, 700 RPM, 20 mv/cm

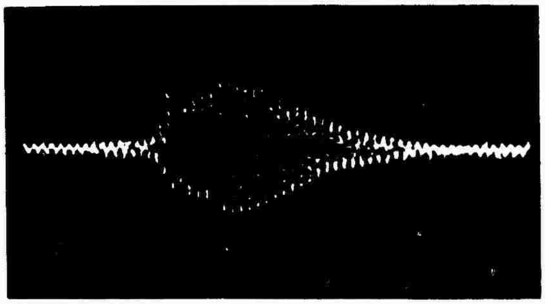

P.8 III MODE, 700 RPM, 5 mv/cm

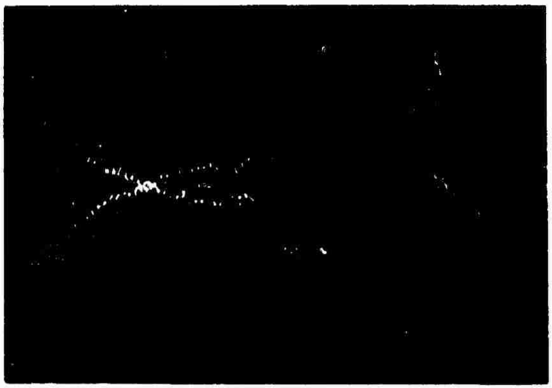

P.9 IV MODE, 700 RPM, 5 mv/cm

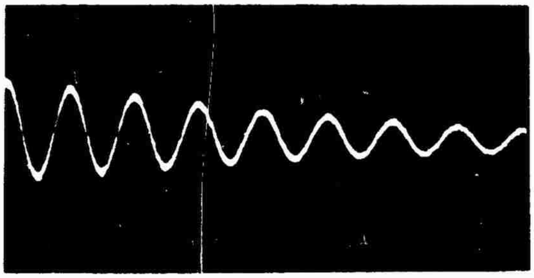

P.10 DECALYING SIGNAL ON ENLARGED TIME BASE

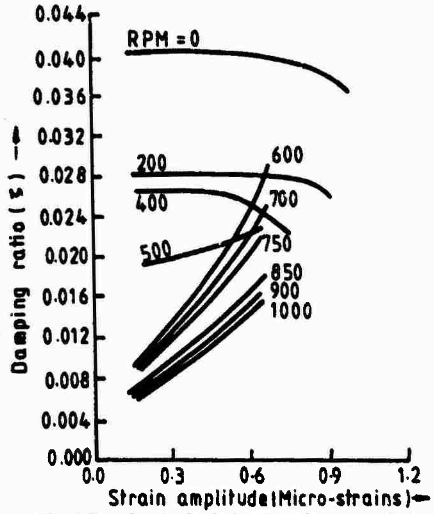

Fig. 8 DAMPING RATIO VS STRAIN AMPLITUDE-MODE I

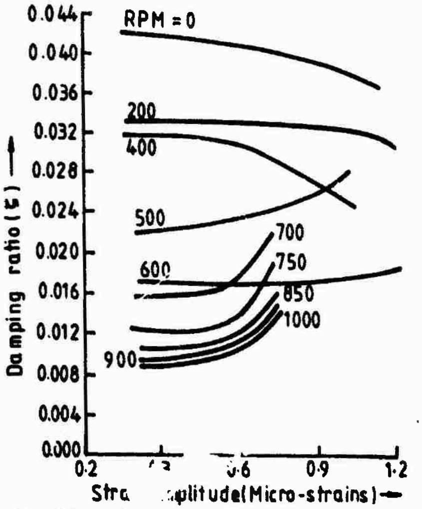

Fig. 9 DAMPING RATIO VS STRAIN AMPLITUDE-MODE II

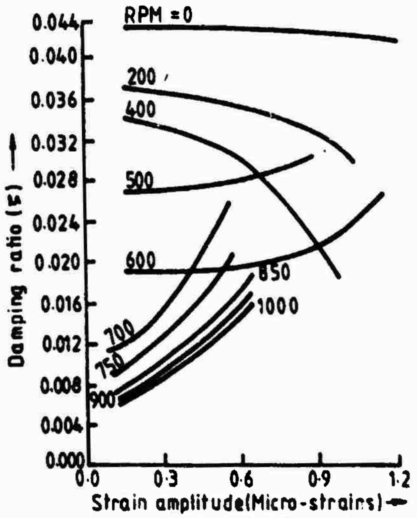

Fig. 10 DAMPING RATIO VS STRAIN AMPLITUDE-MODE III

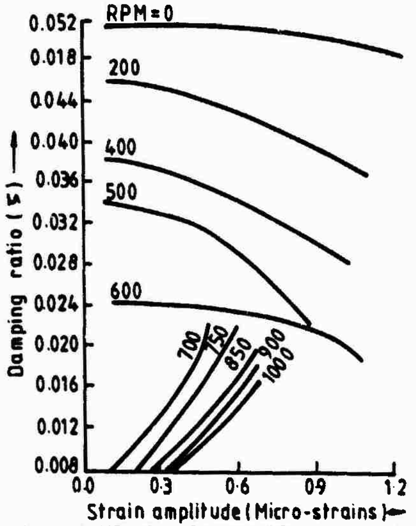

Fig. 11 DAMPING RATIO VS STRAIN AMPLITUDE-MODE IV

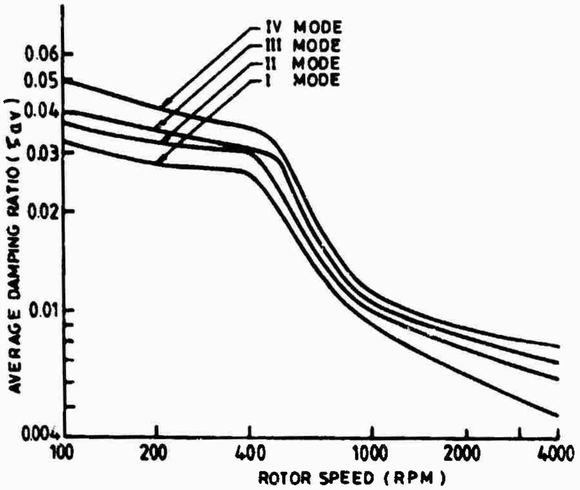

Fig. 12 DAMPING RATIOS Vs ROTOR SPEED

average damping ratios ζ_{av} for the first four modes as a function of rotor speed only, obtained by using the following formula for the entire decay of the signal

$$\delta = \frac{2\pi\,\zeta_{av}}{\sqrt{1-\zeta_{av}^2}} = \frac{1}{n}\ln\frac{x_o}{x_n}$$

where x_o and x_n are the initial and final strain amplitude values over n cycles of decay in the damping signal.

RESULTS AND DISCUSSION

From Figs. 8 to 11, it can be observed that the modal damping values in all the four modes show similar trends of variation with the strain amplitude and speed of rotation. As is well established in literature, the results show that the damping values progressively decrease with the speed of rotation. However an interesting feature revealed by the results is the existence of a threshold speed, at which the model damping values start decreasing rather rapidly. For the case under study, the threshold speed is about 400 rpm, see Fig. 12. It can be observed that below this rpm, the variation in modal damping with the strain amplitude, particularly in 1 mode, is negligible, indicating a predominantly root damping effect. For rotational speeds 700 rpm and above, the root damping effect appears to be negligible and the modal damping values increase with the strain amplitudes. The strain amplitudes are quite small, since the gauges were located very close to the root. From Fig. 12, it is observed that for all rotational speeds, the modal damping values are slightly higher in higher modes. Below the threshold speed of 400 rpm, the modal damping values range from 3 to 5 per cent.

ACKNOWLEDGEMENTS

The authors gratefully acknowledge the help received from Bharat Heavy Electricals Ltd., in the fabrication of the rig and the support given by Aeronautical Research and Development Board, Govt. of India.

REFERENCES

1. Shannon,J.F.,"Investigation of Failures in Jet Engines",Aeronautical Council of Great Britain,R&M, HMSO,1945.

2. Hanson,M.P. et al.,"A Method of Evaluating Loose-Blade Mountaing As A Means of Suppressing Turbine and Component Blade Vibration",Proc.SESA, v.10,p.103,1953.

3. Goodman, L.E. and Klumpp,J.H.,"Analysis of Slip Damping With Reference to Turbine Blade Vibration",J of Applied Mechanics, Trans. ASME, v.23,p.241,1956.

4. Grady,R.F.,"Investigation of Dovetail Damping Contribution of Propulsion Steam Turbine Buckets", GE Report No. B5-94390, November 1967.

5. Grady,R.F.,"Investigation of Material Damping Properties of Propulsion Turbine Blade Materials", GE Report No. B5-94390, December 1967.

6. Wagner, J.T.,"Blade Damping Tests", Westinghouse Engineering Report EC- 401 No. BSN 00024-67-C5494, 1969.

7. Jones, D.I.G.,"Effect of Slip on Response of a Vibrating Compressor Blade", ASME 77-WA/GT-3, 1977.

8. Jones, D.I.G. and Muszynska,A. Vibrations of a Compressor Blade with Slip at the Root", Shock Vib. Bull., No. 48, Pt.2, p.53,1978.

9. Jones, D.I.G. and Muszynska,A., "Design of Turbine Blade for Effective Slip Damping", Shock Vib. Bull., No.49, 1979.

10. Muszynska ,A. and Jones, D.I.G., "On Discrete Modelisation of Response of Blades with slip and Hysteretic Damping", Proc. 5th IFToMM Congress, p.641, 1979.

11.Rieger, N.F. and Beck,"Damping Tests on Steam Turbine Blades", EPRI Project report, RP-1185-1, 1980.

12. Peck, L.C.,Johnson,P.J. and House, D.F.,"Evaulation of Turbine Blade Root Designs to Minimise Fatigue Failures", EPRI Project Report, RP-1185-2, 1982.

13. Jonhson,P.J.,"Evaluation of Damping in Free Standing Low Pressure Steam Turbine Blades", EPRI-016-2, 1982.

14. Rao, J.S.,"Single Blade Dynamics", Proc. Technical Committee Sessions on Rotor Dynamics, 6th IFToMM World Congress, New Delhi,December, 1983

15. Rieger, N.F.,"Blade Fatigue", Proc. Technical Committee Sessions on Rotor Dynamics, 6th IFToMM World Congress, New Delhi,December, 1983.

16. Srinivasan, A.V.,"Vibration of Bladed Disc Assemblies - A Selected Review", Proc. Technical Committee Sessions on Rotor Dynamics, 6th IFToMM World Congress, New Delhi, December 1983.

Discussion

Mr. McLauchlan (Texas A&I University): Did they do anything to characterize the aerodynamic damping?

Mr. Hanagud: No, because I don't think there is any indication from what I have here that they did that. However, that is the significant part. Gasdynamic effects change the blade frequencies quite significantly. Then later, the bulk of the instabilities we get in the problem depend on the blade frequencies. So, I think that is a bigger contribution, but in one way it is significant that they have some other parts isolated. However, I frankly think I might be prejudiced, but you need a system identification technique to get the aerodynamic effects into that. Do the tests, pick up the signals, and then use either the time domain or the frequency domain system identification. You should be able to get that.

A NEW APPROACH FOR GEARBOX MODELLING IN FINITE ELEMENT ANALYSES OF TORSIONAL VIBRATION OF GEAR-BRANCHED PROPULSION SYSTEMS

H. F. Tavares
Cepstrum Engenharia Ltda.
São Paulo, Brazil
formerly with the Directorate of Naval Engineering
Brazilian Navy
Rio de Janeiro, Brazil

and

V. Prodonoff, Ph. D.
PETROBRÁS Research Center
Rio de Janeiro, Brazil

A new modelling procedure for use in analyses of torsional vibration of gear-branched propulsion systems is presented. The method has evolved from considerations on the use of constrained finite element equilibrium equations. It is shown that the process of modelling gearboxes can be carried out through a simple modification of the mass, stiffness and damping matrices of the elements situated immediately after every branch. Starting with a development valid for straight-geared systems, the procedure is then extended to account for gear-branched systems and idler gears. An example is included in order to show a practical application.

INTRODUCTION

The traditional method used in analyses of torsional vibrations of gear-branched systems consists of:

- Establishing a model of inertias and stiffnesses for the system;
- Substituting this model by that of an "equivalent system" which has no gears. This is done by selecting one of the branches as the basis and suitably modifying the inertias and stiffnesses of the other branches;
- Calculating the dynamic behavior of the equivalent system; and
- Obtaining the actual displacements in branches other than the primary one, through a modification of the calculated results.

A new procedure has been devised for application in analyses done by finite element techiques. This method has been developed from considerations on the application of constraint equations to describe gear meshes.

In the next sections the effect of constraint aquations on the shape of the finite element equilibrium equations is first reviewed. The method proposed is then introduced for modelling straight-geared systems. With minor modifications it is extended in order to cope with gear-branched systems and finally the consideration of idler gears is shown to present no difficulties. An example is included at the end, in order to show a practical application of the method.

CONSTRAINED FINITE ELEMENT EQUILIBRIUM EQUATIONS

The displacement-based finite element equilibrium equations that govern the behavior of a structure or continuum can be shown to be

$$[M]\{\ddot{x}\} + [C]\{\dot{x}\} + [K]\{x\} = \{R\} \qquad (1)$$

When some nodal point displacements are subjected to constraints, i.e., when they can be expressed in terms of the independent nodal point displacements, a new vector $\{\bar{x}\}$ containing only these independent displacements can be related with the original vector $\{x\}$ via a rectangular transformation matrix [T]:

$$\{x\} = [T]\{\bar{x}\} \qquad (2)$$

Using (2) in (1) and pre-multiplying the result by the transpose of [T] one obtains

$$[\bar{M}]\{\ddot{\bar{x}}\} + [\bar{C}]\{\dot{\bar{x}}\} + [\bar{K}]\{\bar{x}\} = \{\bar{R}\} \qquad (3)$$

where

$$[\bar{M}] = [T]^T[M][T], \qquad (4.1)$$

$$[\bar{C}] = [T]^T[C][T], \qquad (4.2)$$

$$[\bar{K}] = [T]^T[K][T] \text{ and} \qquad (4.3)$$

$$\{\bar{R}\} = [T]^T\{R\}. \qquad (4.4)$$

In practice the global mass matrix [M] is assembled as

$$[M] = \sum_i [M]_i \qquad (5)$$

where $[M]_i$ is the mass matrix of the i^{th} element expressed in global coordinates, and the summation goes over all elements in the assemblage. In the same manner the structure damping and stiffness matrices and the load vector are obtained. The transformation (4) can therefore be carried out on the element level prior to adding the element matrices to obtain the global matrices and load vector. Problem (3) is then solved in order to obtain $\{\bar{x}\}$ and thus $\{x\}$.

ANALYSIS OF STRAIGHT-GEARED SYSTEMS

A general straight-geared system is shown in fig.1. In this case the inertias j and j+1 correspond to a wheel and a pinion having a speed ratio q, i. e., their angular displacements are related by

$$x_{j+1} = -q.x_j \qquad (6)$$

One can then write

$$\{x\}_{nx1} = [T]_{nx(n-1)}.\{\bar{x}\}_{(n-1)x1} \qquad (7)$$

where

$$\{x\}^T = \{x_1\ x_2 \ldots x_j \,\vdots\, x_{j+1} \,\vdots\, x_{j+2} \ldots x_n\}; \qquad (8)$$

$$[T] = \left[\begin{array}{c:c} [I]_{jxj} & [0]_{jx(n-j-1)} \\ \hdashline [T_{21}]_{1xj} & [0]_{1x(n-j-1)} \\ \hdashline [0]_{(n-j-1)xj} & [I]_{(n-j-1)x(n-j-1)} \end{array}\right] \qquad (9)$$

$$[T_{21}] = \{0\ 0\ \ldots\ 0\ -q\}; \text{ and} \qquad (10)$$

$$\{\bar{x}\}^T = \{x_1\ x_2 \ldots x_j \,\vdots\, x_{j+2} \ldots x_n\}. \qquad (11)$$

As it can be noticed, the displacement x_{j+1} does not appear in (11), but it can calculated by (6).

The following considerations are applicable indistinctly to the mass, damping and stiffness matrices. In order to simplify the presentation, they will be simply denoted [A] when unconstrained and $[\bar{A}]$ when transformed according to (4).

The contribution of the i^{th} element, when $i \leqslant j-1$, can be expressed in global coordinates as

$$[A]_i = \left[\begin{array}{c:c:c} [A_{11}]_{jxj} & [0]_{jx1} & [0]_{jx(n-j-1)} \\ \hdashline [0]_{1xj} & [0]_{1x1} & [0]_{1x(n-j-1)} \\ \hdashline [0]_{(n-j-1)xj} & [0]_{(n-j-1)x1} & [0]_{(n-j-1)x(n-j-1)} \end{array}\right]_{nxn} \qquad (12)$$

where

$$[A_{11}] = \begin{array}{c} \begin{array}{cccc} & \overset{i}{\downarrow} & & \end{array} \\ \begin{bmatrix} 0\ldots0 & 0 & 0 & 0\ldots0 \\ \vdots\ \ \vdots & \vdots & \vdots & \vdots\ \ \vdots \\ 0\ldots0 & 0 & 0 & 0\ldots0 \\ 0\ldots0 & a & b & 0\ldots0 \\ 0\ldots0 & c & d & 0\ldots0 \\ 0\ldots0 & 0 & 0 & 0\ldots0 \\ \vdots\ \ \vdots & \vdots & \vdots & \vdots\ \ \vdots \\ 0\ldots0 & 0 & 0 & 0\ldots0 \end{bmatrix} \end{array} \begin{array}{c} \\ \\ \\ \\ \leftarrow i \\ \\ \\ \\ \\ \end{array} \qquad (13)$$

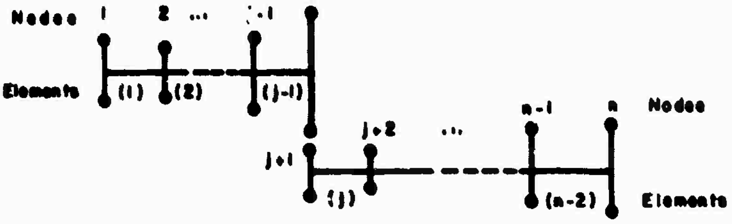

Fig.1 - General Straight-Geared System

and "a", "b", "c" and "d" are the only nonzero values of the contribution. They are placed in the rows and columns that correspond to the element degrees of freedom. As shown in Appendix 1, the mass, damping and stiffness matrices of the elements used in torsional vibration analyses are of order 2x2. Considering, for example, the element stiffness matrix $[K]_e$, one has $a = GJ/\ell$, $b=-GJ/\ell$, $c= -GJ/\ell$ and $d= GJ/\ell$.

By carrying out transformation (4), one obtains by simple partitioned matrix manipulation:

$$[\bar{A}]_i = \left[\begin{array}{c:c} [A_{11}]_{j\times j} & [0]_{j\times(n-j-1)} \\ \hdashline [0]_{(n-j-1)\times j} & [0]_{(n-j-1)\times(n-j-1)} \end{array}\right]_{(n-1)\times(n-1)} \qquad (14)$$

It can be seen that the nonzero components remain unchanged after the transformation.

The same occurs when the i^{th} element is such that $i \geqslant j+1$. In this case

$$[A]_i = \left[\begin{array}{c:c:c} [0]_{j\times j} & [0]_{j\times 1} & [0]_{j\times(n-j-1)} \\ \hdashline [0]_{1\times j} & [0]_{1\times 1} & [0]_{1\times(n-j-1)} \\ \hdashline [0]_{(n-j-1)\times j} & [0]_{(n-j-1)\times 1} & [A_{33}]_{(n-j-1)\times(n-j-1)} \end{array}\right]_{n\times n} \qquad (15)$$

where

$$[A_{33}] = \begin{array}{cc} \begin{array}{cccccc} \overset{j+2}{\downarrow} & & \overset{i}{\downarrow} & & & \overset{n}{\downarrow} \end{array} & \\ \left[\begin{array}{cccccc} 0\ldots 0 & 0 & 0 & 0\ldots 0 \\ \vdots & \vdots & \vdots & \vdots \\ 0\ldots 0 & 0 & 0 & 0\ldots 0 \\ 0\ldots 0 & a & b & 0\ldots 0 \\ 0\ldots 0 & c & d & 0\ldots 0 \\ 0\ldots 0 & 0 & 0 & 0\ldots 0 \\ \vdots & \vdots & \vdots & \vdots \\ 0\ldots 0 & 0 & 0 & 0\ldots 0 \end{array}\right] & \begin{array}{l} \leftarrow j+2 \\ \\ \\ \leftarrow i \\ \\ \\ \\ \leftarrow n \end{array} \end{array} \qquad (16)$$

and therefore

$$[\bar{A}]_i = \left[\begin{array}{c:c} [0]_{j\times j} & [0]_{j\times(n-j-1)} \\ \hdashline [0]_{(n-j-1)\times j} & [A_{33}]_{(n-j-1)\times(n-j-1)} \end{array}\right]_{(n-1)\times(n-1)} \qquad (17)$$

An important modification occurs in the element number i when i = j. For this element one has

$$[A]_i = \left[\begin{array}{c:c:c} [0]_{j\times j} & [0]_{j\times 1} & [0]_{j\times(n-j-1)} \\ \hdashline [0]_{1\times j} & [A_{22}]_{1\times 1} & [A_{23}]_{1\times(n-j-1)} \\ \hdashline [0]_{(n-j-1)\times j} & [A_{32}]_{(n-j-1)\times 1} & [A_{33}]_{(n-j-1)\times(n-j-1)} \end{array}\right]_{n\times n} \qquad (18)$$

where

$$[A_{22}] = [a]; \qquad (19)$$

$$[A_{32}]^T = \{c\ 0\ldots 0\}; \qquad (20)$$

$$[A_{23}] = \{b\ 0\ldots 0\};\ \text{and} \qquad (21)$$

$$[A_{33}] = \begin{bmatrix} d & 0\ldots 0 \\ 0 & 0\ldots 0 \\ \vdots & \vdots \quad \vdots \\ 0 & 0\ldots 0 \end{bmatrix} \qquad (22)$$

and therefore

$$[\bar{A}]_i = \begin{array}{cc} \begin{array}{cccccc} \overset{1}{\downarrow} & & \overset{j}{\downarrow} & \overset{j+2}{\downarrow} & & \overset{n-1}{\downarrow} \end{array} & \\ \left[\begin{array}{ccccc} 0\ldots 0 & 0 & 0 & 0\ldots 0 \\ \vdots & \vdots & \vdots & \vdots \\ 0\ldots 0 & 0 & 0 & 0\ldots 0 \\ 0\ldots 0 & aq^2 & -bq & 0\ldots 0 \\ 0\ldots 0 & -cq & d & 0\ldots 0 \\ 0\ldots 0 & 0 & 0 & 0\ldots 0 \\ \vdots & \vdots & \vdots & \vdots \\ 0\ldots 0 & 0 & 0 & 0\ldots 0 \end{array}\right]_{(n-1)\times(n-1)} & \begin{array}{l} \leftarrow 1 \\ \\ \\ \leftarrow j \\ \leftarrow j+2 \\ \\ \\ \leftarrow n-1 \end{array} \end{array} \qquad (23)$$

As regards the global load vector, one has

$$\{R\}^T=\{R_1 R_2 \ldots R_j \,\vdots\, R_{j+1} \,\vdots\, R_{j+2} \ldots R_n\}_{n\times 1} \qquad (24)$$

and therefore

$$\{\bar{R}\}^T=\{R_1 R_2 \ldots R_{j-1}\ R_j - q.R_{j+1} \,\vdots\, R_{j+2} \ldots R_n\}_{(n-1)\times 1} \qquad (25)$$

These results allow one to assemble all matrices and the load vector needed

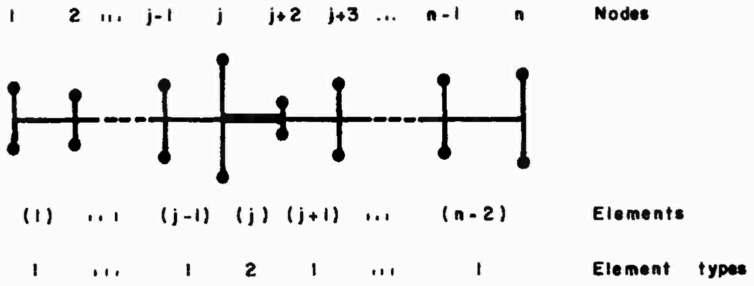

Fig.2 - Substitute Model for the Straight-Geared System

to solve the problem (3).

It is easy to see that the same data would have been generated by considering, from the beginning, that the system of fig.2 replaces the one of fig.1, provided that the element matrices in local coordinates are given by

$$[A]_i = \begin{bmatrix} a & b \\ c & d \end{bmatrix} \tag{26}$$

when $i \neq j$ and by

$$[A]_i = \begin{bmatrix} aq^2 & -bq \\ -cq & d \end{bmatrix} \tag{27}$$

when $i = j$, and that the load vector is given by (25).

Those who are familiar with the use of computer codes having finite element libraries will notice that it is very easy to append into the code a new element subroutine according to these specifications. This is the essence of the method proposed.

ANALYSIS OF GEAR-BRANCHED SYSTEMS

The procedure outlined in the last section can be extended in a quite straightforward manner in order to account for gear-branched systems.

Starting from one extremity of the original system, the degree of freedom corresponding to the first (master) gear encountered is kept as an independent variable. All other gears meshing with it will have their angular displacements eliminated from the vector $\{\bar{x}\}$, since these are not independent variables. The first node after the slave gears will then be connected to the master gear via elements type 2, i.e., elements having matrices given by eq. (27). The speed ratios to be used in (27) are the quotient between the speed of the slave gear and the speed of the master gear. The procedure is repeated in case further branches are encountered, as illustrated in fig.3.

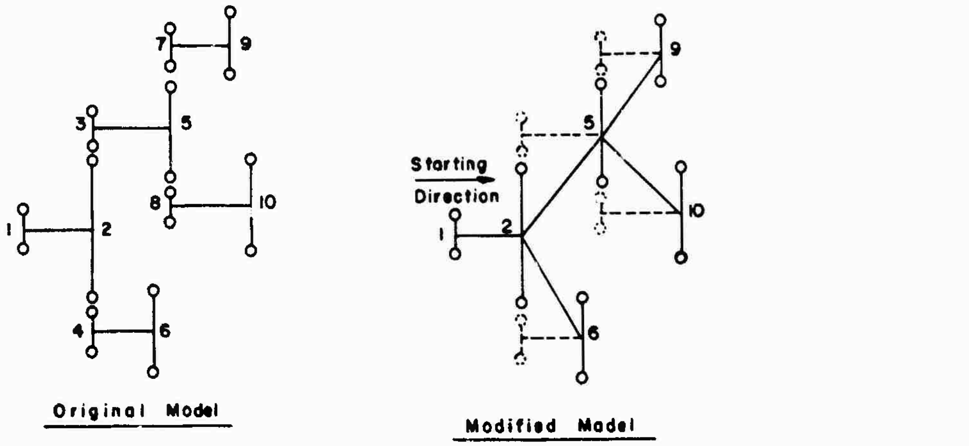

Fig.3 - Example of Application of the Method in Case of a Gear-Branched System

CONSIDERATION OF IDLER GEARS

Idler gears are often employed to change the sense of rotation of the driven shaft. They are used, for example, in some recent twin screw COOOG light frigates and corvettes fitted with a single gas turbine, in order to have the propulsion shafts turning in opposite directions.

The method described in the last sections can still be used for modelling gearboxes fitted with idler gears, provided that the inertia of these idler gears is added to the inertia of the master gear after being corrected by the square of the speed ratio, as usually done in the traditional method.

For example, supposing that m idler gears are fitted between one master and one slave gear, their characteristics being as shown on table 1, one can consider that an equivalent master gear with a polar moment of inertia

$$J'_M = J_M + \sum_{i=1}^{m} \left\{\frac{Z_m}{Z_{g_i}}\right\}^2 \cdot J_{g_i} \qquad (28)$$

is in direct mesh with the slave gear and then use the method proposed in the last sections with the following modifications:

(a) Element type 2 matrices become

$$[A]_i = \begin{bmatrix} aq^2 & (-1)^{m+1}bq \\ (-1)^{m+1}cq & d \end{bmatrix} \qquad (29)$$

(b) The load vector becomes

$$\{R\}^T = \{R_1 R_2 \ldots R_{j-1} R_j + (-1)^{m+1}.q.R_{j+1} \quad R_{j+2} \ldots R_n\} \qquad (30)$$

EXAMPLE

In order to show a practical application of the method proposed, one can consider the system of fig.4, taken from ref. [1]. It is desired to find natural frequencies and modes of vibration of the system.

TABLE 1
Characteristics of the gears

Gear	Nº of Teeth	Polar Moment of Inertia
Master	Z_m	J_m
g_1	Z_{g1}	J_{g1}
⋮	⋮	⋮
g_m	Z_{gm}	J_{gm}
Slave	$q^{-1}.Z_m$	J_s

The element mass and stiffness matrices in local coordinates, before applying the transformation (4), are calculated according to the Appendix 1 to give:

$$[M]_1 = \begin{bmatrix} 10 & 0 \\ 0 & 15 \end{bmatrix} \qquad (31)$$

$$[K]_1 = \begin{bmatrix} 40,000 & -40,000 \\ -40,000 & 40,000 \end{bmatrix} \qquad (32)$$

$$[M]_2 = \begin{bmatrix} 15 & 0 \\ 0 & 5 \end{bmatrix} \qquad (33)$$

Node	Inertia of Gears
1	10
2	30
3	5
4	10
5	15
6	5
7	15

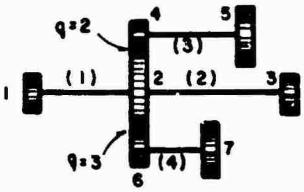

Element	$\frac{GJ}{\ell}$
1	40,000
2	50,000
3	200,000
4	300,000

The numerical values shown are given in consistent units.

Fig.4 - Example of a Gear-Branched System

$$[K]_2 = \begin{bmatrix} 50,000 & -50,000 \\ -50,000 & 50,000 \end{bmatrix} \quad (34)$$

$$[M]_3 = \begin{bmatrix} 10 & 0 \\ 0 & 15 \end{bmatrix} \quad (35)$$

$$[K]_3 = \begin{bmatrix} 200,000 & -200,000 \\ -200,000 & 200,000 \end{bmatrix} \quad (36)$$

$$[M]_4 = \begin{bmatrix} 5 & 0 \\ 0 & 15 \end{bmatrix} \quad (37)$$

$$[K]_4 = \begin{bmatrix} 300,000 & -300,000 \\ -300,000 & 300,000 \end{bmatrix} \quad (38)$$

Considering only the independent degrees of freedom, vector $\{\bar{x}\}$ is given by

$$\{\bar{x}\}^T = \{x_1 \; x_2 \; x_3 \; x_5 \; x_7\} \quad (39)$$

and therefore the contribution of each element in global coordinates is calculated according to (26) and (27) to give

$$[\bar{M}]_1 = \begin{bmatrix} 10 & 0 & 0 & 0 & 0 \\ 0 & 15 & 0 & 0 & 0 \\ 0 & 0 & 0 & 0 & 0 \\ 0 & 0 & 0 & 0 & 0 \\ 0 & 0 & 0 & 0 & 0 \end{bmatrix} \quad (40)$$

$$[\bar{K}]_1 = 10^3 \begin{bmatrix} 40 & -40 & 0 & 0 & 0 \\ -40 & 40 & 0 & 0 & 0 \\ 0 & 0 & 0 & 0 & 0 \\ 0 & 0 & 0 & 0 & 0 \\ 0 & 0 & 0 & 0 & 0 \end{bmatrix} \quad (41)$$

$$[\bar{M}]_2 = \begin{bmatrix} 0 & 0 & 0 & 0 & 0 \\ 0 & 15 & 0 & 0 & 0 \\ 0 & 0 & 5 & 0 & 0 \\ 0 & 0 & 0 & 0 & 0 \\ 0 & 0 & 0 & 0 & 0 \end{bmatrix} \quad (42)$$

$$[\bar{K}]_2 = 10^3 \begin{bmatrix} 0 & 0 & 0 & 0 & 0 \\ 0 & 50 & -50 & 0 & 0 \\ 0 & -50 & 50 & 0 & 0 \\ 0 & 0 & 0 & 0 & 0 \\ 0 & 0 & 0 & 0 & 0 \end{bmatrix} \quad (43)$$

$$[\bar{M}]_3 = \begin{bmatrix} 0 & 0 & 0 & 0 & 0 \\ 0 & 40 & 0 & 0 & 0 \\ 0 & 0 & 0 & 0 & 0 \\ 0 & 0 & 0 & 15 & 0 \\ 0 & 0 & 0 & 0 & 0 \end{bmatrix} \quad (44)$$

$$[\bar{K}]_3 = 10^3 \begin{bmatrix} 0 & 0 & 0 & 0 & 0 \\ 0 & 800 & 0 & 400 & 0 \\ 0 & 0 & 0 & 0 & 0 \\ 0 & 400 & 0 & 200 & 0 \\ 0 & 0 & 0 & 0 & 0 \end{bmatrix} \quad (45)$$

$$[\bar{M}]_4 = \begin{bmatrix} 0 & 0 & 0 & 0 & 0 \\ 0 & 45 & 0 & 0 & 0 \\ 0 & 0 & 0 & 0 & 0 \\ 0 & 0 & 0 & 0 & 0 \\ 0 & 0 & 0 & 0 & 15 \end{bmatrix} \quad (46)$$

$$[\bar{K}]_4 = 10^3 \begin{bmatrix} 0 & 0 & 0 & 0 & 0 \\ 0 & 2,700 & 0 & 0 & 900 \\ 0 & 0 & 0 & 0 & 0 \\ 0 & 0 & 0 & 0 & 0 \\ 0 & 900 & 0 & 0 & 300 \end{bmatrix} \quad (47)$$

The global mass and stiffness matrices are obtained by adding these contributions:

$$[\bar{M}] = \begin{bmatrix} 10 & 0 & 0 & 0 & 0 \\ 0 & 115 & 0 & 0 & 0 \\ 0 & 0 & 5 & 0 & 0 \\ 0 & 0 & 0 & 15 & 0 \\ 0 & 0 & 0 & 0 & 15 \end{bmatrix} \quad (48)$$

$$[\bar{K}] = 10^3 \begin{bmatrix} 40 & -40 & 0 & 0 & 0 \\ -40 & 3,590 & -50 & 400 & 900 \\ 0 & -50 & 50 & 0 & 0 \\ 0 & 400 & 0 & 200 & 0 \\ 0 & 900 & 0 & 0 & 300 \end{bmatrix} \quad (49)$$

The natural frequencies and modes of vibration can be found by solving the eigenvalue problem

$$[\bar{K}]\,\{\bar{x}\} = \omega^2\,[\bar{M}]\,\{\bar{x}\} \quad (50)$$

However, as the system considered is semi-definite, one must eitheir employ special algorithms or the traditional methods in combination with the shifting technique described in ref. [2] to solve this problem.

The results thus obtained are in close agreement with those reported in ref.[1], as shown in tables 2 and 3 below. The mode shapes are plotted in fig. 5.

TABLE 2
Comparison of Eigenvalues

Mode no.	ω^2	
	Calculated	Ref. [1]
1	0	0
2	4,105.3	4,105
3	10,080	10,080
4	14,654	14,650
5	49,711	49,700

CONCLUSIONS

A new technique for modelling gear-branched systems has been developed through the use of finite elements and constraint equations. It has been shown that a simple modification of the matrices of the first element after every pair wheel-pinion leads to the same results obtained through the traditional procedure, in which the original system is transformed in a system with no speed reductions.

TABLE 3

Comparison of Eigenvectors

Modes		Amplitudes						
		(1)	(2)	(3)	(4)	(5)	(6)	(7)
1	Calculated	1,00	1.00	1.00	-2.00	-2.00	-3.00	-3.00
	Ref. [1]	1.00	1.00	1.00	-2.00	-2.00	-3.00	-3.00
2	Calculated	1.00	-0.0263	-0.0446	0.0526	0.0760	0.0789	0.0993
	Ref.[1]	1.00	-0.0262	-0.0445	0.0524	0.0760	0.0786	0.0990
3	Calculated	1.00	-1.52	190	3.04	12.5	4.56	9.19
	Ref.[1]	1.00	-1.52	190	3.04	12.4	4.56	9.20
4	Calculated	1.00	-2.66	5.72	5.33	-53.8	7.99	29.9
	Ref.[1]	1.00	-2.66	5.73	5.32	-53.2	7.98	30.0
5	Calculated	1.00	-11.4	2.88	22.9	-8.38	34.3	-23.1
	Ref.[1]	1.00	-11.4	2.88	22.8	-8.26	34.2	-23.1

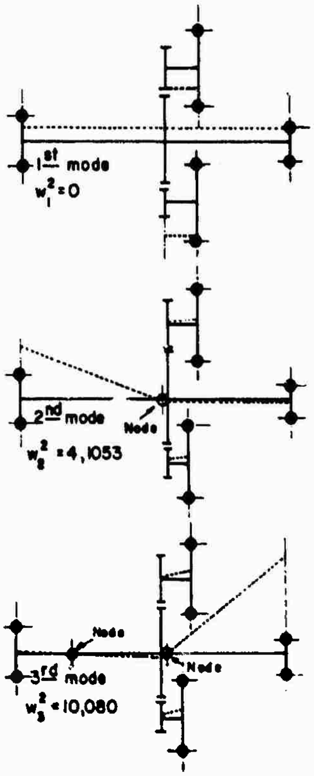

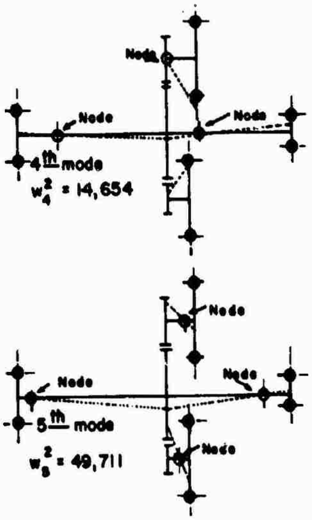

Fig.5 (continued) - Mode Shapes of the Example

Fig.5 - Mode Shapes of the Example

The main advantages afforded by the use of this new method are:

(a) The nodal displacements are directly calculated, thus allowing time savings in stress calculations; and

(b) Its adoption in finite element computes codes having element libraries is easy and straightforward, requiring only the appendage of one subroutine into the master program.

REFERENCES

[1] Ker Wilson, W., "Practical Solution of Torsional Vibration Problems - Vol.1", pp.243-253. Chapman & Hall Ltd., London, England, 1971.

[2] Bathe, K.J., "Finite Element Procedures in Engineering Analysis", pp. 570-571. First Edition, Prentice-Hall Inc., Englewood Cliffs, USA, 1982.

[3] Salzman, R.H., and Pamidi, P.R., "Machinery Vibrations in Marine Systems", Proceedings, International Symposium on Marine Engineering, Tokyo, Japan, 1973.

APPENDIX 1 - FINITE ELEMENT FOR TORSIONAL SYSTEMS

A finite element that can be used in torsional vibration analyses is shown in fig. 6.

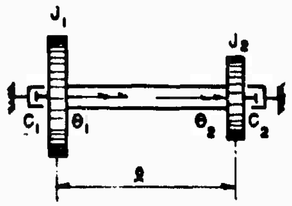

Fig.6 - Finite Element for a Shaft in Torsion

Its mass matrix is given in general by

$$[M]_e = \begin{bmatrix} J_1 + \frac{\rho J_0 \ell}{3} & \frac{\rho J_0 \ell}{6} \\ \frac{\rho J_0 \ell}{6} & J_2 + \frac{\rho J_0 \ell}{3} \end{bmatrix} \qquad (51)$$

and this corresponds to a consistent matrix scheme. In case of a massless shaft representation one takes $\rho = 0$.

The element stiffness matrix is given by

$$[K]_e = \frac{GJ}{\ell} \begin{bmatrix} 1 & -1 \\ -1 & 1 \end{bmatrix} \qquad (52)$$

and the viscous damping matrix by

$$[C]_e = \begin{bmatrix} C_1 & 0 \\ 0 & C_2 \end{bmatrix} \qquad (53)$$

In case of structural damping consideration one can add to $[C]_e$ the structural damping matrix

$$[C]_e^s = \frac{\beta}{2\pi\Omega} [K]_e \qquad (54)$$

when the excitation is harmonic with frequency Ω. According to ref. [3], one can use $\beta = 0.05$ for solid steel shafts.

As one can notice, all these matrices are of order 2x2.

APPENDIX 2 - NOTATION

$\bar{}$ This superscript indicates that the matrix or vector is expressed in the constrained coordinate system

[A] Mass, damping or stiffness matrix

[C] Damping matrix

[I] Unit matrix

[K] Stiffness matrix

[M] Mass matrix

[O] Null matrix

{R} Load vector

{x} Vector of nodal displacements

C_1, C_2 Viscous damping coefficient

G Modulus of Rigidity

J_0 Shaft polar moment of inertia

J_1, J_2 Polar mass moment of inertia

ℓ Element length

q	Ratio between the speed of a slave gear and the speed of the master gear
z	Number of teeth of a gear
β	Structural damping coefficient
Θ	Angular displacement
ρ	Mass density
ω	Natural frequency of vibration
Ω	Harmonic forcing frequency

ISOLATION AND DAMPING

A GRAPHICAL METHOD
OF DETERMINING THE RESPONSE
OF THE CASCADED TWO DEGREE OF FREEDOM SYSTEM

George M. Hieber
Hieber Engineering
Watchung, NJ

There are many occasions when a designer has to install a load onto an existing base structure. If the dynamic characteristics of the load and of the base structure are known individually, the question is: what will happen to the dynamic response of the load when it is connected to the base to form a new system? Assuming the new system results in a configuration that can be modeled as a two degree of freedom system, there are graphical methods available to determine the resulting system frequencies but no quick way to estimate the response amplitude of the load without setting up and solving the appropriate equations.

A method is presented here where the maximum reponse of the load can be obtained graphically. The graphical approach has three advantages:

(1) Results are obtained quickly.
(2) Trends are apparent.
(3) Provides insight into system operation.

The graphics are valid for Qs from 4 to 400. (For both load and base subsystems.) The ratio of load weight to base weight can range from less than 0.001 to 10. The ratio of natural frequencies of load to base (before installation of load) can range from 0.1 to greater than 10.

The results of this investigation show that two widely held points of view regarding two degree of freedom response should be moderated somewhat.

First, when two single degree of freedom systems with similar resonant frequencies are connected in series (cascaded), it is often assumed for conservatism that the response of the upper system (the load) will be $Q_1 \times Q_2$, where Q_1 and Q_2 are the maximum transmissibilities of each single degree of freedom system before connecting them together.

As shown in this report, the above assumption is usuallly excessively conservative. Second, it is shown that the use of the Octave Rule can also be unduly restrictive; that is, the rule of thumb that requires designing the upper system (load) to have a resonant frequency an octave higher than that of the resonant frequency of the lower system (base) in order to prevent excessive response of the load. As a matter of fact, in some cases, designing the load to have a resonant frequency below that of the base may be a more attractive option.

INTRODUCTION

When designing equipment to withstand shock and vibration, the engineer frequently encounters a situation where a load must be installed on a base, resulting in a "piggyback" or cascaded assembly. The problem is: if both the load and the base are considered to be single degree of freedom dynamic systems, each with a predictable response, what will be the response of the load when the assembled system is subjected to vibration?

The purpose of this monograph is to present a graphical method by which the maximum response of such a cascaded load can be simply estimated (to within 10%). Estimating the vibration response to a reasonable degree of accuracy during the design phase will go a long way towards improving ruggedness and reliability of the product. A simple computer program was used to solve for the response of the cascaded two degree of freedom system with various ratios of weight, resonance, frequency and damping. The results of these computations have been used to develop the graph is shown on these pages.

BACKGROUND

Throughout this monograph, the term 2DOF (two degree of freedom system) will be restricted to that type of two degree of freedom system which is composed of two single degree of freedom systems connected in series, or cascaded together. This type of 2DOF system is shown in Figure 1.

Representative Examples

System 1	System 2
Engine	Starter Motor
Printed Ckt. Bd.	Relay
Chassis	Power Supply Module
Antenna	Feed Horn
RR Flat Car	Piggy-Back Trailer
Vehicle Suspension	Seated Driver
Instrument Panel	Instrument Package

NOMENCLATURE

Subsystems as isolated entities

$f_1 = 3.13\sqrt{\frac{k_1}{w_1}}$, base subsystem resonant frequency, Hz*

Q_1, base subsystem maximum transmissibility $T_1 = y_1/y_o$ max

$f_2 = 3.13\sqrt{\frac{k_2}{w_2}}$, load subsystem resonant frequency, Hz

Q_2, load subsystem maximum transmissibility $T_2 = y_2/y_1$ max

k = stiffness, lb/in

w = weight, lb.

c = damping, $\frac{\text{lb-sec}}{\text{in}}$

c_c = critical damping lb-sec/in

$\zeta = c/c_c$-fraction of critical damping (non-dimensional)

$Q = 1/2\zeta$ (non-dimensional)

Assembled 2DOF System

f_L = Lower resonant frequency of system, Hz

f_H = Higher resonant frequency of system, Hz

Q_{2L} = Maximum transmissibility (T_2') of load at f_L

Q_{2H} = Maximum transmissibility (T_2') of load at f_H

R_f = Ratio of isolated resonant frequencies, f_2/f_1

R_w = Ratio of weights, w_2/w_1

T_1' = 2DOF Transmissibility of w_1 (base)

T_2' = 2DOF Transmissibility of w_2 (load)

Some misunderstandings exist regarding the effect of cascading systems together. For instance, some designers believe that a good conservative approach is to assume that if two systems having the same isolated resonant frequency ($f_1 = f_2$) are stacked together, and subjected to an input vibration at the aforementioned resonant frequency, the load weight would vibrate at an amplitude equal to the product of the maximum responses of the isolated systems. Although this condition can be approached if the load becomes infinitesimally small, in general it leads to excessively conservative design and erroneous interpretation of the system dynamics. The reason that the above interpretation is erroneous is that when two single degree of freedom systems are cascaded, a two degree of freedom results. This two degree of freedom system has two natural frequencies (resonances), neither of which is equal to the resonant frequencies of the isolated subsystems. This phenomenon is shown graphically in Figure 2.

Figure 2a represents the transmissibility plot of a single degree of freedom system with a maximum transmissibility of Q**, of 10. Assume that two systems, vibrated one at a time, generate this same transmissibility plot, and that each

---

* Strictly speaking, these formulas solve for the undamped natural frequencies. The frequency at which the greatest motion occurs (maximum transmissibility) is called the resonant frequency, which is slightly lower than the natural frequency. For damping ratios of 0.1 or less, however, the difference becomes insignificant and the terms can be used interchangeably.

** Q is a term which is used to identify the transmissibility at resonance, and is used interchangeably with the term maximum transmissibility. Damping causes Q to be slightly different (less) than the maximum transmissibility at the resonant frequency, but for the low damping usually encountered in structures, the difference becomes inconsequential.

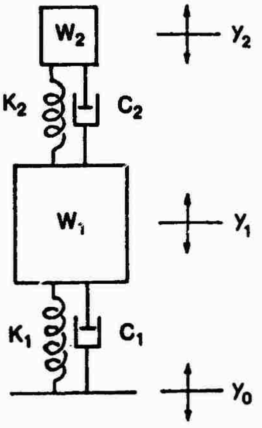

FIGURE 1 - CASCADED TWO DEGREE OF FREEDOM SYSTEM

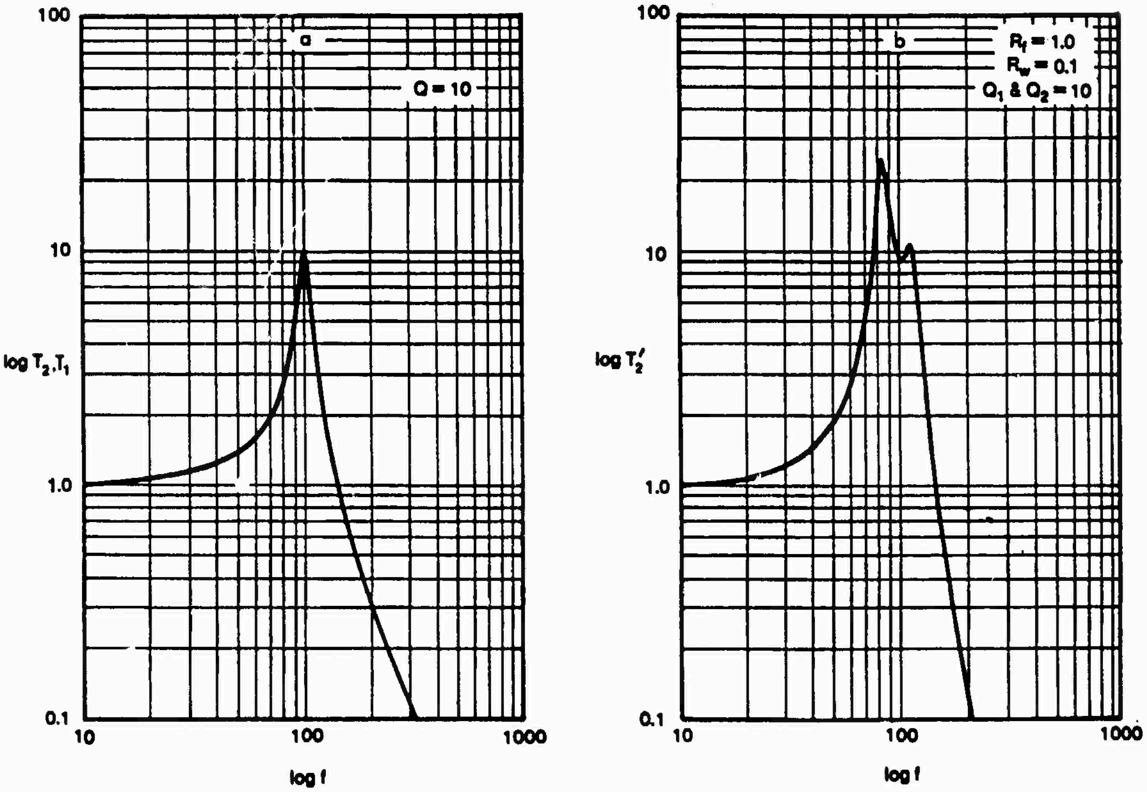

FIGURE 2 - RESPONSE OF CASCADED TWO DEGREE OF FREEDOM SYSTEM, AND OF REPRESENTATIVE SINGLE DEGREE OF FREEDOM SUBSYSTEM

has a resonant frequency of 100Hz. If $R_f = 1.0$, $R_w = 0.1$, and the systems are cascaded, the resulting transmissibility plot of w_2, T_2^1, looks like Figure 2b. Note that there are two resonant frequencies, one at 86.2Hz and the other at 115.4Hz. There is no resonance at 100Hz. In addition, the maximum $Q_{2L} = 25.1$, not 100, so Q_{2L} does not equal $Q_1 x Q_2$. Although it is not wise to cascade subsystems with identical resonant frequencies if w_2 is very small compared to w_1, the situation is not the "bugaboo" some designers anticipate.

The theory behind this has been used in the design of dynamic vibration absorbers for many years. If in the above example, subsystem 2 was to be used as a vibration absorber for subsystem 1 and some disturbance is ocurring at 100Hz, the motion of w_1 at 100Hz would be greatly subdued from what it was before the addition of w_2, whereas the motion of w_2 at 100Hz would be at a transmissibility of $T_2^1 = 9.3$, as shown on Figure 2b.

However, this investigation is not concerned with the design of vibration absorbers (when the excitation is confined to f_1), but rather it is concerned with determining the worst case motion of w_2 as an element in a 2DOF system, which occurs when the excitation is at f_L.

The response of a 2DOF system involves two transmissibilities: that of w_1 and that of w_2. The transmissibility of w_1 does not interest us here, as the maximum transmissibilities of w_1, Q_{1L} and Q_{1H}, will never exceed the Q_1 of w_1 as an isolated subsystem. In other words, if the response of the subsystem 1 was acceptable as an isolated subsystem, then the addition of subsystem 2 will, if anything reduce the w_1 response. This is due to the vibration absorber effect as mentioned above.

Turning to the transmissibility of w_2, we concentrate on the peak, Q_{2L}, at the lower resonant frequency, f_L. The reason is that so long as the damping of both subsystems is approximately the same ($Q_1 \sim Q_{2L}$), Q_{2L} will always be a higher peak then Q_{2H}, as shown in the computer analysis.

As a matter of interest, f_H can be obtained once f_L is picked from Figure 3 by using the simple expression $f_H = f_2 \left(\frac{f_1}{f_L}\right)$.

Although the system designer may find it relatively straightforward to set up the equations and solve for the Q_{2L} of the 2DOF system, it is preferable to have a solution available in a form where trends are obvious, so that iterative computations are not necessary. Figure 3 provides such a solution. It is a set of curves which can not only be used to easily obtain Q_{2L}, but it is also quite apparent how changes in the weight ratio R_w and in the frequency ratio R_f can affect the result.

The curves are drawn for $R_w = 10$ to $R_w = 0.001$, and for $R_f = 10$ to $R_f = 0.1$. Actually, results can be obtained for $R_w < 0.001$, because the curves for the smaller ratios become colinear with that for 0.001. Also, values for $R_f > 10$ are colinear with those of $R_f = 10$, so valid results can be obtained for $R_f > 10$. If the damping for both subsystems is similar, ($Q_1 \sim Q_2$), extensive computer results show that Q_{2L} response can be matched within 5% for values of Q within from 4 to 400.

In order to determine Q_{2L} and f_L, it is necessary to first determine the dynamic characteristics of each subsystem by itself. If the subsystems are available, the resonant frequencies and Qs can be measured by testing one subsystem at a time. If the subsystems are not available, these characteristics must be estimated.

EXAMPLE:

A. GIVEN:

$w_1 = 0.68$ lb. $f_1 = 140$Hz $Q_1 = 30$

$w_2 = 0.15$ lb. $f_2 = 200$Hz $Q_2 = 30$

FIND: Q_{2L} & f_L

$R_w = \frac{W_2}{W_1} = \frac{0.15}{0.68} = 0.22$ $R_f = \frac{f_2}{f_1} = \frac{200}{140} = 1.43$

Referring to Figure 3, $R_w = 0.22$ & $R_f = 1.43$

$K_A = 1.7$ and $K_f = 0.87$

When using the graphs, the characteristics of the base subsystem f_1 and Q_1, are always used as a reference.

Thus, $f_L = K_f f_1$

$Q_{2L} = K_A Q_1$

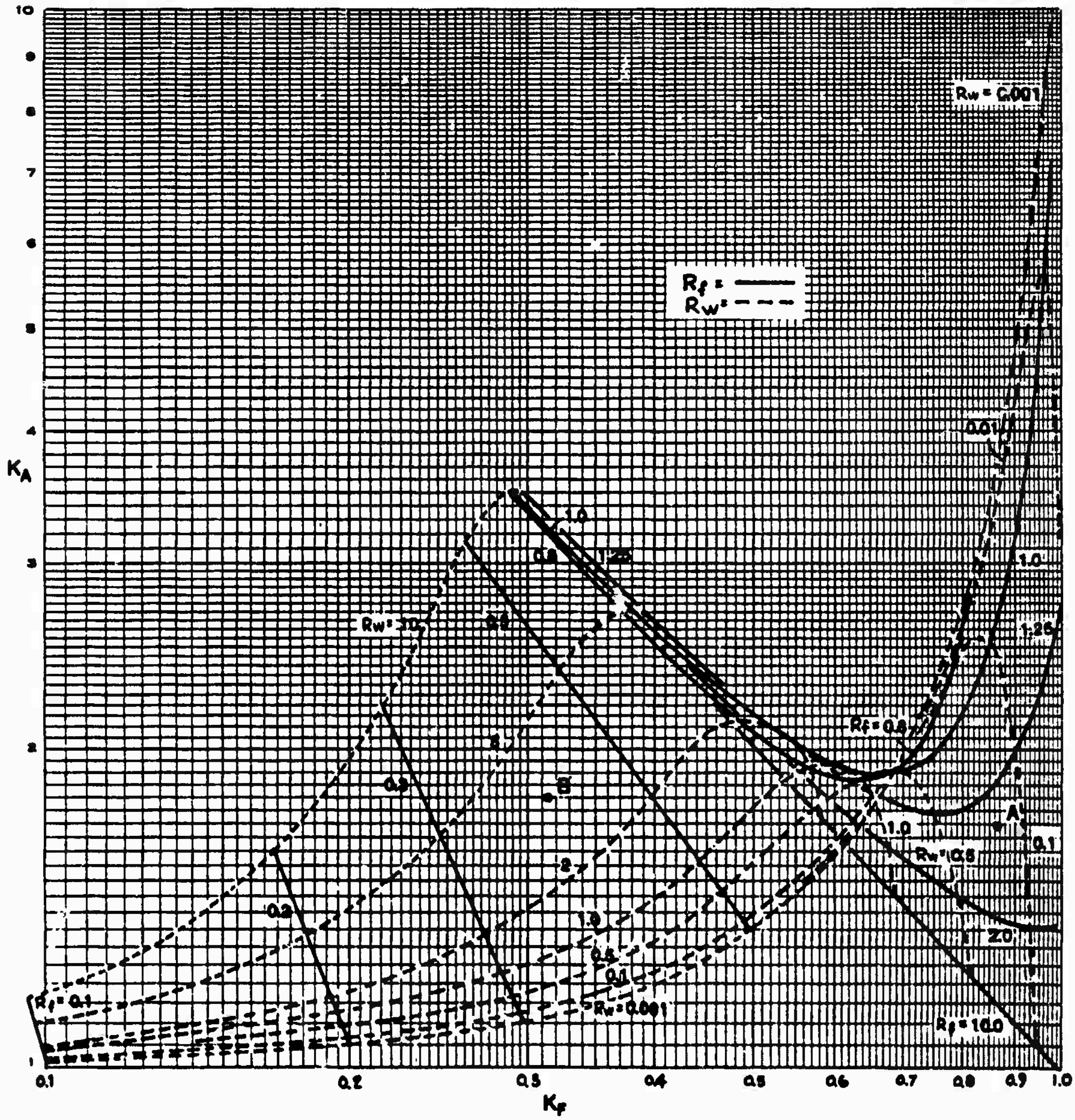

FIGURE 3 - $K_A = \frac{Q_{2L}}{Q_1}$ AND $K_F = \frac{F_L}{f_1}$, VERSUS VARIOUS R_f AND R_W

In order to use this method, the following steps are taken:

1. Calculate or measure the resonant frequencies and maximum transmissibilities of the isolated subsystems, f_1, f_2, Q_1, and Q_2.

2. Compute frequency ratio $R_f = f_2/f_1$ and weight ratio $R_w = w_2/w_1$.

3. Enter Figure 3 and determine where R_w and R_f intersect. From this point of intersection read K_A and K_F.

4. Compute system lower resonant frequency $f_L = K_f f_1$.

5. Compute maximum transmissibility of w_2 at f_L; $Q_{2L} = K_A Q_1$. If $Q_1 = Q_2$, Q_{2L} is the correct answer, and no more steps need to be taken.

6. If $Q_1 \neq Q_2$, either Figure 4 or Figure 5 must then be used, as explained in the text, to obtain a correction factor, C_L or C_H. The corrected Q_{2L} is: $Q_{2L} = (C_{L or H})K_A Q_1$.

7. If in doubt, Figure 5 can be used to see if there is any liklihood that Q_{2H} could be greater than Q_{2L}. This is unlikely, but should be guarded against.

so, $f_L = K_f f_1 = 0.87 \times 140 = \underline{122Hz}$

and $Q_{2L} = K_A Q_1 = 1.7 \times 30 = \underline{51}$

B. GIVEN:

$W_1 = 7$ lb, $f_1 = 87Hz$, $Q_1 = 18$

$W_2 = 25$ lb, $f_2 = 35Hz$, $Q_2 = 18$

FIND: Q_{2L} & f_L

$R_w = \frac{25}{7} = 3.57 \quad R_f = \frac{35}{87} = 0.4$

Referring to Figure 3, $R_w = 3.57$ & $R_f = 0.4$ intersect at "B", where

$K_A = 1.8$ and $K_f = 0.315$

so, $f_L = 0.315 \times 87 = \underline{27.4Hz}$

and $Q_{2L} = 1.8 \times 18 = \underline{32.4}$.

HANDLING DIFFERENCES IN DAMPING

Figure 3 is the main result of this investigation, but, as mentioned before, is valid only if the damping ratio of the load subsystem is the same as that for the base subsystem; in other words, if $Q_1 = Q_2$. If Q_1 is substantially different from Q_2, either by circumstances or by design, Figures 4 and 5 can be used to obtain a correction factor for Q_{2L}, and can also be used to observe trends. Figure 4 is to be used if $R_f > 1$, and Figure 5 if $R_f < 1$. Either Figure may be used if $R_f = 1$. The $R_f = 1$ curve is dashed at values of R_w smaller than 0.1, as those combinations are not recommended by design because very large Q_{2L} can result. The R_f curves are drawn to show the correction factors, C_H and C_L, for systems where Q_1 and Q_2 differ by 128:1. This is the result of changing the difference in damping ratios between the subsystems by factors of 2, 4, 8, 16, 32, 64 & 128. The smaller factors can be obtained by interpolation using divisions proportional to those shown on the graphs.

Assume that in previous examples A, Q_2 is increased 5:1 compared to Q_1, that is, if Q_2 increases from 30 to 150, what will be the affect on Q_{2L}? Since $R_f = 1.43$ ($R_f > 1.0$), Figure 4 is used. A vertical line is drawn at $R_w = 0.22$. An estimation is made for where $R_f = 1.43$ would lie; this latter line would intersect $R_w = 0.22$ at a $C_H = 1.14$, which is the correction factor for the Q_{2L} response if $W_2 = 128\ Q_1$. But Q_{2L} is only 5 Q_1, so it is necessary to interpolate. A nearby Q_2/Q_1 scale is chosen and the interpolation is accomplished by the line construction shown on the Figure. In this case, C_H is found to be 1.1, so:

EXAMPLE A'

$Q_{2L} = C_H \times K_A \times Q_1 = 1.1 \times 1.7 \times 30 = 56.1$

If the same $Q_2/Q_1 = 5.0$ ratio is obtained by lowering Q_1 from 30 to 6, rather than by raising Q_2 from 30 to 150, as was done above, a different answer appears. Although the factors K_A and C_H remain the same, the reference value of Q_1 has been changed from 30 to 6:

$Q_{2L} = 1.1 \times 1.7 \times 6 = 11.2.$

If the relationship between subsystem damping is changed such that $Q_2/Q_1 = 1/5$, the lower part of Figure 4 is used. The intersection of $R_w = 0.22$ and $R_f = 0.4$ is at a value of C_L for $Q_2/Q_1 = 1/128$, but as $Q_2/Q_1 = 1/5$, graphical interpolation is used as shown to obtain $C_L = 0.71$.

EXAMPLE A"

If $Q_2/Q_1 = 1/5$ by reducing Q_2 from 30 to 6,

$Q_{2L} = 0.71 \times 1.7 \times 30 = 36.2.$

If $Q_2/Q_1 = 1/5$ by increasing Q_1 from 30 to 150,

$Q_{2L} = 0.71 \times 1.7 \times 150 = 181$

EXAMPLES B' AND B"

Assume that in Example B, the damping ratio of the load is changed so that $Q_2/Q_1 = 4$. To find the resulting Q_{2L}, Figure 5 is used, because $R_f = 0.4$ ($R_f < 1.0$). A vertical line is drawn at $R_w = 3.57$, and an estimate made of the location of the curve $R_f = 0.4$. The intersection of the curve $R_f = 0.4$ with the line $R_w = 3.57$ is at a point on the C_L scale which would be the correction factor for Q_{2L} if $Q_2/Q_1 = 128$. But since $Q_2/Q_1 = 4$, interpolation is used as shown to obtain $C_L = 2.2$.

EXAMPLE B'

If $Q_2/Q_1 = 4$ by increasing Q_2 from 18 to 72

$Q_{2L} = C_L \times K_A \times Q_1 = 2.2 \times 1.8 \times 18 = 71.3$

If $Q_2/Q_1 = 4$ by decreasing Q_1 from 18 to 4.5,

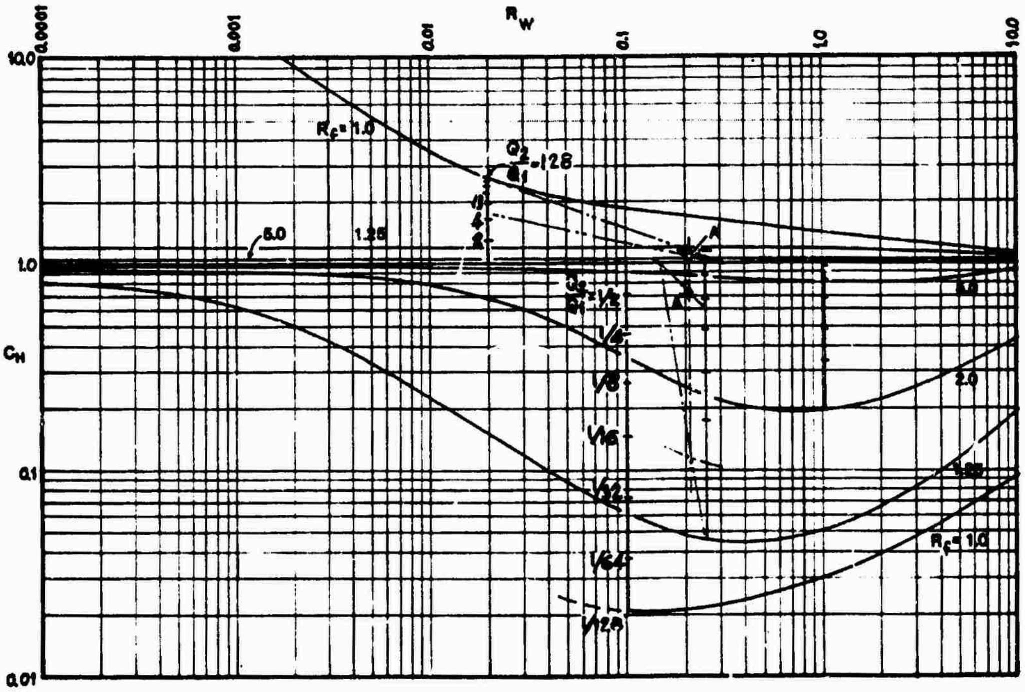

FIGURE 4 - CORRECTION FACTOR C_H, TO BE USED WHEN $Q_1 \neq Q_2$ AND $R_f \geq 1$

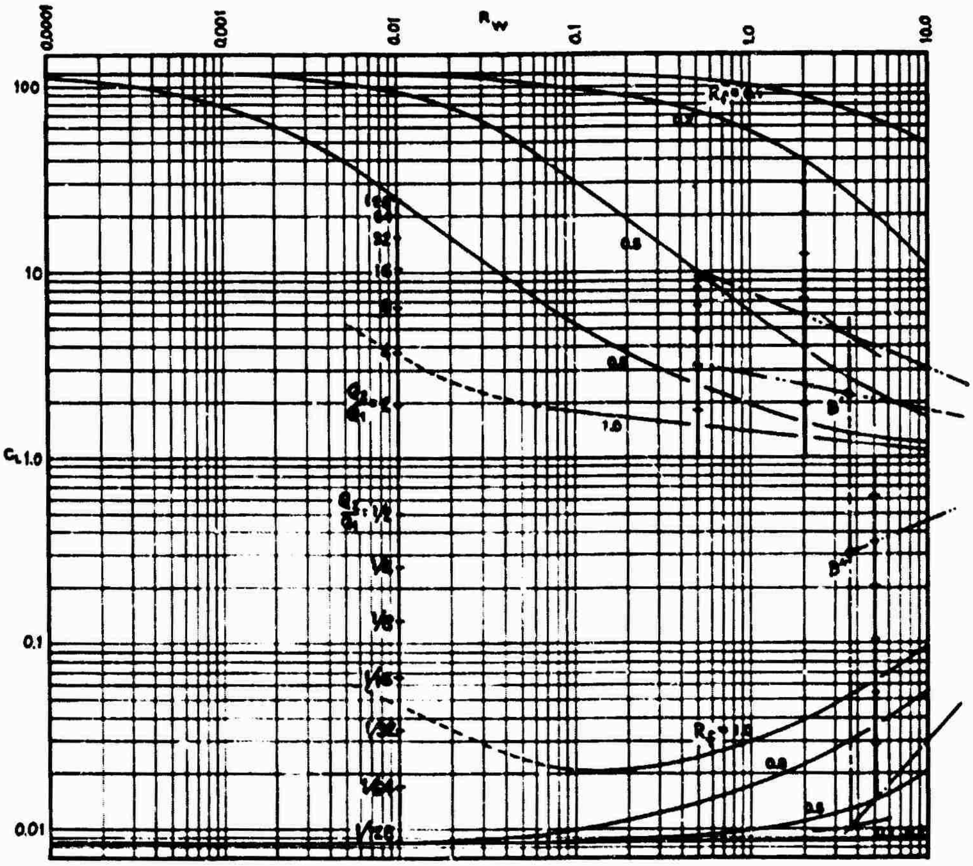

FIGURE 5 - CORRECTION FACTOR C_L, TO BE USED WHEN $Q_1 \neq Q_2$ AND $R_f \leq 1$

Q_{2L} = 2.2 x 1.8 x 4.5 = 17.8

If, on the other hand, the relationship between subsysem damping is changed to Q_2/Q_1 = 1/4, the lower part of Figure 5 is used. An estimate is made of the location of R_f = 0.4. The intersection of the R_f = 0.4 curve with the R_w = 3.57 line is at a point on the vertical scale which would be C_L if Q_2/W_1 = 1/128. Since Q_2/Q_1 = 1/4, interpolation is used to obtain C_L = 0.31.

EXAMPLE B"

If Q_2/Q_1 = 1/4 by decreasing Q_2 from 18 to 4.5,

Q_{2L} = 0.31 x 1.8 x 18 = 10

Of Q_2/Q_1 = 1/4 by increasing Q_1 from 18 to 72,

Q_{2L} = 0.31 x 1.8 x 72 = 40.2

SYSTEM RESONANCES VS. SUBSYSEM RESONANCES

As indicated earlier, the 2DOF resonant frequencies are always unique -- they are not the same as the isolated resonances of the subsystems. (As a matter of interest, however, if f_1 and f_2 differ from one another, the lower system frequency f_L is always lower than the lower of f_1 and f_2; conversely, the higher system frequency f_H is always higher than the higher of f_1 and f_2. In any event, knowing the positions of f_L & f_H with relation to f_1 & f_2 can be helpful if it is necessary to reduce the magnitude of Q_{2L}. If $f_1 = f_2$, then Q_{2L} can be reduced by increasing the damping (and thereby reducing the Q) of either subsystem. But if $f_1 \neq f_2$, then whichever subsystem resonant frequency is closer to f_L should be altered, as it is that subsystem which has the greater effect upon Q_{2L}.

In Example A' & A", a change in Q by a factor of 5:1 has the following effect on Q_{2L}:

Increase Q_2	Increase Q_1
Q_{2L} 51→56.1 (+105%)	Q_{2L} 51→181 (+255%)
Decrease Q_2	Decrease Q_1
Q_{2L} 51→36.2 (-29%)	Q_{2L} 51→11.2 (-78%)

In this example, f_1 = 140Hz, f_2 = 200Hz, and f_L = 122Hz, so altering the damping of subsystem 1 has a more dramatic affect on Q_{2L} than does altering the damping of subsystem 2. The reason is that f_1 is closer to f_L than is f_2.

In example B' & B", a change in Q by a factor of 4:1 has the following affect on Q_{2L}:

Increase Q_2	Increase Q_1
Q_{2L} 32.4→71.3 (+120%)	Q_{2L} 32.4→40.2 (+24%)
Decrease Q_2	Decrease Q_2
Q_{2L} 32.4→10 (-69%)	Q_{2L} 32.4→17 (-47%)

In this example, f_1 = 87Hz, f_2 = 35Hz, f_L = 27.4 Hz, so altering the damping of subsystem 2 has a greater effect on Q_{2L} than does changing the damping of subsystem 1, because f_2 is closer to f_L than is f_1.

ASSURING THAT Q_{2H} IS NOT GREATER THAN Q_{2L}

The assumption herein is that the lower resonant frequency, f_L, is the critical frequency, because the motion of W_2 is always greater at this frequency than at the higher mode resonance f_H. However, if the subsystem resonances are not equal ($f_1 \neq f_2$), and the subsystem with the higher frequency has <u>much</u> less damping than the other subsystem; that is, if $f_1 > f_2$, and $Q_1 \gg Q_2$

or, if $f_2 > f_1$, and $Q_2 \gg Q_1$

It is possible to have a motion at f_H greater than that at f_L. If this happened, and the likelihood is not realized during the design phase, then of course a failure could occur during vibration because the real critical situation was ignored.

To guard against this, Figure 6 can be used. The lower half is used for systems where $R_f < 1.0$.

(Acceptable Q_2/Q_1 ratios are to the upper right.)

The upper half is used for systems where $R_f > 1.0$.

(Acceptable Q_2/Q_1 ratios are to the lower right.)

For instance, assume R_f = 2.0.

If R_w = 0.01, find the place on the graph where R_w = 0.01 intersects R_f = 2.0. This point is at Q_2/Q_1=4.2, which means that if Q_{2H} is to be kept less than Q_{2L}, Q_2 must never be greater than 4.3 Q_1. As an example if Q_1 = 12, Q_2 mut be less than 4.3 x 12 = 50.4. If so, Q_{2H} will be lower than Q_{2L}. If R_w = 0.25, Figure 5 shows that Q_2/Q_1 must not be greater than 70, so if Q_1 = 5, & Q_2 remains less than 350, the resonant peak at f_H will always be less than that at f_L. Note that for larger w_2; i.e., $R_w >$ 0.3, regardless of R_f, the second mode peak will not exceed the first mode peak, Q_{2L}, even if the Q of the higher frequency sybsystem is 100 times that of the lower frequency subsystem. It can also be seen that for small w_2; i.e., $R_w < 0.1$, as R_f departs from 1.0, either to a higher or lower ratio, the system becomes more tolerant of large differences between Q_2 & Q_1, without allowing Q_{2H} to exceed Q_{2L}.

Note that for Examples A & B, the results are well within acceptable limits (B is off the graph) so that Q_{2L} is definitely the critical response for both examples.

RECOMMENDED RELATIONSHIPS BETWEEN ISOLATED RESONANCES, f_1 AND f_2

Because of the concern described earlier that Q_{2L} could possibly equal Q_1 and Q_2, a guideline called the Octave Rule has been established. This rule states that in order to prevent cascaded systems from responding with extraordinarily high Qs, the isolated resonance frequency of system 2 should be twice as high as the isolated resonance of system 1 -- in other words, the resonant frequency f_2 should be an octave above f_1. The idea behind the Octave Rule is the unrealistic but conservative assumption of no loading; that is, the addition of a load to a base will not result in two new natural frequencies, but that the isolated natural frequencies will remain unchanged upon connection of the two subsystems. Under such a situation the worst case would be if $f_1 = f_2$, whereupon the response at the load when excited at the natural frequency would be Q_1 x Q_2, obviously an undesirable result. To prevent this problem, the Octave Rule requires that $f_2 = 2f_1$, whereupon the response of the load will be T_1 x Q_2 at the natural frequency of the load. This would be 1.33 x Q_2.

Although the use of this Octave Rule can be helpful in leading to rugged design, it should not be applied indiscriminately. There are occasions when it could result in unnecessary cost and weight penalties. As a matter of fact, it may well be that going in the opposite direction, that is, designing system 2 (the load) to have an isolated resonant frequency lower than that of system 1 (the base) could prove to be easier and cheaper, and yet, still result in a sufficiently rugged design.

For example, Figure 7a shows the response of W_2 when R_f = 2.0, and Figure 7B when R_f = 0.5.

In both cases, the weight ratio is the same; R_w = 0.1, and $Q_1 = Q_2$ = 10. A comparison of Figures 7a & 7b shows that when R_f = 2.0, Q_{2L} = 13.5 at f_L = 94.5Hz and when R_f = 0.5, Q_{2L} = 13.77 @f_L = 49.5Hz. When the systems of R_f =2.0 and 0.5 are excited by sinusoidal vibration, therefore, there is practically no difference in the maximum response. The tradeoff is allowable displacement versus the stiffness requirement: the displacement per G of the system at 49.5Hz resonance is four times that of the 94.6Hz resonance, but the stiffness requirement for subsystem 2 for R_f = 0.5 need only be 1/16 as stiff as that for R_f = 2.0. This may be a compelling reason in itself to choose the lower resonant system for design. At least designers should be cognizant of this additional option.

Another consideration of the cascaded two degree of freedom system is its response to random vibration. With random excitation, motion exists at all frequencies throughout the spectrum simultaneously, so total RMS response must be measured, which is the sum of the motion at all frequencies.

In equation form, the response of a system to random excitation is:

$$G_{rms} = \sqrt{\int T^2(f)\, W(f)\, df}$$

This total RMS response is obtained by squaring the transmissibility plot, multiplying it by the input spectral density plot point by point along the frequency axis, summing the results, and taking the square root.

If we assume that the spectral density, $w_{(f)}$ is uniform throughout the applicable frequency range, the computation is eased, as the equation becomes:

$$G_{rms} = \sqrt{\int W\, T^2(f)\, df}$$

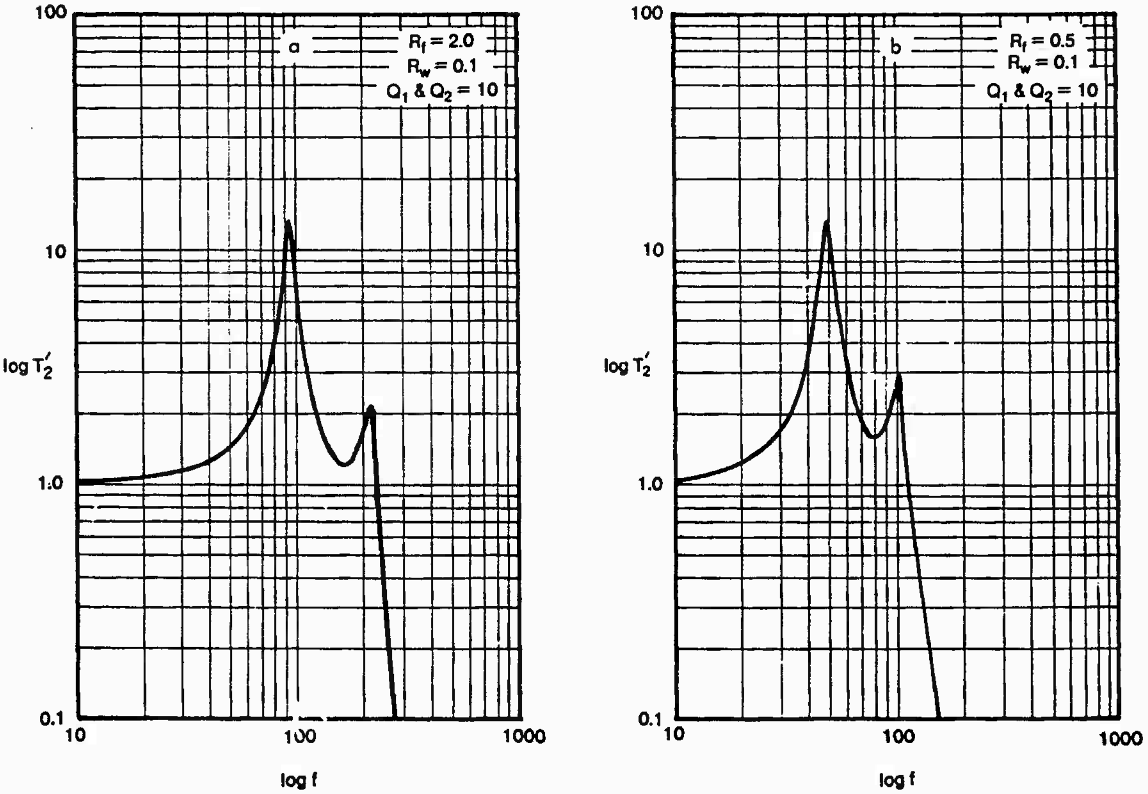

FIGURE 7 - RESPONSE OF CASCADED TWO DEGREE OF FREEDOM SYSTEMS

To compute relative responses among different systems, it is then merely necessary to determine the area under the appropriate transmissibility squared plot, and compare the square roots of the results.

The above process can be used to compare the responses of the $R_f = 1.0$, $R_f = 0.5$ and $R_f = 2.0$ systems to random vibration.

Figure 8 shows linear plots of T^2 vs. frequency of the three systems. The use of linear plots rather than log plots makes it easier to compute and to visualize the response of systems to random vibration. The results show that the random response of the $R_f = 2.0$ system is 0.56 that of the $R_f = 1.0$ system, and the response of the $R_f = 0.5$ system is 0.45 that of the $R_f = 1.0$ system. These results show that a system design of f_2 lower than that of f_1 can provide a good alternate solution to the cascade design problem for both random as well as for sinusoidal excitation, even if w_2 is significantly less than w_1.

CONCLUSION

A method is presented herein where the maximum response of a cascaded 2DOF system can be determined to reasonable accuracy, using graphical methods. The advantage of the use of graphs is that trends can be easily observed.

It is noted that good design practice does not necessarily require that the load (subsystem 2) be designed to have a higher resonant frequency than the base (subsystem 1). Rather, as it is shown, a satisfactory design may properly be one where f_2 is <u>lower</u> than f_1.

BIBLIOGRAPHY

a. Harris and Crede, "The Shock and Vibration Handbook,"second edition, McGraw - Hill, N.Y., 1976

b. Crede, "Shock and Vibration Concepts in Engineering Design," Prentice - Hall, 1965

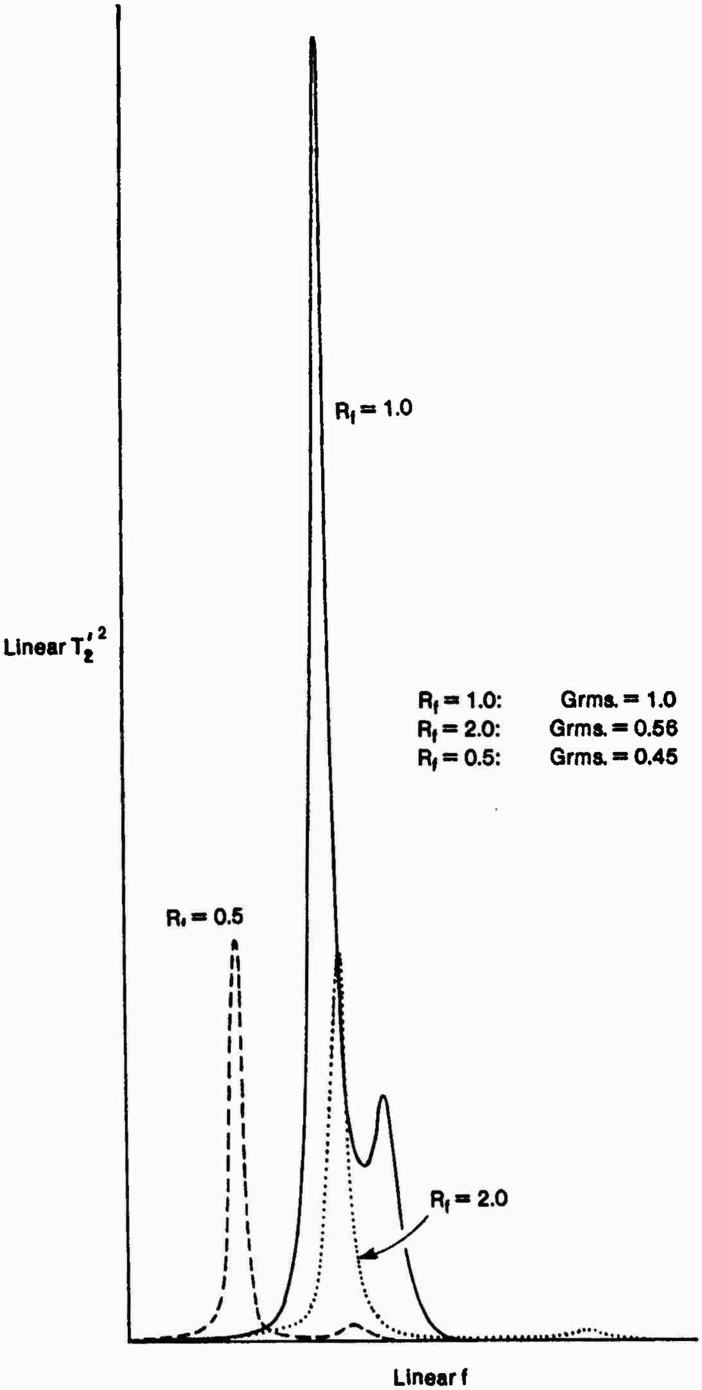

FIGURE 8 - RESPONSE OF 2DOF SYSTEMS TO RANDOM VIBRATION

APPENDIX: DERIVATION OF TRANSMISSIBILITY EQUATIONS

MASS 1: $m_1\ddot{Y}_1 + c_2(\dot{Y}_1 - \dot{Y}_2) + k_2(Y_1 - Y_2) + c_1(\dot{Y}_1 - \dot{Y}_0) + k_1(Y_1 - Y_0) = 0$

Rearranging, $m_1\ddot{Y}_1 + (c_1+c_2)\dot{Y}_1 + (k_1+k_2)Y_1 - c_2\dot{Y}_2 - k_2Y_2 = c_1\dot{Y}_0 + k_1Y_0$ ①

MASS 2: $m_2\ddot{Y}_2 + c_2(\dot{Y}_2 - \dot{Y}_1) + k_2(Y_2 - Y_1) = 0$

Rearranging, $-c_2\dot{Y}_1 - k_2Y_1 + m_2\ddot{Y}_2 + c_2\dot{Y}_2 + k_2Y_2 = 0$ ②

IF INPUT IS $Y_0 = Y_0 e^{j\omega t}$, SOLUTIONS CAN BE

$$Y_1 = Y_1 e^{j(\omega t+\phi_1)} = Y_1 e^{j\omega t} e^{j\phi_1} = \bar{Y}_1 e^{j\omega t}, \text{ where } \bar{Y}_1 = Y_1 e^{j\phi_1}$$

$$Y_2 = Y_2 e^{j(\omega t+\phi_2)} = Y_2 e^{j\omega t} e^{j\phi_2} = \bar{Y}_2 e^{j\omega t}, \text{ where } \bar{Y}_2 = Y_2 e^{j\phi_2}$$

SUBSTITUTING IN ① AND ②,

$$[-m_1\omega^2 + j\omega(c_1+c_2) + k_1+k_2]\bar{Y}_1 - [j\omega c_2 + k_2]\bar{Y}_2 = [j\omega c_1 + k_1]Y_0$$

$$-[j\omega c_2 + k_2]\bar{Y}_1 + [-m_2\omega^2 + j\omega c_2 + k_2]\bar{Y}_2 = 0$$

OR
$$\begin{bmatrix} -m_1\omega^2+k_1+k_2+j\omega(c_1+c_2) & -(k_2+j\omega c_2) \\ -(k_2+j\omega c_2) & -m_2\omega^2+k_2+j\omega c_2 \end{bmatrix} \begin{Bmatrix} \bar{Y}_1 \\ \bar{Y}_2 \end{Bmatrix} \begin{matrix} = \\ = \end{matrix} \begin{Bmatrix} k_1+j\omega c_1 Y_0 \\ 0 \end{Bmatrix}$$

SOLVING FOR $\bar{Y}_1$ AND $\bar{Y}_2$

$$\bar{Y}_1 = \frac{[(-m_2k_1+c_1c_2)\omega^2+k_1k_2+j\omega(k_1c_2+k_2c_1-m_2\omega^2c_1)]Y_0}{D} = \frac{[a_1+jb]Y_0}{D}$$

$$\bar{Y}_2 = \frac{[-c_1c_2\omega^2+k_1k_2+j\omega(k_1c_2+k_2c_1)]Y_0}{D} = \frac{[a_2+jb_2]Y_0}{D}$$

where

$$D = m_1m_2\omega^4-[k_1m_1+(m_1+m_2)k_2+c_1c_2]\omega^2+k_1k_2+j\omega\{k_1c_2+k_2c_1-[(m_1+m_2)c_2+m_2c_1]\omega^2\}$$

$$= a_d + jb_d$$

FINALLY, THE TRANSMISSIBILITIES ARE:

$$T_1' = \left|\frac{\bar{Y}_1}{Y_0}\right| = \sqrt{\frac{a_1^2+b_1^2}{a_d^2+b_d^2}}$$

$$T_2' = \left|\frac{\bar{Y}_2}{Y_0}\right| = \sqrt{\frac{a_2^2+b_2^2}{a_d^2+b_d^2}}$$

TEMPERATURE SHIFT CONSIDERATIONS FOR DAMPING MATERIALS

Dr. Lynn Rogers
AFWAL/FIBA
Area B - Bldg. 45 - Rm. 257
Wright-Patterson AFB, OH 45433
(513) 255-3738 or -5664

Presented at the 56th Shock and Vibration Symposium
October 1985

For the temperature shift function for a particular damping material to be obtained, it must be implicitly defined by a set of complex modulus data. Historical procedures have been marginal because frequency ranges have not been adequate. A new procedure for such data is proposed based on the slope of the temperature shift function, on a fractional model of complex modulus and on apparent activation energy considerations.

INTRODUCTION

For many viscoelastic damping materials, or at least as a first approximation, the dynamic mechanical properties are thermorheologically simple. In particular, the complex modulus

$$G^* = G^*(f_R) \qquad \text{E1}$$

is a function of the reduced frequency

$$f_R = f\alpha_T \qquad \text{E2}$$

which is a product of the actual frequency and the well-known temperature shift function. It is often desirable to divide by a reference reduced frequency and use logarithmic scales

$$\log(f_R/f_{RO}) = \log f + \log \alpha_T - \log f_{RO} \qquad \text{E3}$$

Expressions for the partial derivatives

$$\partial \log G^*/\partial T = (d \log G^*/d \log f_R)(\partial \log f_R/\partial T) = (d \log G^*/d \log f_R)(d \log \alpha_T/dT) \qquad \text{E4}$$

and

$$\partial \log G^*/\partial \log f = (d \log G^*/d \log f_R)(\partial \log f_R/\partial \log f) = d \log G^*/d \log f_R \qquad \text{E5}$$

will be needed.

In the typical explanation of frequency-temperature equivalence [1], a temperature shift curve or function is constructed for each particular set of complex modulus data. The real part (R), the imaginary part (I), and the material loss factor (η) of the complex modulus data are plotted as a function of the reduced frequency. For convenience, the expression for the temperature shift function is usually taken to be unity at the reference temperature. With reference to E1 and E3, the effect of a constant in the temperature shift function, α_T, is to shift the experimental data horizontally, whereas the effect of a reference reduced frequency is to shift any analytical representation horizontally. Historically, the α_T for a particular damping material has been defined empirically by the experimental complex modulus data. The value of α_T at each experimental temperature is selected such that it simultaneously shifts horizontally the three complex modulus data points (R,I,η) to define curves and minimize scatter.

With usage of computers it is convenient to fit the empirical α_T curve with a suitable analytical function.

By contrast to the historical focus on α_T, the present focus is on its slope. Consider complex modulus data taken at the three temperatures, T_1, $(T_1 + \Delta_{1a})$, and $(T_1 - \Delta_{1b})$. For both the data taken at $(T_1 + \Delta_{1a})$ to be shifted to that at T_1,

$$\text{shift } (\Delta_{1a}) = \log \alpha_T(T_1) - \log \alpha_T(T_1 + \Delta_{1a})$$

and the data taken at $(T_1 + \Delta_{1b})$ to be shifted

$$\text{shift } (\Delta_{1b}) = \log \alpha_T(T_1 + \Delta_{1b}) - \log \alpha_T(T_1)$$

and from calculus approximations to derivatives, it follows that

$$\frac{\log \alpha_T(T_1 + \Delta_{1a}) - \log \alpha_T(T_1)}{\Delta_{1a}}$$

$$\approx \frac{\log \alpha_T(T_1) - \log \alpha_T(T_1 - \Delta_{1b})}{\Delta_{1b}}$$

$$\approx \left. \frac{d \log \alpha_T}{dT} \right|_{T = T_1}$$

The satisfactory horizontal shift of complex modulus curve segments is clearly dependent on the slope or derivative of α_T rather than the value of α_T, and that the slope is also a function of T.

WLF EQUATION

A commonly used representation for the temperature shift function is the WLF equation

$$\log \alpha_T = - C_1 D_T/(C_2 + D_T);$$

$$T > T_Z - C_2; \quad D_T = T - T_Z \qquad \text{E6a}$$

which may be written

$$\log \alpha_T = - S_{AZ} D_T/(1 + D_T/C_2) \qquad \text{E6b}$$

where

$$S_{AZ} \equiv C_1/C_2 \qquad \text{E7}$$

Taking the derivative of E6b yields

$$- d(\log \alpha_T)/dT = S_{AZ}/(1 + D_T/C_2)^2 \qquad \text{E8}$$

The slope given by E8 is normalized and plotted in F1 for representative values of the parameter.

EXPONENTIAL EQUATION

Another expression is the exponential

$$\log \alpha_T = - N \log(1 + D_T/C_e);$$

$$T > T_Z - C_e \qquad \text{E9}$$

which may be written

$$\log \alpha_T = -2.3\ C_e S_{AZ} \log(1 + D_T/C_e) \qquad \text{E10}$$

where

$$S_{AZ} \equiv N \log e/C_e \qquad \text{E11}$$

The slope corresponding to the exponential is

$$- d(\log \alpha_T)/dT = S_{AZ}/(1 + D_T/C_e) \qquad \text{E12}$$

and is plotted in F2.

ARRHENIUS EQUATION

The Arrhenius equation is written in the form

$$\log \alpha_T = a_2 R_T \qquad \text{E13}$$

where

$$R_T = 1000/T - 1000/T_Z; \quad T > 0 \qquad \text{E14}$$

and using

$$S_{AZ} \equiv 1000\ a_2/T_Z^2 \tag{E15}$$

may be written

$$\log \alpha_T = (S_{AZ}T_Z^2/1000)R_T \tag{E16}$$

from which

$$-\ d(\log \alpha_T)/dT = S_{AZ}/(1 + D_T/T_Z)^2 \tag{E17}$$

and this is plotted in F1. Alternatively E17 may be written

$$-\ d(\log \alpha_T)/dT = S_{AZ}T_Z^2/T^2 \tag{E18}$$

APPARENT ACTIVATION ENERGY

For some purposes, it is of interest to display the apparent activation energy [2, p. 289, (44)]

$$\Delta H_A = -2.303\ R\ T^2\ d\ \log \alpha_T/dT \tag{E19}$$

where the gas constant is

$$R = 0.00828\ \text{Newton}\cdot\text{kilometers}/\text{gram}\cdot\text{mole}\cdot{}^\circ\text{K}$$

In general, the apparent activation is a function of T. When E18, the slope for the Arrhenius equation, is substituted into E19, we obtain

$$\Delta H_A = 2.303\ R\ S_{AZ}\ T_Z^2 \tag{E20}$$

which is independent of temperature, the standard result for the Arrhenius form.

SLOPE QUADRATIC IN 1/T

This paper proposes the representation for the derivative or slope

$$-\ d(\log \alpha_T)/dT = a(1/T-1/T_Z)^2 + b(1/T-1/T_Z) + S_{AZ} \tag{E21}$$

as the most workable for many damping materials.

Integrating the above representation leads to

$$\log \alpha_T = a(1/T-1/T_Z) + 2.303(2a/T_Z - b)\log T/T_Z + (b/T_Z-a/T_Z^2 - S_{AZ})(T-T_Z) \tag{E22}$$

where the constant of integration has been chosen for convenience to make α_T unity (or log zero) at the reference temperature. The coefficients may be evaluated by fitting the slope through the three points

Slope	Temp	
S_{AZ}	T_Z	E23a
S_{AL}	T_L	E23b
S_{AH}	T_H	E23c

The form of the equation E21 inherently satisfies E23a. Substituting E23b and c results in

$$a(1/T_L-1/T_Z)^2 + b(1/T_L-1/T_Z) + S_{AZ} = S_{AL} \tag{E24a}$$

$$a(1/T_H-1/T_Z)^2 + b(1/T_H-1/T_Z) + S_{AZ} = S_{AH} \tag{E24b}$$

Letting

$$C_A = (1/T_L - 1/T_Z)^2 \tag{E25a}$$

$$C_B = (1/T_L - 1/T_Z) \tag{E25b}$$

$$C_C = S_{AL} - S_{AZ} \tag{E25c}$$

$$D_A = (1/T_H - 1/T_Z)^2 \tag{E26a}$$

$$D_B = (1/T_H - 1/T_Z) \tag{E26b}$$

$$D_C = S_{AH} - S_{AZ} \tag{E26c}$$

$$D_E = D_BC_A - C_BD_A \tag{E27}$$

it follows that the coefficients are evaluated

$$a = (D_BC_C - C_BD_C)/D_E \tag{E28a}$$

$$b = (C_A D_C - D_A C_C)/D_E \qquad \text{E28b}$$

If it happens that

$$a = S_{AZ}\, T_Z^2; \quad b = 2\, S_{AZ}\, T_Z \qquad \text{E29}$$

then this representation reduces to the Arrhenius case. This is a major attraction.

The apparent activation energy for this case is found by substituting E21 into E19

$$\Delta H_A = 0.001907\, [a(1 - \frac{T}{T_Z})^2 + bT(1 - \frac{T}{T_Z}) + S_{AZ} T^2] \qquad \text{E30}$$

SPECIFIC CURVES [3]

Two specific curves used for vibration damping materials were developed empirically and the convenient exponential equation (E9) was adapted. One curve was developed for use with polymers and is designated "ADN" with the parameters

$$N = 11$$

$$C_e = 175.6064/1.8 = 97.5591 \simeq 100.$$

$$S_{AZ} = 0.0489676 \simeq 0.05 \qquad \text{E31a}$$

The WLF equation approximates this curve when

$$C_1/C_2 = 9/175 = 0.0514 \simeq 0.05$$

$$C_2 = 315/1.8 = 175. \qquad \text{E31b}$$

The "DIGJ" curve was developed for the larger temperature ranges required by enamels and is given by

$$N = 14$$

$$C_e = 278/1.8 = 154.44 \simeq 155.$$

$$S_{AZ} = 0.03937 \simeq 0.04$$

$$C_1/C_2 = 12/291.7 = 0.04114 \simeq 0.04$$

$$C_2 = 525/1.8 = 291.7 \simeq 290. \qquad \text{E32}$$

The exponential slope E12 is compared in F3 for the two sets of parameter values given by E31 and E32. It may be seen that the slopes as a function of temperature, T, (rather than of D_T) can be caused to approximate each other more closely by an appropriate choice of T_Z. These two curves are defined by the exponential representation. The curves were determined empirically, and the exponential equation and the parameter values are also empirical. The quadratic in 1/T is an adequate approximation over some range of D_T (probably sufficient for engineering interest) because the curves are themselves approximations as noted above.

DETERMINATION OF THE TEMPERATURE SHIFT FUNCTION

The temperature shift function is implicitly defined by the set of complex modulus data. Historically, the function has been found by shifting data horizontally until curves were defined and scatter minimized; where there is a marginal experimental frequency range, this is not completely satisfactory. It happens that there are theoretical relationships that may be used to determine the slope of α_T from experimental data. The basis of this procedure is the hypothesis that the complex modulus as a function of reduced frequency is adequately approximated in the range of interest by

$$G^* = [G_e + G_g (jr)^{\beta}]/[1 + (jr)^{\beta}]; \quad r = f_R/f_{RO} \qquad \text{E33}$$

which contains fractional powers [4]. Note that as shown by F4, the slope of the magnitude, real and imaginary, in the transition region is a constant. Because the slope of the imaginary is also constant below the transition, it is more convenient and is used. The imaginary component of E33 is

$$G_I = \sin 90\beta (G_g - G_e) r^{\beta}/(1 + 2\cos 90\beta\, r^{\beta} + r^{2\beta})$$

which in the range of interest is proportional to

$$G_I \underset{-}{\propto} r^{\beta}; \quad r < 0.01$$

It follows that

$$\log G_I \overset{\alpha}{=} \beta \log f_R;$$

$$d \log G_I / d \log f_R = \beta \qquad \text{E34}$$

This result may be substituted into the imaginary part of E4 to give

$$(\partial \log G_I/\partial T) = \beta(d \log \alpha_T/dT) \qquad \text{E35}$$

The desired slope is evaluated once the two quantities $\partial \log G_I/\partial T$ and β are determined.

The complex modulus (i.e., the real modulus, the imaginary modulus, and their ratio or loss factor) depends on both temperature and frequency. Temperature is dominant; and the present context is that experimental frequency is marginal (at least to determine α_T). It is necessary to adjust experimental data for the effect of frequency

$$G_I(f_{exp}, T_{exp}) \rightarrow G_{IA}(f_A, T_{exp}) \qquad \text{E36a}$$

$$G_R(f_{exp}, T_{exp}) \rightarrow G_{RA}(f_A, T_{exp}) \qquad \text{E36b}$$

$$\eta(f_A, T_{exp}) = G_{IA}/G_{RA} \qquad \text{E36c}$$

where f_A is a frequency representative of a particular data set, e.g., a geometric average of experimental frequencies. In order to make these adjustments, E34 is substituted into E5

$$\partial \log G_R/\partial \log f = \beta;$$

$$\partial \log G_I/\partial \log f = \beta \qquad \text{E37}$$

or approximately

$$\log G_{RA} - \log G_{Rexp} = \beta(\log f_A - \log f_{exp})$$

or

$$G_{RA} = G_{Rexp}(f_A/f_{exp})^{\beta} \qquad \text{E38a}$$

and similarly

$$G_{IA} = G_{Iexp}(f_A/f_{exp})^{\beta} \qquad \text{E38b}$$

and therefore in the middle of the transition region

$$\eta_A = \eta_{exp}$$

This last equation indicates the validity of fitting a polynomial in temperature

$$\eta = \sum_{k=o}^{N} C_{D_k} T^k \qquad \text{E39}$$

and determining η_{max} and T_Z and its temperature. Accurate representation of properties in the transition is of interest because of possible engineering applications in this region; consequently, the temperature of η_{max} is chosen as the reference.

The next step is to determine β. The expression for η_{max} may be developed from E33

$$\eta_{max} = \frac{(1 - 1/A) \tan\beta\pi/2}{1 + 1/A + 2/A^{1/2} \cos\beta\pi/2};$$

$$A = G_g/G_e \qquad \text{E40}$$

Numerically this equation may be solved iteratively, and the parameter A may be approximated from experimental data.

With β known the imaginary modulus may be adjusted using E38b and fitted to a polynomial

$$\log G_{IA} = \sum_{k=o}^{N} C_{Ak} T^k \qquad \text{E41}$$

and the slope

$$\partial \log G_I/\partial T = d \log G_{IA}/dT = \sum_{k=1}^{N-1} k\, C_{Ak} T^{k-1};$$

$$T \geq T_Z \qquad \text{E42}$$

evaluated as a function of T or at specific points such as T_Z and at a higher temperature, T_H.

It follows that

$$S_{AZ} = \left(d \log G_{IA}/dT \Big|_{T = T_Z}\right)/\beta \qquad \text{E43}$$

and

$$S_{AH} = (d \log G_{IA}/dT\Big|_{T = T_H})/\beta \qquad \text{E44}$$

At this juncture, two points (T_Z, S_{AZ}) and (T_H, S_{AH}) have been defined, and a third relationship is required. It is supplied by hypothesizing that at T_L, a temperature in the glassy region, the apparent activation energy, is a constant, or the derivative

$$d\Delta H_A/dT \underset{-}{\propto} 2a(T/T_Z - 1)/T_Z + b(1 - 2T/T_Z) + 2TS_{AZ} \qquad \text{E45}$$

is set equal to zero at T_L

$$a(2T_L/T_Z^2 - 2/T_Z) + b(1 - 2T_L/T_Z) + 2T_LS_{AZ} = 0 \qquad \text{E46}$$

This may be used as one of two equations

$$C_A = 2(T_L/T_Z - 1)/T_Z \qquad \text{E47a}$$

$$C_B = 1 - 2T_L/T_Z \qquad \text{E47b}$$

$$C_C = -2T_LS_{AZ} \qquad \text{E47c}$$

in lieu of E25. F5 characterizes a temperature shift function obtained by this procedure.

NON-MONOTONIC SLOPE

It is possible to choose values for the WLF parameters S_{AZ}, C_2, and T_Z in E8 to give specified values of slope at three temperatures only if the slope is monotonic as in F1. The same conclusion applies to the exponential parameters in E12 and F2. Some materials possess temperature shift curves with a slope which has an upright "U" shape or an inverted "U" shape. These functions cannot be represented by conventional expressions, but can be easily described by the quadratic in 1/T.

DISCUSSION

Very limited usage with experimental complex modulus data together with engineering judgment suggests that the quadratic in 1/T as determined by the slopes is accurate and efficient. The greatest advantage is that the various temperature regions of data may be considered independently or in uncoupled fashion. That is, the parameter determining slope in only the glassy region, or the transition, or the rubbery, may be determined while not affecting the others.

Another very obvious advantage is representation of a much more general type of slope curve than has been possible in the past. Only experience with viscoelastic materials of interest will determine general adequacy.

It is worthy of note that the reference temperature has no physical significance here; it should be considered to be an empirical parameter which happens to have units of temperature.

REFERENCES

1. Jones, D. I. G., "Temperature-Frequency Dependence of Dynamic Properties of Damping Materials," Journal of Sound and Vibration, Vol. 22, n. 4, 1974, pp 451-470.

2. Ferry, John D., Viscoelastic Properties of Polymers, John Wiley and Sons, 3rd ed., 1980.

3. Rogers, Lynn and Ahid D. Nashif, "Computerized Processing and Empirical Representation of Viscoelastic Material Property Data and Preliminary Constrained Layer Damping Treatment Design," The Shock and Vibration Bulletin, No. 48, September 1978, Part 2, pp 23-37.

4. Rogers, Lynn, "Operators and Fractional Derivatives for Viscoelastic Constitutive Equations," J. Rheology, 27(4), pp 351-372 (1983).

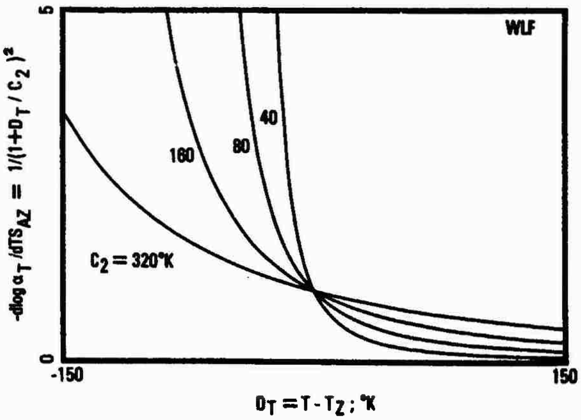

Fig. 1 — WLF normalized slope vs temperature difference

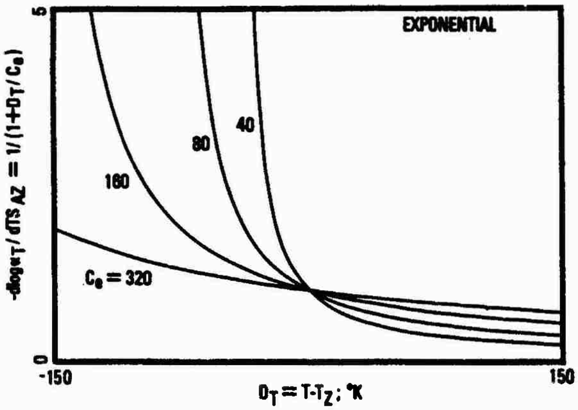

Fig. 2 — Exponential normalized slope vs temperature difference

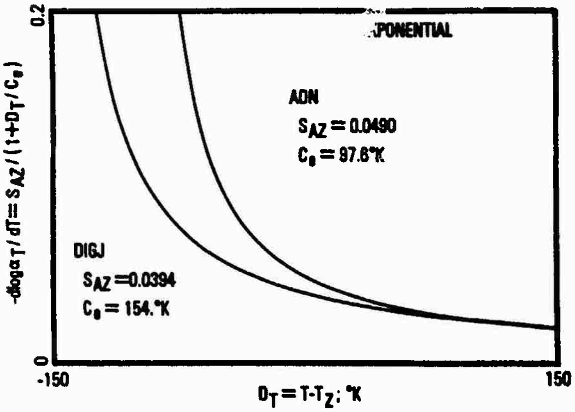

Fig. 3 — Slope vs temperature difference for two curves

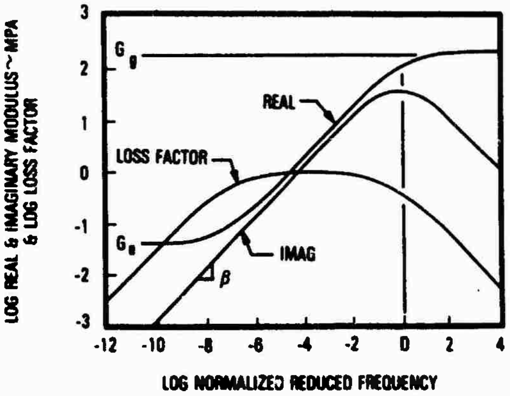

Fig. 4 — Complex modulus

Fig. 5 — Temperature shift function and its properties

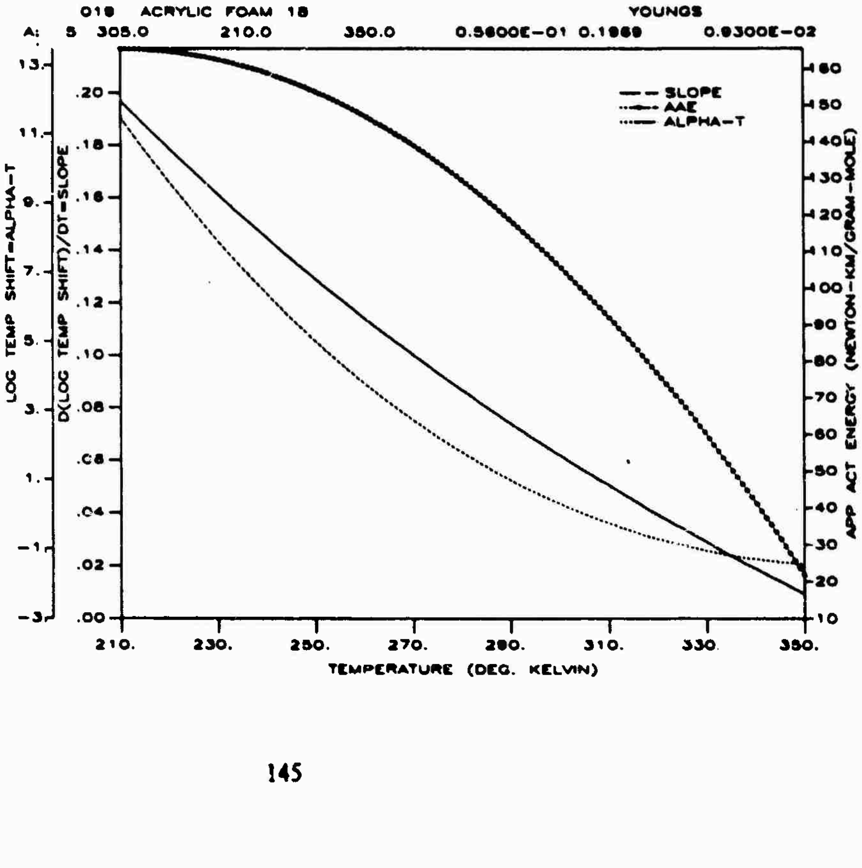

Discussion

Mr. Zak (University of Illinois): Using those fractional derivatives for visco-elastic characterization is opposed to something like the convolution integral or the differential form that has been used over the years. Can you apply this to real time problems or is it used in the frequency domain only? When you calculate the beta, can you have the real time in visco-elastic equations with this fractional derivative formulation, or does it strictly have to be in the frequency domain?

Mr. Rogers: To answer your question as directly as I can, there is a textbook on fractional calculus, but it is not really well known at this particular point, nor are the Laplace transform pairs, and the Fourier transform pairs well known. For the equation I showed, you can take the Fourier transform, or the Laplace transform, and get an explicit, closed form solution for the relaxation modulus and the creep compliance. If you are willing to forego very short time effects, then there are approximate closed form equations that let you get back and forth between the frequency domain and the time domain for relaxation and for creep.

Mr. Zak: Can't you do the whole thing by characterizing your shift function through the other methods that have often been used in the solid propellent rocket business, through the convolution and the Prony series and things of this nature? Or does this give you something you can not do the other way?

Mr. Rogers: The attraction of the fractional calculus, for me, is the great economy of terms. With the Prony series, and a couple other series, you need at least 20 terms, and two constants per term, so you are talking about something like 40 parameters to be evaluated for a particular visco-elastic material to cover a wide frequency range. With fractional calculus, you can do it with something like six terms. You can view the fractional calculus as being empirical, or you can say that because of the economy of terms, there may be some relationship to the very small scale polymer dynamics theory. However, you are right. The convolution integrals, the series types are all satisfactory and workable. I feel there is an economy of computer time and storage to be had by using a fractional calculus.

Mr. Rath (Naval Research Laboratory): You indicated that the activation energy of the Arrhenius equation can be predicted as a constant. Activation energy, which is temperature dependent, is usually state related to that method. Did you say you extended it to the glass transition temperature when the state of the matter is changing? If so, I have difficulty realizing the activation energy will remain at the same value.

Mr. Rogers: The chapters, or the material, that I have read state that Arrhenius temperature shift function, 1/T, gives a constant activation energy, and in fact, it is appropriate in the glassy region of visco-elastic materials. The attractive thing about the quadratic, and 1/T for the slope, is that term is included in the alpha T that results. The other attractive thing is it is not mandatory that you have a monotonic function in alpha T, and there have been some actual materials that do not have it. However, other than that, I am not really prepared to remark about apparent activation energy.

EFFECTIVENESS OF ON-OFF DAMPER IN ISOLATING DYNAMICAL SYSTEMS

S. Rakheja
Research Assistant Professor

S. Sankar
Professor

Department of Mechanical Engineering
Concordia University
Montreal, Canada

Concept of vibration isolation through an on-off damper is investigated. A number of on-off damper control schemes are proposed and analyzed for their isolation performance. The vibation isolation characteristics of the proposed on-off dampers are evaluated through computer simulations and compared to that of a passive damper. Effectiveness of the on-off damper is investigated for single degree-of-freedom system with rigid as well as elastically coupled damper. Isolation characteristics of Ruzicka relaxation isolator and Snowdon's two inertia vibration isolation system with on-off damping are evaluated and compared to the optimal passive isolators. Isolation performance of on-off damper is also investigated for multi-degrees-of-freedom dynamical systems.

INTRODUCTION

Passive shock and vibration isolation systems are undoubtedly the most simple, inexpensive, and reliable means to protect dynamical systems from shock and vibration inputs. Design of an effective isolator involves the selection of suitable spring and damper such that the acceleration transmitted to the payload is minimized. Pass- ive isolators employing optimal linear or non-linear springs and dampers have been extensively investigated by various researchers. However, the inherent per- formance limitations of passive isolators, specifically due to fixed damping, are well known. It has been well established that the isolation performance of an isolator with variable parameters is far superior to that of an isolator with fixed parameters [1].

Active vibration isolation systems with parameters that change automatically with response and excitation variables, provide superior isolation performance. However, active systems in-general, are more costly, more complex and therefore less reliable. Thus the implementation of active shock an vibration isolation systems has been limited to cases, where the performance benefits outweigh the disadvantages of increased costs, complexity and weight [2,3]. Recognizing as both the performance benefits well as limitations of active systems, the concept of semiactive vibration isolation system has been developed [4]. Semiactive isolators require only low level electrical power for the necessary signal processing and provide extremely superior isolation performance than the passive isolators. Semiactive force generators based on inertial (skyhook) damping has been proposed and analyzed by Karnopp et. al. [4] and Margolis [5]. Concept of externally controlled active damper has been analyzed by Crosby and Karnopp [6].

Semiactive isolation systems in general, are similar to the passive isolators in that all suspension elements generate their respective forces passively. However, it is assumed that the damping force generated by the damper can be varied instantaneously. The semiactive dampers proposed in the literature [4,5] generate damper force passively while the sign of the generated force being altered by the semiactive controller. Skyhook semiactive control can provide isolation performance very similar to that of an active system. Although the hardware implementation of such semiactive force generator is significantly simpler and less costly than a complex active vibration control system. The cost and complexity of the skyhook control may still be prohibitive for general applications.

In an attempt to simplify the hardware implementation and to reduce the cost of such semiactive force generators, to a point where general use is feasible, a simplified on-off damper scheme utilizing the absolute and relative velocities of the mass has been proposed

proposed and analyzed [7,8,9]. However, the measurement of absolute velocity, specifically for low frequency applications, may pose certain complexities [10]. In this investigation, a number of on-off damper schemes are analyzed to establish their effectiveness for single as well as multi degrees-of-freedom dynamical systems.

ON-OFF DAMPER CONCEPT

Consider a conventional SDOF spring-mass damper system shown in Figure 1. The acceleration response of the suspended mass due to base excitation can be expressed as;

$$\ddot{x} = -\frac{1}{m}(F_k + F_d) \tag{1}$$

where F_k and F_d are spring and damper forces, respectively. Assuming linear coefficients, the suspension forces are expressed as;

$$F_k = K(x - x_0)$$
$$F_d = C(\dot{x} - \dot{x}_0) \tag{2}$$

where K and C are constant spring rate and damping coefficient, respectively. From the steady state trace of inertia force and suspension forces (Figure 2), it can be established that the amplitude of mass acceleration is

$$|\ddot{x}| = (|F_k| + |F_d|)/m \text{ for } \begin{cases} t_0 < t < t_0 + \tau/4 \\ t_0 + \tau/2 < t < t_0 + 3\tau/4 \end{cases} \tag{3}$$

$$|\ddot{x}| = (|F_k| - |F_d|)/m \text{ for } \begin{cases} t_0 + \tau/4 < t < t_0 + \tau/2 \\ t_0 + 3\tau/4 < t < t_0 + \tau \end{cases} \tag{4}$$

where τ is the period of oscillation. It is evident from equation (3) that the damper force tends to increase the amplitude of mass acceleration during a part of the vibration cycle. The damper force tends to reduce the magnitude of mass acceleration during the remaining part of vibration cycle as demonstrated by equation(4). Poor vibration isolation performance of heavily damped passive systems is attributed to this phenomenon. Deteriorated isolation performance of heavily damped passive isolators becomes more obvious at higher excitation frequencies, when the magnitude of damping force dominates over the spring force. An analogus phenomenon also exists in the passive shock isolation systems. Various dual phase damping mechanisms have been proposed and analyzed to improve the shock isolation characteristics of passive shock isolators [11,12].

An on-off damping mechanism may be realized, which operates as a conventional passive damper with high coefficient of damping during the part of vibration cycle when it acts to reduce the amplitude of mass acceleration. The damping mechanism may be switched off during the portion of the cycle when a passive damper would normally increase the amplitude of mass acceleration. Shock isolation characteristics of such an on-off damper have been investigated in previous studies [13]. Such an on-off mechanism may be accomplished by introducing a two position valve operated by a solenoid relay, to a conventional hydraulic damper. The on-off valve offers certain orifice restriction to the hydraulic flows (high damping) during the on-cycle operation of the damper. The orifice size is modulated to its maximum opening during the off-cycle operation resulting from restrictions offered by the orifice modulated to its largest opening. Moreover, the damping force generated by the on-off damper is of velocity square nature due to orifice flows, while neglecting leakage flows and seal friction [14]. However, passive damping either viscous or velocity squared, exhibit identical behaviour as presented in equations (3) and (4).

ON-OFF CONTROL STRATEGY

Karnopp [4] established that the damping force tends to increase the magnitude of mass acceleration when the sign of absolute velocity of mass opposes the sign of relative velocity. Damper force reduces the magnitude of mass acceleration when absolute velocity of the mass bears the same sign as the relative velocity of mass. Thus a semiactive inertial damper is formulated such that the damper force is reduced to zero when the absolute velocity of mass opposes the relative velocity. The force generated by the semiactive inertial damper is thus expressed as:

$$F_d = \begin{cases} C\dot{x} & \text{for} \quad \dot{x}(\dot{x} - \dot{x}_0) > 0. \\ 0 & \text{for} \quad \dot{x}(\dot{x} - \dot{x}_0) < 0. \end{cases} \tag{5}$$

Two cases may arise when $\dot{x}(\dot{x} - \dot{x}_0)$ is exactly zero. The damper force must be zero when $\dot{x} = 0$. The damper experiences a lock up when $(\dot{x} - \dot{x}_0) = 0$. Such a skyhook semiactive damper can be realized in practice but only at the expense of considerable sophistication. Alternatively, a number of simplified on-off damper schemes are proposed in the following sections.

On-Off Damper I

Krasnicki [8] analyzed a simplified on-off damper based on the above control scheme. The damper force in the case of on-off damper is generated entirely passively and is expressed as:

$$F_d = \begin{cases} C(\dot{x} - \text{[illegible]}) & \text{For} \quad \dot{x}(\dot{x} - \dot{x}_0) > 0. \\ 0. & \text{For} \quad \dot{x}(\dot{x} - \dot{x}_0) < 0. \end{cases} \tag{6}$$

Such an on-off damping force generator may be realized by introducing a two position on-off valve to a conventional passive damper. The damper. The damper force generated is negligible when the valve is modulated to its maximum opening. Realistically, the damping force generated follows the velocity square law due to orifice flows. Moreover, the damper generates a small amount of force during its off-cycle, when the orifice is modulated to its maximum opening. Thus, the on-off damper force can be expressed in the following manner:

$$F_d = \begin{cases} C_v\left|\dot{x} - \dot{x}_0\right|(\dot{x} - \dot{x}_0) & \text{if } \dot{x}(\dot{x} - \dot{x}_0) > 0. \\ C_v'\left|\dot{x} - \dot{x}_0\right|(\dot{x} - \dot{x}_0), & \text{if } \dot{x}(\dot{x} - \dot{x}_0) < 0. \end{cases} \tag{7}$$

where C_v is the coefficient of velocity square damping and C_v' is a fraction of C_v representing the coefficient of damping corresponding to the orifice modulated to its maximum opening. This control scheme is quite simple to implement with a two position on-off valve, however the measurement of absolute velocity may introduce certain complexities.

On-Off Damper II

Alternatively, a second switching scheme devised from the concept of on-off damper is considered. From equations (3) and (4), it was established that damper force causes an increase in amplitude of mass acceleration, whenever forces due to spring and damper bear the same sign. The mass acceleration decreases when damper force opposes the spring force. Since the directions of damper and spring forces are proportonal to the sign of relative velocity and relative displacement respectively, the on-off scheme can be established in the following manner:

$$F_d = \begin{cases} C_v\left|\dot{x}-\dot{x}_0\right|(\dot{x}-\dot{x}_0), & \text{if } (\dot{x}-\dot{x}_0)(\dot{x}-\dot{x}_0) < 0. \\ C_v'\left|\dot{x}-\dot{x}_0\right|(\dot{x}-\dot{x}_0), & \text{if } (\dot{x}-\dot{x}_0)(\dot{x}-\dot{x}_0) > 0. \end{cases} \tag{8}$$

The on-off damper operating with this control scheme will act as a conventional orifice damper with high damping coefficient (C_v), when the sign of relative velocity opposes the sign of relative displacement across the damper. The damper operates with significantly lower value of damping coefficient (C_v'), when the sign of relative velocity across the damper carries the same sign as the relative displacement. This on-off scheme has an advantage over the scheme of damper I in the sense that it utilizes the signal from directly measurable variables.

On-Off Damper III

The acceleration response characteristics of on-off damper in-general, exhibit discontinuities at the time of switching Thus, a significant magnitude of jerk is experienced by the system mass. A third on-off scheme is devised to minimize the jerk experienced by the isolator mass. The control scheme is formulated in the following manner:

$$F_d = \begin{cases} C_v\left|\dot{x}-\dot{x}_0\right|(\dot{x}-\dot{x}_0), & \text{if} (\dot{x}-\dot{x}_0)(\ddot{x}-\ddot{x}_0) > 0 \\ C_v'\left|\dot{x}-\dot{x}_0\right|(\dot{x}-\dot{x}_0), & \text{if} (\dot{x}-\dot{x}_0)(\ddot{x}-\ddot{x}_0) < 0 \end{cases} \tag{9}$$

Such an on-off damper operates as a conventional damper with high value of damping coefficient (C_v), when relative velocity carries the same sign as the relative acceleration of the mass with respect to base. The damping coefficient is significantly reduced when the relative velocity across the damper opposes the relative acceleration of the mass with respect to the base.

VIBRATION ISOLATION PERFORMANCE OF ON-OFF DAMPERS

The equation of motion for the base excited spring-mass system with orifice damper can be expressed as:

$$\ddot{x} + \frac{\eta}{X_{max}}\left|\dot{x}-\dot{x}_0\right|(\dot{x}-\dot{x}_0)+\omega_0^2(\dot{x}-\dot{x}_0) = 0 \tag{10}$$

where $\omega_0^2 = K/m$, X_{max} is the maximum base excitation, and η is the damping parameter given by the following expression:

$$\eta = \frac{C_v}{m} X_{max} \tag{11}$$

Table 1 lists the expressions for damping parameter of a single degree-of-freedom isolator with on-off damping. Equation (10) is solved to determine the vibration isolation performance of on-off dampers, using direct integration techniques. The vibration isolation characteristics of the on-off dampers, using direct integration techniques. The vibration isolation characteristics of the on-off dampers is established by its transmissibility ratio due to harmonic acceleration excitation at the isolator base. The steady state inertia, spring, and damper forces of the SDOF isolator employing on-off damper II is presented in Figure 3. It is observed that the damper assumes a low damping value, whenever the spring and damper forces bear the same sign. The acceleration response of the on-off damper consistently reveals two peaks during each vibration cycle, irrespective of excitation frequency. The two peaks are associated with high and low values of damping. The off-cycle duration of the on-off damper I is significantly smaller than that of dampers II and III, for low excitation frequencies. However, the off-cycle period of on-off damper I increases and eventually approaches that of dampers II and III, as the excitation frequency is increased.

TABLE 1

Damping Parameter of SDOF System with On-Off-Damping

Damping Parameter	On-Off Damper		
η	I	II	III
$\frac{C_v}{m}\ X_{max}$	$\dot{x}(\dot{x}-\dot{x}_0) > 0$	$(\dot{x}-\dot{x}_0)(x-x_0) < 0$	$(\dot{x}-\dot{x}_0)(\ddot{x}-\ddot{x}_0) > 0$
$\frac{C_v'}{m}\ X_{max}$	$\dot{x}(\dot{x}-\dot{x}_0) < 0$	$(\dot{x}-\dot{x}_0)(x-x_0) > 0$	$(\dot{x}-\dot{x}_0)(\ddot{x}-\ddot{x}_0) < 0$

The displacement and velocity transmissibility characteristics of on-off dampers are established as shown in Figures 4 and 5, respectively. Figure 4 illustrates a comparison of displacement transmissibility ratios of on-off dampers to that of a passive damper. The system parameters are selected as $\omega_0 = 10$ rads/s, $C_v/m = 50$ and $C_v'/m = 0.5$ for all the damper schemes. It can be established that on-off dampers provide vibration isolation for excitation frequencies beyond 90% of undamped natural frequency. The velocity transmissibility ratio (Figure 5) of the on-off dampers exhibit similar behaviour as illustrated by Figure 4. On-off dampers II and III exhibit slightly larger resonant peak than the passive damper, however, the isolation performance of dampers II and III is slightly superior to that of on-off damper I.

VIBRATION ISOLATION CHARACTERISTICS OF DYNAMICAL SYSTEMS WITH ON-OFF DAMPING

The vibration isolation characteristics of a number of dynamical systems employing on-off damper is investigated to establish the effectiveness of on-off dampers. Various dynamical systems considered for this investigation are presented in the following subsections.

Relaxation (Ruzicka) Isolator

Ruzicka [15] discussed the relaxation isolator shown in Figure 6. The equations of motion for the isolator with elastically coupled viscous damper are expressed in the following manner:

$$\ddot{x} + 2\zeta\omega_0(\dot{x}-\dot{x}_n) + \omega_0^2(\dot{x}-\dot{x}_0) = 0.$$

$$2\zeta\omega_0(\dot{x}_n-\dot{x}) + N\,\omega_0^2(x_n-x_0) = 0. \qquad (12)$$

where $\omega_0^2 = K/m$, ζ is the ratio of damping coefficient to the critical damping, and N is the ratio of coupling spring stiffness to the isolator spring stiffness. The transmissibility characteristics of Ruzicka isolator with viscous damping can be expressed as;

$$\left|\frac{x}{x_0}\right| = \left[\frac{1.+(2\zeta r(N+1)/N)^2}{(1-r^2)^2 + (2\zeta r(N+1-r^2)/N)^2}\right] \qquad (13)$$

where r is the ratio of excitation frequency ω to ω_0. An optimum Ruzicka isolator with passive damping relates damping factor and the stiffness ratio N to realize a maximum response at the fixed point [16]:

$$\zeta_{opt} = \frac{N}{2(N+1)} \sqrt{\frac{N+2}{2}} \qquad (14)$$

The vibration isolation performance of the relaxation type isolator is investigated by replacing the passive damper by an on-off damper. Thus the damping factor for the relaxation type isolator with on-off damping can be given by the expressions listed in Table 2. Although, the damping force generated by orifice type on-off damper follows the velocity square law, the effectiveness of on-off damper in the relaxation type of isolator can very well be investigated while assuming linear damping.

The transmissibility characteristics of the relaxation type isolator with on-off with on-off damping are established and compared to that of passively damped Ruzicka isolator. The comparative performance of the passive and on-off damper configurations is presented

is presented in Figure 7, for stiffness ratio $N = 5$, and $\omega_0 = 10$ rad/s. The passive isolator exhibits vibration isolation beyond frequency ratio $r = 2.3$. All of the on-off damper configurations reveal vibration isolation beyond frequency ratio $r = 1.2$. The on-off damper II indicates slightly poor performance around isolator's resonant frequency. However, the isolation performance of on-off damper II is definitely superior to that of on-off damper I due to light damping offered by on-off damper II.

Two Degrees of Freedom Dynamical System

Snowdon [17,18] discussed the two inertia system shown in Figure 8, usually referred to as Snowdon vibration isolation system. The equations of motion of the two inertias are given as follows:

TABLE 2

Damping Parameter of Relaxation Isolator with On-Off Damping

Damping Parameter	On-Off Damper		
	I	II	III
$\frac{C}{2m\omega_0}$, if	$\dot{x}(\dot{x}-\dot{x}_n) > 0$	$(\dot{x}-\dot{x}_n)(x-x_n) < 0$	$(\dot{x}-\dot{x}_n)(\ddot{x}-\ddot{x}_n) > 0$
$\frac{C'}{2m\omega_0}$, if	$\dot{x}(\dot{x}-\dot{x}_n) < 0$	$(\dot{x}-\dot{x}_n)(x-x_n) > 0$	$(\dot{x}-\dot{x}_n)(\bar{x}-\bar{x}_n) < 0$

$$m\ddot{x}_s + C(\dot{x}_s-\dot{x}_p) + K(x_s-x_p)=0$$

$$\alpha m\ddot{x}_p + \Delta C(\dot{x}_p-\dot{x}_0) + C(\dot{x}_p-\dot{x}_s) + N K(x_p-x_0) + K(x_p-x_s) = 0 \qquad (15)$$

where α is the ratio of primary mass to secondary mass, Δ is the ratio of damping in the primary isolator to the damping in secondary isolator, and N is the ratio of the spring stiffness of primary and secondary isolators. x_s, x_p, and x_0 represent the displacement of secondary mass, primary mass, and the base, respectively. The transmissibility ratio (ratio of secondary mass displacement to base displacement) of the passively damped isolator is given by;

$$\left|\frac{x_s}{x_0}\right| = \left[\frac{P^2+Q^2}{R^2+S^2}\right]^{1/2} \qquad (16)$$

where

$$P = N - 4\zeta^2 r^2 Z^4 \Delta$$

$$Q = 2\zeta r Z^2(N + \Delta)$$

$$R = \alpha r^4 Z^4 - r^2 Z^2(1. + N + \alpha + 4\zeta^2 \Delta Z^2) + N$$

$$S = -2r^3 \zeta Z^4(1. + \alpha + \Delta) + 2\zeta r Z^2(\Delta + N) \qquad (17)$$

where r is the ratio of excitation frequency ω to the natural frequency λ of the isolator, given by:

$$\lambda = Z\sqrt{K/m} \qquad (18)$$

and

$$Z^2 = [1. + N + \alpha - \sqrt{(1. + N + \alpha)^2 - 4N\alpha}]/2a \qquad (19)$$

Introducing Z in this form normalizes the response curves so that the lower resonance frequency occurs near r = 1. Snowdon's optimization determines the ratio of inertias such that a large isolation range between the two resonances is accomplished. The optimum mass ratio was established as follows:

$$\alpha_{opt} = N - 1. \qquad (20)$$

The vibration isolation characteristics of the two DOF system is investigated for two isolator configurations: on-off damping between the two inertias; and on-off damping between the two masses m_p and m_s and also between m_p and the base. The damping fact of the Snowdon's isolator with on-off damping is evaluated using the expressions presented in Table 3. The vibration isolation characteristics of the isolator with on-off damping are evaluated and compared to that of the passively damped system.

The displacement transmissibility characteristics of the two-DOF system employing one on-off damper between the two inertias is presented in Figure 9 and Figure 10 shows the displacement transmissibility (x_s/x_0) behavior of the isolator employingtwo on-off dampers. A comparison of isolation performance of the two DOF system with on-off damping to that of a passively damped system reveals that all the on-off damper configurations offer superior isolation performance. On-off damper II indicates poor performance around the resonance when compared to passive, on-off damper I and III (Figures 9 and 10). A comparison of Figures 9 and 10 reveals that introduction of two on-off dampers can offer slightly improved isolation performance (on-off damper I). However, the resonant transmissibility ratio of on-off damper II increases significantly.

Three DOF Cab Suspension

Off road vehicles in-general are unsuspended vehicles and offer a difficult ride problem. Ride vibrations of these vehicles is characterized by lightly damped resonance due to their significantly soft tires. The ride vibrtion levels at the driver-seat interface are of significantly large amplitude and

TABLE 3

Damping Parameter of Two DOF Isolator with On-Off Damping

Damping Coefficient	On-Off Damper		
	I	II	III
C	$\dot{x}_s(\dot{x}_s-\dot{x}_p) > 0$	$(\dot{x}_s-\dot{x}_p)(x_s-x_p) < 0$	$(\ddot{x}_s-\ddot{x}_p)(\dot{x}_s-\dot{x}_p) > 0$
C'	$\dot{x}_s(\dot{x}_s-\dot{x}_p) < 0$	$(\dot{x}_s-\dot{x}_p)(\dot{x}_s-\dot{x}_p) > 0$	$(\ddot{x}_s-\ddot{x}_p)(\dot{x}_s-\dot{x}_p) < 0$
ΔC	$\dot{x}_p(\dot{x}_p-\dot{x}_o) > 0$	$(\dot{x}_p-\dot{x}_o)(x_p-x_o) < 0$	$(\ddot{x}_p-\ddot{x}_o)(\dot{x}_p-\dot{x}_o) > 0$
ΔC'	$\dot{x}_p(\dot{x}_p-\dot{x}_o) < 0$	$(\dot{x}_p-\dot{x}_o)(x_p-x_o) > 0$	$(\dot{x}_p-\dot{x}_o)(\dot{x}_p-\dot{x}_o) < 0$

dominate in the frequency range 1 - 3 Hz [14]. An effective ride improvement system at the cab requires heavily damped soft suspensions. However, a heavily damped vibration isolation system leads to poor ride response at the driver seat in the isolation region. The isolation performance characteristics along the bounce, pitch, and roll coordinates can be improved by employing variable or on-off damping. Consider the cab configuration of Figure 11, supported on four corner suspension units. The equations of motion of the 3 DOF passive cab suspension can be expressed in the general form:

$$[M]\{\ddot{y}\} + [D]\{\dot{y}\}+[k]\{y\} = [D_f]\{\dot{y}_0\} + [K_f]\{y_0\} \tag{21}$$

where $[M]$, $[D]$, and $[K]$ are $[3 \times 3]$ mass, damping, and stiffness matrices, respectively. $[D_f]$ and $[K_f]$ are forced damping and stiffness matrices, respectively. $\{y\}$ and $\{y_0\}$ are $\{3 \times 1\}$ vectors of response and excitation coordinates, given by;

$$\{y\} = \{z_c \ \phi \ \theta\}^T \qquad \{y_0\} = \{z_{c0} \ \phi 0 \ \theta 0\}^T$$

The cab suspension units employing on-off damping require the vertical response and excitation coordinates at their respective mounting locations. The response z_c and excitation coordinates at the four suspension locations can be evaluated from the response and excitation variables at the c.g., using geometrical transformation matrix $[A]$ in the following manner:

$$\{z\} = \{z_1 \ z_2 \ z_3 \ z_4\}^T = [A] \ \{y\}$$

$$\{z_0\} = \{z_{01} \ z_{02} \ z_{03} \ z_{04}\}^T = [A] \ \{y_0\} \tag{22}$$

and

$$[A] = \begin{bmatrix} 1. & a_1 & b_1 \\ 1. & a_1 & -b_2 \\ 1. & -a_2 & -b_2 \\ 1. & -a_2 & b_1 \end{bmatrix}$$

The damping force F_j generated by the suspension units employing on-off damping can be expressed as listed in Table 4.

TABLE 4

Force Generated by the Suspension Unit Employing On-Off Damper

Suspension Force F_j	On-Off Damper		
	I	II	III
$D_j(\dot{z}_j-\dot{z}_{0j})$, if	$\dot{z}_j(\dot{z}_j-\dot{z}_{0j}) > 0$	$(\dot{z}_j-\dot{z}_{0j})(z_j-z_{0j}) < 0$	$(\dot{z}_j-\dot{z}_{0j})(\ddot{z}_j-\ddot{z}_{0j}) > 0.$
$D'_j(\dot{z}_j-\dot{z}_{0j})$, if	$\dot{z}_j(\dot{z}_j-\dot{z}_{0j}) < 0$	$(\dot{z}_j-\dot{z}_{0j})(z_j-z_{0j}) > 0$	$(\dot{z}_j-\dot{z}_{0j})(\ddot{z}_j-\ddot{z}_{0j}) < 0.$

The isolation performance characteristics of three DOF cab suspension is assessed in terms of following response ratios:

$$\text{Bounce transmissibility ratio} = \left| z_c/(z_{c0})_{max} \right|$$

$$\text{Pitch transmissibility ratio} = \left| \phi/(\phi_0)_{max} \right|$$

$$\text{Roll transmissibility ratio} = \left| \theta/(\theta_0)_{max} \right| \quad (23)$$

The response transmissibility ratios of the cab suspension are evaluated by solving equation (21), using direct integration routines. The response transmissibility ratios of the cab suspension system employing on-off damping are compared to that of a passively damped cab suspension as shown in Figures 12, 13, and 14.

Bounce transmissibility ratio response of the cab suspension with passive and on-off damping is presented in Figure 12. The isolation characteristics of the cab suspension employing any of the on-off damper configurations is significantly superior to that of passively damped cab suspension, the response characteristics of on-off damper II and III corresponding to resonant frequency is slightly deteriorated when compared to that of a cab suspension however, the bounce response ratio of these dampers is slightly improved in the isolation frequency region. Pitch and roll response ratio of the cab suspension employing on-off dampers (Figures 13 and 14) exhibit identical behaviour as demonstrated by Figure 12.

CONCLUSIONS

Three on-off damper schemes are configured and investigated for their vibration isolation performance. On-off damper I is based on the absolute and relative velocities of the mass. On-off damper II is based on directly measurable relative velocity and relative displacement variables. The on-off damper III is configured to minimize the jerk experienced by isolator mass, and is based on directly measurable response and excitation variables. The vibration isolation performance of the on-off dampers, is in general superior to that of a passive isolator. On-off damper I offers resonance transmissibility ratio identical to that of a passive damper, however, the response behaviour of on-off dampers II and III around the resonant frequency is slightly poor than that of a passive damper.

The effectiveness of on-off dampers is also investigated for two- and three- DOF dynamical systems. A two DOF Snowdon's isolator is investigated when employing on-off dampers. A three- DOF cab suspension employing on-off damping at four corner mounted suspension units is investigated for its bounce, roll and pitch response characteristics. The bounce, roll, and pitch response behaviour of the cab suspension employing on-off damping is also superior to that of passively damped system.

REFERENCES

1. Guntur, R.R. and S. Sankar, "Fail-Safe Vibration Control Using Active Force Generators", Trans. ASME, J. of Vibration, Acoustics, Stress and Reliability in Design, Vol. 105, No. 3, pp. 361-368, 1983.

2. Klinger, D.L., "Guideway Vehicle Cost Reduction, Part II Active Suspension Feasibility", DOT Report No. DOT-TST-76-95, 1976.

3. Karnopp, D.C., "Are Active Suspensions Really Necessary?", ASME Paper No. 78-WA/DE-12, Dec. 1978.

4. Karnopp, D., M.J. Crosby and R.A. Harwood, "Vibration Control Using Semi-Active Force Generator", Trans. ASME, J. of Eng. for Ind., Vol. 98, pp. 914-918, 1974.

5. Margolis, D.L., "Semiactive Suspension for Military Ground Vehicles Under Off-Road Conditions", 52nd. Shock and Vibration Symp., Oct. 27-29, 1981.

6. Crosby, Michael J. and Dean C. Karnopp, "The Active Damper- A New Concept for Shock and Vibration Control", Shock and Vibration Bull, No. 43, pp. 118-133, 1972.

7. Horvat, D. and D.L. Margolis, "An Experimental Comparison Between Semi-Active and Passive Suspensions for Air-Cushion Vehicles", Int. J. of Vehicle Design, Vol. 2, No. 3, 1981.

8. Krasnicki, E.J., "The Experimental Performance of an On-Off Vehicle Utilizing a Semiactive Suspension", Shock and Vibration Bull. No. 54, Pt. 3, pp. 135-141, 1983.

9. Rakheja, S. and S. Sankar, "Vibration and Shock Isolation Performance of a Semi-active On-Off Damper", ASME Paper No. 85-DET-15, ASME Design Engineering Tech. Conf., Cincinnati, Ohio, Sept. 10-13, 1985.

10. Margolis, D.L., "The Response of Active and Semiactive Suspensions to Realistic Feedback Signals", Veh. Sys. Dyn., Vol. 11, pp. 267-282, 1982.

11. Guntur, R.R. and S. Sankar, "Performance of Different Kinds of Dual Phase Damping Shock Mounts", J. of Sound and Vibration, Vol. 84, No. 2, pp. 253-267, 1982.

12. Snowdon, J.C., "Isolation from Mechanical Shock with a Mounting System Having Non-linear Dual Phase Damping", Shock and Vibration Bull., Vol. 41, pp. 21-45, 1970.

13. Rakheja, S., "Shock Isolation Performance of an On-Off Damper", Report, Dept. of Mechanical Engineering, Concordia University, Montreal, 1984.

14. Rakheja, Subhash, "Computer Aided Dynamic Analysis and Optimal Design of Suspension Systems for Off-Road Tractors", Ph.D. Thesis, Concordia University, Montreal, Quebec, Nov. 1983.

15. Ruzicka, J.E., "Resonance Characteristics of Unidirectional Viscous and Coulomb Damped Vibration Isolating Systems", Trans. ASME, J. of Eng. for Ind., Nov. 1967.

16. Zeidler, Dennis E. and Darrel A. Frohrib, "Optimization of a Combined Ruzicka and Snowdon Vibration Isolation Systems", The Shock and Vibration Bulletin, Vol. 42, Pt. 4, pp. 77-84, 1972.

17. Snowdon, J.C., "Vibration and Shock in Damped Mechanical Systems", Wiley, New York, 1967.

18. Snowdon, J.C., "Isolation from Mechanical Shocks with One- and Two-Stage Mounting Systems", J. of Acoustical Soc. of Am., Vol. 31, July 1959.

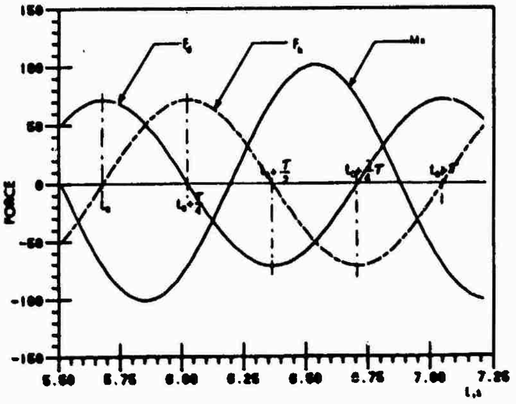

Figure 2: Spring, damper and inertia forces trace of SDOF passive isolator.

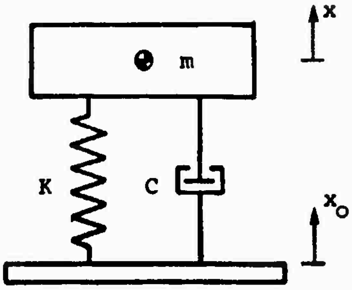

Figure 1: SDOF spring-mass-damper system

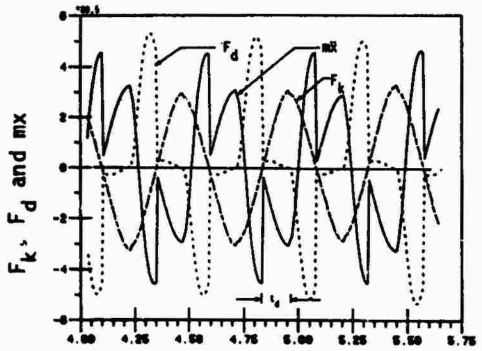

Figure 3: Steady state spring, damper and inertia forces of SDOF isolator.

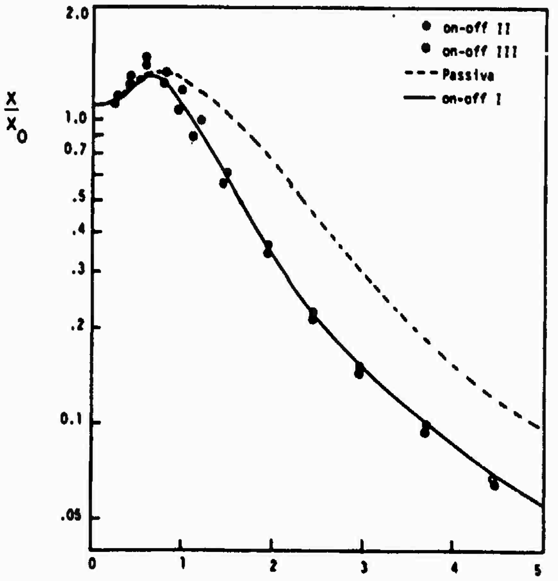

Figure 4: Displacement transmissibility characteristics of on-off dampers.

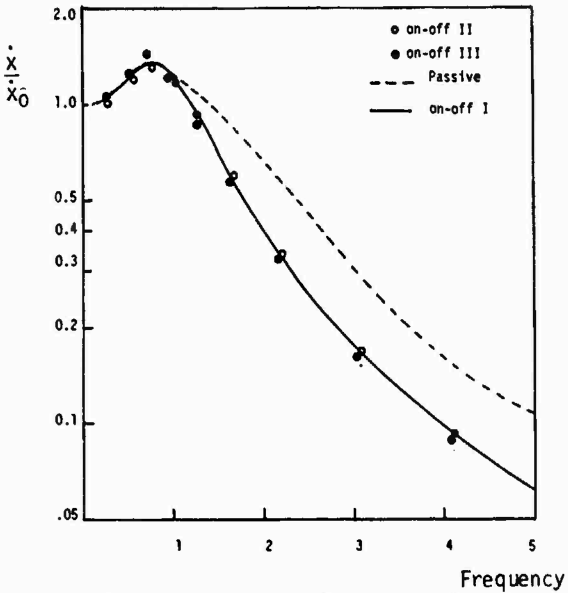

Figure 5: Velocity transmissibility ratio of passive and on-off dampers.

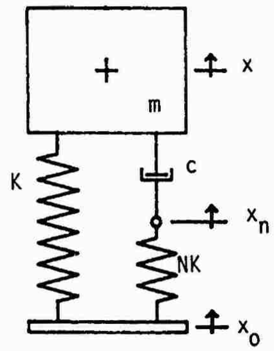

Figure 6: Schematic configuration of vibration isolator with elastically coupled damper.

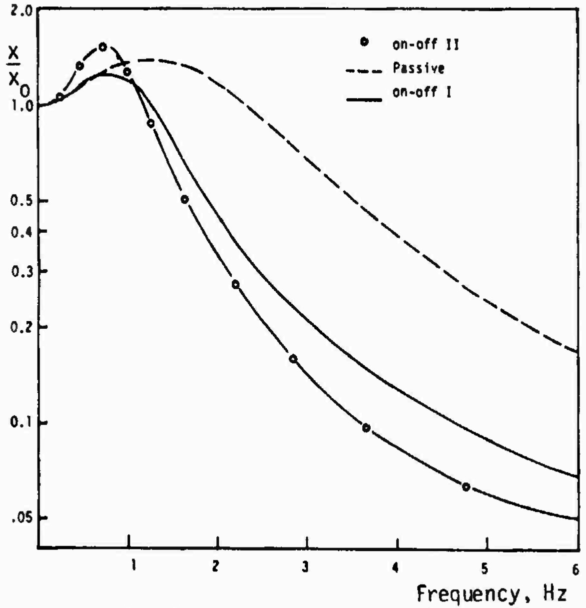

Figure 7· Displacement transmissibility ratio of elastically coupled on-off dampers(ω_0 = 10 rad/s, ζ_{opt}= 0.7795, N = 5)

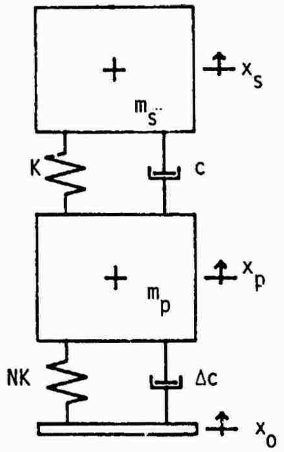

Figure 8: Two- DOF vibration isolator.

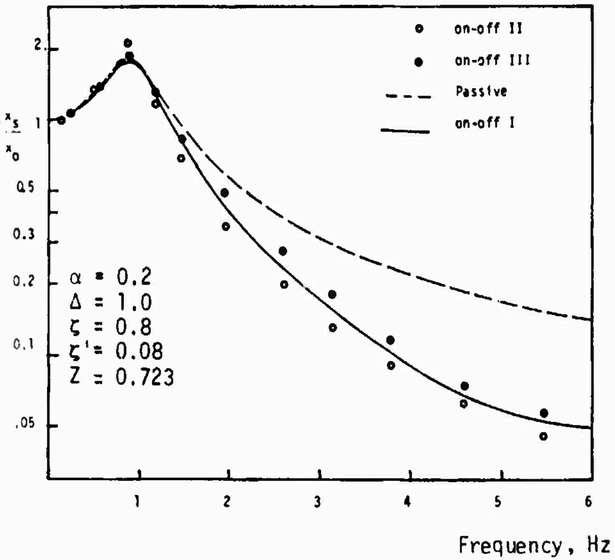

Figure 9: Displacement transmissibility ratio of two DOF system (on-off damper placed between m_s and m_p)

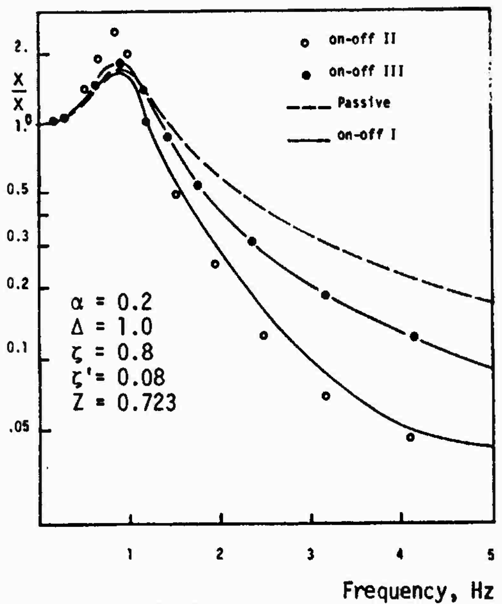

Figure 10: Displacement transmissibility of 2-DOF system employing two on-off dampers.

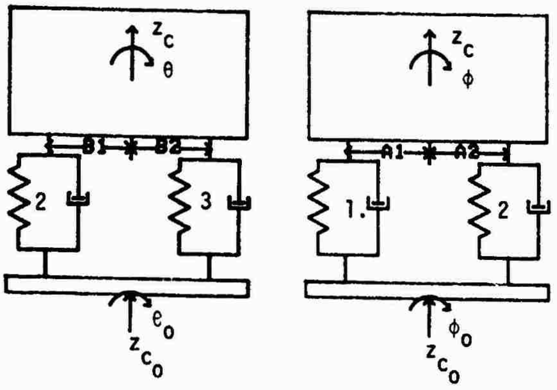

Figure 11: Three DOF cab suspension model

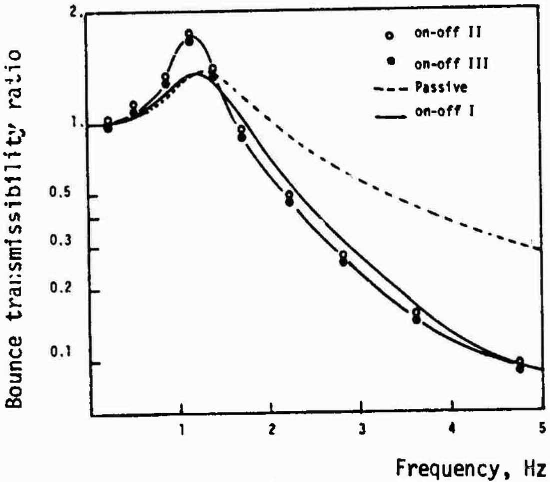

Figure 12: Bounce transmissibility ratio response of cab suspension employing passive and on-off dampers (D_j = 1000 Ns/m).

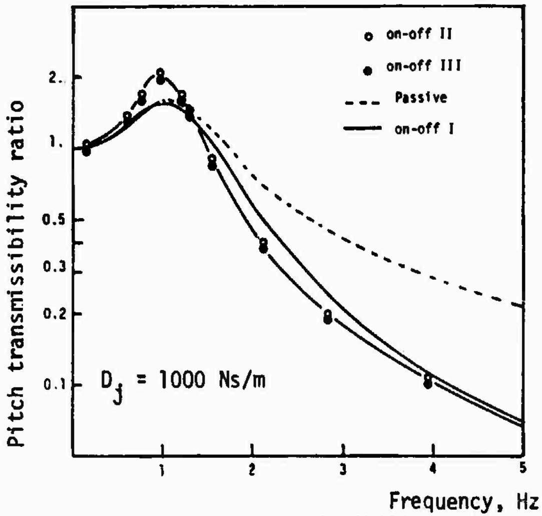

Figure 13: Pitch transmissibility ratio

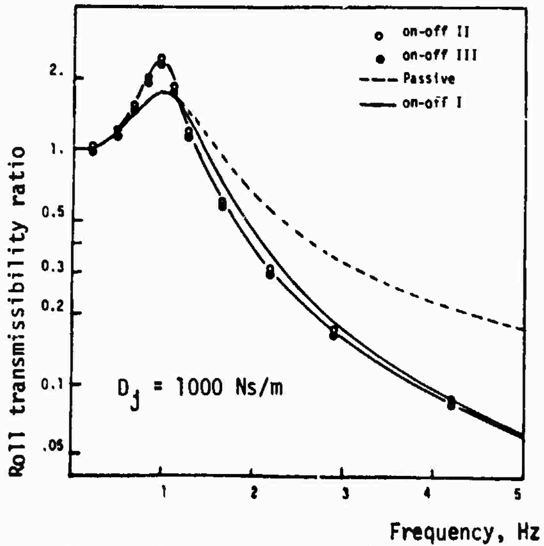

Figure 14: Roll transmissibility ratio of cab suspension.

STRUCTURAL DYNAMICS

BUCKLING OF RING-STIFFENED CYLINDRICAL SHELLS WITH DYNAMIC LOADS

T. A. Butler
W. E. Baker
Los Alamos National Laboratory

C. D. Babcock
California Institute of Technology

Buckling of a ring-stiffened, thin-walled cylinder from dynamic base excitation was investigated in a combined experimental/numerical program. A polycarbonate (Lexan) cylinder was excited with single-frequency harmonic transients to determine the peak base acceleration levels required to induce buckling. Buckling was identified using recorded signals from strain gages and accelerometers, with high-speed video records, and by audibility. Experimental results are compared with numerical results obtained using a freezing-in-time technique. The numerical method is based on modal analysis techniques combined with a statically determined buckling interaction curve. Results of the study indicate that, for the particular types of transients studied, this freezing-in-time technique provides a conservative prediction of when buckling will occur.

I. INTRODUCTION

As one phase of an ongoing program to investigate the buckling of free-standing, nuclear containments under various loadings, the Los Alamos National Laboratory is currently studying buckling of thin-walled, cylindrical shells from dynamic loads. The goal of this work is to assess the current (and past) design and analysis procedures for predicting buckling of steel containment vessels under time-dependent loadings. In particular, in this phase of the work the freezing-in-time method is evaluated. For this analysis method, time-dependent stresses are calculated with a structural dynamic computer code or the stresses are derived from equivalent static loads and then, in either case, are assumed to be static (frozen in time) during performance of bifurcation buckling analyses. Implicit in this procedure is the assumption that the stress field that causes the buckling changes little during the time that it takes the structure to deform into the buckled configuration.

The freezing-in-time method is evaluated based on a series of experiments performed with a ring-stiffened, polycarbonate (Lexan) cylinder that was dynamically loaded by horizontal base excitation. The loading transients consisted of a sine wave signal at particular frequencies that linearly increased in amplitude from zero to a predetermined maximum value. Prior to the dynamic tests the cylindrical shell was buckled under static loads (axial compression and bending) to define the static buckling criterion using an interaction relationship based on previous work [1]. The same shell was then submitted to dynamic excitation with an electrodynamic shake table. Typical test sequences consisted of subjecting the test cylinder to increasing levels of base excitation, until buckling occurred. Buckling was detected by using data from strain gages and accelerometers mounted on the cylinder, high-speed video recordings, and audibility. A numerical model of the cylinder was developed, and the freezing-in-time method was used to predict the buckling levels using stresses predicted by the model and the experimentally derived buckling interaction curve.

Previous research related to the buckling of cylindrical shells has concentrated on the static problem with little effort being focused on buckling response in environments where inertial effects are of importance. Singer [2,3] has performed extensive studies making use of the dynamic characteristics of shells to predict changes in the static buckling behavior with changing boundary conditions. His methods have generally been applied to shells with closely spaced longitudinal stiffeners where the influence of boundary conditions, rather than imperfections predominates. For the shell considered in this study, which has no longitudinal stiffeners, imperfections became an important parameter. In the following sections of this paper, the Lexan model is first described. The test method and results are then summarized and results of the numerical study are presented.

II. TEST SPECIMEN DESCRIPTION

The cylinder used for the experimental studies was constructed from Lexan and was supported with aluminum end rings (Fig. 1). The geometry of the cylinder was designed to provide similarity of essential features with steel nuclear containment structures. The size and spacing of the ring stiffeners were based upon the requirements of ASME Code Case N-284 [4] for prevention of both ring and global buckling under typical design loadings for nuclear containments.

The polycarbonate material used for constructing the cylinder and stiffening rings has two characteristics that make it particularly convenient for dynamic buckling tests; models may be fabricated using a convenient solvent bonding technique, and the material remains elastic throughout a test involving reasonable post-buckling deformations. Therefore, the model may be subjected to buckling deformations many times without substantial change in the response of either the buckling load or the buckled mode shape. Babcock [5] reviewed several investigations where plastics of this type have been used for various buckling studies, both static and dynamic.

The model construction technique results in a high-quality shell with few geometric imperfections, and the axial buckling load is typically from 70 to 95 per cent of the classical value. The first step in the fabrication process is to form the shell on a rolled steel mandrel using a butt joint to connect the edges. A 20 mm (0.79 in.) wide doubler is used at the joint for reinforcement. Solvent bonding is used at this joint and at all other joints between Lexan. After being cut to the desired cross-section, the ring stiffeners are formed to the radius of the shell and oven annealed. This process removes residual stresses in the rings and minimizes accompanying residual stresses and geometric imperfections in the shell. After the Lexan stiffening rings are attached and the Lexan shell is removed from

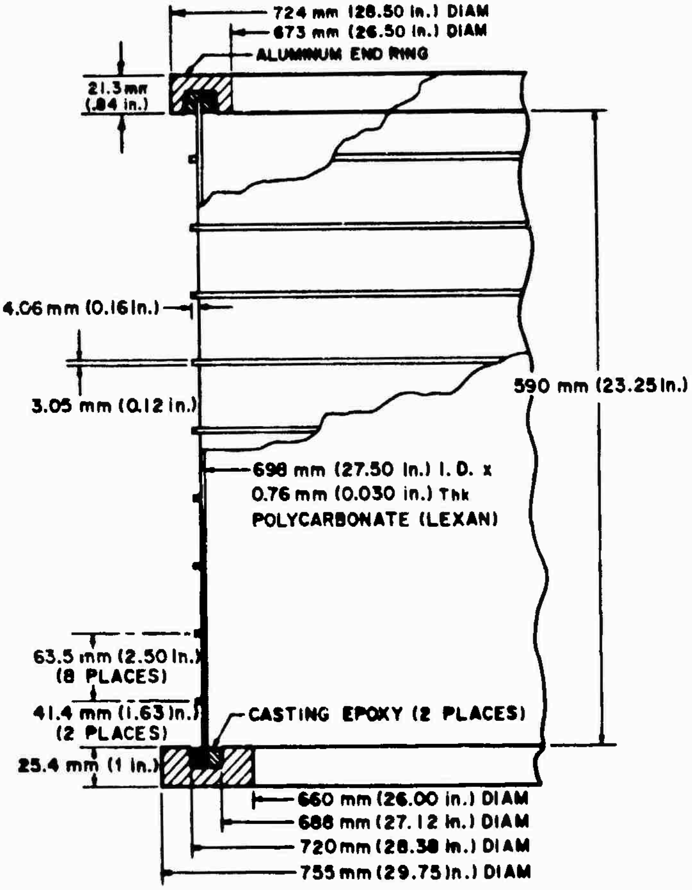

Fig. 1. Details of ring-stiffened, Lexan cylinder.

the mandrel, the ends of the shell are connected to aluminum end rings by setting in a casting epoxy. During the casting process the shell is held in a circular shape with an expanding internal ring.

A standard tension test was used to determine the modulus of elasticity for the Lexan material, which was 2.52 GPa (3.66 x 10^5 psi). A vibrating beam was used to determine the strain rate effects on the modulus of elasticity. The natural frequency of the beam was determined for several different lengths, and the modulus of elasticity was calculated.

For a frequency of 20 to 250 Hz the value of the modulus did not change significantly, indicating little strain rate effect in the frequency range of interest.

III. STATIC TEST PROCEDURE/RESULTS

Preliminary to the dynamic tests, a series of static tests were performed on the cylinder to establish its buckling strength. Both compression and bending tests were conducted. The results of these tests, along with the buckling interaction diagram that is discussed in detail in Ref. 1, were used to define the static buckling criterion used with freezing-in-time analysis.

The static compression tests were conducted with a 200 kN (55 kip) servohydraulic testing machine. Rubber cushions were placed between thick end plates, which provided the load path from the testing machine to the cylinder, and the aluminum end rings of the cylinder to obtain a uniform load distribution around the cylinder. Axisymmetric loading was used, and five tests were performed with the cylinder at different angular positions relative to the end plates. The peak load prior to general collapse varied from 3923 N (882 lb) to 4528 N (1018 lb), and the average was 4092 N (920 lb) with a standard deviation of 249 N (56 lb). The average load at general collapse is approximately 71 percent of the classical buckling load of an unstiffened cylinder of this geometry. Figure 2 shows the model in the buckled configuration.

The bending tests were conducted by clamping the lower end ring to a rigid test fixture and applying a load along a diameter at the top ring. In essence, the shell acted as a short cantilevered beam with a load at the end giving a constant shear distribution along the length of the shell. As with the axial tests, considerable care was taken to ensure minimal deviation from an ideal stress distribution at the clamped end. During the tests, as the load was slowly applied, visible, but stable, shear buckles formed before general collapse at the peak load. For a series of nine tests, the average buckling load was 1770 N (397 lb), and the range was 1710 N (384 lb) to 1850 N (416 lb). Figure 3 shows the cylinder in the buckled condition for this type of loading.

IV. MODAL STUDIES

A. Experimental Results

Several shell modes of the cylinder were determined from low-level vibration tests. Certain shell modes were excited with a speaker driver and the vibration mode shape of the shell was measured with a noncontact fiber optic displacement measuring device. This procedure was followed for each of the shell modes that could be identified and easily excited.

Because the shell material is nonmagnetic, it was convenient to excite the shell with the speaker driver using acoustic coupling. The output from the driver was concentrated on a small area approximately 0.60 cm (0.25 in.) in diameter. This "focusing" was accomplished by fitting the driver with a metal adapter that has a small opening that could be placed close to the shell surface. Excitation with the driver working near its rated output resulted in shell vibrations of sufficient amplitude for measurement.

Natural frequencies were identified by slowly increasing the excitation frequency while monitoring the vibration amplitude at a particular point on the shell surface. The natural frequency was identified as the frequency at which the peak-to-peak amplitude was locally a maximum. The excitation was held constant at this frequency and the mode shape was determined by measuring radial displacement of the shell at selected points with the fiber optic displacement measuring device.

Experimental results are shown in Fig. 4 along with the results of the numerical study described below. Note that the experimental frequencies are quite close to the analytical predictions. The $m=2$ modes were not excited experimentally because the speaker driver was not moved from the axial midpoint of the cylinder, which is a node (zero displacement) for these modes. Only the shell modes were excited during the experimental modal study. The beam bending/shear mode identified on the figure was found from shake table tests, discussed below, to be very close to the analytical value of 43 Hz.

B. Numerical Results

A numerical model of the Lexan cylinder was developed using the BOSOR IV computer code [6]. The model is axisymmetric and has 200 nodal points. The elastic modulus for the Lexan was obtained with uniaxial test specimens of the parent material that was used for fabricating the cylinder. Poisson's ratio was estimated to be 0.4. Standard properties were used for the aluminum in the upper end ring. The lower end ring was not modeled and the bottom of the Lexan cylinder was assumed to be fixed. Each Lexan stiffener was modeled as a discrete ring.

The numerical model was used to predict the mode shapes and frequencies for the circumferential harmonics zero through twelve with the results being shown in Fig. 4. Generalized force for harmonics other than n=1 is zero for single axis horizontal input for the ideal cylinder that is represented numerically and, therefore, modes with $n \geq 2$ were not included in the transient response calculations. It should be noted, however, that the higher harmonics can be excited on the test cylinder because of small geometric imperfections. The modes associated with circumferential harmonic zero are excited only for vertical input. Their inclusion is necessary to account for the small amount of vertical motion that occurs on the shake table during the tests.

Figure 4 shows that the predicted frequencies and mode shapes for harmonics greater than two follow the pattern typically expected for a thin shell with this type of geometry. The predicted numerical values are also very close to those measured during the modal survey tests.

V. VIBRATION TEST METHOD

The vibration tests were conducted on a single-axis, horizontal shake table that was controlled with a digital control system. The method of attaching the cylinder to the shake table presented the problem of changing the buckling response because of the imposed end condition. Because the table and lower end ring on the cylinder were not exactly planar, bolting the ring to the table could introduce stresses in the Lexan shell that were large enough to cause buckling with no added loads. The following mounting procedure was used to overcome this problem. An intermediate ring was machined to fit between the table and the cylinder. It has a groove in the top into which the shell end ring can fit. After bolting this intermediate ring to the table, the groove was partially filled with a casting epoxy and the shell end ring was set into the epoxy and gently clamped while the epoxy cured. After the epoxy had cured, the clamps were tightened slightly. Figure 5 shows a photograph of the cylinder mounted on the shake table.

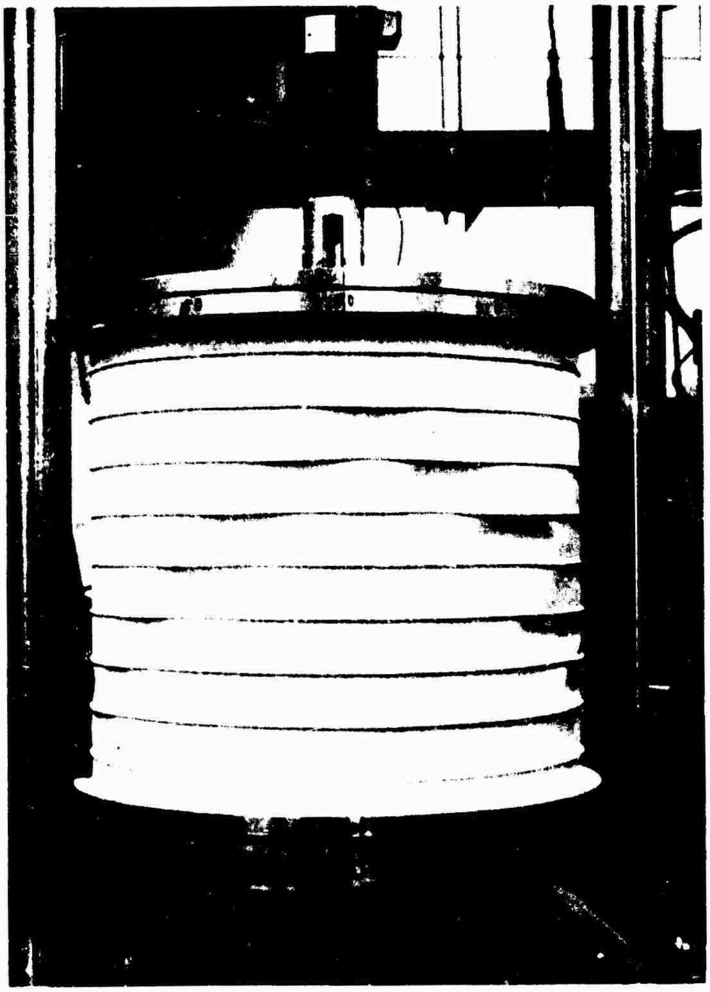

Fig. 2. Buckled configuration of Lexan cylinder under uniform axial compression.

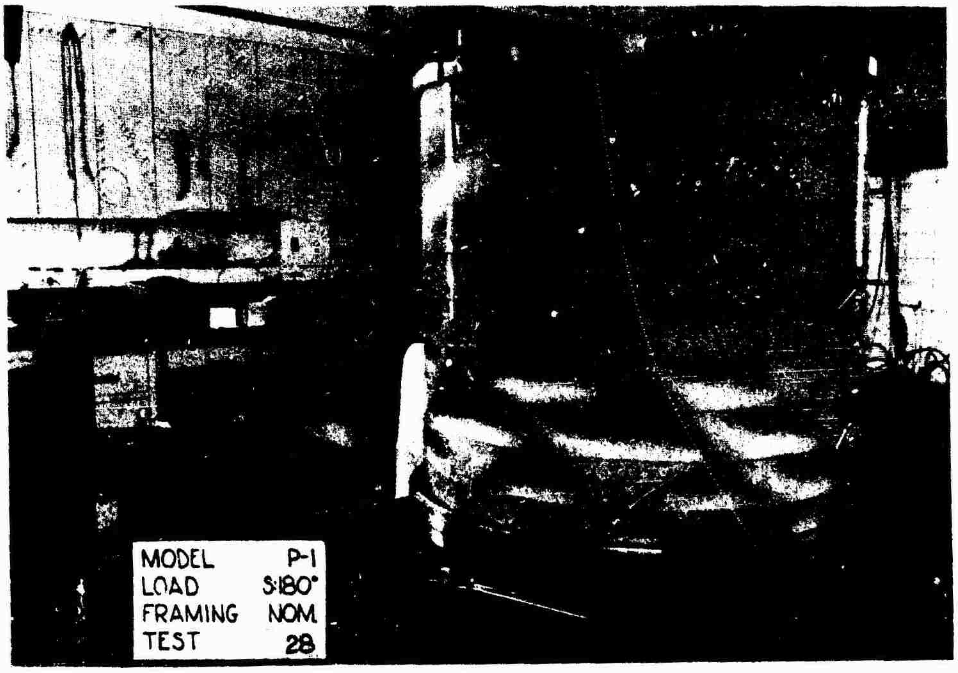

Fig. 3. Buckled configuration of Lexan cylinder under bending load.

During the phase of the research reported in this paper the excitation was sinusoidal in nature. This type of excitation was chosen primarily to simplify analysis of the test results. After the buckling phenomena are well understood for this type of transient, we plan to excite similar cylinders with more complex earthquake-type transients.

The desired acceleration transient for each test was a sine wave at a given frequency that increased linearly in amplitude from zero to a predetermined peak in 40 cycles. The peak acceleration was held for one additional cycle followed by ten cycles of linearly decreasing amplitude to zero acceleration. This particular transient was selected to reduce the chance of failing the cylinder by restricting the number of cycles of buckling that the cylinder could experience during any one test. For a given test, frequency and the peak acceleration were selected, and then the peak acceleration was increased during successive tests until buckling was detected. The decreasing amplitude tail on the transient was necessary to avoid the introduction of a "shutdown" transient, which could cause a severe response at the end of each test. The harmonic tests were performed at frequencies from 10 Hz to 80 Hz in increments of 10 Hz.

Included in the data taken during each test were the three components of input acceleration recorded with accelerometers mounted on the lower ring of the cylinder, three components of output acceleration recorded from accelerometers mounted on the cylinder's upper ring, and four strain measurements. Two of the strain gages were oriented vertically at the "toe" of the cylinder where buckling from compressive stresses was judged most likely to occur (see Fig. 5). These gages were centered between the lower end ring and the first ring stiffener, one being on the inside and the other on the outside. The other two strain gages were on the side of the cylinder, 90 degrees from the first set of gages and centered in the bay just below the center ring stiffener. As with the first pair, the two gages were back-to-back, one inside and the other outside. The orientation of the gages on the shell was 60 degrees from the axial direction.

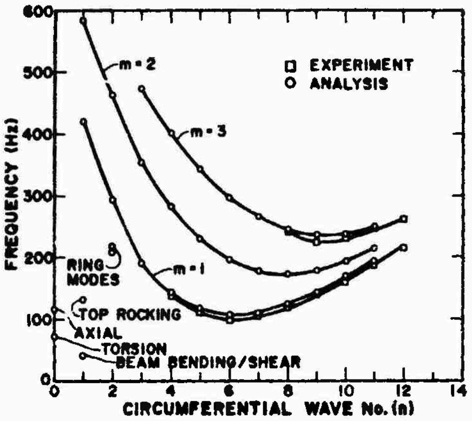

Fig. 4. Modal frequencies for ring-stiffened cylindrical shell.

In addition to recording time histories of these ten transducers, photographic coverage of each test was obtained with two high-speed, video cameras. An equivalent framing speed of 1000 frames per second was used. These records permitted visual identification of when buckling occurred in the areas covered on the cylinder. One of the cameras was oriented toward the toe of the cylinder just above the bottom aluminum ring. The other was oriented to show shear buckling on the cylinder at a location approximately 45 degrees to the direction of excitation.

VI. VIBRATION TEST RESULTS

Several different criteria were used to determine when buckling occurred in the cylinder for each of the tests. Some of these were more effective within certain frequency ranges; however, by using all the criteria, the point at which buckling occurred for each frequency considered was reasonably well identified. Only at one frequency, 80 Hz, was the shaker

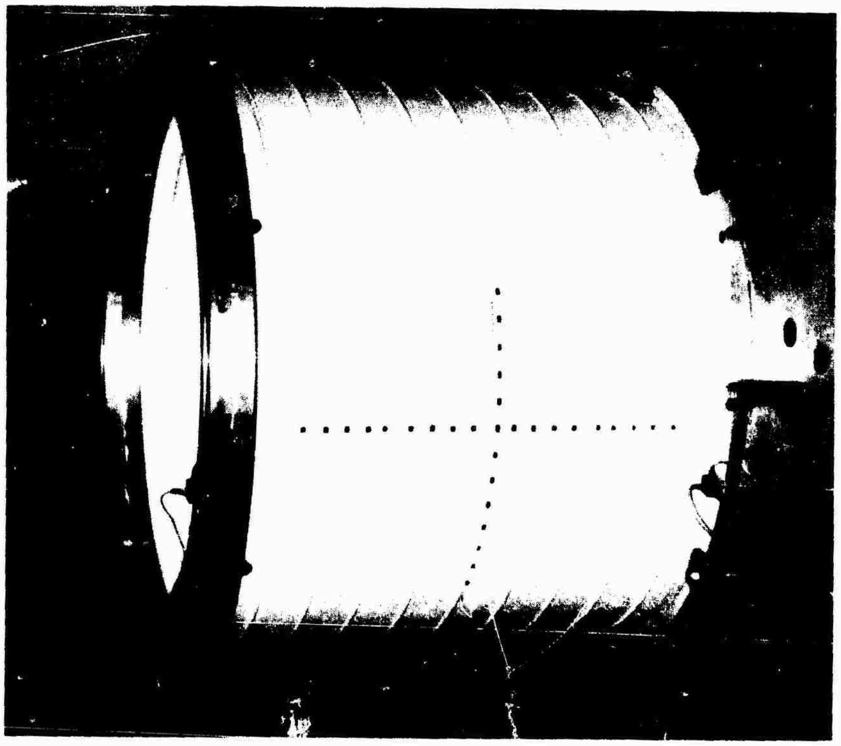

Fig. 5. Lexan cylinder mounted on shake table.

capacity too low to buckle the cylinder. A summary of test results is shown in Fig. 6. The first, and most consistent, method for identification of buckling is labeled "top acceleration" in the figure. For this method acceleration recorded with the accelerometer located on the top ring of the cylinder and oriented in the direction of primary excitation was used along with the mass of the top ring to determine buckling with an equivalent static criterion. When this acceleration first reached a level that the equivalent static load acting on the ring was equal to the static buckling load (1770 N (397 lb)) the cylinder was considered to have buckled. The buckling acceleration was then identified at the same point in time from the accelerometer located at the base of the cylinder and oriented in the direction of excitation.

A second criterion, based solely on the vertical acceleration response verified the first criterion for frequencies above 43 Hz (the fundamental frequency of the cylinder). Figure 7 shows the vertical acceleration record of the top ring for a 60 Hz test and a 70 Hz test. The response initially increases linearly, as would be expected from the prescribed input acceleration. Then at approximately 0.6 s for the 60 Hz case and 0.5 s for the 70 Hz case, a high frequency response component appears and the response becomes nonlinear, as indicated by the peak response for each cyle. Again, the buckling acceleration is identified from the base input at the appropriate point in time. Results using this criterion are within 5 percent of the first criterion and are, therefore, not shown in Fig. 6. Another, similar, method for identifying buckling involves comparing the top acceleration in the horizontal direction with the calculated acceleration. Figure 8 shows both the experimental and analytical acceleration for a 50 Hz test. The calculated response does not include buckling effects, so, by comparing the two signals and determining when the experimental response deviates significantly from the analytical, buckling can be identified. For this 50 Hz test, this criterion for identifying buckling again gives results close to the equivalent static criterion.

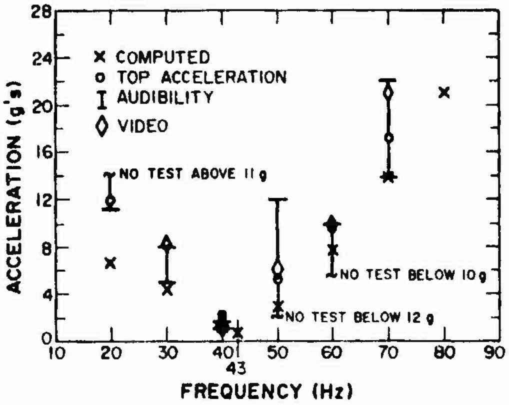

Fig. 6. Required base acceleration to buckle Lexan cylinder as a function of frequency.

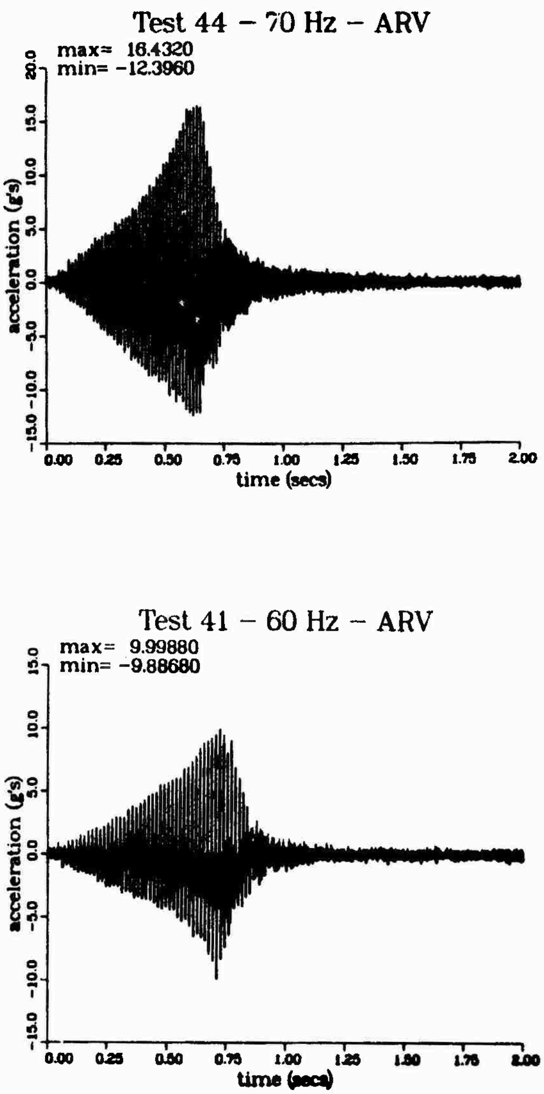
Test 44 – 70 Hz – ARV

Test 41 – 60 Hz – ARV

Fig. 7. Vertical acceleration of top aluminum ring on Lexan cylinder for 60 and 70 Hz tests.

Buckling was also identified for all except the 20 and 80 Hz tests using the recorded video signals. For each of the tests, the video was analyzed frame by frame near the initiation of buckling and the time at which buckling occurred was identified. From Fig. 6 it can be seen that, except for the 70 Hz case, this criterion results in buckling accelerations that are very close to those for the other criteria already discussed. The final criterion used for identifying buckling involved audibility. When buckling occurred the

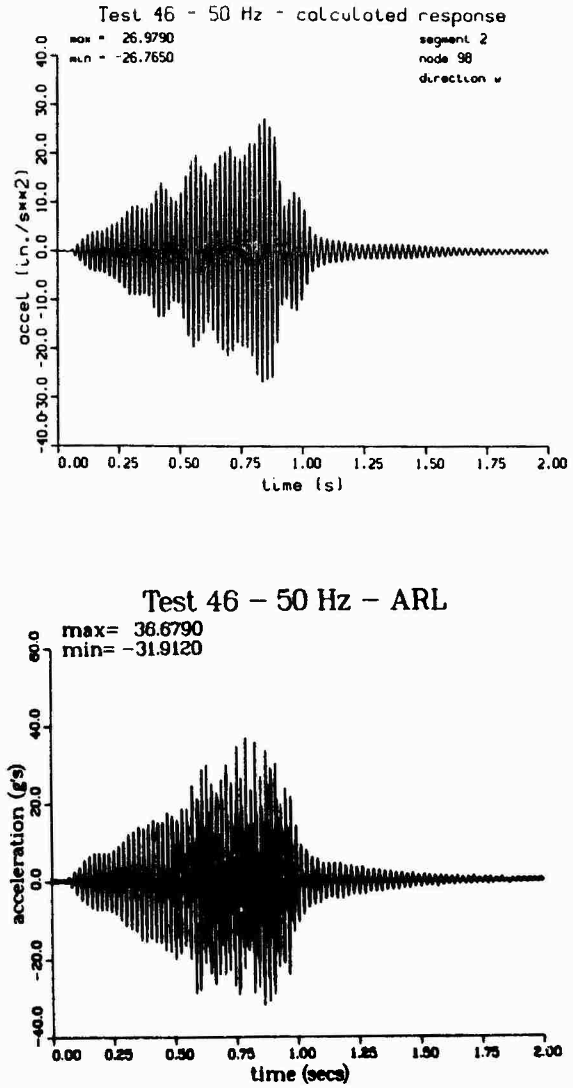

Fig. 8. Horizontal acceleration to top aluminum ring on Lexan cylinder for 50 Hz test.

cylinder responded with an audible popping sound. While each test was being performed two of the experimenters were positioned near the shake table and listened for this characteristic sound. Because the tests were short in duration, the point in time at which the sound occurred could not be identified. It could only be determined that buckling either did or did not occur for each test. In Fig. 6, the lower bar for this criterion indicates a test for which buckling did not occur (no buckling sound was identified), and the upper bar indicates a test for which a buckling sound was identified. If more tests had been performed between the two bars, this criterion may have given more precise results.

VII. ANALYSIS RESULTS

The BOSOR-IV computer code was modified to calculate modal stresses and these, along with the frequencies, generalized masses, and mode shapes were used in a separate computer code that integrates the uncoupled equations of motion in modal coordinates. Modal damping values of 1 per cent of critical, the measured damping of the test cylinder, were used for the calculations. The modal response values are then used to predict the stress in the cylinder at each location for each point in time. These stresses are normalized with the critical buckling stress determined in the static tests discussed above. A postprocessor is then used to plot the maximum normalized stresses at specified points on the shell and these are compared with the buckling interaction curve discussed in detail in Ref. 1.

Figure 9 shows results for calculations of the cylinder response during a given transient. In the figure, the computed point where there is zero shear stress, $N_{s\theta}$=0.0, is at the toe of the cylinder zero degrees from the direction of excitation. The points where there is nearly zero axial stress are at plus and minus 90 degrees from the direction of excitation and the other points are at 15 degree increments between 0 and plus and minus 90 degrees. For each location the plotted point represents the maximum excursion of combined axial and shear stress during the total duration of the transient. When any of the computed stress values are outside of the interaction curve, buckling can be expected. The sequence described here is a freezing-in-time technique and was used to analyze all of the tests.

The numerical model was used to analyze response of the cylinder to the harmonic excitation at each frequency considered in the test series and, in addition, at the fundamental frequency of the cylinder (43 Hz). Results

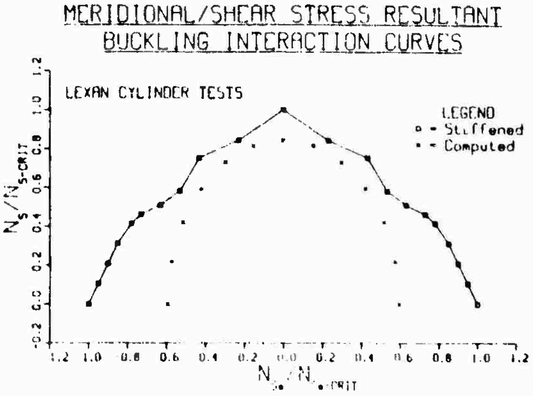

Fig. 9. Computed stress levels on static buckling interaction curve.

of these calculations are shown in Fig. 6, along with the experimental results. The computed buckling acceleration levels are consistently below the experimental data. The primary explanation for this difference is the fact that the computational buckling criterion, when compared with the particular static buckling interaction curve used here, should probably use an integrated stress level over a characteristic area rather than point values. The characteristic area has not yet been determined but should probably be related somehow to the buckling wave length for the cylinder.

Discussion of one particular point on the interaction curve can help clarify this explanation. Consider the point on the curve where the shear stress is zero ($N_{s\theta}$=0.0) and the normalized axial stress is one (N_s=1.0). When the interaction curve was developed, this point was determined with the complete cylinder in a uniform state of axial stress and $N_{s\theta}$ was zero everywhere. On the other hand, for the load cases considered here, the $N_{s\theta}$ stress component is generally zero for only one location on the cylinder; at 0 degrees and 180 degrees to the direction of excitation (that is, at the toe of the cylinder). The axial stress is not constant at this point but varies in both the circumferential and axial directions.

VIII. CONCLUSIONS

A series of harmonic tests were performed to determine whether an analytical freezing-in-time buckling method is appropriate for predicting buckling of a ring-stiffened cylinder. Results of the experimental portion of the research showed that buckling could be identified by three techniques: an equivalent static load method using horizontal response acceleration, vertical response acceleration, and from video coverage. The first two techniques gave results that were in agreement to within 5%. Use of audible emissions has potential application but needs further development.

The computational method for predicting buckling used a model that accurately represented the test shell as evidenced by the excellent agreement between the calculated and predicted shell mode frequencies. However, the buckling load predicted using the freezing-in-time method described in this paper was significantly conservative. Since the excitation frequencies used in this work were below the lowest shell modes, this conclusion is restricted. When excitation frequencies are near those of shell modes, these modes could be excited because of shell imperfections and lower the buckling loads. One reason for the conservatism is thought to be associated with the differences in the stress field in the cylinder during the harmonic tests and the stress field present when the static buckling interaction curve was developed. Further research needs to be performed to determine how the dynamic stress field developed during general transient excitation can be treated to make appropriate use of statically determined buckling interaction curves.

IX. ACKNOWLEDGEMENT

This work is sponsored by the US Nuclear Regulatory Commission, Division of Engineering Technology, Mechanical/Structural Engineering Branch. The encouragement of Dr. Boris Browzin, Project Monitor, is gratefully acknowledged.

X. REFERENCES

1. W. E. Baker and J. G. Bennett, "Experimental Investigation of the Buckling of Nuclear Containment-Like Cylindrical Geometries Under Combined Shear and Bending," Nuclear Engineering and Design, 79 (1984), pp. 211-216.

2. J. Singer, "Recent Studies on the Correlation Between Vibration and Buckling of Stiffened Cylindrical Shells," Zeits. für Flugwissenschaften und Weltraumforschung, 3, No. 6 (1979) pp 333-343.

3. J. Singer and H. Abramovich, "Vibration Techniques for Definition of Practical Boundary Conditions in Stiffened Shells," AIAA Journal, 17, No. 7 (July 1979) pp. 762-769.

4. Code Case N-284, "Metal Containment Shell Buckling," ASME, Boiler and Pressure Vessel Code, Section III, Nuclear Power Plant Components, Division 1, Subsection NE, 1983 edition.

5. C. D. Babcock, "Experiments in Shell Buckling," Thin Shell Structures - Theory, Experiment and Design, Y. C. Fung and E. E. Sechler, Ed., (Prentice Hall, New York, 1974), pp. 345-369.

6. D. Bushnell, "BOSOR 4: Program for Stress, Buckling, and Vibration of Complex Shells of Revolution," in Structural Mechanics Software Series - Vol. 1, N. Perrone and W. Pilkey, Ed. (University Press of Virginia, Charlottesville, Virginia, 1976).

FORCED VIBRATIONS OF STRINGER STIFFENED DAMPED SANDWICH PANEL

N. Kavi and N.T. Asnani
Mechanical Engineering Department,
I.I.T. Delhi-110016, INDIA

Transfer matrix method to determine response of a stiffened sandwich panel consisting of elastic face layers sandwiching viscoelastic core, to a deterministic harmonic loading has been developed. A rectangular sandwich panel with arbitary number of stringers placed at equal or unequal spacings has been considered with the edges perpendicular to stringers simply supported and the edges parallel to stringes with arbitrary boundary conditions. The principle of correspondence of linear viscoelasticity has been applied to take account of the viscoelastic damping. Vibration response of a sandwich panel with two equally spaced stringers to a sinusoidal excitation has been determined and values of the resonant frequencies and associated modal loss factors have been reported.

NOTATIONS

a	stringer pitch for stiffened sandwich panel
b	width of panel
A_i	coefficients defining transverse displacement
A_s	cross-sectional area of stringer
d_o	$(h_1+h_3)/2+h_2$
$\overline{d}$	$d_o/2a$
D_t	$(E_1h_1^3+E_3h_3^3)/12(1-\nu^2)$
E_i	Yong's modulus of stringer,
h_i	Thickness of the layer 'i'
M_x	Bending moment
p_i+jq_i	Roots of characteristic equations
S, S_x	Transverse shear force and nondimensional transverse shear force
U,V,W	Displacements in X,Y and Z-directions
x	Nondimensional ordinate in 'X' direction = X/a
g	Shear parameter $= G(1/E_1h_1+1/E_3h_3)a^2(1-\nu^2)/h_2$
$\overline{y}$	Geometric parameter $= 1+\dfrac{(h_1+h_3 2h_2)^2}{4D_t(1-\nu^2)}\;\dfrac{E_1h_1E_3h_3}{E_1h_1+E_3h_3}$
ρ_i	Mass density of 'i'th layer
ζ	$\dfrac{m\pi y}{b}$
ν	Poisson's ratio
ω	circular frequency
E_s	Elasticity modulus of stringer
C_{wo}	Warping constant about shear centre 'O'
I_η	M.I.of stringer about centroidal axis parallel to 'X' direction
I_ξ	M.I. of stringer about centroidal axis parallel to 'Y'-direction
$I_{\eta\xi}$	Product moment of inertia
ρ_s	Mass density of stringer
C_y	distance shown in Fig. 2
l,r	Subscripts used for left and right side of line of attachment of stringer

Ω frequency parameter

$= (\rho_1 h_1+\rho_2 h_2+\rho_3 h_3)\ \omega^2 a^4/D_t$

1. INTRODUCTION

The sandwich panel consisting of a pair of stiff elastic faces separated by and bonded to a soft central viscoelastic core layer have found extensive application as structural components of aircrafts, spacecrafts, missiles and in many other branches of contemporary structural engineering. Generally these panels are further stiffened by orthogonally placed stringers. Vibration and damping analysis of these structures are of considerable importance and have been investigated in [1,2,3]. In these studies energy methods have been used for deriving equations of motion and solutions have been found for simply supported boundary conditions. In [4] the authors have reported transfer matrix analysis for free vibration of elastic sandwich plates. In the present work the method of transfer matrix has been developed for forced response of stiffened sandwich panel with a deterministic harmonic loading. Rectangular sandwich panel with any number of stringers at equal or unequal intervals and with edges perpendicular to stringers simply supported and edges parallel to stringers with arbitrary boundary conditions have been considered. Variations of all quantities along perpendicular to simply supported edges have been taken sinusoidal satisfying the boundary conditions. This transforms the two dimensional problem into effective one dimensional problem.

The principle of correspondence of linear viscoelasticity has been applied to take into account the viscoelastic damping of the core i.e., the shear modulus of the core is considered complex for forced response. Transverse displacement, slope, bending moment, shear force, longitudinal force and longitudinal displacement have been taken as elements of state vector defining state at a point. The field transfer matrix relating state vectors at any two points of a sandwich bay of the panel has been developed from the governing equations of motion of the bay. The elements of the state vector and the field matrix involve complex quantities due to complex shear modulus of the core. The point transfer matrix relating state vectors across the stringer has been developed from the governing equations of motion of a stringer which takes into consideration its inertia, warping and torsion.

The impressed force has been introduced in a form of a unit transverse shear force varying sinusidally along a perpendicular to the simply supported edges. A state vector having all elements zero except the shear force has been used as an excitation. Making use of the field and the point transfer matrices a relationship between the state vectors at extreme edges of the panel are established. Introducing known boundary conditions at the edges of the panel, non-zero elements of the state vector at one of these edges have been computed from the transfer matrix relationship. Using these computed values, the response in terms of various elements of the state vector at any location of the panel can be evaluated.

2. FIELD TRANSFER MATRIX

Fig. 1 shows a finite stringer stiffened damped sandwich panel with X-wise edges, i.e., the edges perpendicular to the stringers simply supported and the edges parallel to stringers with arbitrary boundary conditions. The modulus of the viscoelastic core is given by $G_v = G + j\beta$ where G = Real part of the modulus and β= Material loss factor. Using G_v in place of G, the sixth order governing differential equation of motion of the sandwich bay is obtained [4] as follows:

$$W_x^{vi} -(3\zeta^2+g\bar{y}+j\beta g\bar{y})W_x^{iv}+\{(3\zeta^4+2\zeta^2 g\bar{y}-\Omega)$$
$$+ j2\beta g\bar{y}^2\zeta\}W_x^{ii}+\{\Omega- \zeta^6- \zeta^4 g\bar{y}+ \zeta^2\Omega+g\Omega)$$
$$+j(\beta g\Omega- \beta g\bar{y}\zeta^4)\}W_x = 0 \qquad (1)$$

The solution of equation (1) is given by

$$W_x = \sum_{i=1}^{6} e^{(p_i+jq_i)x} \qquad (2)$$

The 'n'th derivative of $'W'_x$ w.r.t. 'x' is given by

$$W_x^n = \sum_{i=1}^{6} A_i(p_i+jq_i)^n e^{(p_i+jq_i)x} \qquad (3)$$

Equation (3) may be simplified as

$$W_x^n = \sum_{i=1}^{6} A_i(p_{i,n}+jq_{i,n})(p_{xi}+jq_{xi})$$
$$= \sum_{i=1}^{6} A_i(p_{xi,n}+jq_{xi,n}) \qquad (4)$$

where

$$p_{xi,n} = p_{i,n}p_{xi}-q_{i,n}q_{xi}$$
$$p_{in} + jq_{i,n}=(p_i+jq_i)^n$$
$$p_{xi}= e^{p_i x}\cos q_i x,$$
$$q_{xi}=e^{p_i x}\sin q_i x \qquad (5)$$

and

$q_{xi,n}=q_{i,n}p_{xi}+p_{i,n}\ q_{xi}$

for i = 1,2,...,6.

Hence from equation (4) the vector of W_x and its first five derivatives may be written as

$$\{W_x^n\} = [P_{xr}+jP_{xi}]\{A_i\} \qquad (6)$$

where

$$W_x^n = [W_x \quad W_x^i \quad W_x^{ii} \quad W_x^{iii} \quad W_x^{iv} \quad W_x^v]^T$$

$$[P_{xr}]=\begin{bmatrix} p_{x1,0} & p_{x2,0} & p_{x3,0} & p_{x4,0} & p_{x5,0} & p_{x6,0} \\ p_{x1,1} & p_{x2,1} & p_{x3,1} & p_{x4,1} & p_{x5,1} & p_{x6,1} \\ p_{x1,2} & p_{x2,2} & p_{x3,2} & p_{x4,2} & p_{x5,2} & p_{x6,2} \\ p_{x1,3} & p_{x2,3} & p_{x3,3} & p_{x4,3} & p_{x5,3} & p_{x6,3} \\ p_{x1,3} & p_{x2,3} & p_{x3,3} & p_{x4,3} & p_{x5,3} & p_{x6,3} \\ p_{x1,4} & p_{x2,4} & p_{x3,4} & p_{x4,4} & p_{x5,4} & p_{x6,4} \\ p_{x1,5} & p_{x2,5} & p_{x3,5} & p_{x4,5} & p_{x5,5} & p_{x6,5} \end{bmatrix}$$

$$[P_{xi}]=\begin{bmatrix} q_{x1,0} & q_{x2,0} & q_{x3,0} & q_{x4,0} & q_{x5,0} & q_{x6,0} \\ q_{x1,1} & q_{x2,1} & q_{x3,1} & q_{x4,1} & q_{x5,1} & q_{x6,1} \\ q_{x1,2} & q_{x2,2} & q_{x3,2} & q_{x4,2} & q_{x5,2} & q_{x6,2} \\ q_{x1,3} & q_{x2,3} & q_{x3,3} & q_{x4,3} & q_{x5,3} & q_{x6,3} \\ q_{x1,4} & q_{x2,4} & q_{x3,4} & q_{x4,4} & q_{x5,4} & q_{x6,4} \\ q_{x1,5} & q_{x2,5} & q_{x3,5} & q_{x4,5} & q_{x5,5} & q_{x6,5} \end{bmatrix}$$

Where

$$p_{xi,o} = 1.0 \quad \text{for} \quad i = 1,2,\ldots,6$$

The elements of state vector $\{SV_x\}$are the transverse displacement 'W_x',slope 'W_x^i', bending moment 'M_x', shear force 'S_x', longitudinal force 'N_x' and longitudinal displacement 'U_x'. U_x,N_x M_x and S_x are expressed as functions of 'W_x' and its derivatives [4] as follows.

$$U_x = (U_5+jU_{i5})W_x^v+(U_3+jU_{i3})W_x^{iii} + (U_1+jU_{i1})W_x^i \qquad (7)$$

$$N_x = (G_4+jG_{i4})W_x^{iv}+(G_2+jG_{i2})W_x^{ii} + (G_o+jG_{io})W_x \qquad (8)$$

$$M_x = (M_4+jM_{i4})W_x^{iv}+(M_2+jM_{i2})W_x^{ii} + (M_o+jM_{io})W_x \qquad (9)$$

$$S_x = (V_5+jV_{i5})W_x^v+(V_3+jV_{i3})W_x^{iii} + (V_1+jV_{i1})W_x^i \qquad (10)$$

where

$U_5 = (1-\beta^2)\ g\ (1+\ \beta^2)^2$

$U_{i5}= -2/\{g\ (1+\beta^2)^2\}$

$U_3 = -U_5(2\zeta^2 g\bar{y}-g)\ +U_{i5}\beta(2\zeta^2 g\bar{y}-g)$

$U_{i3}= -\{U_{i5}(2\zeta^2 g\bar{y}-g)+2\beta\ \zeta^2 g\bar{y}-g\}U_5$

$U_1 = -(C_{o1}\ x\ U_{i5}\ -\ C_{oi1}\ x\ U_{i5})$

$U_{i1}= -(C_{o1}\ x\ U_{i5}\ +\ C_{oi1}\ x\ U_5)$

$G_4 = U_5xU_6-U_{i5}xU_{i6},G_{i4}=U_{i5}xU_6+U_5xU_{i6}$

$G_2 = U_3xU_6-U_{i3}xU_{i6},G_{i2}=U_3xU_{i6}+U_6xU_{i3}$

$G_o = U_1xU_6-U_{i1}xU_{i6}-gh\bar{d},G_{io}=U_{i1}xU_6+U_1-\beta gh\bar{d}$

$M_4 = y_{11}G_4,M_{i4}=y_{i1}G_{i4},M_2=y_{11}G_2+1,$

$M_{i2}= y_{11}\ G_{i2}$

$M_o = y_{11}G_o,M_{io}=y_{11}G_{io},V_5=M_4+U_7xU_5$

$V_{i5}= M_{i4}+U_7xU_{i5},V_3=M_2+U_7xU_3,$
$V_{i3}=M_{i2}+U_7xU_{i3}$

$V_1 = M_o+U_7xU_1+\zeta^2(1-\nu),V_{i1}=M_{io}+U_7xU_{i1}$

$C_{o1}= \Omega-\zeta^4\ -g^2(1-\beta^2)(\bar{y}-1)-g\zeta^2(\bar{y}-1)$

$C_{oi1} = g^2(\bar{y}-1)2\beta-g\beta\zeta^2(\bar{y}-1),U_6=g(1-\nu)\zeta^2$

$U_{i6} = \beta g,\ U_7 = y_{11}\ \zeta^2\ (1-\nu),\ y_{11} = \dfrac{\bar{y}-1}{\bar{d}}$

Using the equations (7) to (10) the state vector $\{SV_x\}$ may be written in the following matrix form

$$\{SV_x\}= [C_r + j\ C_i]\ \{W_x^n\} \qquad (11)$$

where

$$\{SV_x\}= [W_x,W_x^i,\ M_x,S_x,N_x,U_x]^T$$

$$[C_r]=\begin{bmatrix} 1 & 0 & 0 & 0 & 0 & 0 \\ 0 & 1 & 0 & 0 & 0 & 0 \\ M_o & 0 & M_2 & 0 & M_4 & 0 \\ 0 & V_1 & 0 & V_3 & 0 & V_5 \\ G_o & 0 & G_2 & 0 & G_4 & 0 \\ 0 & U_1 & 0 & U_3 & 0 & U_5 \end{bmatrix}$$

and

$$[C_i]=\begin{bmatrix} 0 & 0 & 0 & 0 & 0 & 0 \\ 0 & 0 & 0 & 0 & 0 & 0 \\ M_{io} & 0 & M_{i2} & 0 & M_{i4} & 0 \\ 0 & V_{i1} & 0 & V_{i3} & 0 & V_{i5} \\ G_{io} & 0 & G_{i2} & 0 & G_{i4} & 0 \\ 0 & U_{i1} & 0 & U_{i3} & 0 & U_{i5} \end{bmatrix}$$

Using equation (6) equation (11) may be written as

$$\{SV_x\} = [D_{xr} + jD_{xi}]\,\{A_i\} \qquad (12)$$

where

$$[D_{xr}] = [C_r \;\; P_{xr}] - [C_i \;\; P_{xi}]$$

and

$$[D_{xi}] = [C_r \;\; P_{xi}] + [C_i \;\; P_{xr}]$$

State vector at x = 0 is given by

$$\{SV_o\} = [D_{or} + jD_{oi}]\,\{A_i\} \qquad (13)$$

or

$$\{A_i\} = [D_{or} + jD_{oi}]^{-1}\{SV_o\} = [Q_r + jQ_i]\{SV_o\} \qquad (14)$$

Using equations (14) and (12) the state vector $\{SV_x\}$ and $\{SV_o\}$ are related as

$$\{SV_x\} = [T + j\,\overline{T}]\,\{SV_o\} \qquad (15)$$

where

$$[T] = [D_{xr} \;\; Q_r] - [D_{xi} \;\; Q_i]$$

and

$$[\overline{T}] = [D_{xi} \;\; Q_r] + [D_{xr} \;\; Q_i]$$

$[T + j\overline{T}]$ is the field transfer matrix relating the state vector at ordinate 'x' to that at 'o'.

3. POINT TRANSFER MATRIX

The stringer is a thin walled member of open cross-section and is attached to the panel by bonding (Fig. 2). The elements of state vector at either side of line of attachment of stringer are given by compatibility and equilibrium considerations, i.e.,

$$W_J^r = W_J^1, \; W_J^{ir} = W_J^{il} \text{ and } U_J^r = U_J^1$$

$$E_s C_{wo} \frac{\alpha_x}{y^4} + G_s\, j_s \frac{\partial \alpha_x}{\partial y^2}$$

$$= -\rho_s j_c \ddot{\alpha}_x - \rho_s A_s C_y \ddot{W}_c - \rho_s A_s C_z \ddot{U}_c - (N_J^r - N_J^1)\, s_z + M_J^r - M_J^1$$

$$E_s\, I_\eta \frac{\partial^4 W_o}{\partial y^4} + E_s\, I_{\eta\xi} \frac{\partial^4 U_o}{\partial y^4}$$

$$= -\rho_s A_s \ddot{W}_c - (S_J^r - S_J^1) \qquad (16)$$

$$E_s\, I_\xi \frac{\partial^4 U_o}{\partial y^4} + E_s I_{\eta\xi} \frac{\partial^4 W_o}{\partial x^4}$$

$$= -\rho_s A_s \ddot{U}_c + N_J^r - N_J^1$$

Using geometric relations for deformation of stringer and sinusoidal variation of elements of state vector across the simply supported edges.

We have

$$W_{xJ}^r = W_{xj}^1, \; W_{xJ}^{ir} = W_{xJ}^{il}, \; U_{xJ}^r = U_{xJ}^1$$

$$M_{xJ}^r = M_{xJ}^1 + K_m W_x + K_r W_x^i + K_u W_x$$

$$S_{xJ}^r = S_{xJ}^1 - K_t W_x + K_f W_x^i + K_x U_x \qquad (17)$$

$$N_{xJ}^r = N_{xJ}^1 + K_w W_x + K_x W_x^1 + K_y U_x$$

With help of equation (16) the state vector at left and right side of line of attachment of stringer can be related as

$$\{SV\}_j^r = [ST]_J \{SV\}_j^1 \qquad (18)$$

$$[ST]_J = \begin{bmatrix} 1 & 0 & 0 & 0 & 0 & 0 \\ 0 & 1 & 0 & 0 & 0 & 0 \\ K_m & K_r & 1 & 0 & 0 & K_u \\ -K_t & K_f & 0 & 1 & 0 & K_v \\ K_w & K_x & 0 & 0 & 1 & K_y \\ 0 & 0 & 0 & 0 & 0 & 1 \end{bmatrix} \qquad (19)$$

and

$$K_m = (E_s I_{\eta\xi}\, s_z \zeta^4 - \omega^2 \rho_s A_s a^4 c_y)/D_t a^2$$

$$K_r = (E_s C_{ws} \zeta^4 + G_s J_s a^4 \zeta^2 - \rho_s J_s \omega^2 a^4)/D_t a^3$$

$$K_u = (E_s I_\xi \zeta^4 S_z - \rho_s A_s (C_z - S_z)\, \omega^2 a^4)/D_t a^2$$

$$K_t = (E_s\, I_\eta \zeta^4 - \rho_s \omega^2\, A_s\, a^4)/D_t a \qquad (20)$$

$$K_f = (-E_s I_{\eta\xi} s_z \zeta^4 + \rho_s A_s C_y \omega^2\, a^4)/D_t a^2$$

$$K_v = (-E_s\, I_{\eta\xi} \zeta^4)/D_t a$$

$$K_w = (E_s\, I_{\eta\xi} \zeta^4)\;\; (y-1) D_t a^3)/(d_o^2)$$

4. TRANSFER MATRIX CONSIDERING IMPRESSED FORCE

The panel is subjected to a deterministic excitation in form of transverse shear force that varies sinusoidally along a line passing through the middle of 'j'the bay and parallel to stringers. The excitation is given by

$$F_p(y,t) = F \sin\left(\frac{m\pi y}{b}\right) e^{i\omega t} \qquad (21)$$

Omitting sine function and time dependent functions and using S_x = unity, the

$$SF = [0 \;\; 0 \;\; 0 \;\; 1 \;\; 0 \;\; 0]^T \qquad (22)$$

Designating $[T + j\overline{T}]_i$ and $[ST_i]$ as the field and the point transfer matrices for 'i'th bay and 'i'th stringer respectively, $(TI + j\overline{TI})_j$ as the field transfermatrix for half of 'j'th sandwich bay and introducing impressed force vector, the state vector at right edge of the panel is related to that at left edge as follows:

$$\{SV_n\} = [TN + j\,\overline{TN}]\{SV_o\} + [TH + j\,\overline{TH}]\{SF_J\} \tag{23}$$

where

$$[TN + j\,\overline{TN}] = [T + j\,\overline{T}]_n\,[ST]_{n-1}\,\cdots\,[T + j\,\overline{T}]_1$$

and

$$[TH + j\,\overline{TH}] = [T + j\,\overline{T}]_n\,\cdots\,[ST]_j\,[TI + j\,\overline{TI}]_J$$

5. BOUNDARY CONDITIONS

The extreme edges of the panel parallel to stringers may be fixed, free, simply supported or supported on elastic springs, for which boundary conditions are known. Using these boundary conditions, the non-zero elements of state vector at one extreme edge of the panel can be evaluated by use of the transfer matrix relationship. In the analysis described below only fixed and simply supported boundaries have been considered. For fixed boundary edges, at 'o'th and 'n'th stations.

$$W_x = W_x^i = U_x = 0$$

and the state vectors at these stations are given

$$\{SV\}_o = [0 \quad 0 \quad M_x \quad S_x \quad N_x \quad 0]_o^T \tag{24}$$

and

$$\{SV\}_n = [0 \quad 0 \quad M_x \quad S_x \quad N_x \quad 0]_n^T \tag{25}$$

Using equations (24) and (25) in equation (23) and simplifying

$$\begin{Bmatrix}0\\0\\0\end{Bmatrix} = \left(\begin{bmatrix}tn13 & tn14 & tn15\\tn23 & tn24 & tn25\\tn63 & tn64 & tn65\end{bmatrix} + j\begin{bmatrix}\overline{tn13} & \overline{tn14} & \overline{tn15}\\\overline{th23} & \overline{tn24} & \overline{tn25}\\\overline{tn63} & \overline{tn64} & \overline{tn65}\end{bmatrix}\right)\begin{Bmatrix}M_x\\S_k\\N_x\end{Bmatrix} + \left(\begin{Bmatrix}th14\\th24\\tn64\end{Bmatrix} + j\begin{Bmatrix}\overline{th14}\\\overline{th24}\\\overline{th64}\end{Bmatrix}\right)$$

where 't's with subscripts are the elements of the corresponding matrices.

For simply supported boundary edges, at 'o'th and 'nth' stations,

$$W_x = M_x = N_x = 0$$

Hence the state vectors at these stations are given by

$$\{SV\}_o = [0 \quad W_x^i \quad 0 \quad S_x \quad 0 \quad U_x]_o^T \tag{27}$$

$$\{SV\}_n = [N \quad W_x^i \quad 0 \quad S_n \quad 0 \quad U_x]_n^T \tag{28}$$

Using equations (27) and (28) in equation (23) and simplifying

$$\begin{Bmatrix}0\\0\\0\end{Bmatrix} = \left(\begin{bmatrix}tn12 & tn14 & tn16\\tn32 & tn34 & tn36\\tn52 & tn54 & tn56\end{bmatrix} + j\begin{bmatrix}\overline{tn12} & \overline{tn14} & \overline{tn16}\\\overline{tn32} & \overline{tn34} & \overline{tn36}\\\overline{tn52} & \overline{tn54} & \overline{tn56}\end{bmatrix}\right)\begin{Bmatrix}W_x^i\\S_x\\U_x\end{Bmatrix} + \left(\begin{Bmatrix}th14\\th34\\th54\end{Bmatrix} + j\begin{Bmatrix}\overline{th14}\\\overline{th34}\\\overline{th54}\end{Bmatrix}\right) \tag{29}$$

6. DETERMINATION OF FORCED RESPONSE

The response at any point on the panel can be evaluated by use of the foregoing analysis. To determine response at mid-point of 'k'th bay with fixed y wise edges we proceed as follows. From equation (26) we have

$$\begin{Bmatrix}M_x\\S_x\\N_x\end{Bmatrix}_o = -\left(\begin{Bmatrix}th14\\th24\\th64\end{Bmatrix} + j\begin{Bmatrix}\overline{th14}\\\overline{th24}\\\overline{th64}\end{Bmatrix}\right)\left(\begin{bmatrix}tn13 & tn14 & tn15\\tn23 & tn24 & tn25\\tn63 & tn64 & tn65\end{bmatrix} + j\begin{bmatrix}\overline{tn13} & \overline{tn14} & \overline{tn15}\\\overline{tn23} & \overline{tn24} & \overline{tn25}\\\overline{tn63} & \overline{tn64} & \overline{tn65}\end{bmatrix}\right)^{-1} \tag{30}$$

Denoting state vector at mid point of 'k'th bay as $\{SV_{kk}\}$ and using equation (30) we have

$$\{SV\}_{kk} = [TI + j\overline{TI}]_k\ [ST]_{k-1} \cdots \quad [T + j\ \overline{T}]_1 \quad \{SV\}_o$$

$$+ [TI + j\overline{TI}]_k [ST]_{k-1} \cdot\cdot \quad [TI + j\overline{TI}]_J \quad \{SF\}_J \tag{31}$$

Above equation can be simplified as

$$\{SV\}_{kk} = [TK + j\overline{TK}] \quad SV_o + \quad [TJ + j\overline{TJ}]\ \{SF\}_J \tag{32}$$

where

$$[TK + j\overline{TK}] = [TI + j\overline{TI}]_k \cdots\cdot\ [T \ + j\overline{T}]_1$$

and

$$[TJ + j\overline{TJ}] = [TI + j\ \overline{TI}]_k \cdots\cdot\ [TI + j\overline{TI}]_J$$

Further simplification leads to following expression

$$\begin{Bmatrix} W_x \\ W_x^i \\ M_x \\ S_x \\ N_x \\ U_x \end{Bmatrix} = \left(\begin{bmatrix} tk13 & tk14 & tk15 \\ tk23 & tk24 & tk25 \\ tk33 & tk34 & tk35 \\ tk43 & tk44 & tk45 \\ tk53 & tk54 & tk55 \\ tk63 & tk64 & tk65 \end{bmatrix} + j \begin{bmatrix} \bar{t}k13 & \bar{t}k14 & \bar{t}k15 \\ \bar{t}k23 & \bar{t}k24 & \bar{t}k25 \\ \bar{t}k33 & \bar{t}k34 & \bar{t}k35 \\ \bar{t}k43 & \bar{t}k44 & \bar{t}k45 \\ \bar{t}k53 & \bar{t}k54 & \bar{t}k55 \\ \bar{t}k63 & \bar{t}k64 & \bar{t}k65 \end{bmatrix} \right) \begin{Bmatrix} M_x \\ S_x \\ N_x \end{Bmatrix} + \left(\begin{Bmatrix} tj14 \\ tj24 \\ tj34 \\ tj44 \\ tj54 \\ tj64 \end{Bmatrix} + j \begin{Bmatrix} \bar{t}j14 \\ \bar{t}j24 \\ \bar{t}j34 \\ \bar{t}j44 \\ \bar{t}j54 \\ \bar{t}j64 \end{Bmatrix} \right) \tag{34}$$

where 't's are elements of the corresponding matrices.

Proceeding as above the response of state vector at mid-point of 'k'th bay for simply supported end condition at extreme edges is given by

$$\begin{Bmatrix} W_x \\ W_x^i \\ M_x \\ S_x \\ N_x \\ U_x \end{Bmatrix} = \left(\begin{bmatrix} tk12 & tk14 & tk16 \\ tk22 & tk24 & tk26 \\ tk32 & tk34 & tk36 \\ tk42 & tk44 & tk46 \\ tk52 & tk54 & tk56 \\ tk62 & tk64 & tk66 \end{bmatrix} + j \begin{bmatrix} \bar{t}k12 & \bar{t}k14 & \bar{t}k16 \\ \bar{t}k22 & \bar{t}k24 & \bar{t}k26 \\ \bar{t}k32 & \bar{t}k34 & \bar{t}k34 \\ \bar{t}k42 & \bar{t}k44 & \bar{t}k46 \\ \bar{t}k52 & \bar{t}k54 & \bar{t}k56 \\ \bar{t}k62 & \bar{t}k64 & \bar{t}k66 \end{bmatrix} \right) \begin{Bmatrix} W_x^i \\ S_x \\ U_x \end{Bmatrix} + \left(\begin{Bmatrix} tj14 \\ tj24 \\ tj34 \\ tj44 \\ tj54 \\ tj64 \end{Bmatrix} + j \begin{Bmatrix} \bar{t}j14 \\ \bar{t}j24 \\ \bar{t}j34 \\ \bar{t}j44 \\ \bar{t}j54 \\ \bar{t}j64 \end{Bmatrix} \right) \tag{35}$$

where

$$\begin{Bmatrix} W_x^i \\ S_x \\ U_x \end{Bmatrix}_o = -\left(\begin{Bmatrix} th14 \\ th34 \\ th54 \end{Bmatrix} + j \begin{Bmatrix} \bar{t}h14 \\ \bar{t}h34 \\ \bar{t}h54 \end{Bmatrix} \right) \left(\begin{bmatrix} tn12 & tn14 & tn16 \\ tn32 & tn34 & tn36 \\ tn52 & tn54 & tn56 \end{bmatrix} + j \begin{bmatrix} \bar{t}n12 & \bar{t}n14 & \bar{t}n16 \\ \bar{t}n32 & \bar{t}n34 & \bar{t}n36 \\ \bar{t}n52 & \bar{t}n54 & \bar{t}n56 \end{bmatrix} \right)^{-1} \tag{36}$$

7. COMPUTATION OF FORCED RESPONSE

A computer program has been made to compute frequency response of a stringer stiffened sandwich panel subjected to sinusoidally varying line excitation in accordance with foregoing formulations. At an assumed value of frequency, response is computed. Frequency is then stepped up and response at this value of frequency is evaluated. The process is repeated till response is determined for a wide range of frequencies. The displacement response is plotted against frequencies and from this the resonant frequencies are obtained.

8. RESULTS AND DISCUSSION

The frequency response of a stringer stiffened damped sandwich panel with three bays has been computed. The structural data of panel is given in Table-1. The panel is simply supported at X and Y wise edges and is excited by a distributed line loading, the intensity of which varies sinusoidally along Y direction. The maximum amplitude of the loading is unity. The frequency response is computed at mid-point of third bay. Frequency response curves showing transverse displacement against frequency is given in Fig. 3.. Resonant frequencies and loss factors determined from the response curves on the basis of maximum response and half power bandwidth are given in 2nd and 3rd columns of the Table-1. The frequency response curves of the panel with X-wise edges simply supported and Y-wise edges fixed has also been determined and shown in Fig.4, for sinusoidally varying line loading. Corresponding resonant frequencies and loss factors are also given in 2nd and 3rd columns of Table-1.

Resonant frequencies and loss factors of the panel based on damped forced normal modes calculated from [5] has been reported in 4th and 5th columns of the Table-1. In the method reported by D.J. Mead [5], the fictitious harmonic loading on the panel has been used i.e. external distributed harmonic loading has to be in phase with local velocity and proportional to local inertia loading, while in the present analysis the excitation is discrete. As such the differences in the results for resonent frequencies and loss factors found by the above mentioned two methods are not ruled out.

By observing the results in Table-1, it may be seen that the resonant frequencies by the present developed method and by Mead's [5] method are reasonably in agreement and associated loss factor for the 1st mode also tally with each other. However the values of the loss factor for the third mode obtained by the present method are lower than that predicted by [5]. This may be attributed to the difference in the two methods of analysis and to the unavoidable computational errors. In the present analysis the line loading coincided with the nodal line of the second mode. As such the resonant frequency and loss factor in the second mode could not be ascertained.

TABLE - 1: RESONANT FREQUENCIES AND LOSS FACTOR OF STRINGER STIFFENED DAMPED SANDWICH PANEL

Structural data of panel : a = Distance between two consecutive stringers =17.2 cm, b=31.1 cm, $h_1 = h_3 = 0.071$cm, $h_2 = 0.1$ cm, $E_1 = E_3 = .7 \times 10^6$ kg/cm^2, G varies between 102 kg/cm^2 at 100cps to 1400 kg/cm^2 at 10^4 cps, β varies between 0.6 to 1.0 over 100 to 10^4 cps with maximum value = 1.0 at 390 cps. For stringer $K_r = 1.8164$, $K_t = 13072$, No. of stringers = 2, No. of bays = 3

End Conditions	Resonant Frequencies in cps and associated loss factor			
	obtained by transfer matrix for line excitation		Calculated from reported results [5]	
	Resonant frequency	Loss factor	Resonant frequency	Loss factor
X and Y wise edges simply supported	198	0.2	210	.21
	-	-	225	.23
	303	0.25	285	.31
Y wise edges fixed and X wise edges simply supported	212	0.21	225	.23
	-	-	285	.31
	315	0.16	316	.34

REFERENCES

1. Rao, Y.V.K.S.,'Vibrations of unsymmetrical sandwich structures', Ph.D. Thesis I.I.T., Delhi, 1972.

2. Asnani, N.T. and Nakra, B.C., 'Vibration analysis of multilayered beams involving viscoelastic layers', Journal of Institution of Engineers (India) 50 pp. 187-193, (1970).

3. Asnani, N.T. and Nakra, B.C., 'Forced vibration analysis of sandwich beam with viscoelastic core', J.of Aero Soc. of India, 24, pp. 288-294, (1972).

4. Kavi, N. and Asnani, N.T.,'Free vibrations of sandwich plate by transfer matrix method', Journal of Aero.Soc. of India, Vol.30,No.3,4, pp. 187-182 (1978).

5. Mead, D.J.,'Loss factors and resonant frequencies of periodic damped sandwich plates', Journal of Engg. for Industry, Transactions of ASME, Feb. 1976, pp. 75-81.

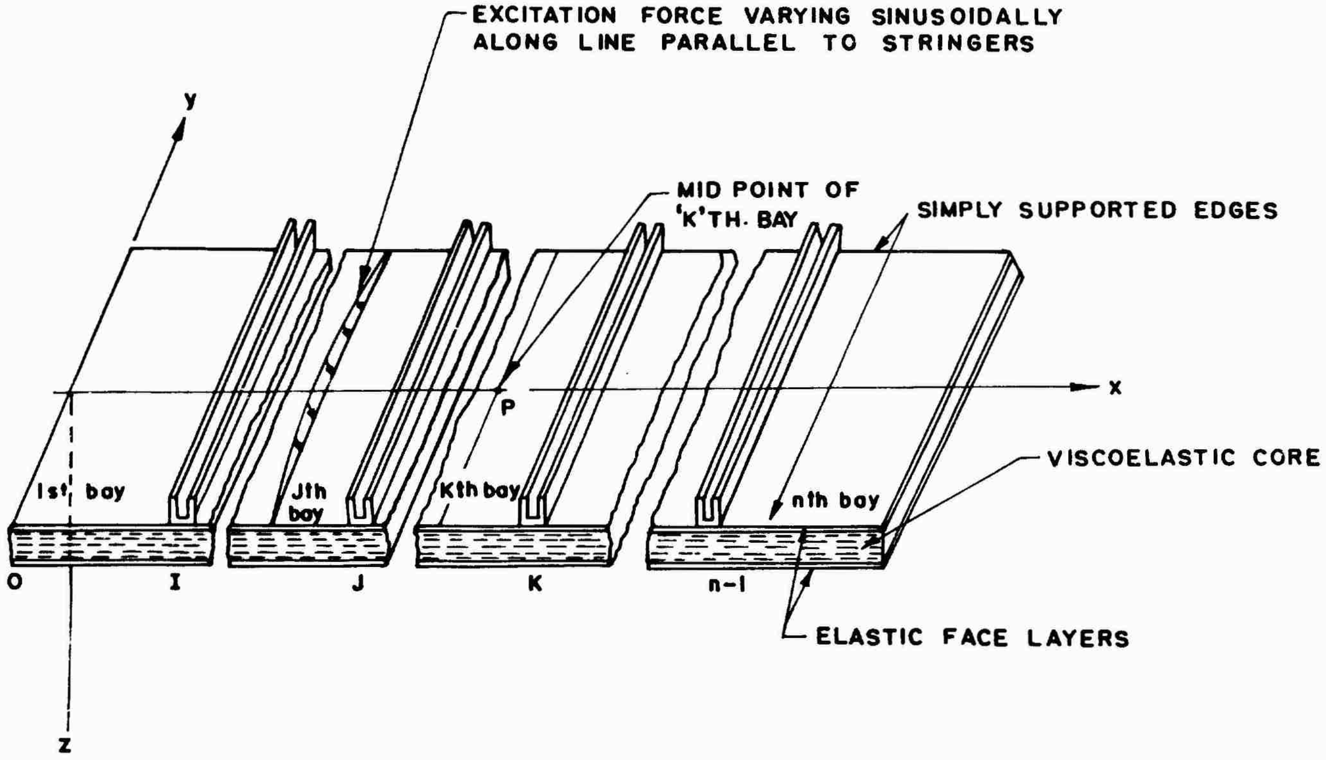

FIG. I CONFIGURATION OF STRINGER STIFFENED SANDWICH PANEL WITH VISCOELASTIC CORE.

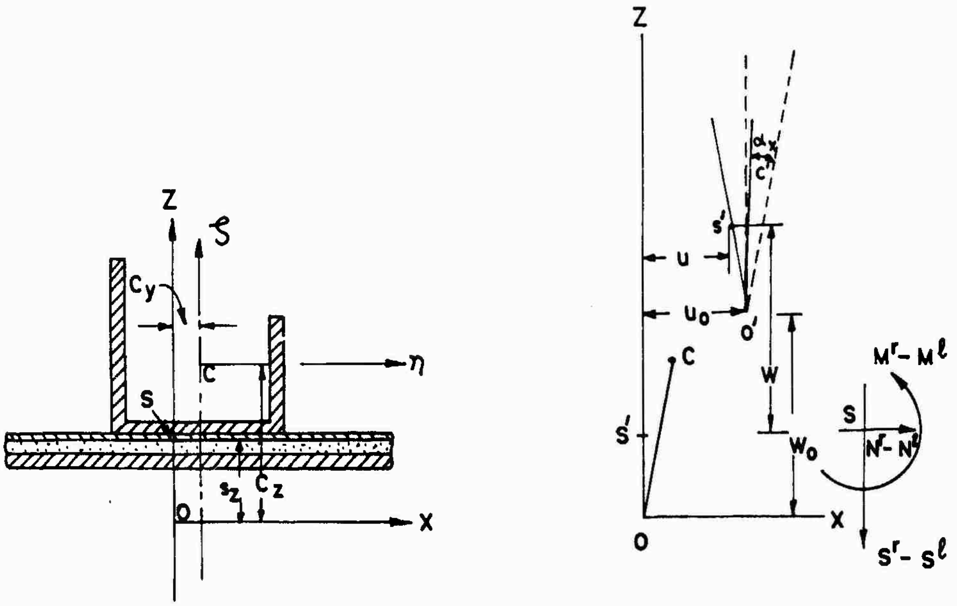

(a)

(b)

FIG. 2 (a) SECTION OF PANEL SHOWING STRINGER CROSS SECTION
(b) DISPLACEMENT OF STRINGER IN MOTION.

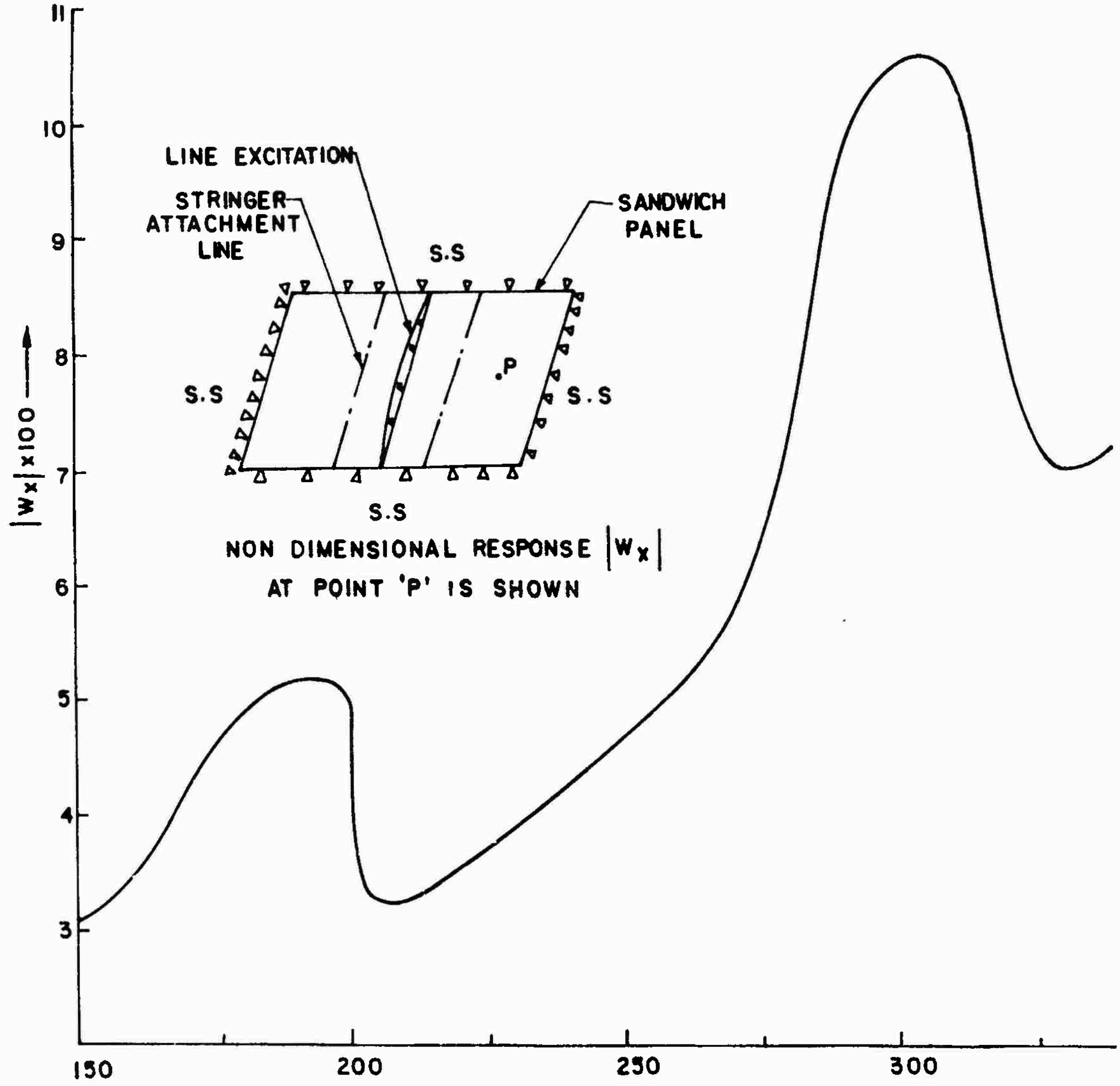

FIG. 3 FREQUENCY RESPONSE OF STIFFENED DAMPED SANDWICH PANEL SIMPLY SUPPORTED AT Y- WISE EDGES SUBJECTED TO SINUSOIDALLY VARYING LINE EXCITATION. (AMPLITUDE OF EXCITATION FORCE = 1 Kg.)

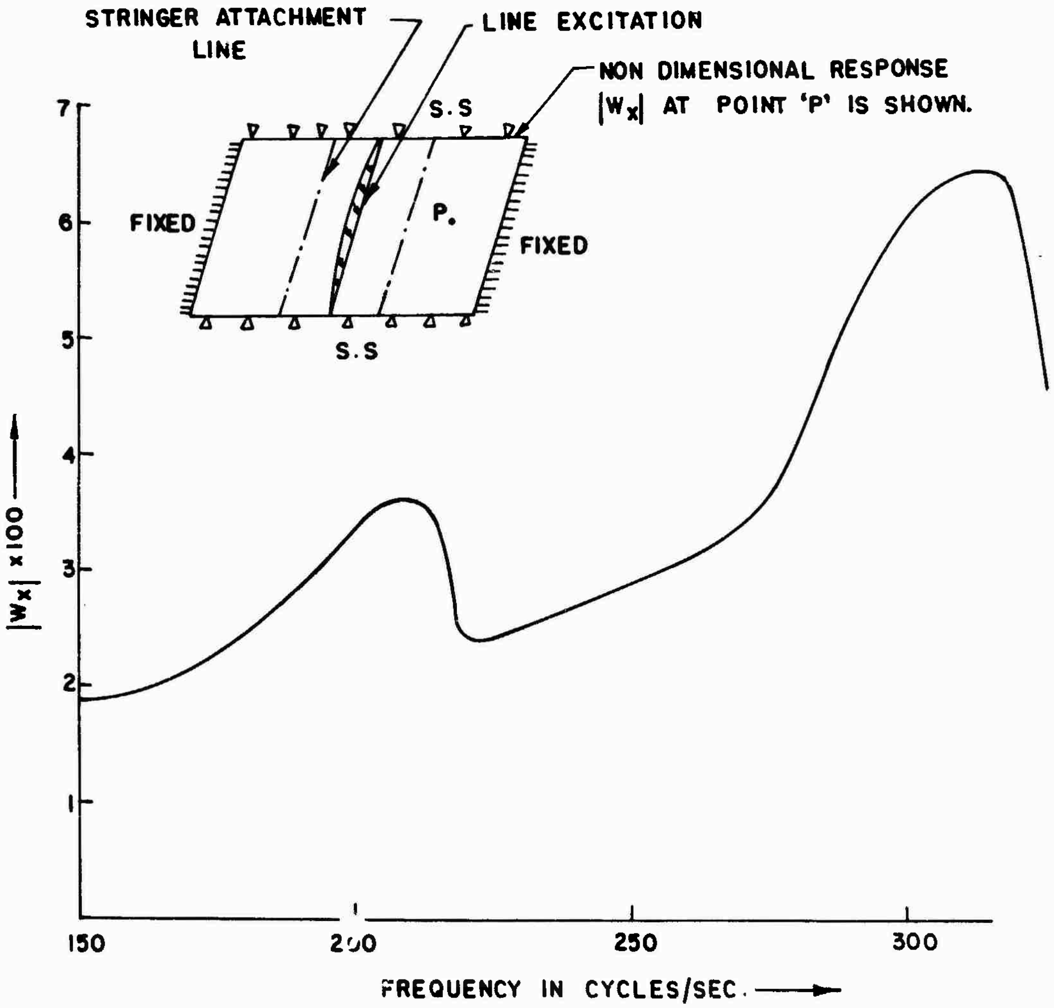

FIG. 4 FREQUENCY RESPONSE OF STIFFENED DAMPED SANDWICH PANEL WITH Y-WISE EDGES FIXED SUBJECTED TO SINUSOIDALLY VARYING LINE EXCITATION (AMPLITUDE OF EXCITATION FORCE=1 Kg)

STRUCTURAL DYNAMIC REANALYSIS USING RITZ VECTORS

L. Kitis
Department of Mechanical Engineering and Aerospace Sciences
University of Central Florida
Orlando, Florida 32816

and

W. D. Pilkey
Department of Mechanical and Aerospace Engineering
University of Virginia
Charlottesville, Virginia 22901

The objective of this paper is to indicate how structural dynamic reanalysis can be done when Ritz vectors [1] are used in mode superposition. Reanalysis methodology gives system response as a function of design parameters without a complete analysis for each parameter change. The generation of Ritz vectors for use in reanalysis requires the solution of linear algebraic equations and an eigenvalue problem of reduced order. An efficient method of formulation and solution of these problems is described.

INTRODUCTION

An alternative to the use of exact system eigenvectors as a basis for reducing the size of a finite element model to perform mode superposition analysis is the use of Ritz vectors. This approach, developed in Ref. [1], reduces computer time, provides error estimates for the dynamic analysis, and automatically includes the advantages of static condensation, Guyan reduction, and static correction due to higher mode truncation. The examples studied in [1] indicate that the superposition of Ritz vectors yields more accurate results, with fewer vectors, than when exact eigenvectors are used.

The purpose of this note is to indicate how structural dynamic reanalysis can be carried out when Ritz vectors are used instead of exact system eigenvectors. The basic objective of reanalysis methods is to compute system response as a function of design parameters without a complete structural analysis for each parameter change. These methods are frequently incorporated into optimization algorithms that require repetitive analyses of large systems [2].

EVALUATION OF RITZ VECTORS

Given mass matrix M, stiffness matrix K, and load vector $\underline{f}$, Ritz vectors are generated recursively using the numerical algorithm given in [1]. Consider a locally modified system in which a relatively small number of entries of the matrices M and K vary with trial design changes. Let the initial matrices be denoted by M_0, K_0 and let design changes be expressed by the sparse matrices ΔM, ΔK. Then the mass and stiffness matrices for the trial design are given by

$$
\begin{aligned}
M &= M_0 + \Delta M \\
K &= K_0 + \Delta K
\end{aligned}
\qquad (1)
$$

The first step in the evaluation of Ritz vectors is to solve for the displacement vector vector $\underline{x}_1^*$

$$K\underline{x}_1^* = \underline{f} \qquad (2)$$

As the stiffness matrix K is changed according to (1), the solution of (2) requires static reanalysis for which there are many algorithms available [3]. One possible approach is to derive a reduced order set of linear equations whose solution gives the modified response $\underline{x}_1^*$ assuming the original response $\underline{x}_{10}^*$ has been computed and stored. To this end, rewrite Eq. (2) in the form

$$(K_0 + \Delta K)\underline{x}_1^* = \underline{f} \qquad (3)$$

and multiply Eq. (3) by the inverse of K_0 to get

$$(I_N + K_0^{-1}\Delta K)\underline{x}_1^* = K_0^{-1}\underline{f} = \underline{x}_{10}^* \qquad (4)$$

where I_N is the NxN identity matrix and N is the order of the matrices K and M. Recalling that ΔK is a sparse matrix, let I, J be integer sets denoting the nonzero rows and the nonzero columns, respectively, of ΔK. Arranging the entries of I and J in ascending order, write

$$I = \{i_1, i_2, \dots, i_q\}$$
$$J = \{j_1, j_2, \dots, j_p\} \qquad (5)$$

Define a condensed stiffness matrix $\overline{\Delta K}$ by taking

$$\overline{\Delta K}_{m,n} = \Delta K_{i_m, i_n}$$

for $1 \leq m \leq q$, $1 \leq n \leq p$. Similarly, define

$$\overline{(K_0^{-1})}_{m,n} = (K_0^{-1})_{j_m, j_n}$$
$$\bar{\underline{x}}_1^* = (x_{1j_1}, x_{1j_2}, \dots, x_{1j_p}) \qquad (6)$$

With these definitions, the reduced order system of linear equations obtained from Eq. (4) can be written as a pxp matrix equation

$$(I_p + \overline{K_0^{-1}}\,\overline{\Delta K})\,\bar{\underline{x}}_1^* = \bar{\underline{x}}_{10}^* \qquad (7)$$

where the k-th entry of the vector on the right hand side is the j_k-th entry of the original response vector $\bar{\underline{x}}_{10}^*$. Since $\underline{x}_{10}^*$ is known, the solution $\bar{\underline{x}}_1^*$ of the set of p linear equations (7) is enough to determine the complete modified response vector $\underline{x}_1^*$. In fact, for $k \notin J$ the response component $\underline{x}_{1_k}^*$ is given by

$$x_{1_k}^* = x_{10_k}^* - \sum_{m=1}^{p}\sum_{n=1}^{q} K_{0_{k,i_n}}^{-1}\,\overline{\Delta K}_{n,m}\bar{x}_{1m}^* \qquad (8)$$

which follows from Eq. (4). Thus, Eq. (7) is an equation of reduced order (p<N) whose solution yields, with Eq. (8), the solution to the problem (3). In order to apply Eqs. (7) and (8), however, it is necessary to calculate the columns i_n, $1 \leq n \leq q$, of the inverse of the original stiffness matrix K_0. One convenient way to do this is to solve

$$K_0\underline{w}_k = \underline{e}_{i_k} \qquad (9)$$

for $\underline{w}_k$, $1 \leq k \leq q$, where $\underline{e}_{i_k}$ is the vector with all entries zero except the i_k-th entry, which is one. Then, $\underline{w}_k$ is the i_k-th column of the inverse of K_o.

The second essential step in the calculation of Ritz vectors is to find $\underline{x}_i^*$ by solving

$$K\underline{x}_i^* = M\underline{x}_{i-1} \qquad (10)$$

for i = 2,3...,L. The reanalysis problem associated with Eq. (10) is only slightly different from the one solved above starting from Eq. (2). Equation (4) becomes

$$(I_N + K_0^{-1}\Delta K)\ \underline{x}_i^* = K_0^{-1}\ (M + \Delta M)\ \underline{x}_{i-1} \qquad (11)$$

The right hand side varies with mass changes, but can easily be found by solving the linear equation

$$K_0\ \underline{u} = (M + \Delta M)\ \underline{x}_{i-1} \qquad (12)$$

Thus, it is only necessary to replace the vector $\underline{x}_{10}^*$ with the vector $\underline{u}$ to apply the reanalysis formulas given above to problem (3). In particular, the reduced order problem (7) becomes

$$(I_p + \bar{K}_o^{-1}\ \overline{\Delta K})\ \bar{\underline{x}}_i^* = \bar{\underline{u}} \qquad (13)$$

where the k-th entry of $\bar{\underline{u}}$ is the j_k-th entry of $\underline{u}$. Equation (8), which gives the components of response that are not included in the reduced vector $\bar{\underline{x}}_i^*$, becomes

$$x_{i_k}^* = u_k - \sum_{m=1}^{p}\sum_{n=1}^{q} K_{0_{k,i_n}}^{-1} \times \overline{\Delta K}_{n,m}\ \bar{x}_{i_m}^* \qquad (14)$$

CONCLUSION

The reanalysis problem for the generation of Ritz vectors has been seen to be a static reanalysis problem and a method of solution has been described. The third essential step in finding Ritz vectors requires the solution of an eigenvalue problem of reduced order [1]. This step may be retained without change, since the numerical effort involved is small compared to the effort involved in the computation of the Ritz vectors.

REFERENCES

1. Wilson, E. L., Yuan, Ming-Wu, Dickens, J. M., "Dynamic Analysis by Direct Superposition of Ritz Vectors," Earthquake Engineering and Structural Dynamics, Vol. 10, pp. 813-821, 1982.

2. Arora, J. S., "Survey of Structural Reanalysis Techniques," ASCE Journal of the Structural Division, April 1976, pp. 783-788.

3. Palazzolo, A. B., Wang, P. B., Pilkey, W. D., "Static Reanalysis Methods," Structural Mechanics Software Series, Volume IV, Eds. N. Perrone, W. D. Pilkey, pp. 413-460.

FATIGUE AND ACOUSTICS

PREDICTION OF METAL FATIGUE USING MINER'S RULE

H. H. E. Leipholz
Departments of Civil and Mechanical Engineering
Solid Mechanics Division
University of Waterloo
Waterloo, Ontario, Canada

In this paper, the concept of a modified Wöhler curve is introduced and used for the prediction of metal fatigue. First, a method is presented by which the modified curve can actually be obtained. Then, experimental evidence is given of the high precision of a fatigue life prediction by means of equation (4) which involves the values $\hat{N}_i$ provided by the modified Wöhler curve. In the last section of the paper, it is indicated how equation (4) can be modified to yield equation (18). This equation is applicable for fatigue life prediction in the case that the load is a stochastic one.

INTRODUCTION

In an earlier paper [1], it has been shown that Miner's rule is a reliable tool for predicting the fatigue life of metal specimens, even in the presence of random loading, provided *the probabilities of classes of equally damaging load cycles are known*. An extension to that paper was given in [2], where a proper damage specifying parameter was defined and the calculation of probabilities of the above mentioned nature was shown. The so developed theory was then applied and experimentally verified in [3]. It turned out to be the case that when using Miner's rule in the form

$$N = \left[\sum_i \frac{\beta_i}{N_i} \right]^{-1} \tag{1}$$

where β_i are the probabilities, and the N_i are expectations of fatigue lifes of the various equally damaging load cycles, the results for the fatigue life N of the specimens were poor, if one used N_i-values obtained from ordinary Wöhler curves. It proved to be necessary to use, for the quantities N_i, values provided by so-called *modified Wöhler curves*.

The aim of this paper is (i) to justify the use of these modified curves, (ii) to show how modified Wöhler curves can be obtained systematically, and (iii) to demonstrate experimentally the usefulness of the modified curves.

In order to simplify the experimental set-up, it is assumed this time that one has specimens of steel 1045-AR which are subjected to load cycle blocks of varying intensity as shown in Fig. 1. The s_i, $i = 1,2,3,\ldots$ are load levels, not necessarily *stress*levels, but levels corresponding to the respective damage parameter used; the n_i are the numbers of cycles per loading block so that

$$\beta_i = n_i/N \tag{2}$$

are the frequencies corresponding to load level i, which are to be used in (1) in place of probabilities.

For the following deliberations, *strain* levels of load cycles have been used as the damage parameter. Therefore, $s_i \equiv \varepsilon_i$ must be observed throughout.

MODIFIED WÖHLER CURVE

A Wöhler curve as shown in Fig. 2 is obtained by subjecting specimens to load cycles with certain peak values s_i which are kept constant until fatigue failure at N_i cycles occurs. The two corresponding values s_i and N_i are used as coordinates in an s,N-plane yielding points of the Wöhler curve. Since each point of the curve is determined by using a new specimen, there is no interaction effect. Therefore, the curve shall be termed "virgin". On the other hand, if a load history corresponding to Fig. 1 is applied to a specimen, there is an interaction effect: *the effect of larger cycles on the behaviour of the specimen when subjected to smaller cycles will be such that these smaller cycles will produce more damage than they would have produced if the specimen would still have been "virgin"*. Consequently, N_i-values from a virgin Wohler curve must be inadequate in this case as they do not reflect the influence which various load blocks will have on each other's damage producing power. One can with good reason assume that owing to the interaction effect, load blocks with

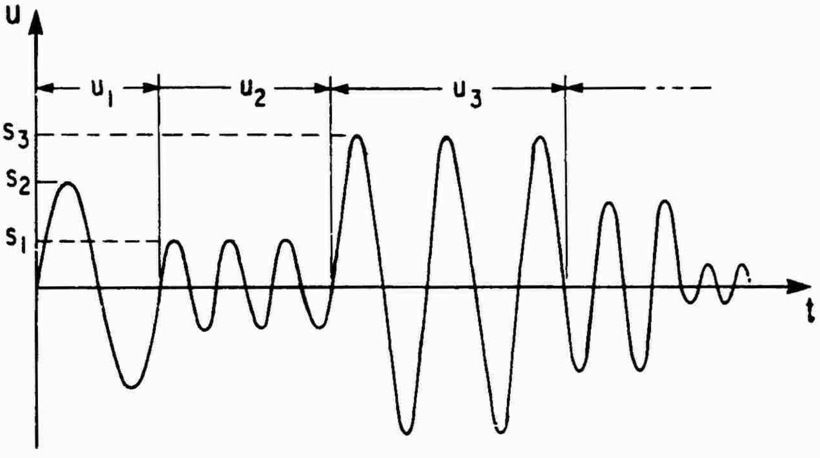

Fig. 1 - Loading with varying intensity

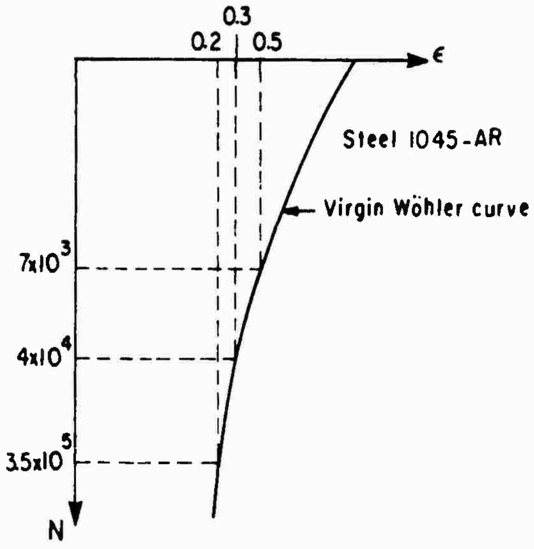

Fig. 2 - Wöhler curve for steel 1045-AR

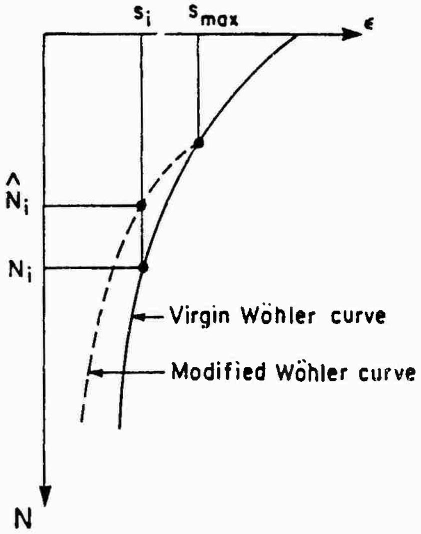

Fig. 3 - Modified Wöhler curve

$s_i < s_{max}$, where s_{max} is the highest load intensity in the loading history, will have, instead of N_i-values, $\hat{N}_i$-values for which

$$\hat{N}_i < N_i . \tag{3}$$

Thus, for damage evaluation of a loading history of the kind shown in Fig. 1, the $\hat{N}_i$-values of a modified Wöhler curve as shown in Fig. 3 should be used. Hence, fatigue life does not follow from equation (1) but from the new equation

$$\hat{N} = \left[\sum_i \frac{\beta_i}{\hat{N}_i} \right]^{-1} , \tag{4}$$

where necessarily $\hat{N} < N$. This reduction of fatigue life (according to (4)) as compared to the fatigue life predicted by the classical Miner's rule (1) is indeed being observed experimentally.

An explanation for the relevance of the modified Wöhler curve follows from recently detected phenomena in fracture mechanics involving the so-called "crack closure". Take for example the report by T. Topper and P. Au in [4]. According to the authors, repeated cycling of a certain intensity leads to decreasing damage production as debris produced by fracture props the crack tip open after a while so that further cracking, and thus damage production, is impaired. Only after a load cycle *with a sufficiently compressive peak* has been applied, damage production by the smaller cycle is reassumed at a higher degree. The effect of the compressive load is very long lasting, up to 200,000 cycles, and, when exceeding a certain compressive threshold, also a very strong one.

The mechanism of damage production and the effect of compressive load peaks on damage

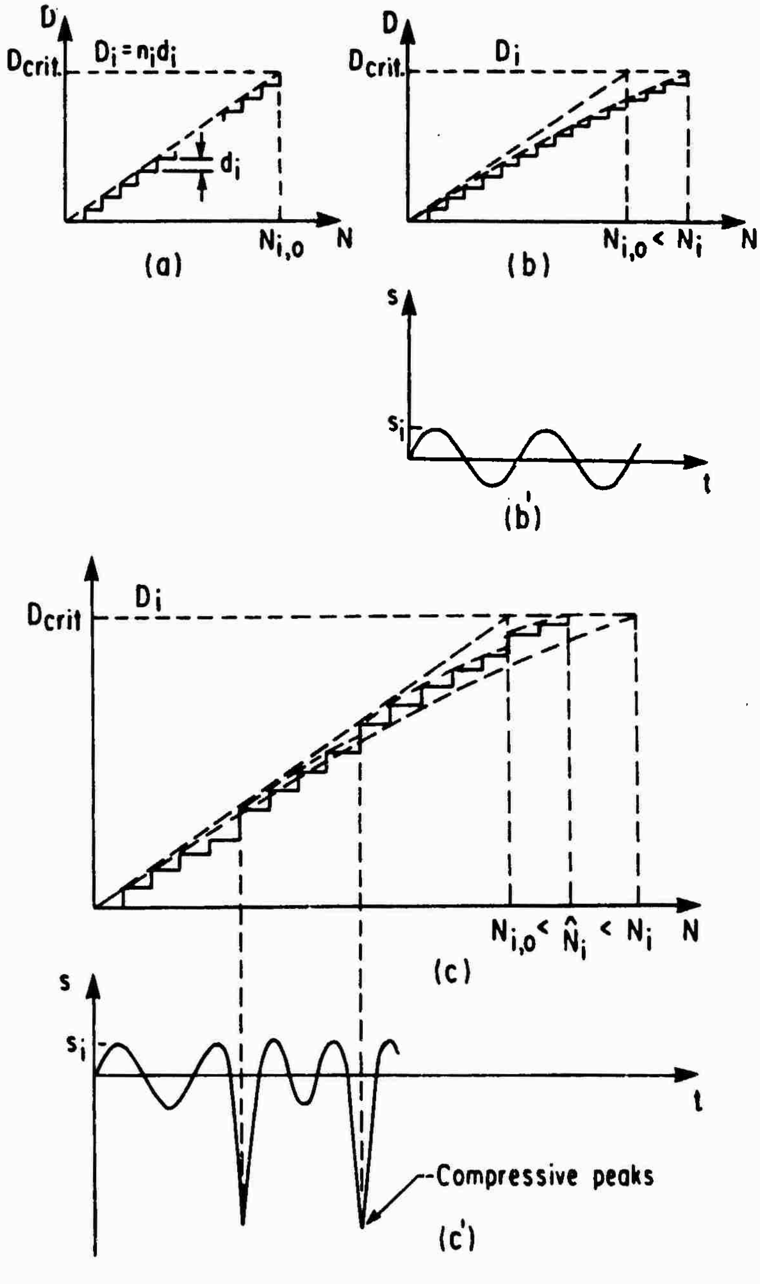

Fig. 4 - Effect of compressive load on damage accumulation

production is explained in Fig. 4. A certain load cycle with intensity s_i is assumed to produce a damage of magnitude d_i. After $N_{i,o}$ cycles, the total damage

$$D_{cr} = N_{i,o} d_i \tag{5}$$

leading to fatigue failure is reached. The corresponding fatigue life is $N_{i,o}$, (see Fig. 4a). However, that is an ideal situation. Actually, due to debris accumulation at the crack tip, the amount of damage per cycle is constantly decreased so that the loading in Fig. 4b' reaches the level D_{cr} only after $N_i > N_{i,o}$ cycles, (see Fig. 4b). Now assume that the load history changes from that in Fig. 4b' to the one in Fig. 4c' involving repeated compressive peak loads. Then, the damage accumulation occurs as shown in Fig. 4c. Due to the compressive peak loads, the damage accumulation is repeatedly accelerated owing to the temporary flattening of the debris and sharpening of the crack tip by the compressive load. Therefore, damage level D_{cr} is reached already after $\hat{N}_i$ cycles, where

$$N_{i,o} < \hat{N}_i < N_i \tag{6}$$

holds.

Realizing that the N_i-values are the abscissae of the virgin Wöhler curve and the $\hat{N}_i$-values that of the modified Wohler curve for one and the same ordinate s_i, it is plausible that the trace of the modified Wöhler curve must in-be as shown in Fig. 3.

But, something else can be concluded: Let be

$$d_i = ps_i, \qquad (7)$$

assuming that the damage d_i of a cycle is proportional to the corresponding damage parameter value s_i, where p is the coefficient of proportionality. Then, with (7) in (5), one obtains

$$D_{cr} = N_{i,o} p s_i. \qquad (8)$$

Using

$$k = D_{cr}/p, \qquad (9)$$

which is a certain constant, one arrives after rearrangement and with (9) in (8) at

$$s_i = kN_{i,o}^{-1}, \qquad (10)$$

which is a hyperbola, the "Wöhler hyperbola", in the s,N-plane [5]. Since (6) holds, one can conclude that this hyperbola is a lower bound for the modified Wöhler curve, see Fig. 5. Hence, one has the practically very important result that the modified Wöhler curve can only be situated in a restricted domain of the s,N-plane which is the hatched domain in Fig. 5.

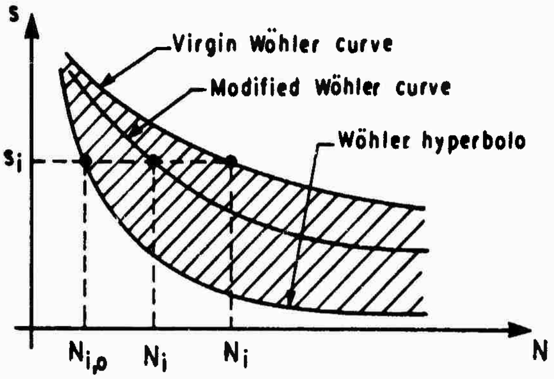

Fig. 5 - Location of the modified Wöhler curve

ON DETERMINING THE MODIFIED WÖHLER CURVE

Assume, n lab tests, each one with n load blocks, have been carried out. For test number i, the fatigue life $N^{(j)}$, the load intensity s_i for block i, and frequencies $\beta_i^{(j)}$ of cycles with intensity s_i in test number j have been reported. Then these quantities are supposed to be related by formula (4) if one sets $N^{(j)} \equiv \hat{N}^{(j)}$. Consequently, one has to expect that

$$\hat{N}^{(j)} = \left[\sum_{i=1}^{n} \frac{\beta_i^{(j)}}{\hat{N}_i}\right]^{-1}, \quad j = 1,2,\ldots n, \qquad (11)$$

In (11), the $\hat{N}_i$ are not known, while the $\beta_i^{(j)}$ are given by the load history, and the $\hat{N}^{(j)}$ have been determined experimentally. Hence, one may solve the set of equations (11) for the unknown $\hat{N}_i$. In this way, one obtains *the abscissae of points on the modified Wöhler curve*. The corresponding ordinates s_i are also known by virtue of the load history. Thus, one can plot n points of the modified Wöhler curve. As a result, one has an approximation to this curve.

The question arises what the significance of the approximation following from a single set of tests would be. The answer is, that it is very high. The reason for that is that the interaction effect between load blocks, which causes the modified Wöhler curve to emerge, is fairly invariant with respect to the triggering compressive load level and its frequency. Take a certain load history. Consider the loading block of highest intensity. Since the load is assumed to be cyclic, this block involves compressive peaks. If the intensity of these compressive peaks is beyond a certain threshold, the "crack closing effect" occurs, and if the frequency of these compressive peaks is again beyond a certain threshold, this effect is constantly upheld. Thus, for this loading history, as for any other satisfying these minimal requirements, the same modified Wöhler curve applies. As a consequence, it is up to a large degree immaterial which specific set of tests one uses to determine points on the modified Wöhler curve. This fact explains the relatively high significance of that single sample of the modified curve as obtained by means of *one* application of (11).

However, the following remarks have to be made in addition: for a derivation of the modified Wöhler curve through (11), no test data should be used which involve s_i values close to the endurance limit of the virgin Wöhler curve. Also test data should be chosen that specifically involve such $\beta_i^{(j)}$ values which yield a coefficient determinant of (11) suitable to make the calculation of the $\hat{N}_i$ values as insensitive as possible to the experimental inaccuracies involved in the test data. How this can be done has been discussed in [6].

Let now an example for determining the modified Wöhler curve be given. Consider the test data in Table 1.

Using the values in Table 1 for the equations in (11) yields

$$\left[\frac{0.02}{\hat{N}_1} + \frac{0.02}{\hat{N}_2} + \frac{0.96}{\hat{N}_3}\right]^{-1} = 57{,}338,$$

$$\left[\frac{0.3}{\hat{N}_1} + \frac{0.1}{\hat{N}_2} + \frac{0.6}{\hat{N}_3}\right]^{-1} = 13{,}507,$$

$$\left[\frac{0.02}{\hat{N}_1} + \frac{0.3}{\hat{N}_2} + \frac{0.68}{\hat{N}_3}\right]^{-1} = 20{,}789.$$

The solutions of these equations are

$$\hat{N}_1 = 4{,}551, \ \hat{N}_2 = 8{,}467, \ \hat{N}_3 = 90{,}391. \qquad (12)$$

TABLE 1
Test data 1-3

Test	Strain Peaks $\varepsilon_i \equiv s_i$	Frequencies $\beta_i^{(j)}$	Experimentally Observed Life $\hat{N}^{(j)}$
j = 1	$s_1 = 0.6$, $s_2 = 0.4$, $s_3 = 0.2$	$\beta_1^{(1)} = 0.02$, $\beta_2^{(1)} = 0.02$, $\beta_3^{(1)} = 0.96$	$\hat{N}^{(1)} = 57{,}338$
j = 2	$s_1 = 0.6$, $s_2 = 0.4$, $s_3 = 0.2$	$\beta_1^{(2)} = 0.3$, $\beta_2^{(2)} = 0.1$, $\beta_3^{(2)} = 0.6$	$\hat{N}^{(2)} = 13{,}507$
j = 2	$s_1 = 0.6$, $s_2 = 0.4$, $s_3 = 0.2$	$\beta_1^{(3)} = 0.02$, $\beta_2^{(3)} = 0.3$, $\beta_3^{(3)} = 0.68$	$\hat{N}^{(3)} = 20{,}789$

Combining these $\hat{N}_i$ values with the corresponding $s_i \equiv \varepsilon_i$ values yields the following points $P_i = (s_i, \hat{N}_i)$ on the modified Wöhler curve:

$$P_1 = (0.6;4{,}551),\ P_2 = (0.4;8{,}467),$$
$$P_3 = (0.2;90{,}391).$$

These points are used to draw the modified curve, in comparison to the virgin curve, in Fig. 6.

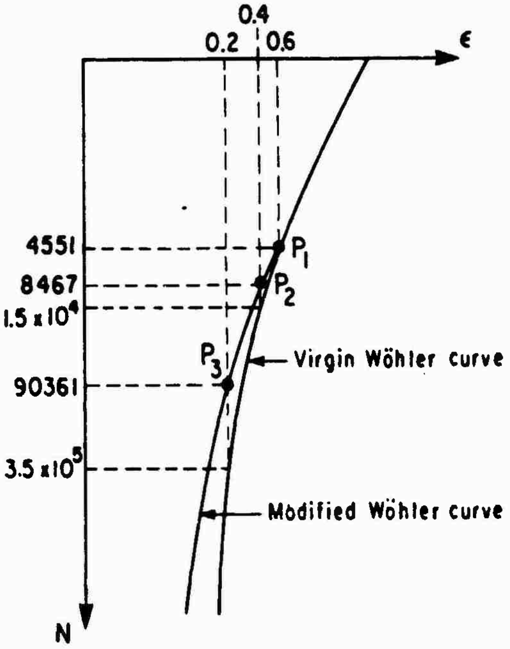

Fig. 6 - Comparison of modified Wöhler curve with virgin Wöhler curve

It should be noted that point P_1 must actually lie on the virgin Wöhler curve (as it fairly well does), since the cycle with the highest intensity, i.e. $s_1 = 0.6$, cannot have a damage increasing effect on itself. If point P_1 should turn out not to lie on the virgin curve owing to always present inaccuracies in the experimental data, one should drop the calculated point P_1 and replace it by that point on the virgin Wöhler curve which corresponds to $s_1 \equiv \varepsilon_1 = 0.6$.

The modified Wöhler curve will subsequently be used to show that for some other tests, the experimentally obtained fatigue life N can fairly accurately be predicted as $\hat{N}$ from equation (4).

EXPERIMENTAL VERIFICATION OF THE MODIFIED WÖHLER CURVE'S RELEVANCE

Consider Table 2. Since the s_i values are here the same as those in tests nos. 1, 2 and 3, the $\hat{N}_i$ values given in (12) can be used for a calculation of $\hat{N}^{(4)}$ by means of (4). The also needed $\beta_i^{(4)}$ values can be found in Table 2. Thus, one has

$$\hat{N}^{(4)} = \left[\frac{0.182}{4{,}551} + \frac{0.182}{8{,}467} + \frac{0.636}{90{,}391}\right]^{-1}$$

and obtains

$$\hat{N}^{(4)} = 14{,}559$$

for fatigue life prediction. This value compares well with the experimentally obtained value $N^{(4)} = 15{,}074$. The *conservative* prediction error is only

$$\frac{(15{,}074-14{,}599)100}{15{,}074} = 3.15\%.$$

This result apparently indicates that equation (4) together with the $\hat{N}_i$-values from the modified Wöhler curve works well indeed.

To support this assertion, let now a set of tests be considered for which not only the $\beta_i^{(j)}$ values but also the values s_i have been varied.

Let the new $s_i \equiv \varepsilon_i$ values be

$$s_1 = 0.5,\ s_2 = 0.3,\ s_3 = 0.2. \qquad (13)$$

The corresponding $\hat{N}_i$-values are read off the previously determined modified Wöhler curve as shown in Fig. 7 yielding the set of values

TABLE 2
Test data 4

Test	Strain Peaks $s_i \equiv \epsilon_i$	Frequencies $\beta_i^{(j)}$	Experimental Life
j = 4	$s_1 = 0.6,\ s_2 = 0.4,\ s_3 = 0.2$	$\beta_1^{(4)} = 0.182,\ \beta_2^{(4)} = 0.182,\ \beta_3^{(4)} = 0.636$	$\hat{N}^{(4)} = 15{,}074$

$$\hat{N}_1 = 6.5 \times 10^3,\ \hat{N}_2 = 2 \times 10^4,\ \hat{N}_3 = 9.04 \times 10^4. \tag{14}$$

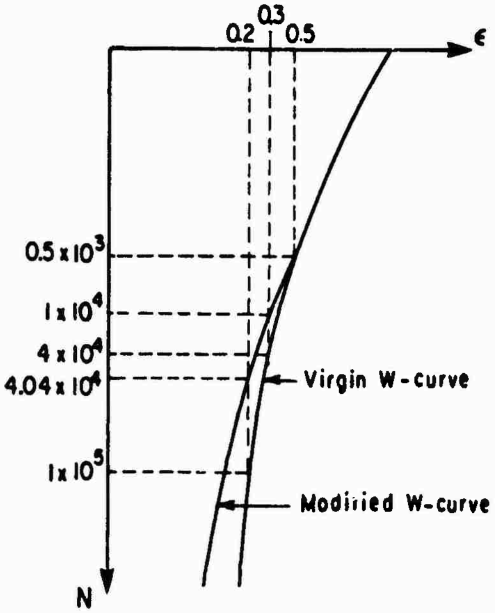

Fig. 7 - $\hat{N}_i$-values for tests A, B and C

Now let three tests, A, B, and C, be given for which the β_i-values and the experimentally determined N-values are reported in Table 3.

TABLE 3
Data for tests A, B, C

Test	A	B	C
β_1	0.02	0.3	0.02
β_2	0.02	0.1	0.3
β_3	0.96	0.6	0.68
$N_{exp.}$	80,876	17,729	41,695

Using the data in this table and the $\hat{N}_i$-values in (14), one obtains by virtue of (4) the fatigue life predictions

$$\hat{N}^{(A)} = \left[\frac{0.02}{0.65\times10^3} + \frac{0.02}{2\times10^4} + \frac{0.96}{9.04\times10^4}\right]^{-1} = 68{,}027,$$

$$\hat{N}^{(B)} = \left[\frac{0.3}{0.65\times10^3} + \frac{0.1}{2\times10^4} + \frac{0.6}{9.04\times10^4}\right]^{-1} = 17{,}349,$$

$$\hat{N}^{(C)} = \left[\frac{0.02}{6.5\times10^3} + \frac{0.3}{2\times10^4} + \frac{0.68}{9.04\times10^4}\right]^{-1} = 39{,}062.$$

Comparing these predictions with the experimentally obtained values in Table 3, one finds the following errors

$$e^A = \frac{(80{,}876-68{,}077)100}{80{,}876} = 15.9\%$$

$$e^B = \frac{(17{,}729-17{,}349)100}{17{,}729} = 2.13\%$$

$$e^C = \frac{(41{,}695-39{,}062)100}{41{,}695} = 6.3\%$$

These errors indicate that the predictions are on the safe side and sufficiently accurate.

In order to stress the latter point, let the fatigue life be predicted for test A using the classical formula (1). From Fig. 7 one obtains for

$$s_1 = 0.5,\ s_2 = 0.3,\ s_3 = 0.2,$$

The N_i values

$$N_1 = 6.5 \times 10^3,\ N_2 = 4 \times 10^4,$$
$$N_3 = 4 \times 10^5.$$

Thus, equation (1) yields

$$N_{pred.} = \left[\frac{0.02}{6.5\times10^3} + \frac{0.02}{4\times10^4} + \frac{0.96}{4\times10^5}\right]^{-1} = 167{,}308.$$

This value is to be compared with $N_{exp.} = 80{,}876$ yielding the error

$$e = \frac{(80{,}876-167{,}308)100}{80{,}876} = -106.9\%$$

The error indicates that the prediction by means of (1) is on the *unsafe* side. Also the error is rather large, 6.72 times larger than the error e^A, which had been calculated using the data provided by (4). These findings stress the relevance of (4) and of the modified Wöhler curve which is the foundation of (4).

Finally, let an extreme case be introduced. It is a test which involves the s_i-values

$$s_1 = 0.4,\ s_2 = 0.25,\ s_3 = 0.1, \tag{15}$$

and the β_i-values

$$\beta_1 = 0.005,\ \beta_2 = 0.005,\ \beta_3 = 0.99. \tag{16}$$

The remarkable fact is that $s_3 = 0.1$ is *below the endurance limit* of the virgin Wöhler curve and that the frequencies of the higher peak loads, i.e. $s_1 = 0.4$ and $s_2 = 0.25$, are *minimal*, namely $\beta = 0.005$, but still sufficient to trigger the interaction effect, as will be seen. Owing to the interaction effect, the damage producing power of the cycles with $s_3 = 0.1$ will be significantly increased, while, according to the classical Miner's rule, i.e. according to (1), these load cycles would not at all contribute to fatigue damage.

From Fig. 8, the N_i- and the $\hat{N}_i$-values are read off as follows:

TABLE 4
Comparison of Wöhler- and modified Wöhler data

$s_1 = 0.4$	$N_1 = 1.5 \times 10^4$	$\hat{N}_1 = 1.5 \times 10^4$
$s_2 = 0.25$	$N_2 = 1 \times 10^4$	$\hat{N}_2 = 4 \times 10^4$
$s_3 = 0.1$	$N_3 = \infty$	$\hat{N}_3 = 1 \times 10^6$

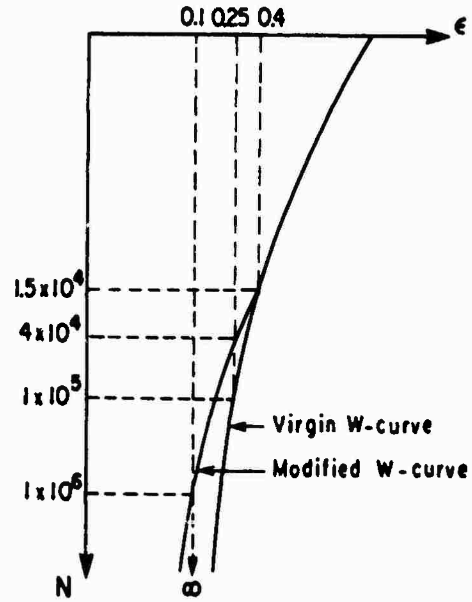

Fig. 8 - $s_3 = 0.1$ is below the endurance limit of the virgin curve

Using (16) and the $\hat{N}_i$-values of Table 4 in (4) yields

$$\hat{N} = \left[\frac{0.005}{1.5\times10^4} + \frac{0.005}{4\times10^4} + \frac{0.99}{1\times10^6}\right]^{-1} = 689{,}655.$$

The experimentally determined fatigue life for this case was

$$N_{exp.} = 821{,}615. \tag{17}$$

Hence, the prediction error following from applying equation (4) is

$$e = \frac{(821{,}615-689{,}655)100}{821{,}625} = 16\%$$

and it is on the safe side.

Let now the classical Miner's rule be used for a prediction of fatigue life, i.e. let equation (1) be applied. Then, one obtains

$$N = \left[\frac{0.005}{1.5\times10^4} + \frac{0.005}{1\times10^4} + \frac{0.99}{\infty}\right]^{-1} = 2{,}631{,}579.$$

Comparing this value with the experimental one in (17), one finds the error to be

$$e = \frac{(821{,}615-2{,}631{,}579)100}{821{,}615} = -220\%$$

This error is on the *unsafe side* and 13.75 times larger than the previous error related to (4). This fact indicates clearly that equation (4) is superior to the classical equation (1) and that the modified Wöhler curve, which leads to (4), is indeed very relevant.

STOCHASTIC LOADING

Assume that the specimen, whose fatigue life is to be predicted, is subjected to stochastic loading. Let this loading be such that i = 1,2,3..., classes of equally damaging events characterized by means of the values s_i of a damage parameter s can be identified. Let the occurrences of these classes in the load history be given by the probabilities p_i. Let there exist a *modified* Wöhler curve which relates the damage parameter values s_i for the $\hat{N}_i$-values introduced earlier. It is then claimed that

$$E(N) = \left[\sum_i \frac{p_i}{E(\hat{N}_i)}\right]^{-1} \tag{18}$$

yields the expected fatigue failure of the specimen under the stochastic loading.

The derivation of (18) is as follows. Let the subsequent considerations be based on two axions: If f is a random quantity and E[f] its expectation, then the relationships

$$E[\sum_i a_i f_i] = \sum_i a_i E[f_i], \quad a_i = \text{constants}, \tag{19}$$

$$E[\prod_i f_i] = \prod_i (E[f_i]), \text{ where the } f_i \text{ are statistically independent} \tag{20}$$

hold true.

The damage for load block i with n_i cycles and with damage d_i per cycle is

$$D_i = n_i d_i. \tag{21}$$

The total damage D a specimen can take is considered to be a physical constant. Therefore,

$$D = \hat{N}_i d_i \text{ for } any \text{ i.}$$

Hence,

$$d_i = D/\hat{N}_i. \tag{23}$$

Morover, by definition,

$$n_i = p_i N, \tag{24}$$

where N is the fatigue life.

Obviously,

$$D = \sum_i D_i . \tag{25}$$

Based on (19), one has by virtue of (25),

$$E(d) = \sum_i E(D_i). \tag{26}$$

Based on (20), one has by virtue of (21),

$$E(D_i) = E(n_i)E(d_i). \tag{27}$$

Using (27) in (26) yields

$$E(D) = \sum_i E(n_i)E(d_i). \tag{28}$$

Yet, from (24) follows

$$E(n_i) = p_i E(N). \tag{29}$$

Using (29) in (28) yields

$$E(D) = E(N)\sum_i p_i E(d_i) \tag{30}$$

and

$$1 = E(N)\sum_i p_i \frac{E(d_i)}{E(D)} . \tag{31}$$

Based on (20) and (22), one can claim that

$$E(D) = E(d_i)E(\hat{N}_i) \text{ for } \mathit{any} \text{ i}. \tag{32}$$

With (32) in (31) one finds

$$1 = E(N)\sum_i \frac{p_i}{E(\hat{N}_i)} , \tag{33}$$

which finally yields

$$E(N) = \left[\sum_i \frac{p_i}{E(\hat{N}_i)}\right]^{-1} .$$

That is (18) as had to be shown.

The conclusion is that fatigue life prediction using the modified Wöhler curve concept is indeed possible also in the case of certain classes of stochastic loading, provided the probabilities p_i of classes of damaging events with the intensities s_i are known. To a certain extent, work done by El Menoufy, H. H. E. Leipholz, and T. H. Topper in [3] is in anticipation of this conclusion.

ACKNOWLEDGEMENT

My thanks are due to Mr. D. Dowdell, Research Assistant, Department of Civil Engineering, University of Waterloo, for collecting the experimental data. The financial support by NSERC through Grant No. A7297 is also gratefully acknowledged.

REFERENCES

1. G. Phillipin, T. H. Topper and H. H. E. Leipholz, " Mean Life Evaluation for a Stochastic Loading Programme with a Finite Number of Strain Levels Using Miner's Rule," Shock and Vibration Bulletin 46, Part 3, pp.97-101, 1976.

2. G. Phillipin, T. H. Topper and H. H. E. Leipholz, "On the Mean Life Evaluation of a Material with Ideal Elasto-Plastic Behaviour, Subjected to a Stochastic Loading Programme with a Finite Number of Strain Levels," Shock and Vibration Bulletin 47, Part 2, pp.33-41, 1977.

3. M. El Menoufy, H. H. E. Leipholz and T. H. Topper, " Fatigue Life Evaluation, Stochastic Loading, and Modified Life Curves," Shock and Vibration Bulletin 52, Part 4, pp.11-19, 1982.

4. T. H. Topper and P. Au, "Cyclic Strain Approach to Fatigue in Metals," AGARD-Lecture Series-118, NTIS, Springfield, Virginia, pp.11-1 to 11-25, 1981.

5. H. H. E. Leipholz, "Lifetime Prediction for Metallic Structural Components Subjected to Loading with Varying Intensity," Proc. of CFC10 (Tenth Canadian Fracture Conference), J. T. Pindera, ed., M. Nijhoff Publ. BV, The Hague, pp.43-64, 1983.

6. D. J. Dowdell, H. H. E. Leipholz and T. H. Topper, "The Modified Life Law Applied to SAE-1045 Steel," Int. J. of Fracture, to appear.

Discussion

Mr. Zurnacian (Northrop Electronics Division): Would you say this finding is applicable to a broad class of engineering materials?

Mr. Leipholz: We have checked it for aluminum and for steel.

Mr. Getline (General Dynamics): What was your test specimen?

Mr. Leipholz: It was an unnotched specimen.

Mr. Getline: Was it polished?

Mr. Leipholz: Yes.

Mr. Getline: This is not the real world, unfortunately.

Mr. Leipholz: Yes.

Mr. Getline: Miner's Rule applies, if and when it does apply, only for that portion of the curve that you showed. If you continue up to the low frequency end, eventually you will arrive at ultimate stress, and where the sequence of stresses is not necessarily important within the area that you showed. When you get up to these high levels, where you get an occasional stress that will take it to yield or rupture, the whole thing breaks down.

Mr. Leipholz: Of course. However, that does not speak against the theory.

Mr. Getline: No, however, this actually occurs. I did all the sonic fatigue work on the Space Shuttle mid-fuselage, and we ran into these situations. Second, when you take a piece of aluminum plate, with which I am mostly familiar, and when you sculpture it and mill it, the fatigue properties change greatly. So, you do not have the same properties to deal with from one piece to another.

Mr. Leipholz: No. You see, if you talk about fatigue as I did, but I assume that I am talking to experts, it is quite clear that any kind of theory that you bring forward is for a specific material, and for a specific way to process the material. You do not have one theory for everything.

Mr. Getline: When you deal with random loading, rather than with block loading as you described, you can consider the area under an S-N curve, a fatigue curve representing the energy the piece of structure can absorb during its useful life. If you take the random loading, as the energy you put into it, you can develop a curve for that, where that curve moves forward in time until there is an intersection of the two curves which will give you an equivalent to Miner's Rule on an energy basis.

Mr. Leipholz: You can do it, or you can do it in a different way by really calculating, for a certain random loading, the kind of probabilities that the various parts of that random loading have. That gives you a very precise prediction. However, if you compare the theory with experiments, you must have well-defined experiments. The theory is, of course, only valid in the range that you define.

Mr. Galef (TRW): It would be very helpful to me if you would clarify the differences between your work and the work Freudenthal of Columbia did back in 1960, and Fuller of Boeing did in 1962. It sounds very similar.

Mr. Leipholz: Yes, it sounds similar. I might mention that I have had some correspondence with Professor Leibowitz on it, who is from NYU. The difference is indeed that we explain the physical reasoning behind it while Freudenthal came to the same conclusion; you must have a modified curve. However, he based it on statistical observations, so that is the difference. We tried to explain why that is from physical reasoning, so we can indeed predict where the modified curve would lie without carrying out 100,000 experiments.

OPTIMIZATION OF AEROSPACE STRUCTURES SUBJECTED TO RANDOM VIBRATION AND FATIGUE CONSTRAINTS

V.K. Jha
Spar Aerospace Limited
Ste. Anne de Bellevue, Quebec

and

T.S. Sankar and R.B. Bhat
Concordia University
Montreal, Quebec

Aerospace structures have to be designed with very strict reliability requirements, at the same time these structures should be as light as possible in weight to minimize the cost of launching into space. These structures are often subjected to random excitations with power spectral density varying in an arbitrary manner in the frequency domain. With the advent of the space shuttle, it is likely that these structures may have to be designed to withstand many launches, and hence fatigue will be an important factor along with other considerations while optimizing the design. An approach for handling and incorporating fatigue design constraints in optimizing aerospace structures has been presented in this paper.

Miner's criterion of cumulative fatigue damage has been used to formulate the fatigue constraint to ensure that the total expected fatigue damage over the required period of fatigue life does not exceed unity. The fatigue constraint is used in conjunction with other probabilistic constraints such as those on displacements, stresses and on component sizes, when subjected to random vibration loads, to arrive at an optimum design. An optimum design of a typical satellite antenna structure has been realized using the proposed approach of handling fatigue constraints.

INTRODUCTION

Aerospace structures have to be designed with very strict reliability requirements while their weight is kept to a minimum. They are subjected to random excitations during launch and the atmospheric part of their flight. Hence, their design must take the random nature of the responses into consideration. With the advent of the space shuttle, it is likely that these structures may have to be designed to withstand many launches, and consequently, fatigue will be an important consideration in optimizing the design.

An analytical technique to calculate the response of satellite antenna structures when subjected to random excitations during launch has been presented by Jha et al [1]. A method of optimizing these structures with probabilistic constraints was also presented by the same authors [2]. They followed an approach to synthesize structural analysis and optimization procedures that was proposed by Sobieski and Bhat [3] for the optimum design of structures.

An approach for incorporating fatigue design constraints in optimizing aerospace structures is presented in this paper. Miner's criterion [4] of cumulative damage has been used to formulate the fatigue constraint, and the sturcture is designed to ensure that the total expected fatigue damage over the service life does not exceed unity. The fatigue constraint is used in conjunction with other probabilistic constraints such as those on displacements, stresses and on component sizes, when subjected to random vibration loads. The design of a typical satellite antenna structure is optimized using the proposed approach of handling fatigue constraints.

DESCRIPTION OF AN ANTENNA SYSTEM

A satellite antenna structure is generally a circular dish, having the form of a paraboloid. The antenna serves the primary function of receiving and transmitting the communication signals reaching the spacecraft. The antenna is an integral part of the communications subsystem of any satellite. The structural survival of an antenna is of utmost importance for the successful operation of any satellite. A schematic of an antenna structure is shown in Figure 1.

OPTIMIZATION WITH PROBABILISTIC CONSTRAINTS

When a structure is subjected to random loading, the response is also random. Hence, any constraints applied on these response quantities must be probabilistic. Structural optimization with probabilistic constraints can be stated as following:

Minimize $W(X)$

Subject to

$$P(G_j(X) < G_j \text{ spec}) > Pj, \; j=1, \text{ NCON} \quad (1)$$

where $W(X)$ is the weight of the structure and P denotes the probability distribution.

The constraints specified in the inequality (1) imply that the probability that $G_j(X)$, which represents a parameter like stress or displacement, is less than or equal to a specified value G_j is greater than or equal to a probability P_j. Here NCON is the number of such constraints in the problem. Constraint (1) could also be expressed in an integral form as:

$$\int_{-\infty}^{G_{j\text{spec}}} f_j[G_j(X)]\, df_j > P_j \quad (2)$$

where $f_j[G_j(X)]$ is the probability density function of the parameter $G_j(X)$.

Since the excitations on the structure have been assumed to be Gaussian and the structure is taken to be a linear system, the response parameters defining the constraints $G_j(X)$ are also by definition Gaussian. Let $\bar{G}_j(X)$ be the first moment or the mean value of the parameter $\{G_j(X)\}$. Further, let G_j be the second moment or the standard deviation of the parameter $G_j(X)$. For the required limiting probability P_j, and the specified constraint value $G_{j\text{spec}}$ on G_j, tables for the unit normal variate give a value of

$$\frac{G_{j\text{spec}} - \bar{G}_j(X)}{\sigma\, G_j}$$

corresponding to the probability level P. Let this value be denoted by η_j. The condition stated through the probabilistic constraint of equation (2) can then also be satisfied by the adjoint deterministic constraint stated by the inequality expression.

$$\frac{G_{j\text{spec}} - \bar{G}_j(X)}{\sigma\, G_j} > \eta_j \quad (3)$$

Since the excitation is taken as a centered random process with zero mean, the mean value of $G_j(X)$ is zero, and G_j will become equal to the root mean square value of the parameter $\{G_j(X)\}$. Hence equation (3) may be expressed as

$$\frac{G_{j\text{spec}}}{G_j \text{ rms}} > \eta_j \quad (4)$$

The value of η_j will vary depending upon the acceptable probability level P_j specified on the constraint. The value of η_j is equal to 1 if P_j is equal to 0.65, 2 if P_j is equal to 0.95 and 3 if P_j is equal to 0.9927. The selection of the probability level P_j will be different for different situations and applications. Its value depends upon the risks involved if the structure fails, i.e. the risks involving cost, human life, health hazard, etc. With the variation in the specified probability level, the optimum solution for a structure will change. In general, a high reliability imposition in the probability will result in a heavier structure. A value of η_j equal to 2 has been chosen in designing the satellite antenna structure.

DESIGN REQUIREMENTS FOR THE ANTENNA STRUCTURE

Design requirements for the spacecraft antenna structures include requirements on frequency, displacement, structural integrity, size and shape and manufacturability of the antenna.

The design requirements are:

i) The first natural frequency of the antenna structure should be greater than 15 Hz.

ii) The maximum displacement of any point on the antenna structure should not exceed 2.54×10^{-2}m, when subjected to the random vibrations as shown in Fig. 2. The confidence level associated with this requirement should be at least 95%.

iii) The maximum stress in any element of the antenna structure should not exceed $1.38 \times 10^{8}\text{Nm}^{-2}$, when the structure is subjected to the random vibrational loading specified in Fig. 2.

iv) Minimum thickness of any section must be 5.0×10^{-4}m. This requirement is based upon the manufacturability requirements.

v) Fatigue failure must not occur for at least 36000 sec.

The above requirements reflect the general nature of the requirements imposed on the antenna design in the aerospace industry, at present.

DESCRIPTION OF THE FINITE ELEMENT MODEL

The finite element mathematical model of the antenna structure is presented in Fig. 3.

The model consists of 33 nodes connected with 24 plate elements and 24 beam elements. Out of the 33 nodes, 32 nodes have six degrees of freedom, and the central node is fixed representing the boundary conditions for the structure. The total number of degrees of freedom of the system used in the present analysis is 192. The size of the elements near the base has been kept smaller in comparison to the elements on the outer edges of the structure. The finer division near the base has been done because the most critical stresses are expected near the base since the smaller element size would ensure greater accuracy in the estimate of stresses in the plate elements. The coordinate system used for the analysis is shown in Fig. 3. The excitation axis of the structure has been taken as the z axis. This is the direction in which the most damaging excitations are experienced by the antenna structure.

FORMULATION OF THE DESIGN PROBLEM FOR OPTIMIZATION

The purpose of the optimization is to design an antenna with minimum possible weight and yet capable of meeting all the imposed design requirements. Hence, for the optimization, the particulars are:

The objective function is the weight of the structure and is specified in the form f(X), where X is the vector of design parameters.

The four parameters, describing the antenna design selected for optimization and shown in Fig. 4 are stated below:

a) The thickness of the dish;
b) The height of the ribs at the back of the dish;
c) The width of the ribs; and
d) The thickness of the ribs.

The thickness of the dish and the height of the ribs are assumed to be linearly decreasing from the central support of the dish to the outer edge, and the slope parameter defining the thickness and the heights at various locations are to be optimized.

The variables for optimization, thus, are:

x_1, the slope defining thickness of the plate;

x_2, the slope defining the height of the ribs;

x_3, the width of the ribs; and

x_4, the thickness of the rib section.

The constraints on the optimization, which reflect all the design requirements are as follows:

The Deterministic Constraints

1. Natural frequency > 15 Hz.
2. 0.002 radians $< X_1 < 0.05$ radians.
3. 0.02 radians $< x_2 < 0.05$ radians.
4. $7.6 \times 10^{-3}\text{m} \leq x_3 < 2.54$ m
5. $5.0 \times 10^{-4}\text{m} < x_4 < 0.254$ m

The Probabilistic Constraints

1. P[Maximum displacement $< 2.54 \times 10^{-2}$m $>$ 95%
2. P[Maximum stress in ribs $< 1.38 \times 10^{8}$ Nm^{-2} $>$ 95%
3. P[Maximum stress in dish surface $< 2.38 \times 10^{8}$ Nm^{-2} $>$ 95%
4. Expected cumulative damage in 36000 sec $<$ 1.

Thus the problem is now fully defined for carrying out an optimal design using the procedure established earlier [2].

Optimum Design of the Antenna without Fatigue Constraints:

The design scheme of [2] was used for optimization.

The initial values of the design variables were chosen by using the standard beam formulae to satisfy the stress displacement constraints. This was done to choose realistic and meaningful starting values. The weight saving thus obtained then becomes quite meaningful.

The Initial Design Parameters:

The parameters describing the initial design of the antenna are given by the following:

$x_1 = .004$ radians

$x_2 = .05$ radians

$x_3 = 1.27 \times 10^{-2}$m

$x_4 = 1.30 \times 10^{-3}$m

Weight of the structure = 8.9 kg

First natural frequency = 8.4 Hz

Maximum RMS displacement = 1.2×10^{-2}m

Maximum RMS stress = 8.11×10^{7} Nm^{-2}

Initial analysis also indicates that the starting design does not satisfy the frequency and stress constraints.

The Final Design of the Antenna:

After the completion of the automated optimum design performed by employing the Computer-Aided Design Procedure a feasible design realizing a weight less than the initial in-feasible design is obtained. The design history of the optimization cycle is shown in Fig. 5.

The final optimum design is obtained as follows:

$x_1 = 0.02$ radians

$x_2 = 0.08$ radians

$x_3 = 1.72 \times 10^{-2}$m

$x_4 = 7.6 \times 10^{-4}$m

Objective function = 5.08 kg

First natural frequency = 15.06 Hz

Maximum RMS displacement = 4×10^{-4}m

Maximum RMS stress = 5.69×10^{7} Nm^{-2}

FORMULATION OF THE FATIGUE CONSTRAINTS

The failure criterion used in modelling the fatigue constraint is based upon the hypothesis proposed by Miner [4] and Palmgren [5]. This is a simple deterministic criterion and has been considered appropriate in formulating the fatigue constraint in many structural dynamic problems. Here it is assumed that each cycle of the random stress response inflicts an incremental damage which depends upon the peak amplitude of the excursion. Each succeeding cycle inflicts additional damage and the failure occurs when the total damage reaches one hundred percent.

To quantatively establish the fatigue strength for a specific material, a large number of identical samples are to be tested with varying stress amplitudes. The results of such tests when plotted define the S-N (stress vs number of cycles to failure) curve or the fatigue curve for the material. A typical S-N curve is shown in Figure 5. The fixed stress amplitude is S, the number of cycles until failure occurs at stress S is N. For many materials, the curve is well approximated by a straight line when log S is plotted against log N, that is, S-N curve may be approximated by the equation,

$$N S^b = c \qquad (5)$$

where b and c are material dependent constants.

According to Palmgren-Miner hypothesis, when n cycles of stress amplitude S have been experienced, the material has used up a fraction of its fatigue life equal to n/N, where N is the number of cycles at which failure occurs under uniform stress amplitude S, as indicated by the S-N curve. Thus, if the material experiences n_i cycles of stress amplitude S_i for $i = 1,2,\ldots M$, the total cumulative damage is given by

$$D = \sum_{i}^{M} n_i/N_i \qquad (6)$$

According to Palmgren-Miner hypothesis the material will undergo a fatigue failure when the total cumulative damage D, reaches unity. Palmgren-Miner hypothesis imposes no restrictions regarding the order of application of various stress levels, and is thus applicable to random loading processes in which the stress may vary from one cycle to another.

In order to use the Miner's criterion in formulating the fatigue constraint, it is to be assumed that the response of the structure may be considered as a narrow band process. The validity of this assumption will be later checked before applying the fatigue constraint. Let f_0 be the expected frequency of the narrow band response in cycles/sec and T be the time in seconds for which the structure has to withstand the fatigue environment. Then the expected number of stress cycles in time T will be given as f_0T.

Let p(a) be the probability density of stress peaks. Expected number of cycles with peak stress varying from a to a+da is $p(a).da.f_0.T$. Let N(a) be the number of cycles at which failure will occur for a constant amplitude stress of 'a'. Then according to the Miner's criterion, the accumulated damage for cycles in the range of 'a' and 'a+da' is

$$\frac{n(a)}{N(a)} = f_0T\, p(a).da/N(a) \qquad (7)$$

The total expected damage E[D(t)] is given by

$$E[D(t)] = f_0 t \int_0^\infty \frac{p(a)}{N(a)}\, da \qquad (8)$$

If the response is assumed to be a Gaussian stationary random process, then the peaks have a Rayleigh distribution, given by

$$p(a) = \frac{a}{\sigma_y^2} \exp(-a^2/2\, \sigma y^2) \qquad (9)$$

where σ_y is the RMS response of the stress. Substituting Eqs. (5) and (9) in Eq. (8)

$$E[D(t)] = \frac{f_0T}{C\sigma_y^2} \int_0^\infty a^{b+1} \exp(-a^2/2\, \sigma_y^2)da$$

$$= \frac{f_0T}{C} (\sqrt{2}\, \sigma_y)^b\, \Gamma(1 + b/2) \qquad (10)$$

The condition for failure may be stated as

$$\frac{f_0 t}{\zeta} (\sqrt{2}\,\sigma_y)^b\, \Gamma(1 + b/2) > 1 \qquad (11)$$

Thus fatigue constraint specifying that the structure should not fail for T seconds is:

$$\frac{f_0 T}{\zeta} (\sqrt{2}\,\sigma_y)^b\, \Gamma(1 + b/2) < 1 \qquad (12)$$

FREQUENCY RESPONSE ANALYSIS

The fatigue constraint developed in Eq. (12) can now be used together with other design constraints to arrive at an optimum weight structure which will satisfy all the design constraints including fatigue. In the process of deriving the fatigue constraint, it was assumed that the response of the antenna structure is a narrow band random process. Before using the fatigue constraint given in Eq. (12), this assumption regardig the narrow band response is to be verified. The frequency response of a multi-degree of freedom system subjected to harmonic excitations is given by [6].

$$Y_i = \sum_{r=1}^{n} \phi_{2r} \frac{T_r}{M_r \omega_r^2} \frac{\ddot{x}(\omega)}{[\{1-\omega/\omega_r)^2\}^2 + 4\zeta^2\omega^2/\omega_r^2]^{\frac{1}{2}}} \qquad (13)$$

where:

Y_i is the peak displacement,

T_r is the participation factor for the rth mode,

M_r is the generalized mass for the rth mode,

ζ is the structural damping,

$\ddot{x}$ is the peak acceleration of the excitation,

ω is the rth natural frequency for the system, and

ω is the frequency of excitation in rad/sec.

The frequency response computation was carried out in the present context using the SPAR finite element program [7]. Additional software was generated to enable SPAR to compute the frequency response. A plot of the frequency response is shown in Fig. 6. As can be seen from this figure, the response of the antenna is a narrow band process and the predominant natural frequency of the structure is 22.5 Hz. Thus, the fatigue constraint developed as per Eq. (12) can be justifiably used for the antenna structure.

Optimum Design of the Antenna with Fatigue Constraint:

The satellite antenna structure optimized before without the fatigue constraint is now considered to include the fatigue constraint. The initial values chosen for the design parameters are the same as the optimum design parameters calculated before without the fatigue constraint. The initial values of the design parameters have been chosen in this manner to clearly bring out the effect upon the optimized weight of the structure due to inclusion of the fatigue constraint. All the other constraints imposed on the design without the fatigue constraint have been retained. The fatigue constraint as developed in Eq. (12) is included. The expected cumulative damage in 36000 sec. is constrained to be less than unity.

Including the fatigue constraint, the following optimum solution is arrived at:

Minimum weight = 12.3 lb (5.6 kg)

First natural frequency = 17.6 Hz

Maximum RMS displacement = 0.004" (0.010 cm)

Maximum RMS stress = 512 psi(37.2 kg/cm^2)

Design variables x_1 = 0.002 radians

x_2 = 0.089 radians

x_3 = 0.629" (1.597 cm)

x_4 = 0.032" (0.018 cm)

The final analysis for the minimum weight design of the antenna including the fatigue constraint is automatically produced by the software package developed. The change in the weight of the antenna structure and also the change in the values of the design parameters during various iterations are plotted in Fig. 7. The weight of the antenna continuously increases through various iterations. This is due to the fact that the starting design here was the optimum design without the fatigue constraints and to satisfy the fatigue constraint the structure must be made stronger in comparison to the previous optimum design that was achieved without the fatigue constraints. The design variables x_1 to x_4 show very little change in their values because the starting values correspond to the optimum design wiothout fatigue constraints and hence there is very little room for change in their values.

DISCUSSIONS AND CONCLUSIONS

The minimum weight of the antenna structure considering the fatigue constraint is 12.3 lb (5.59 kg) as compared to the minimum weight of 11.2 lb (5.09 kg) for the structure without the fatigue constraint. Thus an increase of 9.8 percent in weight is the penalty for including the fatigue constraint. The weight of the structure will also depend upon the time limits for the fatigue environment. The weight of the structure will increase with the increase in duration of the fatigue environment. At present, fatigue normally does not enter into the design requirement for spacecraft structures because the loads are applied only for a very short duration. However, with the advent of the space shuttle it is very likely that some structures will have to undergo loads for more than one launch, and then fatigue will become an important design requirement. Thus the proposed system of designing spacecraft structure can be used for designing structure to include fatigue requirements.

REFERENCES

1. Jha, V.K., Sankar, T.S., and Bhat, R.B. "Dynamic Behavior of a Satellite Antenna Structure in Random Vibration Environment" Shock and Vibration Bulletin #53, May 1983.
2. Jha, V.K., Sankar, T.S., and Bhat, R.B., "Computer Aided Synthesis of a Satellite Antenna Structure with Probabilistic Constraint", Shock and Vibration Bulletin, #53, May 1983.
3. Sobieski, J. and Bhat, R.B., "Adaptable Structural Synthesis Using Advanced Analysis and Optimization Coupled by a Computer Operating System", AIAA/ASME/ASCE, 20th Structural Dynamics and Materials Conference, St. Louis, April 1979.
4. Miner, M.A., "Cumulative Oamage in Fatigue", J. Applied Mechanics, Vol. 12, 145, 1945, pp. 159-164.
5. Palmgren, A., "Die Lebensdaur von Kugellagern", Ver. deut. Ingr., 24, pp. 339-341.
6. Lin, Y.K., "Probabilistic Theory of Structural Dynamics, McGraw-Hill, New York, 1967.
7. Wheatstone, W.D., "SPAR Structural Analysis Reference Manual", NASA CR-158970-1, 1978.

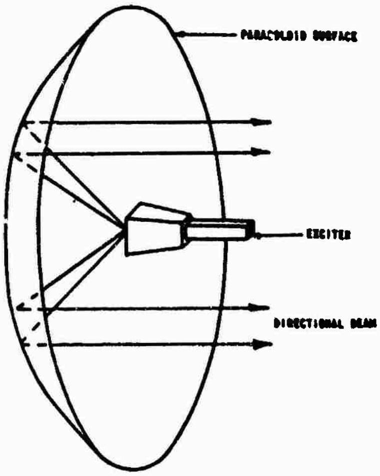

Fig. 1. An Antenna Reflector

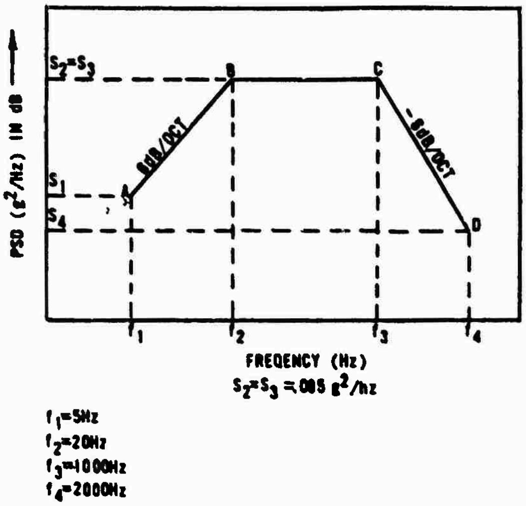

Fig. 2. Design Load for Cantilever Beam

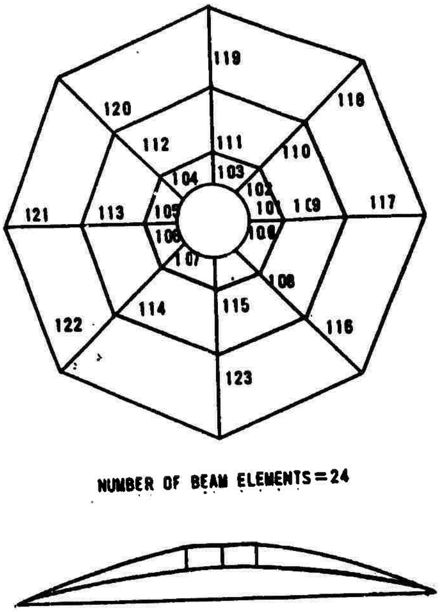

Fig. 3. Beam Elements in Finite Element Model of the Antenna Reflector.

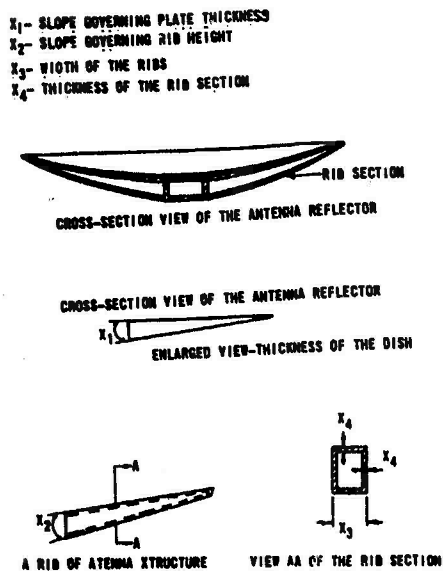

Fig. 4. Design Variables to be Optimized for the Antenna Reflector.

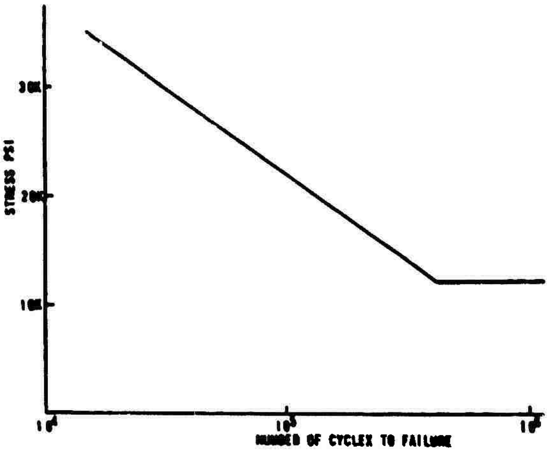

Fig. 5. Typical S-N Curve.

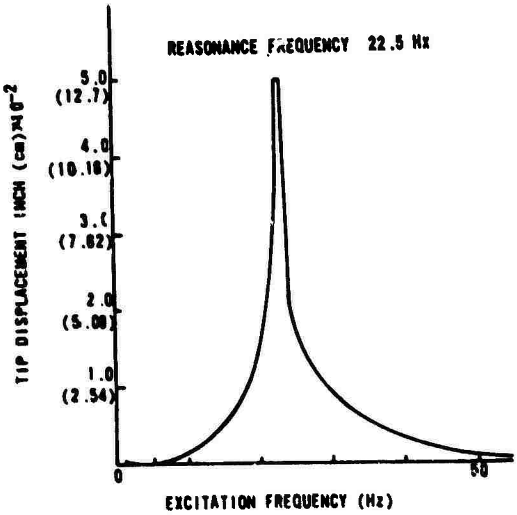

Fig. 6. Frequency Response of the Antenna Structure.

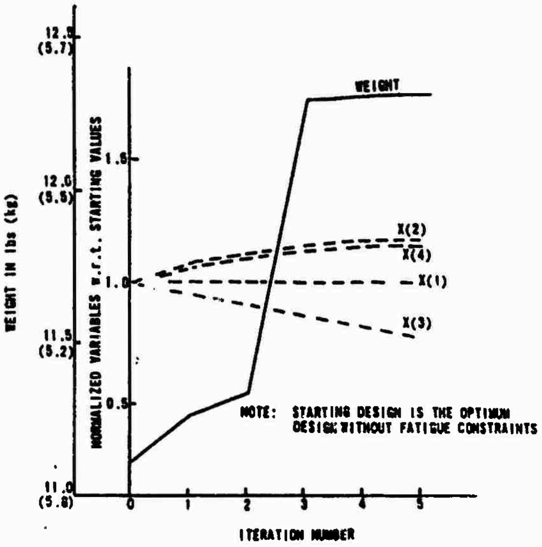

Fig. 7. Design History - Optimization of the Reflector with Fatigue Constraints.

EVALUATION OF VIBRATION SPECIFICATIONS FOR STATIC AND DYNAMIC MATERIAL ALLOWABLES

S. P. Bhatia and J. H. Schmidt
Northrop Corporation, Electronics Division
Hawthorne, California

SUMMARY

A technique was developed previously to correlate sine, shock and random specifications for selecting the highest load or acceleration producing environment for comparison with the static (yield or ultimate) material allowables. The proposed method in this paper extends the above technique so that it not only allows for the direct comparison between sine, shock and random environments using a static (yield) allowable, but also makes this comparison more comprehensive by accounting for fatigue producing environments and the corresponding lower dynamic (fatigue) material allowables. The concept of "equivalent stress" for random vibrations is introduced. The proposed technique allows for a quick and an accurate assessment of the worst vibration environment using both the static and dynamic allowables, helps selection of alternate materials and provides the direction that detailed structural analysis must proceed.

INTRODUCTION

When a structural design is required to meet different vibration environments, it is common not to determine the worst environment, nor to include the effect of these environments on the selection of different materials. In most cases, designs are analyzed in detail for each one of the above environments based on finite element or other methods. After completing this detailed analysis, the structure is either considered satisfactory or modifications are made to the design and/or materials based on each one of these environments. This is a time consuming and uneconomical procedure for structural analysis. It is more desirable to compare all the environments to select the worst one prior to proceeding with the detailed analyses.

The method proposed in this paper provides the engineer with a quick, yet accurate and comprehensive approach to assess different environments that are modified to allow a direct comparison of these on the basis of a common static (yield or ultimate) material allowable. The fatigue producing sine and random environments are adjusted to a common basis with the shock environment so that the effect of static as well as dynamic material allowables is taken into account. This technique also allows evaluation of different materials depending upon the severity of each one of the various environments, whether these are controlled by static or dynamic material allowables. For random vibration environment, the concept of equivalent stress is presented so that this single stress is sufficient to allow comparison of this environment with other environments. This concept also called "reduced stress" was proposed by Harris and Crede (Ref. 1). However, the calculations based on this stress do not result in an accurate damage assessment. The proposed method overcomes this difficulty by accurately taking into account the cumulative damage caused by random vibration environment on the basis of the equivalent stress.

GENERAL APPROACH

As presented in Ref. 2, the vibration environments of sine, shock and random can be directly related and compared to assess the severity of one environment versus another. However, this evaluation is limited to one of comparing the different environments on the basis of acceleration, load or stress in relation to a static (yield or ultimate) material allowable.

In order to be more comprehensive for evaluation of different vibration environments, the possibility exists that a sine or random environment of fairly long duration may be the most severe based upon the detailed fatigue analysis. Using the technique described in Ref. 2 sine, shock, and random vibration environments can be graphically displayed and thus evaluated as shown in Figure 1. This environment comparison does not include any consideration for fatigue. As will be shown, the sine and random environments can be modified to include the effect of lower dynamic material allowables based on the fatigue limits.

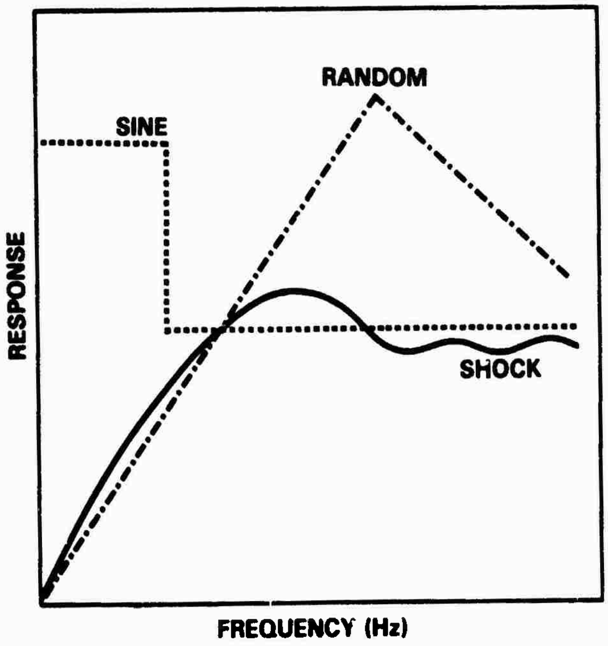

Figure 1. Combined response plots based on static allowable only

The curve for random environment in Figure 1 was based on the definition that 3σ (three sigma) stress levels produce limit loads or stresses that will compare directly to static (yield) material allowables. This does not take into account the fatigue producing characteristic of the random environment.

In order to produce a modified random curve, it is necessary to determine a single stress level that directly reflects consideration for fatigue. Moreover, the dynamic material allowables rather than static material allowables need to be considered for random as well as sine environments which are applied for a specified duration. Three distinct regions of a fatigue S-N curve, as shown in Figure 2, must be addressed as follows:

1) Region A represents a sine or random environment that is of sufficiently short duration so that a comparison to static (yield) material allowable is applicable. This reverts to the previous method of Ref. 2. The results of this comparison are thus the same as those shown in Figure 1.

2) Region B represents a sine or random environment that is of sufficiently long duration to produce enough cycles at any frequency (1×10^8 cycles or greater) so that comparison with dynamic (endurance) material allowable, S_E is required. This case requires only slight modifications. The sine and random curves need to be multiplied by the factor, K_1, defined below based on yield allowable:

$$K_1 = \frac{S_Y}{S_E} \qquad (1)$$

where S_Y = yield allowable, and

S_E = endurance allowable.

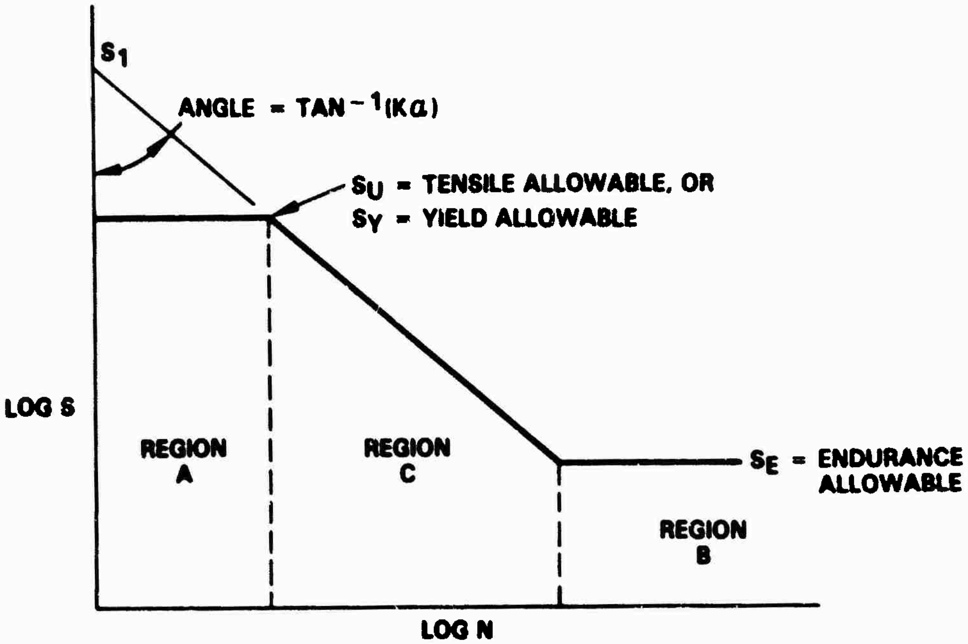

Figure 2. A typical S-N curve

3) Region C is the difficult region and its solution is discussed further in this paper. This region is linearized on a log-log plot by best fitting the following equation using least squares or other methods to the S-N material data points so that

$$N = \left(\frac{S_1}{S}\right)^{K\alpha} \tag{2}$$

Equation (2) can also be written as

$$\log S = \log S_1 - \frac{1}{K\alpha}(\log N) \tag{3}$$

where S = stress level,

N = number of allowable cycles at stress level S,

S_1 = hypothetical stress level to cause fatigue failure at one cycle, and

$K\alpha$ = a material property defined as the inverse of slope of the S-N curve on a log-log scale as shown in Figure 2.

By utilizing Miner's rule for fatigue damage,

$$D = \sum_{i=1}^{m} \left\{ \frac{n_{i\sigma}}{N(S_{i\sigma})} \right\} \tag{4}$$

where D = cumulative fatigue damage, normally set at 1.0 but can be quite different depending upon the material, load sequence and other factors (Ref. 3). The results of this method are not affected by a particular value of D,

m = maximum limit of i in $S_{i\sigma}$ levels,

$n_{i\sigma}$ = number of applied cycles at various stress levels, $S_{i\sigma}$, and

$N(S_{i\sigma})$ = number of allowable cycles at stress levels, $S_{i\sigma}$.

Postulating that for a given structure there exists one equivalent stress level, S_{EQ}, and corresponding number of allowable cycles, $N(S_{EQ})$ that produce damage, D_{EQ}, so that

$$D_{EQ} = \frac{n}{N(S_{EQ})} \tag{5}$$

Since the damage assessment is the same, i.e., $D_{EQ} = D$, equations (4) and (5) yield,

$$\frac{n}{N(S_{EQ})} = \sum_{i=1}^{m} \left\{ \frac{n_{i\sigma}}{N(S_{i\sigma})} \right\} \tag{6}$$

If equation (2) is used to substitute $N(S_{EQ})$ and $N(S_{i\sigma})$ into equation (6), the result is

$$\frac{n}{\left(\frac{S_1}{S_{EQ}}\right)^{K\alpha}} = \sum_{i=1}^{m} \left\{ \frac{n_{i\sigma}}{\left(\frac{S_1}{S_{i\sigma}}\right)^{K\alpha}} \right\} \tag{7}$$

If a Gaussian distribution is assumed with m = 3(3σ stress levels),

$$n_{1\sigma} = 0.683n \tag{8}$$

$$n_{2\sigma} = 0.271n \tag{9}$$

$$n_{3\sigma} = 0.0433n \tag{10}$$

By definition,

$$S_{2\sigma} = 2\,S_{1\sigma} \tag{11}$$

$$S_{3\sigma} = 3\,S_{1\sigma} \tag{12}$$

Substituting from equations (8) through (12) into equations (7) and rearranging:

$$\frac{S_{EQ}}{S_{1\sigma}} = \beta = \left|0.683 + 0.271(2)^{K\alpha} + 0.0433(3)^{K\alpha}\right|^{1/K\alpha} \tag{13}$$

$$\text{or} \quad S_{EQ} = \beta\, S_{1\sigma} \tag{14}$$

Where S_{EQ} is applicable in the region,

$$S_E \le S_{EQ} \le S_Y \tag{15}$$

As can be seen from equation (13), β depends only upon the material property $K\alpha$. The variation of β with the material property $K\alpha$ is shown in Figure 3. β is slightly dependent upon the type of distribution chosen, i.e., Gaussian or Rayleigh, but it is independent of any other variable including the material property S_1, number of applied cycles n, and the stress level $S_{1\sigma}$. Its value is less than three for most of the materials. The relationship shown in equation (14) is important, since this now allows the previous procedure based on static allowables to be extended to include an evaluation of vibration environments for fatigue as well.

PROCEDURE

In general, various components in a structure are made from different materials. To take into account the mechanical properties of these materials, the following procedure is presented to modify different vibration environments so that these are directly comparable.

(a) Compute the ratio $K_1 = S_Y/S_E$ for all the materials. The largest ratio will probably be the worst case.

(b) Obtain $K\alpha$ and β for all materials.

(c) Based on the test duration specified, calculate the number of applied cycles at various frequencies as follows,

$$n = f \times t \tag{16}$$

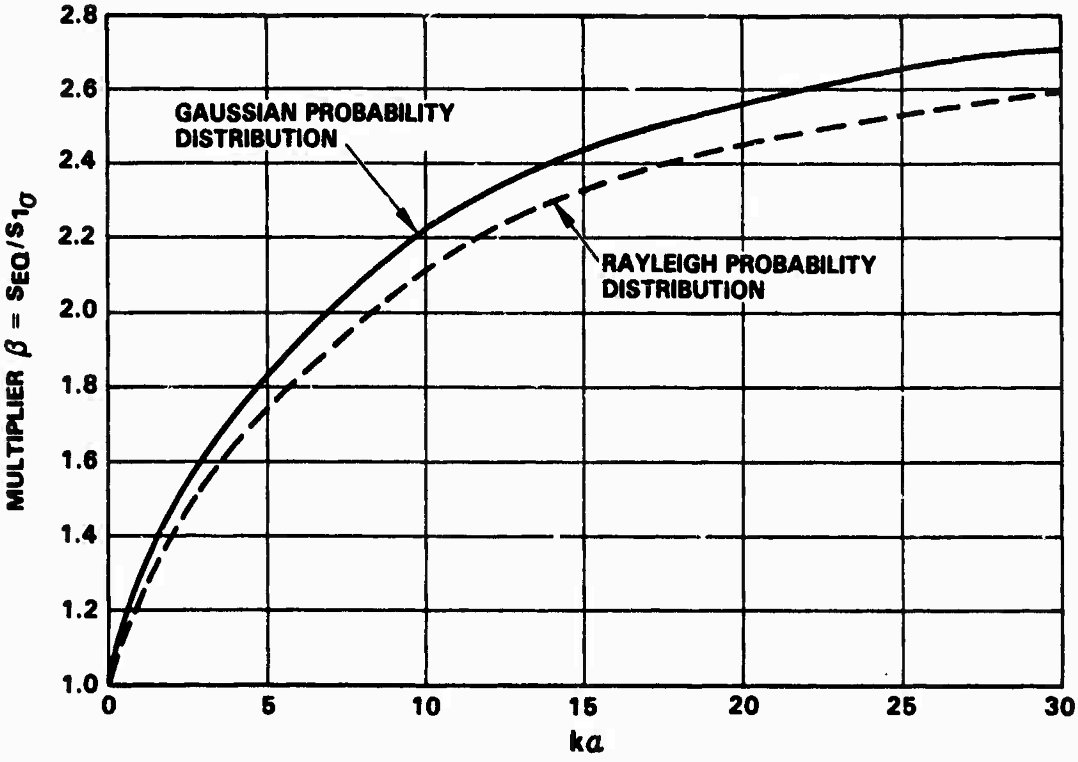

Figure 3. Variation of multiplier β vs. k

where n = number of applied cycles,

f = frequency, Hz,

t = test duration, seconds. For sine environment, it is the dwell time at frequency f.

(d) Obtain the fatigue allowable stress S_F corresponding to number of cycles, n from equation (3) so that,

$$\log S_F = \log S_1 - \frac{1}{K\sigma} (\log n) \qquad (17)$$

(e) Modify the sine environment by multiplying with the factor K_2, where

$$K_2 = \frac{S_Y}{S_F} \qquad (18)$$

(f) Modify the random environment by multiplying with the factor K_3 defined by

$$K_3 = \beta \left(S_Y / S_F \right) \qquad (19)$$

(g) Using the factors K_2 and K_3 defined above in equations (18) and (19) for sine and random environments, respectively, all the environments are directly comparable on a common static (yield) material allowable basis. The effect of lower dynamic (fatigue) material allowables is also taken into account. The modified environments of Figure 1 are plotted in Figure 4. It should be noted that multiplication of the random environment by 3σ is no longer necessary.

(h) Factors K_4 and K_5 are introduced to compare results obtained from this procedure for random environment to those of the previous method. If the random environment is of sufficient duration and the concept of the equivalent stress is not known, it will be desirable to use the endurance limit, S_E, in obtaining the factor K_4 defined below,

$$K_4 = 3 \left(\frac{S_Y}{S_E} \right) \qquad (20)$$

It should be noted that three in equation (20) is based on 3σ. If the random environment is compared with the static (yield) material allowable without taking into account the effect of its fatigue characteristics as reported in Ref. 2, the multiplier K_5 based on 3 levels is used, where

$$K_5 = 3 \qquad (21)$$

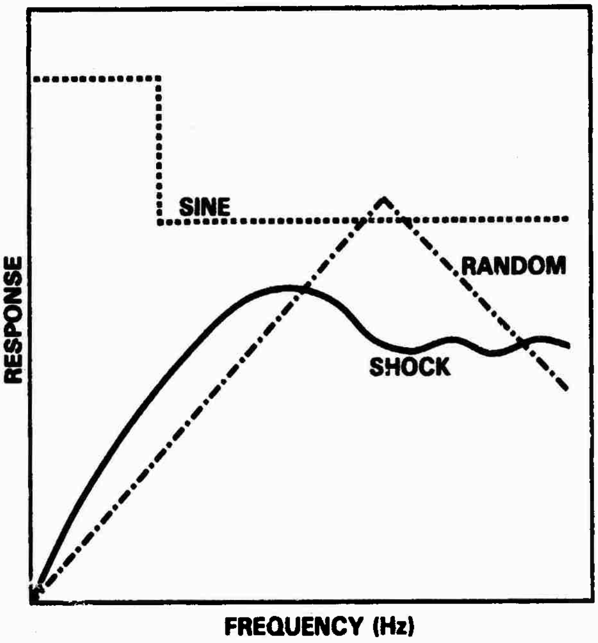

Figure 4. Combined response plots modified for static and dynamic allowables

Comparison of the various multipliers K_3 through K_5 is discussed in the following illustrations.

ILLUSTRATIONS

To apply the technique proposed in this paper, two different materials with the following properties are considered. It should be noted that these materials listed below in Table 1 are selected to cover two extremes of the ratio K_1.

TABLE 1

	EXAMPLE A	EXAMPLE B
Material	Al 7075	SAE 1018
S_Y MPa (ksi)	365.5 (53)	275.9 (40)
S_E MPa (ksi)	89.7 (13)	237.9 (34.5)
$K_1 = S_Y/S_E$	4.08	1.16
S_1 MPa (ksi)	1849.7 (268.2)	650.3 (94.3)
$K\alpha$	5.72	15.12
β	1.890	2.440
t (seconds)	1440	1440

To account for dynamic as well as static material allowables, the test duration is evaluated at various natural frequencies. Assuming a frequency range from 100 to 10,000 Hz, the various factors are calculated as shown in Table 2.

TABLE 2

CALCULATION OF THE VARIOUS FACTORS

Frequency, f (Hz)	Number of Applied Cycles, n	Allowable Fatigue Stress, S_F		K_2[1] For Example		K_3 For Example		K_4 For Example	
		Example A MPa(ksi)	Example B MPa(ksi)	A	B	A	B	A	B
100	1.44×10^5	231.7 (33.6)	296.6 (43.0)	1.58	1.00	2.99	2.44	12.24	3.48
500	7.20×10^5	175.2 (25.4)	266.2 (38.6)	2.09	1.04	3.95	2.54	12.24	3.48
1000	1.44×10^6	155.2 (22.5)	254.5 (36.9)	2.36	1.08	4.46	2.64	12.24	3.48
2000	2.88×10^6	137.2 (19.9)	243.4 (35.3)	2.66	1.13	5.03	2.76	12.24	3.48
10,000	1.44×10^7	103.4 (15.0)	218.6 (31.7)	3.53	1.16	6.67	2.83	12.24	3.48

---

[1] K_2 is allowed to vary between one and K_1 so that $S_E \le S_F \le S_Y$.

The sine response acceleration is multiplied by the factor K_2 so that it can be compared with the shock response spectra. It should be noted that K_2 is kept between 1.0 and K_1 to ensure that S_F is within S_E and S_Y. Furthermore, the random vibration response is multiplied by K_3 based on the concept of the equivalent stress, S_{EQ}, which results in the same cumulative damage as the full spectrum of random vibration environment. All three response spectra are plotted in Figures 5 and 6. The environments are directly comparable since these have been modified for comparison with the static (yield) material allowable. The worst environment is predicted to be random for material A and shock for material B. Thus material A is found to be dynamic (fatigue) critical and material B is judged to be static (yield) critical. The particular environments should be evaluated for further detailed analysis of these materials. The values of multiplier K_4 are also listed in Table 2. Comparison of the random environment based on K_3, K_4 and K_5 for materials A and B is shown in Figures 7 and 8 respectively. These diagrams illustrate that the equivalent stress modifies the random vibration environment to the appropriate levels for material A as well as B without imposing unnecessary severity or too little increase for comparison with the sine and shock environments.

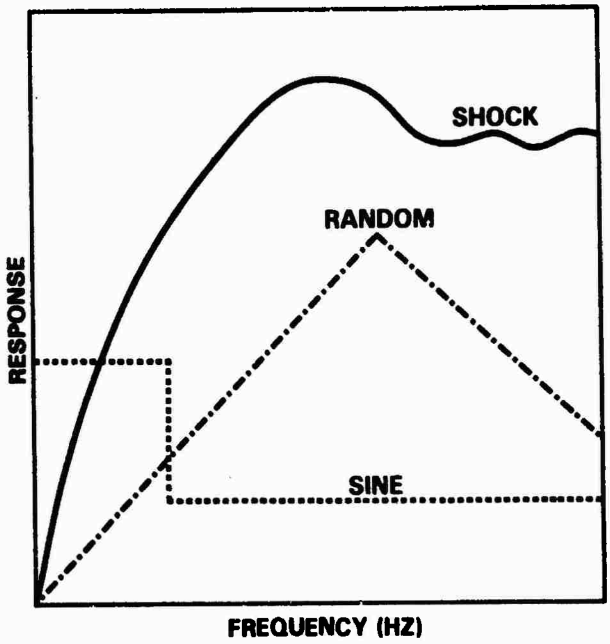

Figure 6. Combined response plots for material B

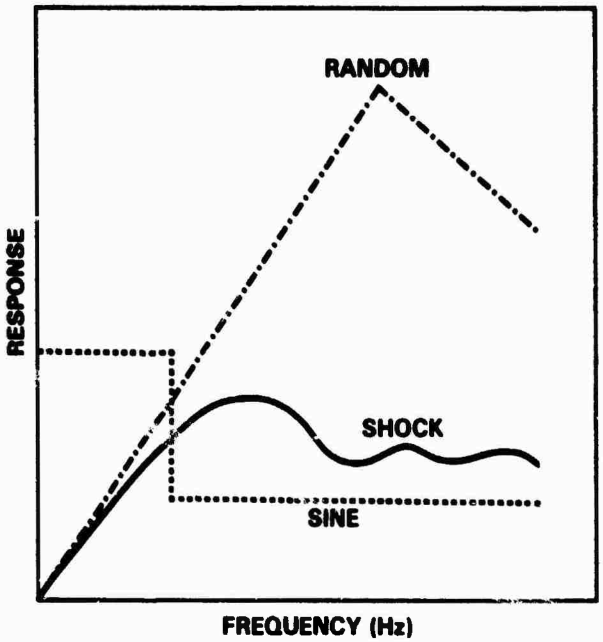

Figure 5. Combined response plots for material A

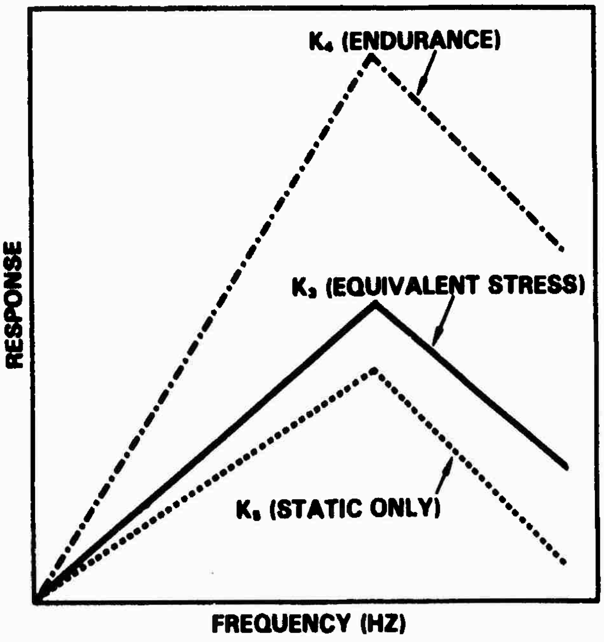

Figure 7. Random vibration response plots for material A modified by different factors

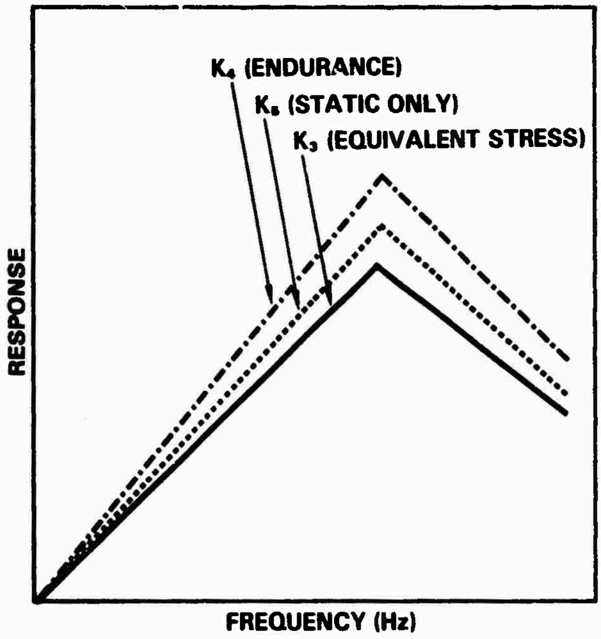

Figure 9. Random vibration response plots for material B modified by different factors

CONCLUSIONS

The method proposed modifies the fatigue producing sine and random environments and takes into account the dynamic material allowables. The concept of equivalent stress provides means to reduce random vibration spectrum to a single stress level with equivalent damage so that comparison with the dynamic material allowable is possible. Direct comparison of sine, shock and random environment on the basis of a common static (yield or ultimate) material allowable is obtained to select only one worst environment for further detailed structural analysis. This is expected to make the analytical evaluation of structures more economical and more comprehensive.

REFERENCES

1. Harris, C.M. and Crede, C.E., Shock and Vibration Handbook, pp. 11-14 to 11-19, McGraw-Hill Book Co., Inc., New York, NY, 1961.
2. Schmidt, J.H., "Quick Look Assessment and Comparison of Vibration Specifications", Shock and Vibration Bulletin 51, Shock and Vibration Information Center, Naval Research Laboratory, Washington D.C., 1981.
3. Faupel, J.H., and Fisher, F.E., Engineering Design, pp. 785-788, John Wiley & Sons, New York, NY, 1981.

Discussion

Mr. Galef (TRW): For reasons that were brought out in Professor Leipholz's paper, there is really no region B, or endurance limit region, except for sinusoidal stress. To clarify that, the occasional 3 sigma, 4 sigma, or 5 sigma limits (by the way, we will have to learn to start multiplying by numbers other than three; there is no particular reason for always talking about 3 sigma limits), the occasional high cycle will start a crack that will continue to propagate at the stresses well below the endurance limit. This has to be considered.

Mr. Bhatia: Yes, you are right. In this procedure we have simplified the S-N curve. However, the method will be applicable if there is no endurance limit. You just drop the line all the way.

Mr. DeLeon (ITT Gilfillan): Where did you get the dynamic material properties?

Mr. Bhatia: We got some from MIL Handbook 5D, and there are aerospace material handbooks available which have some of these properties. In some cases we also had to contact the supplier.

SUPERSONIC FLOW INDUCED CAVITY ACOUSTICS

Leonard L. Shaw
Wright-Patterson Air Force Base
Dayton, Ohio

A wind tunnel test was performed on a cavity model with variable length and depth. It was tested at three supersonic Mach numbers of 1.5, 2.16 and 2.86. Four unit Reynolds numbers, 1.0, 2.0, 3.0, 4.0 million were tested. The model was tested at two angles of attack and two yaw angles. Two cavity widths were tested. Acoustic data were obtained for almost all combinations of the test parameters. Strong acoustic resonance was obtained for many of the configurations and all three Mach numbers. Levels as high as 165 dB were measured. Reynolds number was shown to strongly affect excitation of specific resonant modes. Angle of attack affected the levels as well as yaw. An important result of the effort is the affect of model scale. It was shown that by changing the cavity size, but keeping all other parameters equal, change in the flow induced acoustic levels as large as 20 dB can occur. The purpose of this paper is to document as much of the acoustic data as possible so that the data trends will be available for the user.

INTRODUCTION

Aircraft weapons bays exposed to free stream flow may experience an intense aeroacoustic environment in and around the bay. Experience has taught that the intensity of this environment can be severe enough to result in damage to a store or its internal equipment, or to the structure of the weapons by itself. To assure that a store and the sensitive internal equipment can withstand this hazardous environment and successfully complete its mission, they must be qualified to the most severe sound pressure levels anticipated for the mission. If the qualification test levels are too high, the store and its internal equipment will be overdesigned resulting in unnecessary cost and possible performance penalities. If the levels are below the in-flight levels, the store or its internal equipment may catastrophically fail during performance of the mission. Thus, it is desirable that the expected levels in weapon bays be accurately predicted.

A large number of research efforts have been directed toward understanding flow induced cavity oscillations. However, the phenomenon is still not adequately understood to allow one to predict the fluctuating pressure levels for various configurations. This is especially true at supersonic flow speeds where only a small amount of data are available. Only a few of the many past studies present any supersonic data. Reference 1 presents fluctuating pressure data for Mach numbers up to 5 for various length-to-depth (L/D) ratio cavities. It was conclusively shown that the highest levels occur for an L/D ratio near 2.0. The fluctuating pressure levels presented in Reference 1, even the highest ones, are much lower than data obtained more recently.

Supersonic data up to a Mach number of 3 are available in Reference 2 for three L/D ratios and two Reynolds numbers. The most important result of these data, relative to the current study, is that the narrowband tone generation was eliminated by increasing the flow Reynolds number. By increasing the unit Reynolds number from 0.3 million to 1.5 million completely suppressed the narrowband tone. Thus, the reason the fluctuating pressure levels in Reference 1 are lower than other data is believed to be due to a high test Reynolds number. The actual test Reynolds number was not given.

Additional supersonic data for Mach numbers up to 2 are presented in Reference 3. These data showed that narrowband tone amplification can occur for higher Reynolds number at Mach number 2. The tunnel unit Reynolds number are given but the important value is the local Reynolds number at the cavity leading edge. This value depends on the distance from the test surface leading edge to the cavity leading edge, unfortunately this measurement is not always given.

Based on the above requirements a joint program with the NASA Langley Research Center, Supersonic Aerodynamics Branch was performed. Their interest was mainly static pressure distribution and boundary layer definition. They instrumented the model with static pressure ports and used a static pressure probe to study the boundary layer. The Structural Vibration and Acoustics Branch instrumented the model with microphones to fully define the flow induced acoustics environment in the cavities. The acoustic data were recorded and reduced by the Structural Vibration and Acoustics Branch while the static pressure data were recorded by NASA. The wind tunnel tests were performed at NASA Langley Research Center in the Unitary Flow Facility in Building 1251. Since almost three hundred different test configurations/conditions were tested, a voluminous amount of acoustic data were obtained. Essentially all of the data were published in Reference 6. The purpose of this paper is to document as much of the acoustic data as possible so that data trends from essentially all of the configuration/conditions will be available to the user. This is necessary since the flow induced cavity acoustics levels in a cavity have been shown to be very sensitive to configuration and flow condition, thus making it almost impossible to generalize the results for many configurations.

DESCRIPTION OF THE WIND TUNNEL MODEL AND INSTRUMENTATION

The model consisted of an open rectangular cavity installed in a aerodynamically shaped body. The body was aerodynamically shaped to eliminate shock wave interactions between the wind tunnel walls and the model. Figure 1 shows a side view of the model and Figure 2 shows a front view. The cavity is seen in Figure 2 to be in the center of the model. The model was sting mounted from the rear. The down stream wall of the cavity was remotely adjustable.

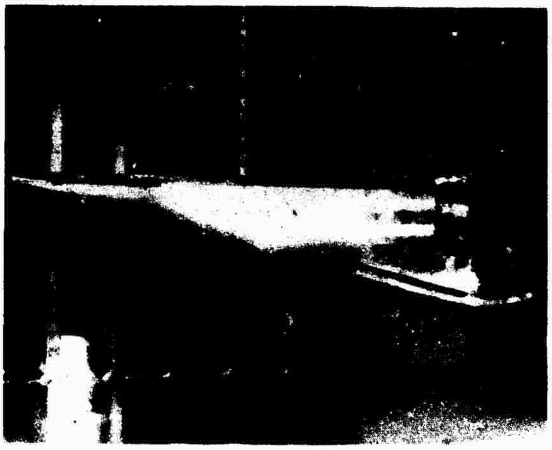

Figure 1 Side View of Model

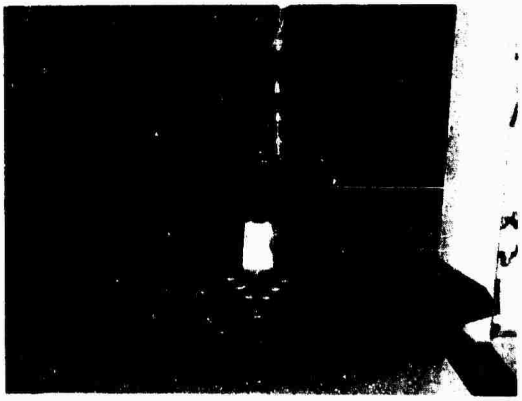

Figure 2 Front View of Model

Figure 3 shows the rear wall in an aft most position. Cavity lengths from 1.5 inches to 12.0 inches were tested. The cavity floor was adjustable to four different depths, but to change the depth required shutting the tunnel down and taking the model apart. The four depths tested were 0.5, 1.0, 2.0, and 2.5 inches. The width of the cavity was also altered by adding spacer blocks to each side. Figure 4 shows the various spacer blocks used to vary the width of the cavity. Since cavity width has been shown to have a very small affect on the flow induced acoustic levels, acoustic data were obtained for only two widths, 2.5 and 1.0 inches.

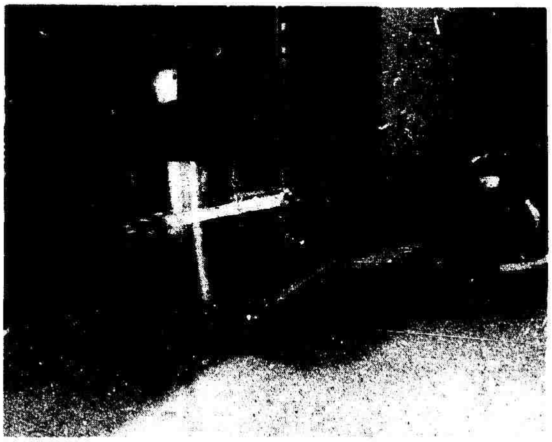

Figure 3 Long Cavity Configurations

Figure 4 Spacer Blocks For Various Widths

The cavity floor was instrumented with 14 high intensity microphones. The microphones were Gulton Industries MVA-2400 1/4 inch piezoelectric transducers. They were located in the cavity as shown in Figure 5. They were spaced every 0.60 inches in the front half of the cavity and 1.20 inches in the back half. Since the downstream wall moved forward to change the length of the cavity, part of the microphones were covered during most of the runs. The signals from the microphones were amplified and recorded on magnetic tape and later reduced in the laboratory.

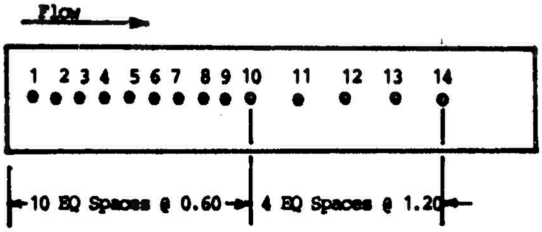

Figure 5 Microphone Locations

DESCRIPTION OF TEST PROCEDURES

The model was installed in the wind tunnel as shown in Figure 1. The cavity was set at a depth of 2.5 inches, and width of 2.5 inches, and length of 12 inches and acoustic data were recorded. The length was changed to 7.5 and 3.75 inches and data recorded at each one. The Mach number was then changed to 2.16 and data were recorded for each one of the three lengths. The angle of attack was changed to -5 degrees and data recorded for each length. Mach number was then changed to 2.86 and each of the parameters were varied and data recorded for each condition. The only changes which required shutting the tunnel down were changing the depth of the cavity or the width. The length was controlled remotely by a motor driven rear wall.

DISCUSSION OF RESULTS

The acoustic data recorded during the wind tunnel test were reduced into narrowband (11.7 Hertz) spectra and plotted with multiple spectra on a plot to illustrate the effect of each test parameter. Spectra for each of the test parameters are presented and discussed below.

Mach Number

It has been believed that flow induced cavity acoustic pressure oscillations were not significantly excited at supersonic speeds (See Reference 2 and 3). The results of this test show that this is not the case. Figure 6 shows spectra for Mach numbers 1.5, 2.16, and 2.86 for Reynolds number of 2.0 million and length-to-depth ratio of 3. The resonant frequencies increase with Mach number as the Rossiter equation predicts. This can be seen at each of the resonant frequencies. The amplitude of the lowest resonant frequency decreases with increasing Mach number. This is what would have been predicted prior to this test. However, a very important result of this test is seen for the second resonant frequency. The amplitude for the second resonant frequency at Mach number 2.16 is nearly as high as the Mach number 1.5 case. In fact, for the fourth and sixth resonant frequency the amplitude for Mach number 2.16 is much greater than at Mach number 1.5. The broadband levels decrease at least 10 dB as the Mach number increases from 1.5 to 2.16 and 2.86. Similar Mach number effects were seen for other cavity configurations and in some cases even more dramatic variation in the amplitude of the resonant frequencies occurred.

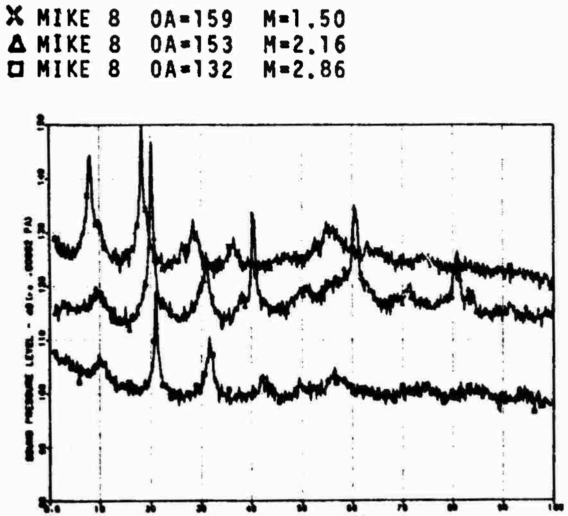

Figure 6 Spectra Showing Effect of Mach Number, D=2.0, L=6, W=2.5, RE=2.0 A=0, B=0

Angle of Attack

Angles of attack of 0 and -5 degrees were tested. In general, having the cavity at a -5 degree angle of attack increases the acoustic levels in the cavity. Both broadband levels and resonant frequencies levels are increased. Figure 7 shows spectra at 0 and -5 degrees for a Mach number of 2.86 and length-to-depth ratio of 3. The broadband levels increased about 7 dB and the resonant frequencies as much as 25 dB. The sixth resonant frequency was not excited at 0 degrees angle of attack but is 20 dB above the broadband level for -5 degrees angle of attack. Thus the angle of attack of a cavity could significantly (25 dB) increase the flow induced acoustic levels at supersonic flow speeds.

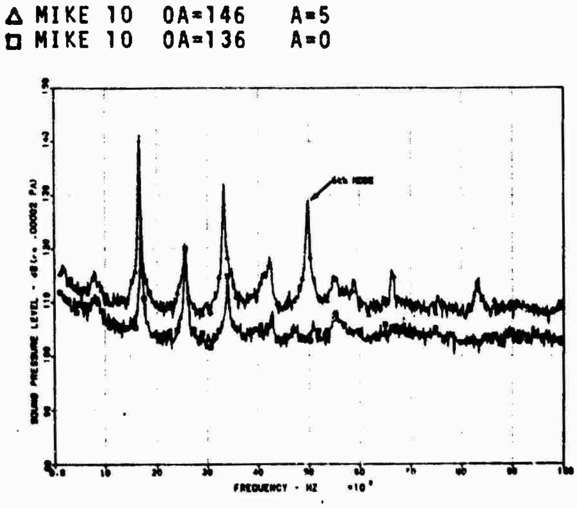

Figure 7 Spectra Showing Effect of Angle of Attack, D=2.5, L=7.5, W=2.5, RE=2.0, B=0

Reynolds Number

Unit Reynolds numbers of 1, 2, 3, and 4 million were achieved during the test. Figure 8 shows spectra for all four Reynolds numbers for a Mach number of 2.86 and length to depth ratio of 6. The broadband levels show an ordered increase with increasing Reynolds number. One cannot say that Reynolds numbers alone caused the increase since wind tunnel pressure is changed to change Reynolds number which also changes the dynamic pressure. Since the effects of dynamic pressure are well defined they can be accounted for leaving the real Reynolds number effect. To go from a Reynolds number of 1 million to 2 million requires doubling the tunnel pressure which also doubles the dynamic pressure for a constant Mach number. This causes a 3 dB increase in the flow induced acoustic levels in the cavity. If this 3 dB increase is accounted for the actual Reynolds number effect is minimized. This is true except at the fifth resonant frequency where the level shoots up 30 dB for a Reynolds number of 1 million per foot. These surprises can be important since an aircraft flying at supersonic speeds at higher altitude can experience a Reynolds number of 1 million per foot.

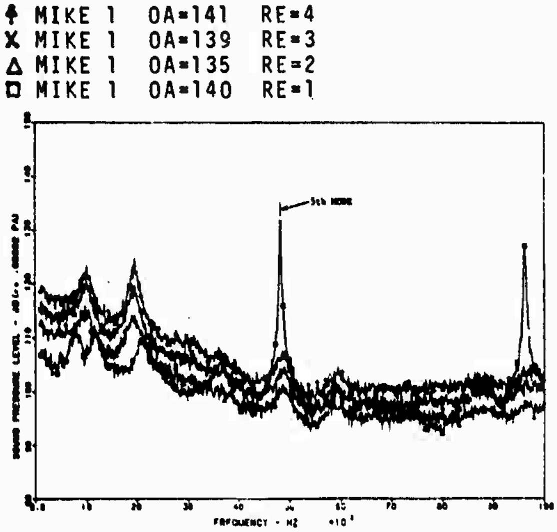

Figure 8 Spectra Showing Effect of Reynolds Number, D=1.0, L=6, W=2.5, M=2.86, A=0, B=0

Yaw

The model was tested at yaw angles of 0 and 3 degrees. Figure 9 shows spectra for 0 and 3 degrees yaw for a Mach number of 2.16 and length-to-depth ratio of 3. For these and other spectra yaw generally have little impact on the levels. especially the broadband levels. However, in some cases 3 degrees of yaw greatly increased the resonant frequency amplitudes as seen in Figure 9 for the first resonant frequency.

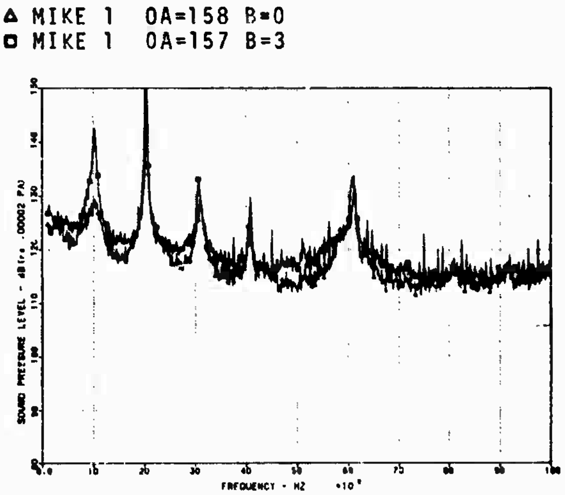

Figure 9 Spectra Showing Effect of Yaw, D=2.0, L=6, W=2.5, RE=2.0, A=0, M=2.16

Depth

The model was tested at depths of 0.5, 1.0, 2.0 and 2.5 inches. Figure 10 presents data for depths of 0.5, 1.0, and 2.0 inches for a Mach number of 1.5. There are significant variations in both the broadband and resonant frequency levels. For the 0.5 inch depth there are no resonant excitation frequencies. This is because the model length was 6 inches which gave a length-to-depth ratio of 12. At this length-to-depth ratio flow induced acoustic excitation do not normally occur because the free stream flow reattaches to the cavity floor preventing feedback to occur within the cavity. At a cavity depth of 1.0 inch fairly strong excitation occurs, especially at the second resonant frequency. This is a length-to-depth ratio of 6. For the 2 inch depth the levels are even higher at most all frequencies. This is a length-to-depth ratio of 3. For different cavity lengths depth had dramatic affects also. For example, at a length of 1.5 inches depth mode response occurred at very high frequencies.

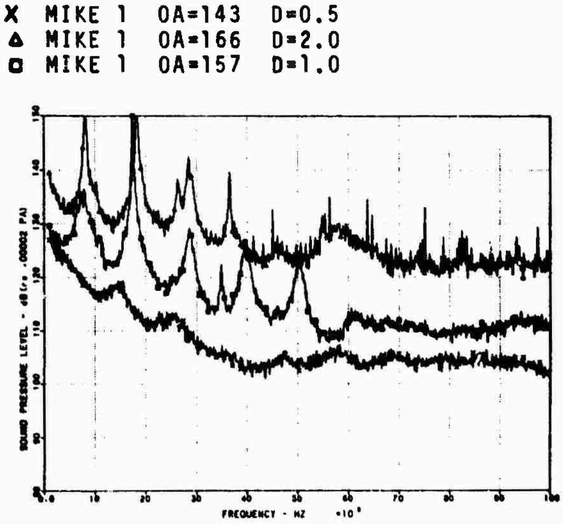

Figure 10 Spectra Showing Effect of Depth, L=6, W=2.5, RE=2, M=1.5, A=0, B=0

Length

The model was tested at lengths of 1.5, 3, 6, and 12 inches. Results for all four lengths are shown in Figure 11 for a Mach number of 1.5 and depth of 1.0 inch. First looking at the spectra there appears to be no trend with length. The reason for this is that all of the spectra are from microphone 2 which means that for each length microphone 2 is at different normalized longitudinal locations. Since it is well known that the resonant frequencies exhibit longitudinal mode shapes, having the measurement location at different normalized longitudinal locations would cause different levels to be measured. This partly explains the wide variation of the data. The other cause is that the length-to-depth ratio is greatly different (L/D from 1.5 to 12). For the 12 inch long case (L/D=12) there is no resonant response. For the 6 inch case (L/D 26) there is a fair amount of response. For the 3 inch case (L/D=3) there is strong response. For the 1.5 inch case (L/D=1.5) there also is response but it occurs at much higher frequencies since the resonant frequencies scale with length.

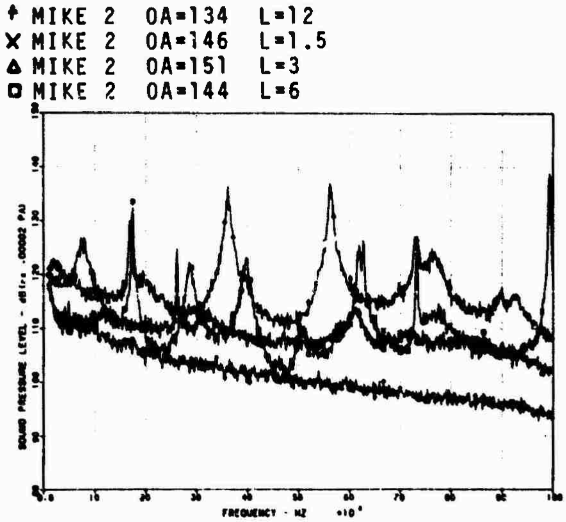

Figure 11 Spectra Showing Effect of Length, D=1.0, W=2.5, RE=2.0, M=1.5, A=0, B=0

Width

Data were obtained for two cavity widths of 1.0 and 2.5 inches. Figure 12 shows the data for both widths for Mach number of 2.86 and length-to-depth ratio of 6. The results were enlightening in that a smaller effect of width was anticipated. In general the smaller width had mixed effect on amplitudes but clearly reduced the frequency of the resonant modes. The resonant frequencies have clearly been shown to be a function of cavity length, not any function of width. A possible explanation for the decrease in frequency at the smaller width is the boundary layers occurring on the side wall of the cavity. This causes the acoustic feedback waves to propagate mostly through boundary layer velocity gradients resulting in the waves being bent and traveling a slightly longer distance to reach the leading edge making the cavity appear slightly longer, thus causing the resonant frequency to decrease slightly. This decrease in resonant frequency was seen in all the narrow cavity data for all the test conditions.

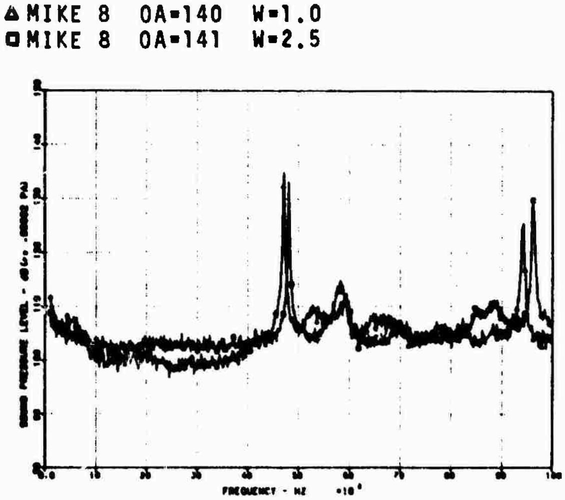

Figure 12 Spectra Showing Effect of Width, D=1.0, L=6.0, RE=1.0, M=2.86, A=0, B=0

Spatial

Microphones were located along the floor of the cavity at fourteen locations. Only part of the microphones were exposed at the shorter cavity lengths. Data from microphones 1-4 for a cavity length of 3 inches and Mach number of 2.16 are shown in Figure 13. The broadband levels vary as much as 12 dB and the resonant frequency amplitude vary as much as 18 dB. It is important to know the measurement location in a cavity. Generally the broadband levels increase towards the rear of the cavity. The resonant frequencies represent standing waves in the cavity so each measurement location will be at a different location on the wave. The lowest resonant frequency has one node near the center of the cavity and the second resonant frequency has two nodes. Microphones 1-4 are located at normalized locations of 0.2, 0.4, 0.6, and 0.8 respectively for the 3 inch length cavity. It is seen in Figure 13 that for mode 1 the levels vary greatly but at mode 2 there is only a small change in amplitude. The reason is the measurement locations fall at different positions on the standing waves. For mode 2 they happen to fall at approximately equal amplitude positions.

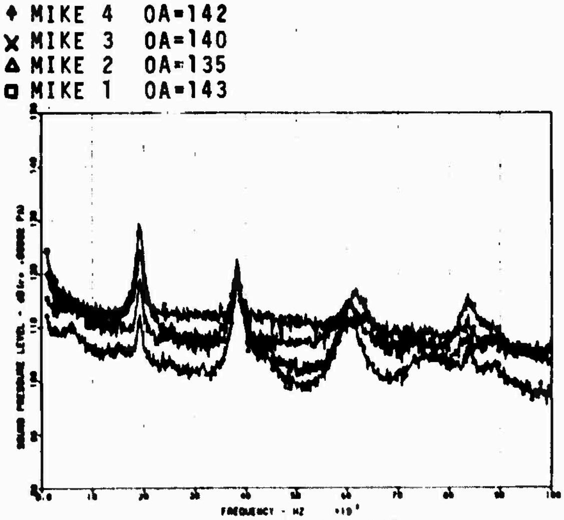

Figure 13 Spectra Showing Effect of Spatial Location, D=1.0, L=3, W=2.5, RE=2.0, M=2.16, A=0, B=0

Scale

There is question as to what affect the scale of the cavity has on the flow induced acoustic environment (e.g. see Reference 2). Specific combinations of cavity length and depth were selected to give the same L/D ratio. Figure 14 presents data for four cavities with the same L/D ratio of 3. Different microphones were selected to be at the same normalized measurement location for each cavity. This normalized location is 0.4 from the leading edge. The data represent the same L/D ratio and the same location on the standing waves in the cavities. If one resonant frequency is selected and compared to the other scale data, the affect of scale size can be determined. Consider the 6 inch length case and the mode near 1,/50 Hertz. Compare it to the 3 inch long cavity and there should be a peak at about 3,500 Hertz and there is one. However, it is 14 dB lower. Now compare it to the 1.5 inch case and there should be a peak near 7,000 Hertz and there is but its amplitude is back up to be same level as the 6 inch case. Other comparisons like this could be made and show different results also. This points out the problem of scaling the data from one scale size to another, especially from model size to full scale aircraft. The problem is not understood but is believed to be due to not accounting for the boundary layer scale at the leading edge of the cavity. However, in this case the boundary layer was the same thickness for each scale size but the results did not show a specific trend with scale size. This leads one to believe that the feedback mechanism is also a function of the boundary layer thickness.

♦ MIKE 1	OA=158	D=0.5	L=1.5
× MIKE 5	OA=139	D=2.5	L=7.5
△ MIKE 4	OA=158	D=2.0	L=6.0
□ MIKE 2	OA=151	D=1.0	L=3.0

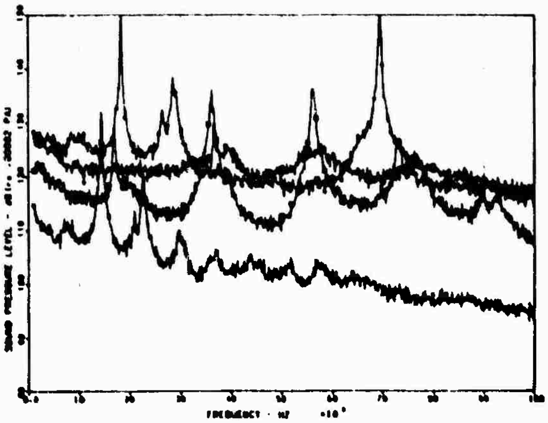

Figure 14 Spectra Showing Effect of Scale Size, W=2.5, RE=2.0, M=1.5, L/D=3.0

CONCLUSIONS

The results of this wind tunnel test clearly indicate that strong flow induced acoustic pressure oscillations can occur in cavities exposed to supersonic free stream flow. Overall levels as high as 165 dB can be generated. The scale of the model selected for testing may not give as high of levels as a model of another scale size. This could lead to significant errors in predicting full scale environments. Differences as large as 20 dB can occur.

REFERENCES

1. Plumblee, H.E., Gibson, J.S. and Lassiter, L.W. "A Theoretical and Experimental Investigation of the Acoustic Response of Cavities in an Aerodynamic Flow," WADD-TR-61-75, USAF, March 1962.

2. Heller, H.H., Holmes, G. and Covert, E.E., "Flow-Induced Pressure Oscillations in Shallow Cavities," AFFDL-TR-70-104, December 1970.

3. Heller, H.H., and Bliss, D.B., "Aerodynamically Induced Pressure Oscillations in Cavities-Physical Mechanisms and Suppression Concepts," AFFDL-TR-74-133, February 1975.

4. Speaker, W.V., and Ailman, C.M., "Spectra and Space-Time Correlations of the Fluctuating Pressures at a Wall Beneath a Supersonic Turbulent Boundary Layer Perturbed by Steps and Shock Waves," NASA CR-486, May 1966.

5. Rossiter, J.E., "Wind Tunnel Experments on the Flow over Rectangular Cavities at Subsonic and Transonic Speeds," R&M No 343B, Royal Aircraft Establishment, 1964.

6. Shaw, L.L., and Reed, S.A., "Supersonic Flow Induced Cavity Acoustics," AFWAL-TM-85-21J-FIBG, December 1985.

U.S. GOVERNMENT PRINTING OFFICE:1986-491-626/40009